Geochemical thresholds for vanadium throughout Korea and at potential development sites

Joo Sung Ahn[1], Seung-Jun Youm[1], Yong-Chan Cho[1]
[1]Mineral Resources Division, Korea Institute of Geoscience and Mineral Resources, Korea

Abstract. As the industrial demand and use of vanadium increases, it is necessary to explore its new sources in Korea. In this study, using geospatial chemical data, we derived geochemical threshold values for the entire country and identified areas prospective for vanadium deposits. The regional (country-wide) threshold value was derived using logarithmic transformation of raw data (n = 23,548) of the first- and second-order stream sediments collected across the country in the late 1990s and the early 2000s. The median +2 median absolute deviation (MAD) and Tukey inner fence (TIF = Q75 +1.5 interquartile range) values were 116 mg/kg and 200 mg/kg, respectively. Of these, the TIF standard, which showed 0.6 % of data exceeding the threshold, was judged to be appropriate for distinguishing clear enrichment or contamination of vanadium. In the case of the Geumsan and Pocheon, areas with potential for vanadium development, the TIF and median +2 MAD values of 259 mg/kg and 218 mg/kg, respectively, can be used as the criteria for evaluating the impact of environmental pollution before and after deposit development.

1 Introduction

Vanadium is widely used not only in alloys but also for specialized industrial applications, and the demand for vanadium is expected to increase further (Imtiaz et al. 2015). However, most of the world's reserves are stored in three countries, China, Russia, and South Africa, and more than 90% of the world's production is concentrated in these countries. In Korea, the possibility of the existence of vanadium deposits is suggested in the Geumsan area located in the central part and the Pocheon area located in the northern part of the country (Kim et al. 1994; Lee et al. 1997), and high-efficiency beneficiation and smelting technologies are being developed to secure stable vanadium raw materials.

Vanadium, like most heavy metal elements, has no human health effect or may be beneficial at low concentrations; however, it can be toxic at high concentrations. Prolonged exposure to vanadium has been shown to have toxic effects on the respiratory and digestive systems, kidneys, liver, skin, immune system, and cardiovascular system (Jayawardana et al. 2015). However, compared to those on toxic heavy metal elements such as lead and cadmium, environmental studies on vanadium are insufficient, as are worldwide environmental regulations for soils and drinking water.

One of the various purposes of creating a geochemical map is to derive the geochemical background and threshold values. The geochemical background concentration of a specific element can be said to indicate the average concentration exhibited by geological conditions and geochemical reactions in a natural environment where no contamination has occurred. In the case of vanadium, domestically and internationally, environmental standards are insufficient; therefore, the use of regional or local geochemical threshold data is necessary. In particular, this information can be used as a pollution criterion or remediation target value in post-mine development impact assessment and can be applied as basic data for risk assessment. The purpose of this study was to use the national geochemical dataset of Korea (KIGAM 2007) to establish the national-scale regional threshold and the local threshold values of vanadium in the potential mine development areas.

2 Regional geochemical map of Korea

The national geochemical mapping project was performed with the final goal of producing a geochemical map for each element and establishing domestic evaluation criteria for the evaluation of geochemical disasters in Korea (KIGAM 2007). The geochemical map was produced in compliance with the IUGS Global Geochemical Baselines mapping program (Darnley et al. 1995). Sample collection was performed using surficial sediments in first- and second-order streams as representative samples of national catchment basins. Each sample represented composite material over a stream length of 50 m, and approximately 100 g of samples was obtained by wet sieving through a 100-mesh sieve (<150 μm). The entire target area was approximately 97,753 km^2, and 23,696 samples were collected at a density of approximately one site per 4.13 km^2 (Figure 1).

For stream sediment samples, quantitative analyses were performed to determine the concentrations of major and minor oxides, including Al_2O_3, CaO, Fe_2O_3, K_2O, MgO, MnO, Na_2O, P_2O_5, SiO_2, and TiO_2, and 26 trace elements, including As, Ba, Be, Bi, Cd, Ce, Co, Cr, Cs, Cu, Eu, Hf, Li, Mo, Nb, Ni, Pb, Rb, Sb, Sc, Sr, Th, V, Yb, Zn, and Zr using X-ray fluorescence (XRF), inductively coupled plasma-atomic emission spectroscopy (ICP-AES), and neutron activation analysis (NAA). Rigorous quality control was performed using certified reference materials, field duplicate samples and analytical blanks. The precision and accuracy of the analytical data were satisfactory.

Finally, provincial geochemical maps for 22 elements were produced using an interpolation technique of inverse distance weighting (KIGAM 2007).

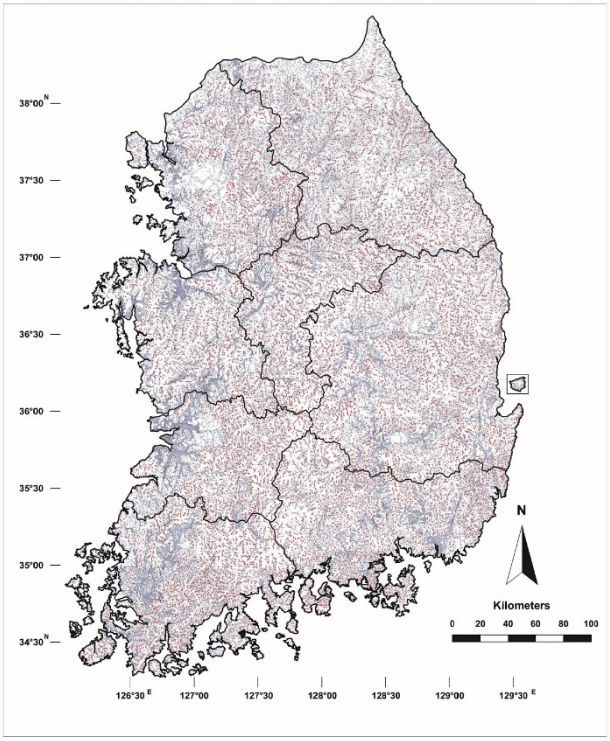

Figure 1. Stream distributions and sampling locations of the Geochemical Atlas of Korea (KIGAM 2007)

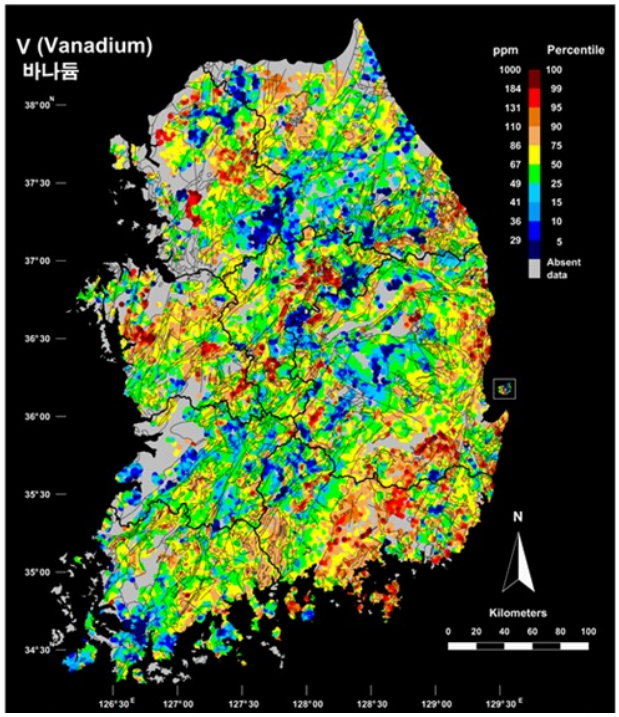

Figure 2. Geochemical map of vanadium in Korea (KIGAM 2007)

3 Geochemical threshold values for vanadium

3.1 Regional distribution

A vanadium geochemical map of Korea is shown in Figure 2. Points in blue indicate a low content of less than 50 mg/kg, and those in red indicate a high content of 100 mg/kg or more. The vanadium content in stream sediments is generally governed by the mineralogical composition of the parent material. Vanadium appears at relatively high concentrations (> 80 mg/kg) in the Okcheon Supergroup, Josen Supergroup, Gyeonggi Gneiss Complex, and Precambrian banded biotite gneiss. In contrast, the concentration is relatively low (< 50 mg/kg) in plutonic rocks, including granites of the Cretaceous, Jurassic, and Permo-Triassic periods. The distribution of vanadium content in the geochemical map agrees well with the distribution of such rock formations (KIGAM 2007). In the geochemical map, specific enriched zones in the range of 100–300 mg/kg are identified. These zones can be considered promising sites for vanadium deposit development.

3.2 Regional geochemical threshold

The vanadium content of the stream sediment samples in Korea was in the range of 2.1–1,000 mg/kg, with a median value of 66.8 mg/kg and an average value of 71.5 mg/kg (Figure 3). As can be seen in the histograms and box plots, the original data (Figure 3) of vanadium content are largely skewed to the right (skewness 4.34) with 821 outliers exceeding the upper inner fence value of 142 mg/kg, which is a typical asymmetric pattern of geochemical data. Therefore, a common logarithm transformation was applied for calculation of the geochemical threshold resulting in a generally symmetrical form as shown in Figure 3.

The calculated median +2 MAD was 116 mg/kg, with 1,908 data points exceeding the threshold value, accounting for 8.1% of the total data (Table 1). This value was higher than the 90th percentile (110 mg/kg) and lower than the 95th percentile (131 mg/kg). In the case of TIF, the threshold value was 200 mg/kg, with 151 data points (corresponding to 0.6%) exceeding this value. The threshold value was much higher than even the 97.5th percentile (151 mg/kg). As expected, the TIF method provided higher threshold values than the more conservative median +2 MAD method. A comparison of the two methods for calculating the geochemical threshold of vanadium in Korea showed that the median +2 MAD method derived a threshold value between the 90th and 95th percentiles, while the TIF approach resulted in a higher threshold value, above the 97.5th percentile. This is similar to the calculations of geochemical thresholds of 59 elements in Australian surface soil in the NGSA project (Reimann & Caritat 2017), 53 elements in European agricultural soil in the GEMAS project (Reimann et. 2018), and eight potentially toxic elements in Bulgarian soil quality monitoring networks (Yotova et al. 2018).

The average upper crust content that can be considered as the geochemical background concentration of vanadium has been suggested to be 53 mg/kg (Wedepohl 1995), 97 mg/kg (McDonough and Sun 1995), 110 mg/kg (Adriano 1986), or 135 mg/kg (Kabata-Pendias 2011). Compared with these values, the median +2 MAD

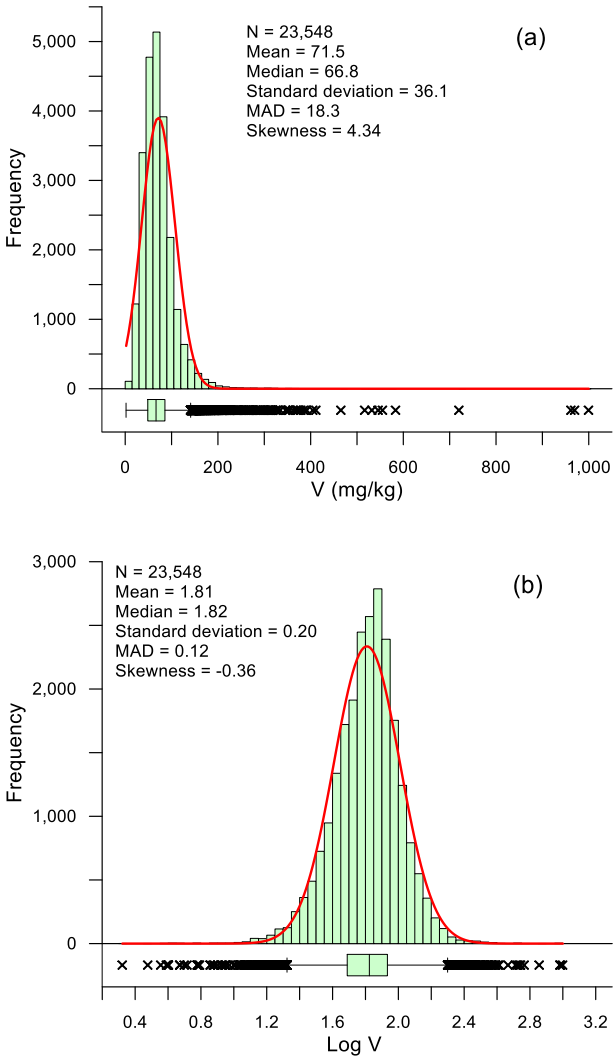

Figure 3. Histograms and boxplots of the raw (a) and log-transformed (b) vanadium data of stream sediments in Korea

value of 116 mg/kg as a geochemical threshold has no discrimination and is a conservatively low standard leading to too many points to be evaluated as a results of vanadium enrichment or contamination. In the case of TIF, the obtained value is two to four times that of these threshold values, and only 0.6% of the total data exceeded the threshold limit. This is much lower than the 2.5% outlier ratio of classical statistics, and can be judged as a completely enriched or contaminated point based on a rather high trend.

3.3 Local distribution and geochemical threshold of vanadium

The distribution of the Okcheon Supergroup in the Geumsan area and the iron mine in the Pocheon area are promising areas for the development of vanadium deposits in Korea. The presence of high vanadium content was known in accordance with the high uranium content in the Geumsan area from previous exploration surveys. The iron mine in the Pocheon area, in which titanium-bearing magnetite

Table 1. Statistics and geochemical threshold values for vanadium of stream sediments in Korea

Statistics	V (mg/kg)	N (> threshold)
N	23,548	
Min	2.1	
Q25	49	
Median	67	
Q75	86	
Q90	110	2,340 (9.9%)
Q95	131	1,168 (5.0%)
Q97.5	151	591 (2.5%)
Max	1,000	
IQR (Q75-Q25)	37	
Median +2 MAD*	116	1,908 (8.1%)
TIF*	200	151 (0.6%)

*Calculated from the log-transformed data
IQR : interquartile range

is concentrated in an alkaline porphyry rock body, also has vanadiferous titanomagnetite ores.

Table 2 shows the results of the geochemical threshold calculation using median +2 MAD and TIF based on log-transformed data for 33 locations in Geumsan and 20 locations in Pocheon around each potential development site. The vanadium content in the Geumsan area ranged from 56 to 270 mg/kg, with an average of 122 mg/kg and median of 116 mg/kg. Regarding geochemical thresholds, the median +2 MAD was 177 mg/kg and the TIF was 259 mg/kg. This is a much higher result than the value derived for the entire country, indicating that vanadium is relatively enriched in this area.

The vanadium content in the Pocheon area ranged from 37 to 236 mg/kg, with an average of 100 mg/kg and median of 93 mg/kg. The median +2 MAD and TIF geochemical thresholds were 218 mg/kg and 377 mg/kg, respectively (Table 2). The derived threshold values were higher than those of the Geumsan area. This is because the difference between the 75th and 25th percentiles is greater, that is, the content dispersion is larger.

When compared to the value of 200 mg/kg determined to be the domestic regional geochemical threshold, we believe that the values of 259 mg/kg and 218 mg/kg obtained using the TIF method for the Geumsan area and the median +2 MAD for the Pocheon area, respectively, are appropriate and valid as the local geochemical thresholds for each research area. The fact that the calculated geochemical thresholds in the Geumsan and Pocheon areas are substantially higher than those of the entire country implies the enrichment of vanadium in these areas, suggesting that in response, environmental management standards should be set high. The derived geochemical threshold can be used as basic data for assessing environmental pollution resulting from surface disturbances or waste generation because of the development of vanadium deposits in these areas.

Table 2. Statistics and geochemical threshold values for vanadium content in stream sediments from the Geumsan and Pocheon areas

Statistics	Geumsan (mg/kg)	Pocheon (mg/kg)
N	33	20
Min	56	37
Q25	94	58
Mean	122	100
Median	116	93
Q75	141	123
Q90	178	177
Q95	211	199
Q97.5	249	217
Max	270	236
IQR (Q75-Q25)	47	65
Standard deviation	49.1	55.1
Skewness	1.20	0.99
Median +2 MAD*	177	218
(N > threshold)	(4)	(1)
TIF*	259	377
(N > threshold)	(1)	(0)

*Calculated from the log-transformed data
IQR : interquartile range

4 Conclusion

Regional and local geochemical thresholds for vanadium, which has insufficient environmental standards, were derived using the first- and second-order sediment geochemical data from the Korean national geochemical map prepared in the early 2000s. A threshold for anomalous vanadium concentrations was determined by using median +2 MAD and TIF statistics. The median +2 MAD and TIF values were derived as 116 mg/kg and 200 mg/kg, respectively, as regional thresholds of vanadium for the country. When applying the TIF, the outlier rate was 0.6%, which is a rather high standard compared to suggested upper crust contents; however, it is expected to be used as a standard to clearly classify enrichment caused either by the presence of vanadium mineralization or by anthropogenic contamination.

Regarding local geochemical thresholds for the Geumsan and Pocheon areas, which were suggested to have potential for vanadium mine development, the derived values were 259 mg/kg (TIF) and 218 mg/kg (median +2 MAD), respectively. We believe that each value will serve as a basis for evaluating the developmental impact in each area.

Acknowledgements

This research was supported by the Basic Research Project (Code: 23-3412-2) of the Korea Institute of Geoscience and Mineral Resources funded by the Ministry of Science and ICT, Korea.

References

Adriano DC (1986) Trace elements in the terrestrial environment. New York: Spring-Verlag.

Darnley AG, Bj€orklund A, Bølviken B, Gustavsson N, Koval PV, Plant JA, Steenfelt A, Tauchid M, Xuejing X, Garrett RG, Hall GEM (1995) A Global Geochemical Database for Environmental and Resource Management. Final Report of IGCP Project 259. Earth Sciences 19. Paris: UNESCO Publishing.

Imtiaz M, Rizwan MS, Xiong S, Li H, Ashraf M, Shahzad SM, Shahzad M, Rizwan M, Tu S (2015) Vanadium, recent advancements and research prospects: A review. Environ Intl 80: 79–88.

Jayawardana DT, Pitawala HMTGA, Ishiga H (2015) Geochemical evidence for the accumulation of vanadium in soils of chronic kidney disease areas in Sri Lanka. Environ Earth Sci 73:5415–5424.

KIGAM (2007) Geochemical Atlas of Korea (1:1,800,000), Series 9. Korea Institute of Geoscience & Mineral Resources

Kim KH, Lee HJ, Chon HT (1994) Ore genesis of the Yonchon titaniferous iron ore deposits, South Korea. Econ Environ Geol 27:117–130.

Lee CH, Lee HK, Shin MA (1997) Barium-vanadium muscovite of coaly metapelite in the Hoenam area of the Ogcheon Supergroup, Korea. J Geol Soc Korea 33:55–64.

McDonough WF, Sun S (1995) The composition of the Earth. Chem Geol 120:223–253.

Reimann C, Caritat Pde (2017) Establishing geochemical background variation and threshold values for 59 elements in Australian surface soil. Sci Tot Environ 578:633–648.

Reimann C, Fabian K, Birke M, Filzmoser P, Demetriades A, Negrel P, Oorts K, Matschullat J, Caritat Pde, The GEMAS Project Team (2018) GEMAS: Establishing geochemical background and threshold for 53 chemical elements in European agricultural soil. Appl Geochem 88:302–318.

Wedepohl KH (1995) The composition of the continental crust. Geochem Cosmochim Acta 59:1217–1232.

Yotova G, Padareva M, Hristova M, Astel A, Georgieva M, Dinev N, Tsakovski S (2018) Establishment of geochemical background and threshold values for 8 potential toxic elements in the Bulgarian soil quality monitoring network. Sci Tot Environ 643:1297–1303.

Reassessing the source controls of Ni sulfide mineral systems

Daryl E. Blanks[1], David A. Holwell[1], Marco L. Fiorentini[2], Isra S. Ezad[3], Jason M. Bennett[2], Stephen F. Foley[3], Weronika Gorczyk[2], Nicole Januszczak[4], Lisa Hart-Madigan[5], Steven Rennick[6]
[1]Centre for Sustainable Resource Extraction, University of Leicester, UK
[2]Centre for Exploration Targeting, School of Earth Sciences, University of Western Australia, Perth, Australia
[3]School of Natural Sciences, Macquarie University, New South Wales, Australia
[4]Resource Centre of Excellence, BHP, Toronto, Canada
[5]Metals Exploration, BHP, London, UK
[6]Metals Exploration, BHP, Perth, Australia

Abstract. The composition of magmatic sulfide deposits is controlled by the metal budget of the magma, which itself is controlled by the composition of the mantle source and degree of partial melting. Traditional models assume that high degrees of partial melting (>15%) are required to sufficiently liberate Cu and PGE from sulfide and Ni from olivine, assuming peridotitic mantle rocks. However, we show that hydrous pyroxenite in the mantle hosts Ni and other critical metals in minerals such as phlogopite and amphibole, which have significantly lower melting temperatures than olivine. We propose a classification of magmatic sulfide deposits that reflects (1) the source composition; and (2) the melting regime. We show that Ni-fertile magmas may be formed in a broader range of geotectonic settings than previously thought if sourced from metasomatised mantle, opening up exploration search spaces for critical battery metals.

1 Mantle source of Ni-Cu-Co-PGE sulfide deposits

Nickel alongside Cu, Co and the platinum-group elements (PGE) are important metals required for sustainable growth and the green energy transition. These metals are concentrated in magmatic sulfide deposits, the crystallise from mantle-derived melts that ascend through the lithosphere. The major depository phases of these metals in the mantle include sulfides, metal alloys, oxides and olivine. All models for the formation of Ni-Cu-Co-(PGE) deposits require the liberation and mobilisation of these metals during partial melting.

The simplistic model of priming mantle-derived melts in Ni, Cu, PGE, etc from the melting of sulfides, oxides and silicates requires high degrees of partial melting (>~15 %) triggered by a significant heat driver (e.g. a mantle plume) that melts the sulfide-bearing and olivine-rich peridotite source. The metals can be later sequestered in the crust by sulfide liquid droplets if the magma undergoes sulfide saturation (Naldrett, 2011).

However, relevant thermal anomalies are isolated in space and time, so that the conditions required to form Ni-Cu-(PGE) deposits have been limited through time. Existing models for mantle melting applied to the formation of mafic-ultramafic magmas that host Ni-sulfide deposits have thus far focussed on 'dry' peridotite melting in closed systems (Naldrett, 2011). Although this model is useful to demonstrate the release of Ni from olivine and Cu and PGE from sulfides at varying degrees of mantle melting, it is overly simplistic in terms of the assumed mantle composition. Nonetheless, it has been the basis for most genetic models of magmatic sulfide deposits.

2 Reassessing the source

The mantle is well known to be extremely heterogenous, and therefore, the assumption that the source of all magmatic sulfide deposits is a peridotite is likely a large simplification and, in many cases, inappropriate.

Metasomatised domains in the mantle contain a much more varied mineralogical assemblage, as shown in mantle xenolith datasets from around the globe (e.g. Aulbach et al., 2021). Preliminary results from our work on a series of variably metasomatised mantle xenoliths and from experimental partitioning studies show that a number of other minerals, including phlogopite, amphibole and apatite, can also host significant quantities of Ni and other base metals. We highlight the contrasting mineralogy of two mantle rock types that may be important sources for Ni-Cu-PGE fertile magmas.

2.1 Peridotite mantle

Peridotite is principally comprised of olivine and pyroxene with accessory sulfide, oxide and other trace phases, whereby the bulk of the Ni is hosted in olivine, with some in sulfide. The silicate minerals which host Ni have high melting temperatures, such that a high degree of melting (>20 %) is required to sufficiently liberate the metals from these phases. As such, deposits from this melting scenario are likely to be Ni rich but also host to appreciable Cu and PGE due to the dissolution of sulfide alongside olivine.

2.2 Hydrous pyroxenite mantle

Metasomatically enriched mantle domains are host to more exotic mineralogical assemblages. The composition of these mantle domains can be diverse; they are dominated by clinopyroxene and may comprise hydrous minerals such as amphiboles and micas, in addition to Fe-Ti oxides, phosphates and carbonates.

Critically, the presence of hydrous and volatile-bearing minerals causes these mantle source rocks

to melt at much lower temperatures than dry peridotites. Some of these minerals such as phlogopite, a common mineral in hydrous pyroxenites, have high partition coefficients for Ni (~9), similar to that for olivine (Foley et al., 2022; Ezad and Foley, 2022, Ezad et al., 2023), and may also concentrate other first-row transition elements (Ezad and Foley, 2022). As such, it is possible to form a Ni-rich melt by melting minerals such as phlogopite at lower temperatures without the need to melt significant amounts of olivine and sulfide.

3 Deposit classification as a function of source composition and melting regime

We highlight four scenarios for Ni-Cu-PGE deposit formation from a peridotite and pyroxenite mantle highlighting the controls of the source composition and degree of melting required, as an explanation for the geochemical differences within the Ni-Cu-Co-PGE mineral system.

3.1 High degree melting of a peridotite source (Ni-rich)

This type of deposit forms as a result of high degrees of partial melting (>15%) of a peridotite source where olivine is the dominant source of Ni (Naldrett, 2011). Nickel is liberated at high degrees of partial melting when olivine begins to melt, at the expense of Cu and PGEs which will become diluted at these large volumes. This type of deposit requires a significant heat driver, such as mantle plume or the high mantle potential temperatures such as those known to have existed during the Archean.

3.2 Moderate degree melting of a peridotite source (PGE-rich)

This type of deposit would form at moderate degrees of partial melting from a peridotite source at ~15% partial melting, whereby sulfide (the principal host to Cu and PGE) is completely exhausted, but not diluted by further melting, resulting in significant enrichments in PGEs relative to Ni. This type also requires a significant heat driver required to liberate these metals by S exhaustion in the source and form large, tholeiitic layered igneous complexes that are typical hosts to PGE deposits. Examples of this type include the many PGE deposits of the Bushveld Complex, South Africa; the Stillwater Complex, Montana; and the Duluth Complex, Minnesota.

3.3 High degree melting of a hydrous pyroxenite source (Ni-rich)

The metals in this deposit type are principally hosted within the hydrous minerals, e.g., phlogopite (Ezad et al., 2023), capable of forming Ni-fertile melts. Amphiboles and phlogopite within hydrous pyroxenites melt at lower temperatures than anhydrous peridotite, their exhaustion at approximately 30% partial melting (Foley et al., 2022) results in melts rich in Ni. Due to the low melting temperature of these hydrous and volatile-rich minerals, a plume is not necessary, and thus deposits of this type may form in a wider range of settings, where a heat driver exists. Potential examples of this deposit type include the many deposits of the Central Asian Orogenic Belt, China.

3.4 Low degree melting of hydrous pyroxenite source (Cu-Au-Te-PGE rich)

In cases where hydrous pyroxenite sources contain abundant sulfide and carbonates, their incipient melts (<5% partial melting) are carbonated and can dissolve Cu and PGEs at oxidised conditions (Ezad et al., 2023). These carbonated melts may percolate to shallower depths metasomatising the overlying lithosphere priming it with Cu and PGE rich domains, which may be subsequently remelted and transported in alkaline melts or through physical processes (e.g., Blanks et al., 2020) to form distinct deposit types.

Examples of this process and deposit type being the Cu-Au-Te magmatic sulfide deposits associated with alkaline rocks and include Sron Garbh, Scotland, and Mordor, Australia.

4 Implications

We highlight that partial mantle melts can be enriched in Ni alongside other base metals by melting a range of metasomatised mantle source rocks at lower temperatures than peridotite. We propose that hydrous pyroxenitic mantle offers an alternative source of Ni and other metals and can fertilise partial melts in addition to the conventionally considered olivine and sulfide. Crucially, the implication here is that the lower temperature partial melting of a metasomatised source can produce melts that are fertile in Ni +/- other metals and that Ni sulfide deposits may be found in a more diverse range of geotectonic settings than previously recognised.

Acknowledgements

This work is part of the Craton Margin Exploration Targeting 4D (CMET-4D) project, funded by BHP and involving the University of Leicester, the Centre for Exploration Targeting at the University of Western Australia and Macquarie University. I.S.E and S.F.F acknowledge funding from an ARC Laureate Fellowship (FL180100134) awarded to S.F.F.

References

Aulbach S, Giuliani A, Fiorentini M, et al (2021) Siderophile and chalcophile elements in spinels, sulphides and native Ni in strongly metasomatised xenoliths from the Bultfontein kimberlite (South Africa). Lithos 380–381: 105880

Blanks DE, Holwell DA, Fiorentini M (2020) Fluxing of mantle carbon as a physical agent for metallogenic fertilization of the crust. Nat Comms 11:4342
Ezad I, Saunders M, Scheka S, et al. (2023) Incipient carbonate melting drives precious metal and sulfur mobilisation in the mantle. Nat Comms Preprint
Ezad I and Foley S (2022) Goldschmidt 2022 Abstract 11537
Foley S, Ezad I, van der Laan SR, Shu C (2022) Goldschmidt 2022 Abstract 11550
Naldrett AJ (2011) Fundamentals of magmatic sulfide deposits. Rev Econ Geol 17:1-50

Mafic magmatism in the Central Iberian Zone: Towards a better understanding of Sb mineralization?

Héctor R. Campos-Rodríguez[1], Eric Gloaguen[1,2], Anthony Pochon[2], Johann Tuduri[2], Stanislas Sizaret[1], Pablo Higueras[3], Giada Iacono-Marziano[1], Saturnino Lorenzo[3], José-María Esbri[3], Marc Poujol[4], Valentin Mollé[1]
[1]Université d'Orléans/CNRS/BRGM/ISTO, UMR 7327, F-45071 Orléans, France
[2]BRGM, F-45060 Orléans, France
[3]Instituto de Geología Aplicada & Departamento de Ingeniería Geológica y Minera. E.I.M.I. Almadén, Universidad de Castilla-La Mancha, Plaza Manuel Meca1, E-13400 Almadén (Ciudad Real), Spain
[4]Univ Rennes, CNRS, Géosciences Rennes – UMR6118, F-35000 Rennes, France

Abstract. This work presents the geochemical and geochronological characterization of mafic sills of the Central-Iberian Zone, in order to unveil their possible relationships with Sb mineralization. These sills are located within three different synclines where several Sb mineralization are observed: La Codosera Syncline (CS) hosts the largest Sb mineralisation in Europe; Almadén Syncline (AS) hosts a world-class Hg deposit and some small Sb deposits; Guadalmez Syncline (GS) hosts several Sb±Hg deposits. Whole rock geochemistry of the mafic rocks and U-Pb dating on apatite reveal several differences among the three areas. The rocks from the CS present a sub alkaline affinity, whereas the rocks from AS and GS have an alkaline affinity. Primitive mantle normalized diagrams of the CS mafic samples show E-type MORB patterns with Cs and Pb positive anomalies and K, Ba, and Rb negative anomalies that are more marked in samples spatially related to Sb mineralization. The geochronological data allow to propose the existence of a mafic magmatic event that took place around 357±13Ma in the CIZ. Our data is temporarily concordant with a mafic event reported in the Armorican Massif, which is genetically associated with Sb mineralization in the same domain.

1 Introduction

Most of the Sb deposits are formed in an epigenetic hydrothermal setting (Obolensky et al. 2007) and can be divided into several types considering both the source of metals and fluids: a) epithermal type (veins); b) metamorphic hydrothermal; c) reduced-intrusion related (Schwarz-Schampera 2014). Antimony deposits that formed in tectonic convergence settings underwent strong compressive deformation and the mineralizing fluids are produced by metamorphic reactions (Groves et al. 1998). This classification does not seem very relevant for the formation of Sb±Au deposits in the Massif Central at the end of the Variscan Orogeny (310-300Ma). These deposits formed in an extensive context during a magmatic-hydrothermal event (Bouchot et al. 2005). Within the Armorican Massif, also part of the Variscan Belt (VB) recent studies have demonstrated a strong spatial and genetic relationship between Sb mineralization and a large mafic event dated at 360Ma (Pochon et al. 2016, 2017, 2018, 2019). In other parts of the VB such as the Central Iberian Zone (CIZ), located in the Iberian Massif, several Sb±Hg±W±Au mineralization have also been reported. In the case of the world class Almadén deposit, a link between mafic magmatism and Hg mineralization has been determined (Higueras 1995; Higueras et al. 1995, 2013; Hall et al. 1997). Moreover, a genetic link between the antimony mineralization and the hydrothermal activity associated to Devonian volcanism and with magmatic processes has been suggested (Arribas and Gumiel 1984; Gumiel and Arribas 1987); nevertheless, no studies investigated the possible relationship among mafic rocks and Sb mineralization in the CIZ.

Here we present the geochemical and geochronological characterization of three different structures (synclines) of the CIZ (Figure 1 and

Figure **2**). All of them host several mafic sills intruding a metasedimentary sequence (Schist Greywacke Complex, SGC) from Neoproterozoic to Carboniferous age (Bea et al. 2003); as well as Sb±Hg±W±Au mineralization. The Codosera Syncline hosts the Sb±W mineralization of San Antonio; the Almadén Syncline hosts the world class Hg deposit of Almadén and the Guadalmez Syncline hosts several Sb±Hg deposits.

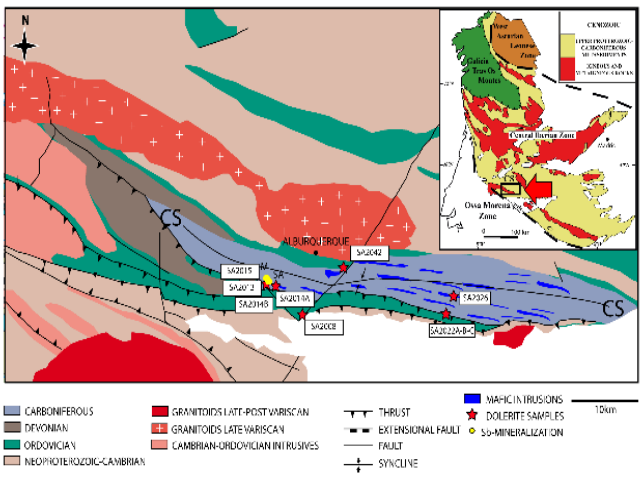

Figure 1. La Codosera Syncline (CS) at the Central Iberian Zone, in the Iberian Massif. Location of the structure and mafic samples studied in this work.

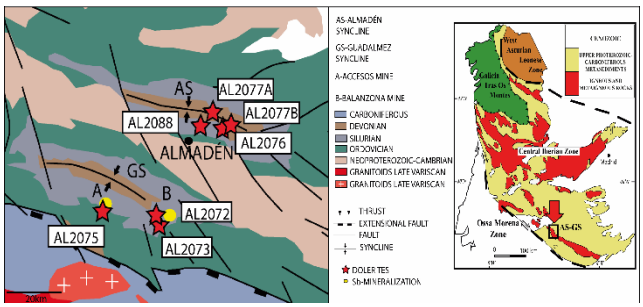

Figure 2. Almadén (AS) and Guadalmez Synclines (GS)at the Central Iberian Zone, in the Iberian Massif. Location of the structures and mafic samples studied in this work.

2 Methodology

2.1 Whole rock geochemistry analyses

Whole rock geochemical analyses of 17 samples were performed at ALS laboratories in Dublin (Ireland). Major elements were analyzed using inductively coupled plasma atomic emissions spectrometry (ICP-AES) after a lithium borate fusion. In order to measure trace elements, the samples were fused using lithium borate ($LiBO_2$), the product (fused beads) underwent acid dissolution for being analyzed by inductively coupled plasma-mass spectrometry (ICP-MS)

2.2 Geochronology- U-Pb dating on apatite

Geochronological analyses were carried out in both thick-polished sections of 150µm and separated crystals of 6 dolerite samples.

The U-Pb geochronology was performed by LA-ICP-MS (Laser ablation-inductively coupled plasma-mass spectrometry) in the facilities of Géosciences Rennes. The Laser ablation system is composed by an Excimer ESI NWR193UC coupled with a Q-ICP-MS Agilent 7700x

Each punctual analysis consisted on 20 seconds of background collection, followed by 60 seconds of ablation and 15 seconds of wash-out delay. Two analytical session were performed. In the first one a rectangular ablation was performed (dimensions 30µm x 40µm) in four samples (SA2022C, SA2026 and AL2073) whereas in the second one a simple spot of 40µm was used for the rest of the samples (SA2014A, AL2075 and AL2076). In both of the analytical sessions the repetition rates were 5Hz.

The analyzed sequence consisted in two analyses of the Madagascar apatite standard (ID-TIMS age of 473±0.7Ma, Thomson et al., 2012), 1 analysis of the Durango apatite standard (31.44±0.18Ma, McDowell et al., 2005), one analysis of the McClure apatite standard (523.51±2.09Ma, Schoene & Bowring, 2006) followed by 6 analyses of apatite samples. The sequence was repeated maximum 6 times and the end of the session consisted of three analyses, 1 of the Durango and 2 of the Madagascar standards.

3 Results and Discussion

3.1 Alteration features

In order to quantify the alteration degree of the dolerites and to investigate the mobility of major elements, all samples have been plotted into the Al-CCPI alteration box plot (Large 2001)

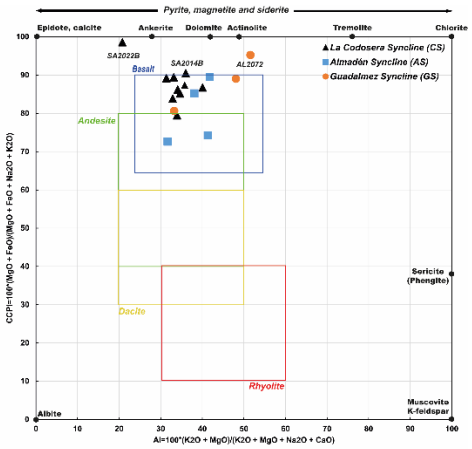

Figure 3. Alteration diagram from Large (2001). Most of the samples fall into the basalt field, showing that the alteration did not compromise their primary geochemical signature.

According to Figure 3 most of the studied samples from the Codosera (CS), Almadén (AS) and Guadalmez Synclines (GS), fall into the basalt field. This means that, even if they experienced some alteration, their primary geochemical signatures are preserved. The three samples that do not fall into the basalt field are not going to be considered in the following discussion.

3.1 Whole rock geochemistry analyses

Whole rock analyses of 14 samples show some differences between CS, AS and GS. According to the Zr/TiO_2 vs Nb/Y diagram (Winchester and Floyd 1977). The CS samples fall into the classical basalt field whereas the AS and GS samples fall into the alkali basalt field. The data is consistent with previous studies regarding the geochemistry of these mafic sills.

Primitive mantle normalized diagrams shown in Figure 4 display high positive anomalies in Cs and Pb suggesting sediment addition and/or the assimilation of country rocks. On the other hand, high negative anomalies in K and Rb, and to a lesser extent in Ba could be associated with both the presence of phlogopite in the source as well as hydrothermal and metamorphic processe (Sun and McDonough 1989). These anomalies are stronger for all the samples spatially related to Sb-mineralization in the CS and the GS. All samples are depleted in HREE and enriched in LREE.

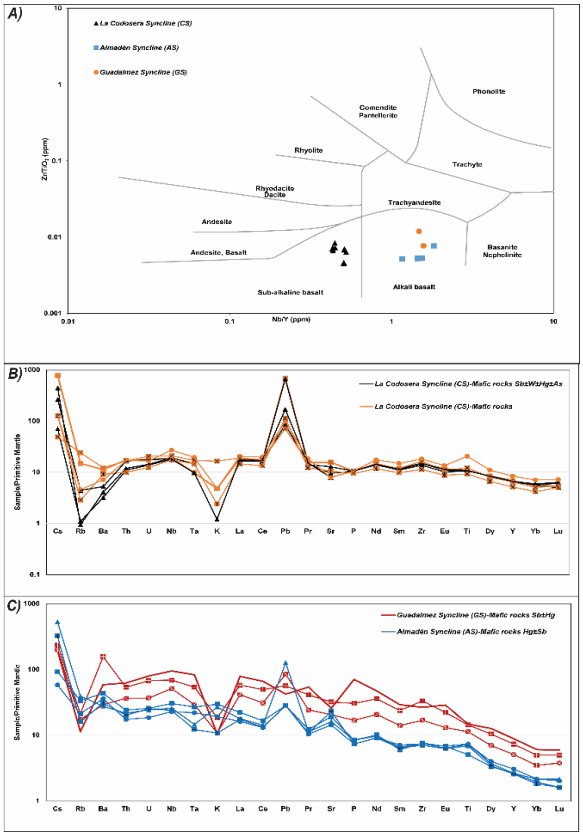

Figure 4. A) Samples from CS, AS and GS plotted into the Zr/TiO2 vs Nb/Y diagram from (Winchester and Floyd 1977). The samples from SA fall into the classical basalt field whereas those coming from GZ fall into the alkali basalt field; B and C) Primitive mantle normalized spider diagram for samples coming from CS (B), AS and GS (C). PM normalizing values taken from (Sun and McDonough 1989).

3.2 U-Pb geochronology apatite

The U-Pb geochronology results are plotted in both, the Tera-Wasserburg diagram using IsoplotR (Vermeesch 2018); as well as in the weighted average ^{207}Pb corrected date (WACD) diagram, which is calculated using the Pb evolution model of Stacey and Kramers (1975).

Regarding the results obtained from samples coming from the CS, AS and GS (**Erreur ! Source du renvoi introuvable.**), two main groups of dates can be observed (considering the errors within each sample). The first group includes samples:

A) SA2014A (CS): Discordia date (Dd)=355.7±17.1Ma/ ^{207}Pb WACD date=357±13Ma.

B) SA2022C (CS) : Dd =352.80±18.9Ma/ ^{207}Pb WACD= 354.5.4±5.4Ma.

C) SA2026 (CS) : Dd=337±23.7Ma/ ^{207}Pb WACD=344.7±4.8Ma.

The second group includes samples.

D) AL2073 (GS) : Dd = 360±25.6Ma / ^{207}Pb WACD=381±7.3Ma.

E) AL2076 (AS): Dd=358.2±11.9Ma / ^{207}Pb WACD=379.3±8.2Ma.

A low-grade metamorphism (up to greenschist facies) has been reported in the studied areas (Higueras et al. 1995, 2013; López-Moro et al. 2007) We assume that sills experienced a fast cooling and solidification (giving their thickness) with no further modification. These dates are thus interpreted as the intrusion age of the mafic sills.

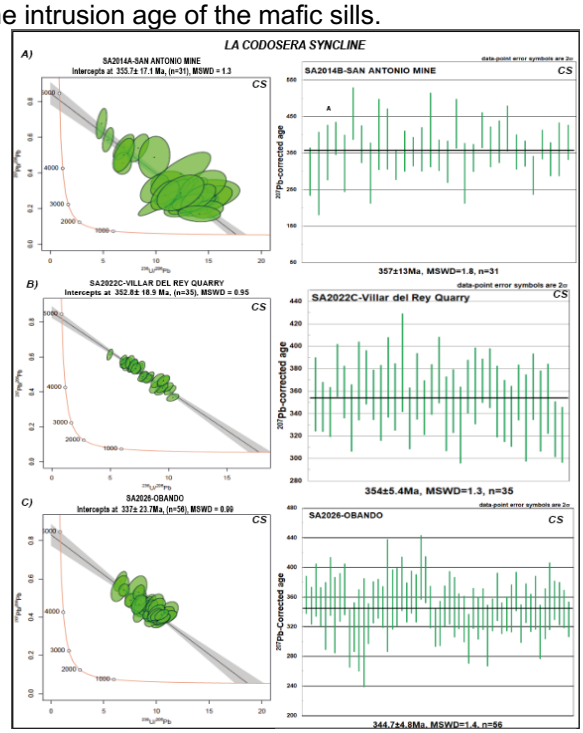

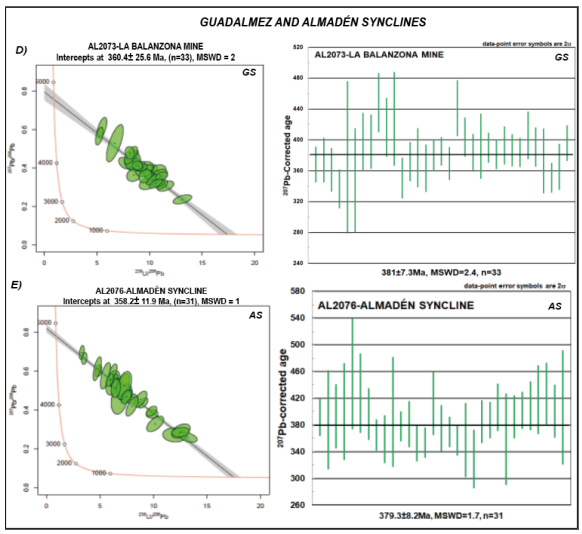

Figure 5. Tera-Wassebourg diagram and their related ^{207}Pb corrected ages for the mafic rocks coming from the Almadén and Guadalmez Synclines.

Our previous intrusion ages show three different stages one at 380Ma, another at 360Ma and the last at 345Ma. The second stage is concordant with the ages reported in the AM by Pochon et al. (2016), which are temporarily related to a peak in Sb mineralization in the AM dated at 360Ma (Pochon et al. 2019).

Conclusions

A spatial link between Sb-mineralization and mafic magmatism is proposed in the CIZ

-Primitive mantle normalized diagrams show negative anomalies in K and Rb that could be

associated with hydrothermal and metamorphic processes. These anomalies are stronger for the samples spatially related to Sb-mineralization. According to these diagrams, all samples are depleted in HREE and enriched in LREE. The samples coming from the GS are more enriched in REE than those coming from AS, suggesting that these magmas could be more differentiated or that the source of both is different.

-Our results allow to propose the existence of three mafic magmatic stages that took place from Late Devonian to Carboniferous times in the CIZ at around 380Ma (AS and GS), 360Ma (CS) and 345Ma (CS). The second stage that we revealed in this study, is concordant with the mafic event dated at 363.4±5.4 in the AM by Pochon et al. (2016), which is related to Sb mineralization peak in the same domain dated at 360Ma (Pochon et al. 2019). In our case, the magmatism that matches temporarily with this peak is located in the CS (related to Sb±W). The rocks in this area present a subalkaline affinity. On the other hand, the magmatism spatially related to Sb±Hg in the GS and Hg±Sb in the AS present an alkaline affinity and is older than the one we reported in the CS.

-The genetical link between Sb-mineralization and mafic magmatism in the CIZ is still a matter of study

Acknowledgements

This work was funded by the ANR (ANR-19-MIN2-0002-01), the AEI (MICIU/AEI/REF.: PCI2019-103779) and author's institutions in the framework of the ERA-MIN2 AUREOLE project, as well as by Project SBPLY/17/180501/000273, Consejería de Educación, Regional Government of Castilla-La Mancha, Spain.

References

Arribas, Gumiel P (1984) First Ocurrece of a Strata-Bound Sb-W-Hg Deposit in the Spanish Hercynian Massif. In: Wauschkuhn A, Kluth C, Zimmerman RH (eds) Syngenesis and epigenesis in the formation of mineral deposits. Spriger-Verlag, Berlin-Heidelberg, pp 469–481

Bea F, Montero P, Zinger T (2003) The nature, origin, and thermal influence of the granite source layer of Central Iberia. J Geol 111:579–595. https://doi.org/10.1086/376767

Bouchot V, Ledru P, Lerouge C, et al (2005) 5: Late Variscan mineralizing systems related to orogenic processes: The French Massif Central. Ore Geol Rev 27:169–197. https://doi.org/10.1016/j.oregeorev.2005.07.017

Groves DI, Goldfarb RJ, Gebre-Mariam M, et al (1998) Orogenic gold deposits: a proposed classification in the context of their crustal distribution and relationship to other gold deposit types. Ore Geol Rev 13:7–27. https://doi.org/10.1016/S0169-1368(97)00012-7

Gumiel P, Arribas A (1987) Antimony deposits in the Iberian Peninsula. Econ Geol 82:1453–1463. https://doi.org/10.2113/gsecongeo.82.6.1453

Hall CM, Higueras PL, Kesler SE, et al (1997) Dating of alteration episodes related to mercury mineralization in the Almadén district, Spain. Earth Planet Sci Lett 148:287–298. https://doi.org/10.1016/s0012-821x(97)00041-1

Higueras P (1995) Procesos petrogenéticos y de alteración de las rocas magmáticas asociadas a las mineralizaciones de mercurio del distrito de Almadén. Universidad de Castilla-La Mancha

Higueras P, Morata D, Munha J (1995) Metamorfismo de bajo grado en facies prehnita-pumpellyita en las metabasitas del Sinclinal de Almadén. Boletín la Soc Española Mineral 18:111–125

Higueras P, Oyarzun R, Lillo J, Morata D (2013) Intraplate mafic magmatism, degasification, and deposition of mercury: The giant Almadén mercury deposit (Spain) revisited. Ore Geol Rev 51:93–102. https://doi.org/10.1016/j.oregeorev.2012.12.004

Large RR (2001) The Alteration Box Plot: A Simple Approach to Understanding the Relationship between Alteration Mineralogy and Lithogeochemistry Associated with Volcanic-Hosted Massive Sulfide Deposits. Econ Geol 96:957–971. https://doi.org/10.2113/96.5.957

López-Moro FJ, Murciego A, López-Plaza M (2007) Silurian/Ordovician asymmetrical sill-like bodies from La Codosera syncline, W Spain: A case of tholeiitic partial melts emplaced in a single magma pulse and derived from a metasomatized mantle source. Lithos 96:567–590. https://doi.org/10.1016/j.lithos.2006.12.006

McDowell FW, McIntosh WC, Farley KA (2005) A precise 40Ar-39Ar reference age for the Durango apatite (U-Th)/He and fission-track dating standard. Chem Geol 214:249–263. https://doi.org/10.1016/j.chemgeo.2004.10.002

Obolensky AA, Gushchina L V., Borisenko AS, et al (2007) Antimony in hydrothermal processes: solubility, conditions of transfer, and metal-bearing capacity of solutions. Russ Geol Geophys 48:992–1001. https://doi.org/10.1016/j.rgg.2007.11.006

Pochon A, Beaudoin G, Branquet Y, et al (2017) Metal mobility during hydrothermal breakdown of Fe-Ti oxides: Insights from Sb-Au mineralizing event (Variscan Armorican Massif, France). Ore Geol Rev 91:66–99. https://doi.org/10.1016/j.oregeorev.2017.10.021

Pochon A, Branquet Y, Gloaguen E, et al (2019) A Sb ± Au mineralizing peak at 360 Ma in the Variscan belt. BSGF - Earth Sci Bull 190:. https://doi.org/10.1051/bsgf/2019004

Pochon A, Gloaguen E, Branquet Y, et al (2018) Variscan Sb-Au mineralization in Central Brittany (France): A new metallogenic model derived from the Le Semnon district. Ore Geol Rev 97:109–142. https://doi.org/10.1016/j.oregeorev.2018.04.016

Pochon A, Poujol M, Gloaguen E, et al (2016) U-Pb LA-ICP-MS dating of apatite in mafic rocks: Evidence for a major magmatic event at the Devonian-Carboniferous boundary in the Armorican Massif (France). Am Mineral 101:2430–2442. https://doi.org/10.2138/am-2016-5736

Schoene B, Bowring SA (2006) U-Pb systematics of the McClure Mountain syenite: Thermochronological constraints on the age of the 40Ar/39Ar standard MMhb. Contrib to Mineral Petrol 151:615–630. https://doi.org/10.1007/s00410-006-0077-4

Schwarz-Schampera U (2014) Antimony. In: Gunn G (ed) Critical Metals Handbook, First Edit. John Wiley & Sons, Ltd., pp 70–98

Stacey JS, Kramers JD (1975) Approximation of terrestrial lead isotope evolution by a two-stage model. Earth Planet Sci Lett 26:207–221. https://doi.org/10.1016/0012-821X(75)90088-6

Sun S-S, McDonough WF (1989) Chemical and isotopic systematics of oceanic basalts: Implications for mantle composition and processes. Geol Soc Spec Publ 42:313–345. https://doi.org/10.1144/GSL.SP.1989.042.01.19

Thomson SN, Gehrels GE, Ruiz J, Buchwaldt R (2012) Routine low-damage apatite U-Pb dating using laser ablation-multicollector- ICPMS. Geochemistry, Geophys Geosystems 13:1–23. https://doi.org/10.1029/2011GC003928

Vermeesch P (2018) IsoplotR: A free and open toolbox for geochronology. Geosci Front 9:1479–1493. https://doi.org/10.1016/j.gsf.2018.04.001

Winchester JA, Floyd PA (1977) Geochemical discrimination of different magma series and their differentiation products using immobile elements. Chem Geol 20:325–343. https://doi.org/10.1016/0009-2541(77)90057-2

On the origin of volatile-rich minerals associated with magmatic sulfides

Maria Cherdantseva[1], Marco Fiorentini[1], Chris Fisher[1], Laure Martin[2], Matvei Aleshin[2]
[1] Centre of Exploration Targeting, School of Earth Sciences, The University of Western Australia, Perth, Western Australia
[2] Centre for Microscopy, Characterisation and Analysis, The University of Western Australia, Perth, Western Australia

Abstract. Magmatic sulfides such as chalcopyrite, pyrrhotite and pentlandite hosted in mafic-ultramafic intrusions are commonly found in intimate spatial association with volatile-rich minerals such as calcite, apatite, amphibole and phlogopite. These volatile-rich minerals have been previously ascribed to form due to late magmatic or secondary processes, involving highly fractionated liquids and/or metamorphic fluids. However, our new results from detailed study of the nature of this association in three different intrusions supported by experiments has led us to the conclusion that these minerals could be, at least in some instances, primary. In this case we explain the presence of halos enriched in volatile-rich silicates, carbonates and phosphates to be a crystallization product of initially immiscible carbonate melt exsolved from silicate magma together with sulfide liquid. Wherein, in our experiments, carbonate melt always envelopes sulfide globules indicating their affinity and presence of wetting agent in carbonate melt. In this study we present isotopic signatures and trace element distributions of three minerals commonly found in spatial association with sulfides (calcite, apatite, and baddeleyite/zircon) to investigate a potential source of carbonate melt in mafic magma.

1 Introduction

The origin of volatile-rich and/or incompatible element-enriched minerals such as calcite, apatite, and baddeleyite/zircon associated with magmatic sulfides in mafic-ultramafic systems has been a topic of debate for decades. Some researchers have suggested that they could form due to precipitation of late magmatic fluids (Aird and Boudreau 2013; Barnes et al. 2017) or as a late hydrothermal overprint (Wernette et al. 2020). However, the morphological and mineralogical features of this association raise questions about these interpretations. In fact, these minerals coat the sulfide globules, forming halos with sharp margins to the host mafic-ultramafic rocks (Schoneveld et al. 2020). Furthermore, distinct mineralogy includes the presence of calcite, which is not typical of fractionated residual liquid, nor are ilmenite or zircon a typical product of late magmatic fluid precipitation (Keevil et al. 2020). On the basis of experimental results, we put forward the hypothesis that this association could reflect the presence of high-temperature immiscible carbonate melt, which exsolved from the silicate magma coevally with sulfide melt. Wherein, we observe that carbonate melt will preferentially adhere to sulfide globules enveloping them, effectively acting as a buoyancy aid facilitating their entrainment in the magma. However, the source of such a carbonate melt has not yet been constrained. To investigate the source and origin of the halos surrounding the compound sulfide globules, we studied the isotopic and trace element compositions of calcite, apatite and zircon/baddeleyite, which are typically found within mineralogical assemblage of these halos, in selected samples from mineralized intrusions from three different systems: Norilsk, Russia; Rudniy, Mongolia and Valmaggia, Italy.

2 Geological background

This research utilized olivine gabbro from the Norilsk1 and Kharaelakh intrusions, which contain sulfide globules from the Norilsk-Talnakh camp in northern Siberia, Russia. These elongated mafic-ultramafic intrusions, also known as chonoliths, can reach up to 360 m in thickness and 25 km in length and were formed in an intracontinental rift. All the intrusions were emplaced at shallow depths and occur as layered sequences of olivine and picritic gabbro-dolerite, gabbronorite-dolerite, gabbro-anorthosite, plagio-lherzolite, troctolite, and gabbro-diorite (Ryabov et al. 2014).

The Rudniy olivine gabbro intrusion in NW Mongolia is a small composite magmatic body with disseminated sulfide globules, representing one of the numerous mafic-ultramafic intrusions in the Torgalyk Complex surrounding the Tuva depression. These intrusions were formed in the Early Devonian as part of the Altai-Sayan large igneous province (Vorontsov et al. 2010).

In contrast, the Valmaggia ultramafic pipe is a small intrusion composed of peridotite with disseminated sulfide globules located in the Ivrea Zone in northwest Italy. This zone represents a part of the lower continental crust and lithospheric mantle exposure formed during the Alpine Orogeny. (e.g., Fiorentini and Beresford 2008).

Selected samples from these localities are characterized by the presence of magmatic sulfide mineralization in the form of disseminated sulfide globules that are commonly composed of pyrrhotite, pentlandite and chalcopyrite. These globules are commonly coated by rounded envelopes of volatile-rich and/or incompatible element-enriched minerals that are distinctly different from the host intrusion. They commonly comprise plagioclase, amphibole (kaersutite, hornblende and hastingsite), phlogopite, clinopyroxene, ilmenite, zircon (and/or baddeleyite),

apatite and calcite. Three of those minerals – calcite, apatite and zircon were chosen to study the trace element and isotope compositions as indicators of the origin of the mineralization and associated haloes.

3 Materials and Methods

Cameca IMS-1280 large-geometry secondary ion mass spectrometry (SIMS) at the Centre for Microscopy, Characterization, and Analysis (CMCA), the University of Western Australia (UWA), has been used to conduct in-situ measurements of oxygen isotopes ($\delta^{18}O$) in zircon and calcite and carbon isotopes ($\delta^{13}C$) in calcite associated with magmatic sulfide globules. To carry out the measurements, fragments of the sulfide globules and haloes around them were mounted in epoxy pucks together with the standard materials: 91500 (9.90 ± 0.3 ‰) and SLZ1 (12.1 ± 0.4 ‰) as primary and secondary standards for oxygen isotopes in zircon, respectively; NSB18 (7.19 ± 0.3 ‰) and 21ca5 (22.2 ± 0.4 ‰) as primary and secondary standards for O isotopes in calcite; NSB18 (-5.014 ± 0.035 ‰) for carbon isotopes in calcite. Before the SIMS analyses, the mounts were coated with a 30 nm-thick Au layer. The drift was monitored by examining standards every five sample analyses.

Laser ablation inductively coupled plasma mass spectrometry (LA-ICP-MS) at the CMCA, UWA, was used to measure trace element concentrations in apatite, calcite and zircon. NIST610 and NIST612 were used as primary standards. They were analyzed before and after every 10 unknown sample spots. Madagascar apatite and 91500 zircon were used as secondary standards for apatite and zircon analyses. Trace element concentrations were within 10% of their certified values. Calcite from the Oka complex was used to monitor calcite analyses. Concentrations of Zr (for zircon) and Ca (for calcite and apatite) were used as internal standard to calculate the trace element concentrations. Major and minor element composition was studied using a JEOL 8530F scanning electron microscope at the CMCA, UWA.

4 Results

Data on $\delta^{18}O$ and rare earth element (REE) distribution in zircon from the Rudniy intrusion are not provided, because the grains were too small to be analyzed.

The chondrite-normalized distribution of REE in zircon and apatite shows enrichments. Specifically, zircon from haloes around sulfide globules from Norilsk and Valmaggia is up to two orders of magnitude more enriched in all REE than zircon derived from highly fractionated magmas (Fig. 1a, e.g., Shi et al. 2022). Apatite from all three localities are characterized by enrichments in light REE with moderate (Rudniy) to steep (Valmaggia) negative slopes in their patterns (Fig. 1b). Apatite from Norilsk and Rudniy intrusions are also characterized by strong to moderate negative Eu anomalies.

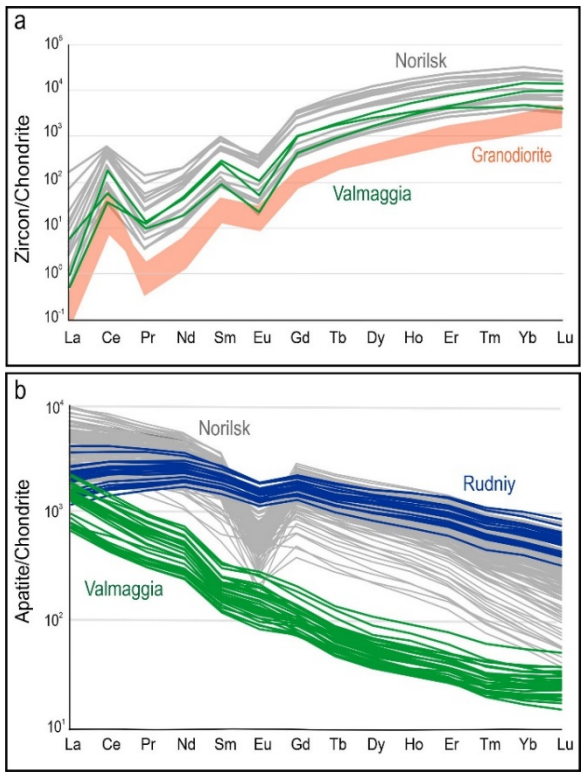

Figure 1. Chondrite-normalized REE distribution in (a) apatite and (b) zircon from Norilsk (Russia), Valmaggia (Italy), Rudniy (Mongolia). Data normalized after (McDonough and Sun 1995)

Oxygen isotope composition of zircon and carbon isotope compositions of calcite from three different deposits are variable for different samples (Figs. 2 and 3). When examining oxygen isotopes in zircon, the Valmaggia intrusion shows values between 4-6 ‰ (Fig. 2), while the zircon from the Norilsk deposit displays a variety of compositions, with values ranging from 1 to 10 ‰ in different samples.

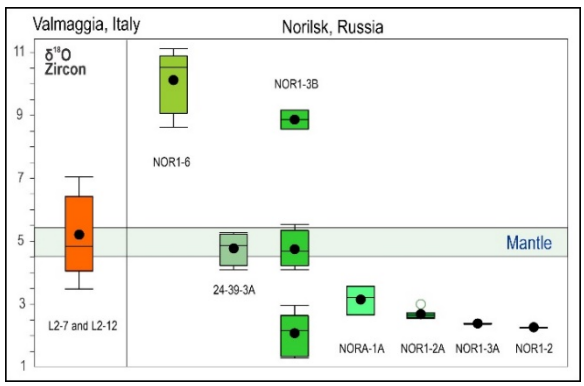

Figure 2. Oxygen (δ18O) isotope compositions of zircon found in haloes enveloping magmatic sulfide globules from Norilsk (Russia) and Valmaggia (Italy) intrusions.

The carbon isotopes in calcite can be divided into two main groups. Samples from the Valmaggia pipe, as well as some samples from the Norilsk deposit,

exhibit values between -16 to -10 ‰ (Fig. 3). In contrast, calcite from the Rudniy and Norilsk intrusions falls in a range between -6 to 0 ‰. The oxygen isotopes for all samples have values ranging from 5 to 15 ‰.

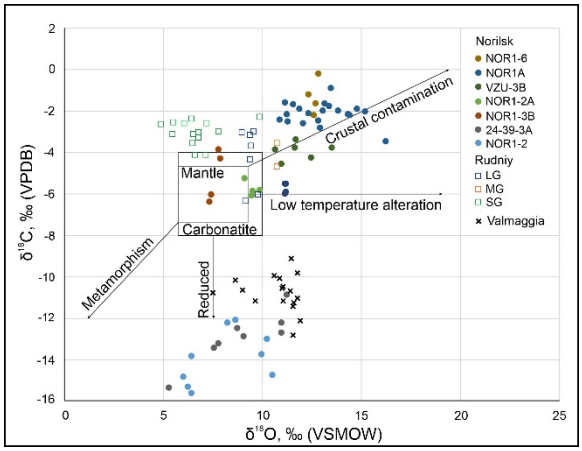

Figure 3. Oxygen (δ18O) and carbon (δ13C) isotope compositions of calcite associated with magmatic sulfide globules from Norilsk (Russia), Rudniy (Mongolia) and Valmaggia (Italy).

3 Discussion and conclusions

The paragenetic association of magmatic sulfides with volatile- and incompatible element-rich phases has been interpreted to reflect the former presence of (supercritical) fluids and/or vapour bubbles, which would physically adhere to the droplets of sulfide liquid upon emplacement and crystallization of the magma. These compound bubbles would significantly increase the buoyancy of sulfide liquid, acting as a natural analogue of an industrial flotation process (Mungall et al. 2015). According to this theory, upon solidification of the magma, these bubbles would form the hollow spaces that would be later filled with late stage highly fractionated magmatic liquid (Le Vaillant et al. 2017). However, our study shows that the specific association, composition, zonation, and trace element geochemistry of accessory minerals contained within the haloes surrounding the sulfides cannot be explained by late filling of former bubbles, nor it can form from primary supercritical fluids (Blanks et al. 2020). In fact, if apatite and zircon had formed from late magmatic fluids, their REE concentrations would have been significantly lower (Fig. 1a, (Shi et al. 2022)). Furthermore, special conditions are required to mobilize Ti and Zr in late hydrothermal fluids (Rubin et al. 1993; Ayers et al. 2012); even crystallization of pure calcite would require the presence of Ca cations in excess of what is anticipated for residual silicate magma, which is very unusual in magmatic environments.

However, this association could have been formed due to exsolution of an immiscible carbonate melt from a mafic magma. The intimate spatial relationship documented in several natural examples suggest that carbonate droplets tend to wet sulfide liquid (Cherdantseva et al., in review). Accordingly, the sharp margins of the haloes could be explained by three liquid immiscibility, rather than by the preservation of gas bubbles, which could be problematic under pressure in a crystal mush, as it could cause the bubbles to explode or escape in low-pressure areas. Also, the unusual enrichment of REE relative to what is expected from fractionated silicate magma in zircon and apatite, especially light REE in apatite, can advocate for the carbonatitic origin of those minerals. In fact, the REE distribution patterns from samples in this study coincide with REE patterns reported for carbonatites and alkali-rich systems, such as Kovdor or Songwe Hill (Broom-Fendley et al. 2017; Milani et al. 2017).

The mineral assemblage crystallized from carbonate melt contains mostly volatile-rich phases, specifically, water-rich amphiboles and phlogopites, as well as hydrous calcium silicates and Cl- and F-rich apatite. Carbonate melts generally have relatively low density (2.7 g/cm^3) and viscosity (0.0067±0.0006 Pa s). Considering volume ratios, the average density of a compound globule made up of carbonate-sulfide liquids would be similar to that of mafic silicate melts; however, the addition of volatiles in carbonate melt could play a role in further increasing the buoyancy of the sulfide compound globules.

We may be able to utilize the geochemical and isotopic data gathered from this study to shed light on the origin of the carbonate melts that appear to surround the sulfide droplets found in the intrusions. These intrusions were observed at varying levels within the Earth's crust, prompting the question of whether the gathered information can be used to provide insight into the unknown source of these liquids. Whereas carbonate liquid is known to form in the mantle (Panina and Motorina 2008), the exsolution of carbonate melts in mafic silicate magmas is not a common occurrence. The data presented here indeed portray a complex scenario. Our study shows that different sources of carbonate liquid could be involved in their origin. For example, the relationship of oxygen and carbon isotopes in calcite indicates that a wide range of sources may be involved (Fig. 1), emphasizing the role of crustal contamination in the genesis of carbonate-rich liquids. This also indicates the variety of crustal material that could be assimilated. Thus, the points that fall in the field of reduced conditions could be formed due to assimilation of carbonaceous graphitic shale. This process could potentially trigger the oversaturation of magma with carbon dioxide (Virtanen et al. 2021) to the extent of exsolution of immiscible carbonate liquid. This process is also generally ascribed to be crucial in adding the additional source of sulfur required to trigger sulfide saturation in magmas emplaced at various depths (Mavrogenes and O'Neill 1999). Specifically, the carbon isotope values characteristic for Valmaggia (deep crust) and several samples from the Norilsk intrusions (shallow crust) could reflect assimilation of some reduced carbon (e.g., coal measures), and/or

reflect mass dependent fractionation due to CO_2 degassing (Gales et al. 2020).

Nevertheless, some of the isotopic signatures still point to a strong mantle contribution as a preferred source for the origin of the immiscible carbonate coats surrounding the sulfide globules (Fig. 3). This piece of evidence indicates that even despite the long and complicated history of crystallization of the magmatic intrusions, a carbonate liquid sourced from the mantle could accompany sulfide droplets all the way across the lithosphere. Along this journey, the carbonate coat may isolate sulfide liquid, preventing it from being re-dissolved in the host silicate melt upon ascent. If this process operated widely, it would be possible to envisage the occurrence of large mineralized camps where mass concentrative processes could have accumulated mantle-derived metal-rich magmatic sulfides without any necessary role for crustal contamination, effectively opening up new search space for nickel-sulfide provinces.

Acknowledgements

We acknowledge the support of the UWA through the SIRF scholarship granted to MC. The funding was provided by the Australian Research Council through grant DP190102422 awarded to MF.

References

Aird HM, Boudreau AE (2013) High-temperature carbonate minerals in the Stillwater Complex, Montana, USA. Contrib to Mineral Petrol 166:1143–1160. https://doi.org/10.1007/s00410-013-0913-2

Ayers JC, Zhang L, Luo Y, Peters TJ (2012) Zircon solubility in alkaline aqueous fluids at upper crustal conditions. Geochim Cosmochim Acta 96:18–28. https://doi.org/10.1016/j.gca.2012.08.027

Barnes SJ, Mungall JE, Le Vaillant M, et al (2017) Sulfide-silicate textures in magmatic Ni-Cu-PGE sulfide ore deposits: Disseminated and net-textured ores. Am Mineral 102:473–506

Blanks DE, Holwell DA, Fiorentini ML, et al (2020) Fluxing of mantle carbon as a physical agent for metallogenic fertilization of the crust. Nat Commun. https://doi.org/10.1038/s41467-020-18157-6

Broom-Fendley S, Brady AE, Wall F, et al (2017) REE minerals at the Songwe Hill carbonatite, Malawi: HREE-enrichment in late-stage apatite. Ore Geol Rev 81:23–41

Fiorentini ML, Beresford SW (2008) Role of volatiles and metasomatized subcontinental lithospheric mantle in the genesis of magmatic Ni-Cu-PGE mineralization: Insights from in situ H, Li, B analyses of hydromagmatic phases from the Valmaggia ultramafic pipe, Ivrea-Verbano Zone (NW Italy). Terra Nov 20:333–340. https://doi.org/10.1111/j.1365-3121.2008.00825.x

Gales E, Black B, Elkins-Tanton LT (2020) Carbonatites as a record of the carbon isotope composition of large igneous province outgassing. Earth Planet Sci Lett 535:116076. https://doi.org/10.1016/j.epsl.2020.116076

Keevil HA, Namur O, Holness MB (2020) Microstructures and late-stage magmatic processes in layered mafic intrusions: Symplectites from the sept iles intrusion, Quebec, Canada. J Petrol 61:1–25. https://doi.org/10.1093/petrology/egaa071

Le Vaillant M, Barnes SJ, Mungall JE, Mungall EL (2017) Role of degassing of the Noril'sk nickel deposits in the Permian-Triassic mass extinction event. Proc Natl Acad Sci U S A 114:2485–2490. https://doi.org/10.1073/pnas.1611086114

Mavrogenes JA, O'Neill HSC (1999) The relative effects of pressure, temperature and oxygen fugacity on the solubility of sulfide in mafic magmas. Geochim Cosmochim Acta 63:1173–1180

McDonough WF, Sun S-S (1995) The composition of the Earth. Chem Geol 120:223–253

Milani L, Bolhar R, Frei D, et al (2017) Light rare earth element systematics as a tool for investigating the petrogenesis of phoscorite-carbonatite associations, as exemplified by the Phalaborwa Complex, South Africa. Miner Depos 52:1105–1125

Mungall JE, Brenan JM, Godel B, et al (2015) Transport of metals and sulphur in magmas by flotation of sulphide melt on vapour bubbles. Nat Geosci 8:216–219. https://doi.org/10.1038/ngeo2373

Panina LI, Motorina I V. (2008) Liquid immiscibility in deep-seated magmas and the generation of carbonatite melts. Geochemistry Int 46:448–464. https://doi.org/10.1134/S0016702908050029

Rubin JN, Henry CD, Price JG (1993) The mobility of zirconium and other "immobile" elements during hydrothermal alteration. Chem Geol 110:29–47. https://doi.org/10.1016/0009-2541(93)90246-F

Ryabov VV, Shevko AY, Gora MP (2014) Trap Magmatism and Ore Formation in the Siberian Noril'sk Region

Schoneveld L, Barnes SJ, Godel B, et al (2020) Oxide-sulfide-melt-bubble interactions in spinel-rich taxitic rocks of the Norilsk-Talnakh intrusions, Polar Siberia. Econ Geol 115:1305–1320. https://doi.org/10.5382/ECONGEO.4748

Shi Q, Guo H, Liu C, Lai Y (2022) Genesis and Metallogenic Characteristics of the Zhunsujihua Granitic Intrusions in Sonid Left Banner, Inner Mongolia, China. Minerals 12:. https://doi.org/10.3390/min12050606

Virtanen VJ, Heinonen JS, Molnár F, et al (2021) Fluids as primary carriers of sulphur and copper in magmatic assimilation. Nat Commun 12:. https://doi.org/10.1038/s41467-021-26969-3

Vorontsov AA, Yarmolyuk V V., Fedoseev GS, et al (2010) Isotopic and geochemical zoning of Devonian magmatism in the Altai-Sayan rift system: Composition and geodynamic nature of mantle sources. Petrology 18:596–609. https://doi.org/10.1134/S0869591110060032

Wernette B, Li P, Boudreau A (2020) Sulfides, native metals, and associated trace minerals of the Skaergaard intrusion, Greenland: evidence for late hydrothermal fluids. Miner Depos 55:1197–1214. https://doi.org/10.1007/s00126-019-00924-1

Role of carbon in the formation of Ni-Cu-PGE mineralization in the Valmaggia ultramafic pipe: Insights from laser-ablation-time-of-flight ICP-MS

Shelby Clark[1], Marek Locmelis[1], Dany Savard[2], Marilena Moroni[3], Marco Fiorentini[4]
[1]Department of Geosciences and Geological and Petroleum Engineering, Missouri University of Science & Technology, Rolla, Missouri, USA
[2]LabMaTer, Département des Sciences Appliquées, Université du Québec à Chicoutimi, Chicoutimi, Québec, Canada
[3]Department of Earth Sciences, University of Milan, Italy
[4]School of Earth Sciences, The University of Western Australia, Perth, Australia

Abstract. Understanding the processes that control sulfide transport and deposition in the deep lithosphere is a critical step in the search for ore deposits in lower crustal rocks. The magmatic sulfide ore-bearing Valmaggia pipe in the Ivrea-Verbano Zone (Italy), an exposed cross section of the subcontinental lithospheric mantle and overlying crust, allows for unique insight into ore-forming processes in the lower crust. Sulfides in the pipe are spatially associated with carbonates and hydrous silicates. Previous studies suggested that the sulfides were physically introduced into the pipe via a bubble-pair transport model, i.e., upward flotation of sulfide droplets attached to vapor bubbles. To further evaluate sulfide ore-forming processes, we integrate new petrographic observations with laser-ablation time-of-flight-ICP-MS trace element mapping of sulfide-carbonate-hydrous silicate relationships. We show that carbonates and hydrous silicates exist in varying sizes, compositions, textures and orientations in relation to sulfide phases, and are not restricted to a singular textural or chemical relationship. Similarly, sulfide textures vary and may or may not exhibit rimming by volatile phases. Our data show that bubble-pair transport cannot fully explain the textural relationships between sulfides and volatile-rich minerals, but rather suggest that at least some of the sulfides and carbonates co-precipitated from the same fluid/melt.

1 Introduction

The number of new and significant ore deposit discoveries is declining (Schodde, 2020). One possible way to increase the discovery of magmatic Ni-Cu-platinum-group element (PGE) sulfide deposits is to open new exploration space in (exhumed) lower crustal rocks that are often neglected in exploration models. However, the chemical and physical processes that form magmatic sulfide deposits in the lower crust remain elusive.

One key area to study the formation of lower crustal magmatic sulfide deposits is the Ivrea-Verbano Zone (IVZ) in northwest Italy (Fig. 1A). The IVZ is a rare example of an exposed cross section of the subcontinental lithospheric mantle and overlying crust (Mehnert, 1975; Garuti et al. 1980). The IVZ hosts five variably metasomatized ultramafic pipes (Fig. 1B) containing Ni-Cu-PGE mineralization with grades of up to 11.9% Cu, 10.7% Ni, and 5 ppm PGE (Zaccarini et al. 2014). The sulfide mineralization appears to be spatially associated with carbonate minerals and hydrous silicates such as phlogopite and amphibole. However, the relationship between volatile-rich minerals and sulfides, and to what extent (carbonated) hydrous fluids played a role in ore genesis, remains to be fully understood.

Previous studies suggested that the sulfides were physically introduced into the pipes via a bubble-pair transport model wherein SCLM sulfides attached to supercritical CO_2 bubbles migrated upwards into the pipes (Blanks et al. 2020; Locmelis et al. 2021). To further test this hypothesis, we integrate new petrographic observations with laser-ablation time-of-flight inductively coupled mass spectrometry (LA-ICP-TOF-MS) trace element mapping of sulfide-carbonate-hydrous silicate relationships for the best preserved IVZ pipe at Valmaggia. The data are used to evaluate whether 1) sulfides were introduced into the Valmaggia pipe attached to CO_2 bubbles, or whether 2) sulfides and carbonates co-precipitated from a high temperature fluid or melt rich in S and $CO_2/CaCO_3$.

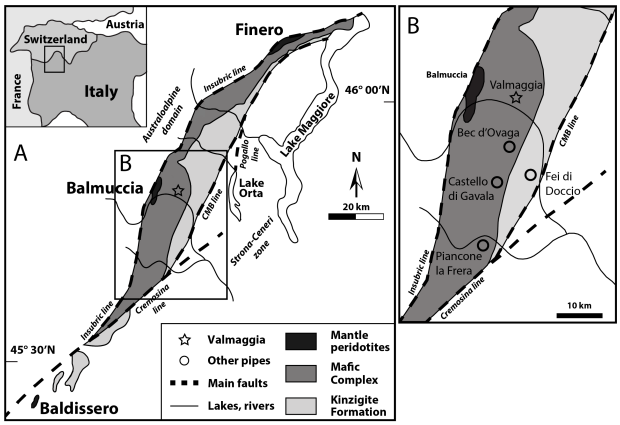

Figure 1. A: Simplified geologic map of the Ivrea Verbano Zone. B: Location of the ultramafic pipes, including Valmaggia (star). Modified after Fiorentini and Beresford (2008) and Locmelis et al. (2016).

2 Geologic Setting

The IVZ (Fig. 1) in the Western Alps, Italy, hosts five discordant ultramafic pipe-like intrusions hosted by the Mafic Complex and Kinzigite Formation (Fig. 1B). Locmelis et al. (2016) showed that the 249 Ma Valmaggia pipe was initially emplaced as an almost pure dunite. Later metasomatic pulses at 209.4 ± 5.1 Ma and 207.8 ± 2.0 Ma (Sessa et al. 2017;

Figure 2. *Reflected light image of sample VMG1B from the core domain of the Valmaggia pipe. Insets show zoomed-in reflected light images of pyrrhotite (Po) and pentlandite (Pn) blebs/globules. The red arrows indicate the perpendicular direction of sulfide-carbonate contacts.*

Locmelis et al. 2021) produced a secondary hydrous assemblage dominated by phlogopite and amphibole with locally abundant carbonates. The Valmaggia pipe hosts blebby and semi-massive sulfide mineralization in its rim portion, compared to a smaller (< 1 mm) disseminated assemblage in the core. Locally, the sulfides are rimmed by and/or intergrown with carbonates, phlogopite and amphibole, particularly in the rim portion.

3 Samples and Methods

Four polished thin sections from the Valmaggia pipe were investigated, i.e., two from the core (VMG1B and VMG7) and two from the rim (I-6A and I6B). The sections were studied using transmitted and reflected light microscopy using a Leica DVM 6 digital microscope in the Department of Geosciences and Geological and Petroleum Engineering (GGPE) at Missouri University of Science and Technology.

Major and minor element compositions of sulfides, carbonates and silicates were determined using a JEOL JXA-8200 electron microprobe equipped with wavelength and energy dispersive spectrometers (EDS and WDS) in the Department of Earth and Planetary Sciences, Washington University, St. Louis, Missouri, USA. Precision and accuracy were better than 3-5% (2σ).

A total of 27 quantitative sets of maps (^{23}Na to ^{238}U) were generated by time-of-flight LA-ICP-TOF-MS (Savard et al. 2023) using a 7, 9, and 19 µm beam size. The analysis focused on sulfide grains that were in contact and/or or spatially close to volatile phases (carbonates and/or hydrous silicates).

4 Sulfide – Carbonate Relationships

Sulfide mineralization in the core of the Valmaggia pipe is commonly disseminated, consisting of < 1 mm patches and composite blebs of pyrrhotite + pentlandite ± chalcopyrite (Fig. 2). Sulfide mineralization in the rim is semi-massive, consisting of polyphase blebs composed of pyrrhotite + pentlandite ± chalcopyrite several microns up to 1 cm in the longest direction (Fig. 3A). In both domains, sulfides are commonly embayed with, or rimmed by, carbonate phases (Fig. 3) and/or hydrous silicates (phlogopite, amphibole). The TOF-LA-ICP-MS data show that sulfides spatially related to carbonates are variably enriched in lithophile elements in the rim (< 20-370 ppm Na, 100-7400 ppm Mg, < 40-390 ppm Al, and < 330-676 ppm Ca) and the core (< 20-530 ppm Na, < 50-1100 ppm Mg, < 40-280 ppm Al, < 330-580 ppm Ca).

Carbonates in the studied samples are generally dolomitic, with less common calcite and Ca-Mg-Fe carbonate phases. The Ca-rich carbonate phases commonly occur adjacent to, or in direct contact with sulfides (Figs. 3A and 4A). Conversely, Ca-poor and Fe-rich phases are mostly surrounded by and intermixed with silicate phases and restricted to sulfide-poor or -absent areas.

Three distinct carbonate groups were identified in this study:

1) Carbonates in direct contact with sulfide grains/blebs in sulfide-rich areas. These grains contain 15-20 wt.% Mg, 20-30 wt.% Ca, 2-3 wt.% Fe, with 1500-2000 ppm Mn, 40-60 ppm Pb, < 90-2780 ppm Ni, and < 30-170 Cu;

2) Carbonates not in direct contact with sulfides, but near small, disseminated sulfide grains (<150 µm) in sulfide-poor areas. These grains contain 34-50 wt.% Mg, < 0.5 wt.% Ca, 10-15 wt.% Fe, 0.5-0.7 wt.% Mn, < 90-120 ppm Ni, and < 30-34 ppm Cu;
3) Carbonates within sulfide grains as vein fill (only in sample VMG7). These grains contain 8-9 wt.% Mg, 20-22 wt.% Ca, 2-3 wt.% Fe, 3-6 wt.% Mn, < 90-265 ppm Ni, and < 30-90 ppm of Cu.

5 Bubble transport vs. chemical precipitation of sulfides in the Valmaggia pipe

Two possible models for the origin of sulfide mineralization in the Valmaggia pipe are discussed: physical bubble-pair transport and chemical sulfide-carbonate co-precipitation.

A physical bubble transport mechanism for sulfides from the upper crustal Norilsk-Talnakh deposit in Russia was recently proposed by Barnes et al. (2019). These authors identified several key characteristics that may be indicative of a bubble transport, including:

1) Crystalline silicate caps uniformly oriented in the direction of lower lithostatic pressure "above" sulfide blebs or globules ("segregation vesicles"), indicating the buoyant migration of the vapor bubble upwards;
2) Flattening of sulfide globules perpendicular to the direction of ascent (gravitational settling);
3) Internal differentiation in the sulfide globule;
4) Differentiation in the silicate "cap".

Similarly, studies by Mungall et al (2015) and Yao and Mungall (2020) conducted experimental and natural studies confirming that under certain conditions, vapors can exsolve from a melt and act as a 'raft' for immiscible sulfide droplets to migrate upwards through a melt.

Here we further investigate the possibility of bubble transport in the Valmaggia pipe via trace element TOF-LA-ICP-MS mapping. Our observations show several lines of evidence that are not consistent with a simple bubble transport model. For example, the mineral textures observed in the samples studied here do not follow the criteria identified by Barnes et al. (2019). There is no obvious uniform orientation of the volatile-rich components associated with sulfides that would indicate pressure-controlled ascent of sulfide-bubble pairs (Fig. 2). Further, uniform flattening of sulfides is not observed although the effect of flattening should theoretically be stronger considering the emplacement depth and impact of high pressure on crystal settling.

Cuspate "embayments" within sulfides are rarely rimmed with carbonates or other volatile-bearing phases. Comb-textured carbonate aggregates

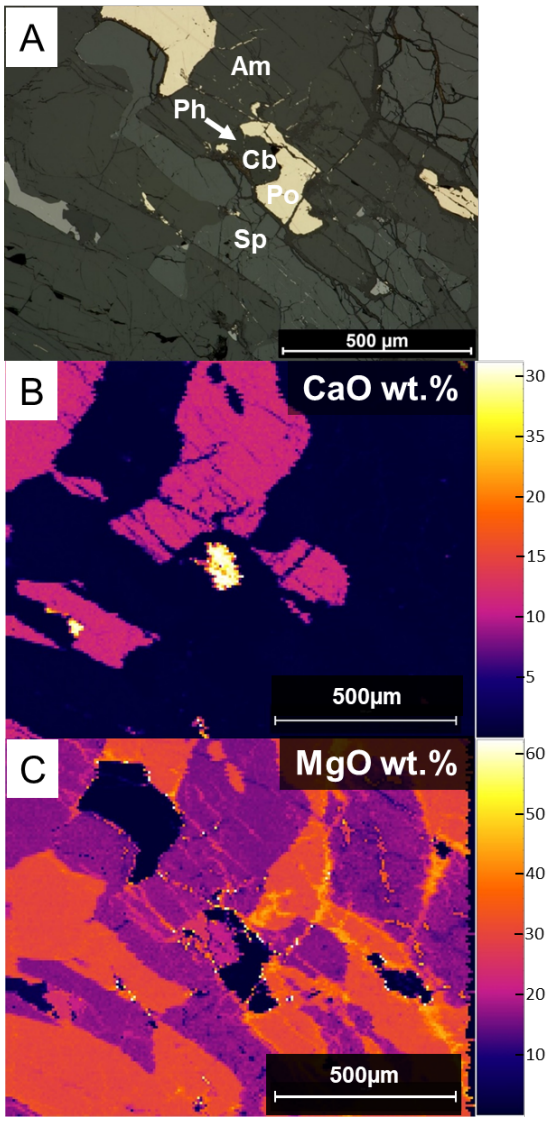

Figure 3. A: Reflected light image of a monophase pyrrhotite grain with a Mg-Ca carbonate grain embayment from sample I6B. B-C: Time-of-flight LA-ICP-MS elemental weight % maps analyzed with a 7 µm beam size. Yellow indicates the highest concentration measured for CaO (B) and MgO (C). Am = amphibole, Cb = carbonate, Po = pyrrhotite, Sp = spinel, Ph = phlogopite.

adjacent to sulfides (which may indicate late-stage carbonate precipitation) were documented by Sessa et al. (2017) and Blanks et al. (2020), but not observed in this study, possibly indicating more than one carbonate mineralization event. The absence of uniform relationships between sulfides and volatile-bearing phases suggests that their formation (or preservation) likely was not uniform throughout the pipe. Furthermore, it is noted that internal differentiation of sulfides and silicate caps (*cf.* Barnes 2019) remain to be fully investigated; however, our currently available data do not show any textural or compositional evidence for mineral-scale differentiation processes.

In contrast to a simple bubble transport model, several textural and geochemical observations appear to favour co-precipitation of sulfides, carbonates, and (metasomatic) silicates. For example, the enrichment of lithophile elements (Ca,

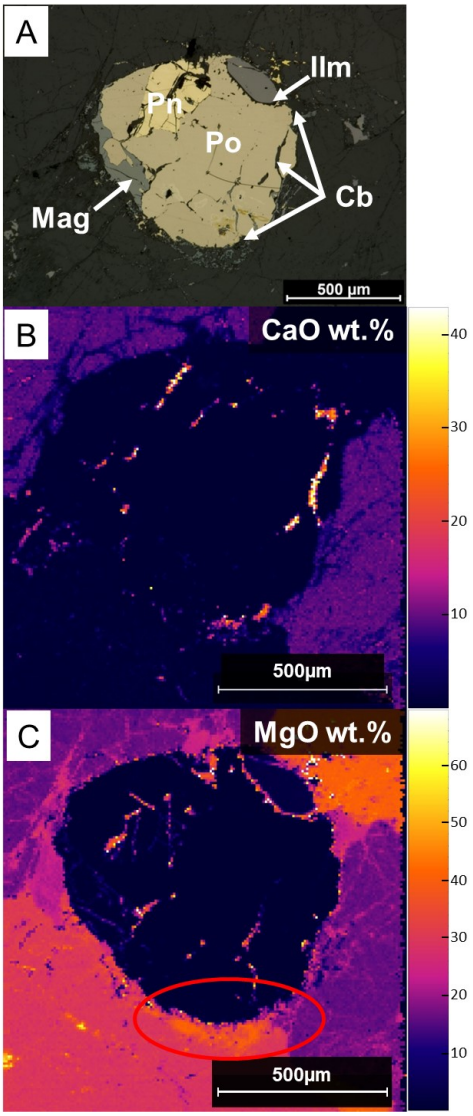

Figure 4. A: Reflected light image of a composite pyrrhotite-pentlandite bleb with accessory ilmenite, magnetite, and carbonate phases surrounding the bleb (center) from sample VMG1B. B-C: Time-of-flight LA-ICP-MS elemental weight % maps analyzed with a 7 µm beam size. Yellow indicates the highest concentration measured for CaO (B) and MgO (C). Am = amphibole, Cb = carbonate, Po = pyrrhotite, Mag = magnetite, Ilm = ilmenite.

Mg, Na, Al) in pyrrhotite and chalcophile elements (Cu, Ni, Fe, Pb) in carbonate phases indicates that the composition of sulfides and carbonates are controlled by the same geochemical process. This is further indicated by the occurrence of varying carbonate compositions (Ca-rich vs Mg- and Fe-rich). Carbonate inclusions in sulfides (Figs. 4B, 4C) have a composition similar to that of the rimming carbonates: this relationship cannot be explained with a simple bubble transport model as it is not physio-chemically compatible. Rather, it indicates that a carbon-rich fluid was present during sulfide ore formation.

The observations presented here possibly indicate co-exsolution of a carbonate phase and sulfide minerals from a S and CO_2 saturated fluid/melt. The findings from this study highlight the need for more comprehensive research on the roles of volatile phases in the transport and deposition of S and metals in the deep lithosphere.

Acknowledgements

M. L. acknowledges support through the National Science Foundation (NSF) CAREER award #1944552 “Investigating the source, transport and deposition of economically important metals in the lower continental crust”.

References

Barnes, S. J., Le Vaillant, M., Godel, B., & Lesher, C. M. (2019). Droplets and bubbles: solidification of sulphide-rich vapour-saturated orthocumulates in the Norilsk-Talnakh Ni–Cu–PGE ore-bearing intrusions. Journal of Petrology, 60(2):269-300.

Blanks, D. E., Holwell, D. A., Fiorentini, M. L., Moroni, M., Giuliani, A., Tassara, S., González-Jiménez, J.M., Boyce, A., & Ferrari, E. (2020). Fluxing of mantle carbon as a physical agent for metallogenic fertilization of the crust. Nat Communications, 11(1):4342.

Garuti, G., Rivalenti, G., Rossi, A., Siena, F., Sinigoi, S., 1980. The Ivrea–Verbano mafic ultramafic complex of the Italian western Alps: discussion of some petrologic problems and a summary. Rendiconti della Societa Italiana di Mineralogia e Petrografia 36:717-749.

Locmelis, M., Fiorentini, M.L., Rushmer, T., Arevalo Jr, R., Adam, J. and Denyszyn, S.W. (2016). Sulfur and metal fertilization of the lower continental crust. Lithos, 244:74-93.

Locmelis, M., Moroni, M., Denyszyn, S.W., Webb, L.E., Fiorentini, M.L., Sessa, G., Caruso, S., Mathur, R. and Nanzad, B. (2021). On the formation of magmatic sulphide systems in the lower crust by long-lived mass transfer through the lithosphere: Insights from the Valmaggia pipe, Ivrea Verbano Zone, Italy. Terra Nova, 33(2):137-149.

Mehnert, K. R. (1975). The Ivrea Zone, a model of the deep crust. Neues Jahrbach fuer Mineralogie: Abhandlungen 125:156-199.

Mungall, J. E., Brenan, J. M., Godel, B., Barnes, S. J. & Gaillard, F. (2015). Transport of S, Cu and Au in magmas by flotation of sulphide melt on vapour bubbles. Nat Geoscience 8:216–219.

Savard, D., Dare, S., Bédard, L.P. and Barnes, S.-J. (2023). A New Mapping Protocol for Laser Ablation (with Fast-Funnel) Coupled to a Time-of-Flight Mass Spectrometer (LA-FF-ICP-ToF-MS) for the Rapid, Simultaneous Quantification of Multiple Minerals. Geostandards and Geoanalytical Research. Accepted Author Manuscript.

Sessa, G., Moroni, M., Tumiati, S., Caruso, S., & Fiorentini, M. L. (2017). Ni-Fe-Cu-PGE ore deposition driven by metasomatic fluids and melt-rock reactions in the deep crust: the ultramafic pipe of Valmaggia, Ivrea-Verbano, Italy. Ore Geol Rev, 90:485-509.

Schodde, R. (2017). Recent trends and outlook for global exploration. In Prospectors & Developers Association of Canada (PDAC) Convention, Conference Proceedings.

Yao, Z., & Mungall, J. E. (2020). Flotation mechanism of sulphide melt on vapour bubbles in partially molten magmatic systems. Earth and Planet Science Lett, 542:116298.

Zaccarini, F., Garuti, G., Fiorentini, M. L., Locmelis, M., Kollegger, P., & Thalhammer, O. A. (2014). Mineralogical hosts of platinum group elements (PGE) and rhenium in the magmatic Ni-Fe-Cu sulfide deposits of the Ivrea Verbano Zone (Italy): an electron microprobe study. Neues Jahrbuch für Mineralogie, 191:169-187.

Ni-Cu-Co-Bi mineralization in Valea Muntelui ultramafic complex (Cindrel Mountains, Romania)

[1]George Dincă, [1]Gavril Săbău, [1]Andra Filiuță
[1]Geological Institute of Romania, 1 Caransebeș St., Bucharest, Romania

Abstract. This paper presents the discovery of Ni-Cu-Co-Bi mineralization in Valea Muntelui ultramafic bodies from the Southern Carpathians. Core samples from two exploration drill holes in the ultramafic body were studied using optical microscopy and SEM/EDS measurements. All of the described ore minerals were discovered in highly serpentinized ultramafic rocks, with the mineral association consisting of ferromagnesian and calcic amphiboles, chlorite, talc, and dolomite, as well as chromiferous spinel grains partially transformed into magnetite. Pentlandite, pyrrhotite, cubanite, cobaltite, chalcopyrite, nickeline, maucherite, parkerite, native Bi, native Pb and natural Cu-Zn alloys were identified. The mineralization process appears to be linked to metasomatic fluids and the redox process leading to the development of a reducing character of the fluids. This research is the first description of Ni-Cu-Co-Bi mineralization in the region, and the first mention of parkerite in Romania and the Balkan Region.

1 Introduction

The studied area is located in the northern part of the Central Southern Carpathians (northeast of the Cindrel Mountains), west of the Olt River Valley, and approximately 2.0 km southwest of the town of Rășinari, Romania.

An unusual Ni-Cu-Co-Bi mineralization appears in Valea Muntelui ultramafic bodies included in the medium-grade Lotru Metamorphic Suite of the South Carpathian basement units.

The mineralization is located along the Valea Muntelui Brook, being hosted in a metamorphosed dunite-peridotite-gabbroic complex preserving abundant textural relics (Codarcea, 1965). The ultramafic rocks, as also amphibolite and eclogite pods equally pointing to mantle- and ocean crust-derived protoliths, appear scattered on a regional scale in the dominantly plagioclase-gneiss matrix of a Variscan tectono-metamorphic complex, marking a suture zone and overlying reworked Early Paleozoic gneissic-granitic basement units (Săbău and Negulescu, 2014).

2 Samples and Methods

Core samples from two exploration drill holes in the ultramafic body were studied. To perform this study, over 20 polished sections of ore samples, were analyzed by optical microscopy under reflected light. The optical microscope used was a Zeiss Imager A2m with an attached Zeiss Axiocam ICc 5 MP camera. Mineral symbols recommended by the Commission on New Minerals, Nomenclature and Classification of the International Mineralogical Association were used for mineral abbreviation in figures and tables (Warr, 2021). For the determination of the chemical composition, SEM/EDS measurements were conducted at the Geological Institute of Romania using a Hitachi TM3030 SEM on uncoated samples with an acceleration voltage of 15 kV, emission current of 25400 nA, focused beam in scanning mode, at a working distance of 7.5-9 mm, and variable counting times averaging 120 s, aimed to optimize noise to signal ratio, visually appreciated from the smoothness of the background spectrum. Elemental analysis was done through Bruker's QUANTAX 70 EDS system.

3 Results

The host rocks are represented by transformed peridotites with a complex history, with medium grade metamorphic and retrograde overprints, as well as attenuation of the chemical gradients towards the host rocks. All of the below-mentioned ore minerals were identified in highly serpentinized and carbonated varieties. Frequent domain textures suggest the preexistence of coarsely developed grains, but their former boundaries appear diffuse, and the composition is exclusively made up of secondary minerals. The mineral association consists of ferromagnesian and calcic amphiboles often with zonal or overgrowth structure, chlorite, talc, and dolomite. The presence of dolomite and talc indicates metasomatic alteration with the contribution of carbonate fluids and silica, of the same nature as listvenitization, but without the installation of a quartz – carbonate – K-white mica association characteristic for the completion of this process (Halls and Zhao, 1995). Several chromiferous spinel grains partly transformed into magnetite were identified, which imply a preliminary stage of iron release during the serpentinization of ultramafic association. Iron oxide crystals with dimensions up to 0.1 mm, sometimes with idiomorphic outlines, are disseminated in the rock. In one of the samples the mineralization is concentrated along former cracks and former grain boundaries.

3.1 Pentlandite, Pyrrhotite, Chalcopyrite and Cubanite

The carbonate+talc altered samples display a noteworthy mineralogical assemblage of: pentlandite, pyrrhotite, cubanite, cobaltite, and chalcopyrite (Fig. 1) disseminated throughout the sample, indicating a higher

concentration of sulfides compared to other serpentinite varieties from the region. The empirical composition of pentlandite from Valea Muntelui is $Ni_{3.51}Co_{0.16}Fe_{5.11}S_{8.22}$, Co varying from 1 to 3 wt%.

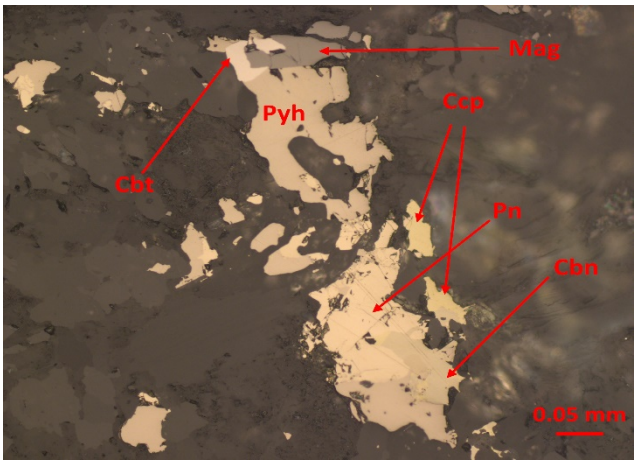

Figure 1. Reflected light photomicrograph of the common ore mineral association, formed by: pentlandite (Pn),, chalcopyrite (Ccp), pyrrhotite (Pyh), cubanite (Cbn) magnetite (Mag) and cobaltite (Cbt).

Chemical analyses of chalcopyrite and cubanite from Valea Muntelui gave the following formulas: $Cu_{1.04}Fe_{0.99}S_{1.97}$ and $Cu_{0.90}Fe_{2.04}S_{3.06}$.

3.2 Nickeline and Maucherite

Nickeline was identified in samples from Valea Muntelui in association with pyrrhotite and magnetite (Fig. 2). The calculated formula is $Ni_{0.93}Fe_{0.05}As_{1.02}$, being slightly enriched in Fe (up to 2.5 wt%).

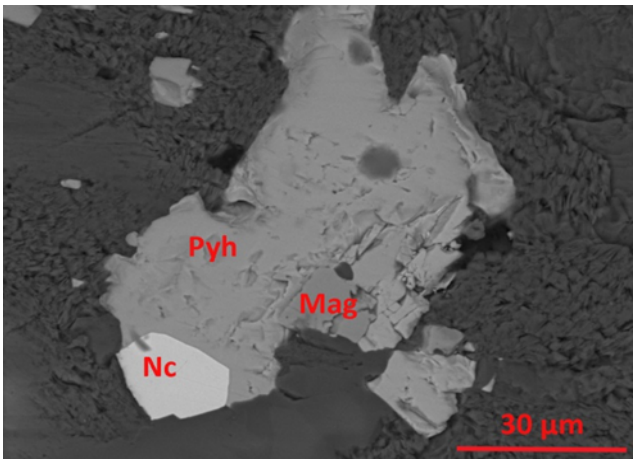

Figure 2. Back-scattered electron image showing a nickeline crystal (Nc) with pyrrhotite (Pyh) and magnetite. (Mag)

Maucherite is a rare Ni arsenide previously described in the South Carpathians by Popescu (1968) in the Bădeni Ni mineralization (Leaota Mountains), in a Ni-Co-Ag mineralization from Nimaia Valley, East Făgăraș Mountains (Lupulescu, 1982), and at Iacobeni, East Carpathians, associated with cobaltite and tučekite (Săbău, 2015). Presence of maucherite in Cindrel Mountains has not been reported so far. In the studied samples maucherite has been found in association with pentlandite and chalcopyrite (Fig. 3). Crystals can reach up to 150 µm in lenght.

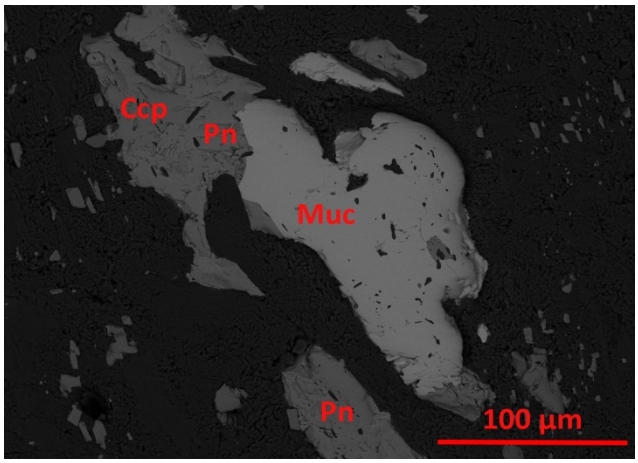

Figure 3. Back-scattered electron image showing a maucherite crystal (Muc) with pentlandite (Pn) and chalcopyrite. (Ccp)

The calculated empirical formula of maucherite is $Ni_{10.91}Fe_{0.34}Co_{0.18}As_{7.50}Sb_{0.07}$.

3.3. Co and Bi minerals

Cobaltite has been identified quite frequently as euhedral singular crystals in serpentine (Fig. 4) and in association with pentlandite, chalcopyrite, pyrrhotite and cubanite (Fig. 1). Chemical analyses of cobaltite from Valea Muntelui gave the following formula: $Co_{0.78}Ni_{0.10}Fe_{0.11}As_{1.05}S_{0.97}$.

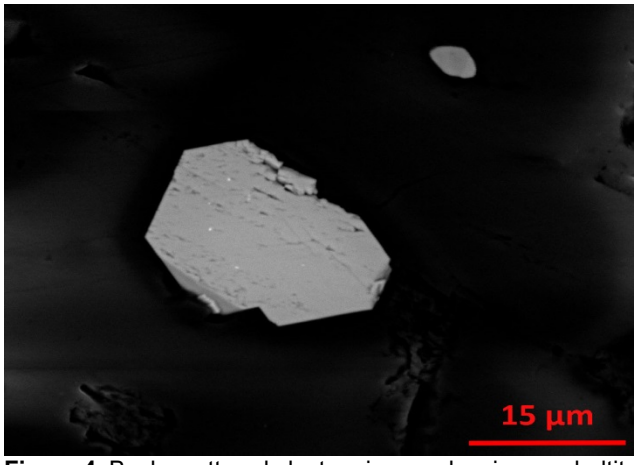

Figure 4. Back-scattered electron image showing a cobaltite crystal**.**

Cobaltite from the studied samples always presents Ni and Fe in the composition, with contents up to 4 wt%.

Parkerite was identified in only one sample from Valea Muntelui. It occurs as a 10 µm inclusion in pyrrhotite, presenting a rim of native Bi (Fig. 5). To our knowledge this is the first mention of parkerite in Romania an in the Balkan Region. The calculated empirical formula of parkerite is $Ni_{2.77}Co_{0.12}Fe_{0.70}Bi_{1.35}As_{0.18}S_{1.89}$. Parkerite from Valea Muntelui is lead free similar to parkerite from the Uralian Emerald Mines, Ural Mountains (Russia) described by Koroteev et al. (2017). The studied parkerite crystal is enriched in Fe and Co as shown in the chemical composition (Table 1).

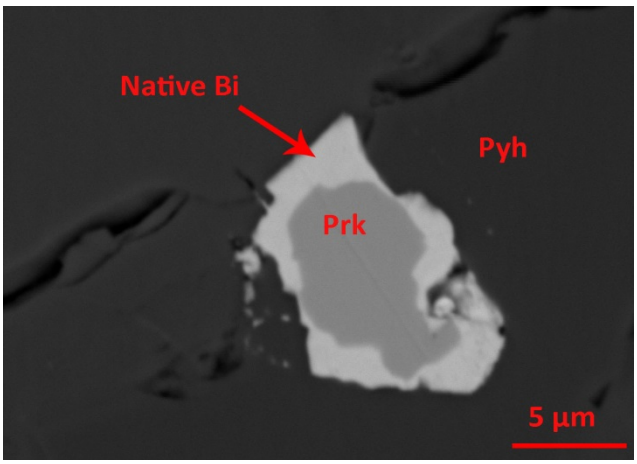

Figure 5. Back-scattered electron image showing parkerite (Prk) with native Bi rim included in pyrrhotite. (Pyh)

Table 1. Representative chemical composition of investigated Ni-Cu-Co-Bi minerals based on SEM-EDS analyses. Pn-pentlandite; Nc-nickeline; Muc-maucherite; Cbt-cobaltite; Prk-parkerite; Cbn-cubanite; Ccp-chalcopyrite

Element (wt%)	Pn	Nc	Muc	Cbt	Prk	Cbn	Ccp
Ni	26.94	40.60	51.60	3.61	28.80	-	-
Co	1.22	-	0.87	27.45	1.22	-	-
Fe	37.33	2.12	1.51	3.57	6.95	41.91	32.49
Cu	-	-	-	-	-	23.73	36.55
As	-	57.27	45.30	46.83	2.41	-	-
Sb	-	-	0.72	-	-	-	-
Bi	-	-	-	-	49.86	-	-
S	34.50	-	-	18.53	10.75	34.36	30.96
Total	100.00	100.00	100.00	100.00	100.00	100.00	100.00

3.4 Cu-Zn natural alloys

Natural Cu-Zn alloy was identified as small disseminated grains in association with native Pb. The natural Cu-Zn alloy shows the dominant composition of $Cu_3(Zn, Fe)_2$, with irregular zones richer in Fe and Ni, corresponding to the approximate composition $Cu_5Zn_3(Ni, Fe)_2$.

Table 2. SEM-EDS analyses of Cu-Zn phases.

Element (wt%)	Phase 1	Phase 2
Cu	56.83	49.31
Zn	38.40	32.67
Ni	-	15.67
Fe	4.77	2.35
Total	100.00	100.00

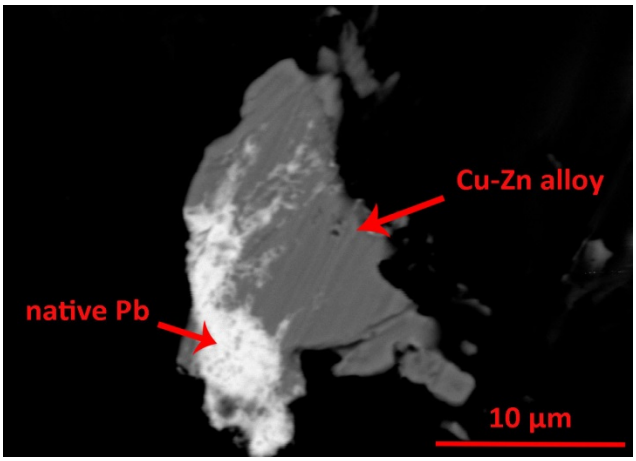

Figure 6. Back-scattered electron image showing association of native Pb with Cu-Zn alloy.

4 Discussion and conclusions

Ni-Cu-Co-Bi mineralization is described for the first time in this area, alongside native elements and alloys indicating a highly reducing chemical environment. The pertaining mineral phases appear in highly serpentinized and metasomatized metaultramafic rocks characterized by a talc-dolomite-chlorite assemblage more or less completely installed. The talc and dolomite-enriched metasomatized samples present a special mineral association, with Ni and Co sulfides and arsenides, native metals (Pb, Cu alloys, Bi) and parkerite, which, to our knowledge, is still unknown from other ultrabasic outcrops. The assemblage is typically represented by small grains disseminated in the altered rock or clustered along micro-lineaments which represent former circulated cracks or grain boundaries, indicating its formation during serpentinization and carbonate metasomatism following it or acting coevally.

The possible source of the elements involved is probably multiple, caused by fluid transport and mixing during metasomatic exchange processes. Decomposing olivine, in which Ni and Co are compatible, as well as pre-existing orthomagmatic Fe-Ni sulfides are the most probable source for siderophile elements. Base metals, As and Bi are most probably externally-derived, transported from the host rocks. Such mineralizations are known in structurally lower positions of the metamorphic basement, where they are considered shear zone-related (Popescu et. al, 2013, and refs. therein).

The onset of a reducing environment is triggered by the serpentinization of Mg-Fe – bearing silicates. Mg is preferentially incorporated in serpentine minerals, from which Fe is expelled and constrained to form magnetite, implying the oxidation of part of Fe^{2+} and the correlative reduction of the coexisting carbonaceous-aqueous fluid phase, which could transiently produce hydrogen and/or highly reduced C-bearing species (Berndt et al., 1996). This mechanism was invoked also for the formation of Fe-Ni alloys in serpentinized peridotites (Frost, 1985).

The complexity and unusual composition of this mineralization is a reflection of the combination of sources and processes operating during incorporation of ultramafic rocks in a tectonic mélange, medium-grade metamorphism, retrograde alteration, and chemical mass-transfer with the surrounding rocks.

Acknowledgements

We thank MINERAL PROIECT INVEST SA for the access to samples from Valea Muntelui. and the GeoEcoLab Laboratory, Geological Institute of Romania, for the acces to the SEM-EDS facilities. The authors acknowledge the financial support by the national research project PN23-39-02-03.

References

Berndt, M.E., Allen, D.E., Seyfried W.E Jr,. Reduction of CO_2 during serpentinization of olivine at 300 °C and 500 bar, *Geology, 24/4, 351-354*

Codarcea-Dessila, M. (1965), Studiul Geologic și Petrografic al Regiunii Rășinari-Cisnădioara-Sadu, *Mem. Com. Geol., Inst. Geol. Rom., Bucureşti vol. 6, 96 pp.*

Frost B.R. (1985) On the Stability of Sulfides, Oxides, and Native Metals in Serpentinite, *J. of Petrology 26/1, 31-63*.

Koroteev, V.A., Popov, M.P., Erokhin Yu. V., Khiller V.V. (2017) Parkerite and bismutohauchecornite in chromitites of the Urals: Example of the Uralian Emerald Mines, *Dokl. Earth Sc. 473, 438–440.*

Lupulescu, M. (1982): Prezenţa unei mineralizaţii de nichel, cobalt și argint în partea estică a Munţilor Făgăraş (V. Bârselor). [On the presence of a Ni-, Co- and Ag-bearing mineralization in the Eastern part of the Făgăraş Mts. (Bârse Valley)], *An. Univ. Bucureşti. Ser. Geol, 30, 27-31.*

Popescu. Gh.C. (1968): Asupra prezenţei maucheritului în mineralizaţia de nichel de la Bădeni (Munţii Leaota). [On the presence of maucherite in the Ni-bearing mineralization at Bădeni. Leaota Mts.], *Stud, cercet. Geol. Geofiz. Geogr., Ser. Geol, 13. 431-435*.

Popescu Gh.C., Neacșu A., Buia G., Damian G., Damian F. (2013) Perspectives of rare metals and dispersed elements ore deposits in Romania. A review. *Romanian J. of Mineral Deposits 86/1, 1-41*

Săbău, G. (2015) Co,Ni – bearing assemblages in the metamorphosed Mn ore from Iacobeni, Sub-Bucovinian Nappe System, East Carpathians, *Presentation, "Mircea Savul" Scientific Symposium, University of Iași, 24 october 2015*

Săbău, G., Negulescu, E. (2014) A monazite U-Th-Pb_T metamorphic ages survey in the South Carpathian basement units: delving into tectonic stacking and differential exhumation. *Buletini i Shkencave Gjeologjike, Special Issue Vol. 1/2014, Proc. XX Congress of Carpathian Balkan Geological Association (CBGA 2014), 24-26 September 2014, Tirana, Albania, 219-222*

Warr, L. N. (2021) IMA–CNMNC approved mineral symbols., *Mineral. Mag. 85, 291–320*.

Magmatic sulphide mineralization and prospectivity in the Tantalite Valley Complex, Namibia

Daniel Ferreira[1], Bjorn Von der Heyden[1], Martin Klausen[1], Laure Martin[2]
[1] *Department of Earth Sciences, Stellenbosch University, South Africa*
[2] *Centre for Microscopy, Characterization, and Analysis, University of Western Australia, Perth, Australia*

Abstract. The formation of immiscible sulphide melt within mafic-ultramafic magmas and its concentration of base-, semi-, and precious metals constitutes an important process in the formation of magmatic sulphide deposits. This study investigates the Tantalite Valley Complex in southern Namibia and the formation of sulphides within the complex and their potential to host valuable metals by examining the processes that led to sulphide melt segregation and accumulation. The research concludes that the TVC comprises a sequence of trough shaped layers of ultramafic dunite, harzburgite, websterite, pyroxenite, as well as troctolite and other gabbroic rock types whose stratigraphy has been complicated by faults and mineralization manifesting as disseminated sulphides within stratiform layers most notably within a pyroxenite layer. Furthermore, the sulphur in the system is derived from the mantle. Sulphide melt saturation is believed to have occurred due to high degrees of fractionation. Precious metals exist in both solid solution and discrete precious metal bearing minerals found within and associated with the sulphide phases. The R-factor for the complex stands at approximately 3 000 suggesting that a small fraction of sulphide melt formed, mixing to moderate degrees with the silicate magma before concentrating in a pyroxenite layer.

1 Introduction

The Tantalite Valley Complex (TVC) is a mafic-ultramafic igneous intrusion found within the core of the Pofadder Shear Zone which crosscuts the Richtersveld Subprovince (Figure 1). To date, previous exploration has been centred on uncovering massive Ni-Cu sulphide deposits. No previous research has been undertaken to investigate the potential for platinum group element (PGE) mineralisation. Mafic-ultramafic intrusions of this nature often yield economic deposits having concentrated base-, semi- and precious-metals, in the form of either sulphur-rich massive Ni-Cu (Co) sulphide deposits or sulphur-poor disseminated PGE deposits. Should a mineralised horizon or reef exist within the complex, its concentration of base-, semi- and precious-metals could warrant further investigation and prompt an in depth look into the economic potential of the complex with regards to PGEs.

Our research aims to analyse the metallogenesis of the complex and to assess its prospectivity for PGE mineralisation. From this we aim to gain better insight into the primary and secondary processes responsible for these concentrations of metals as well as their mineral makeup and associations.

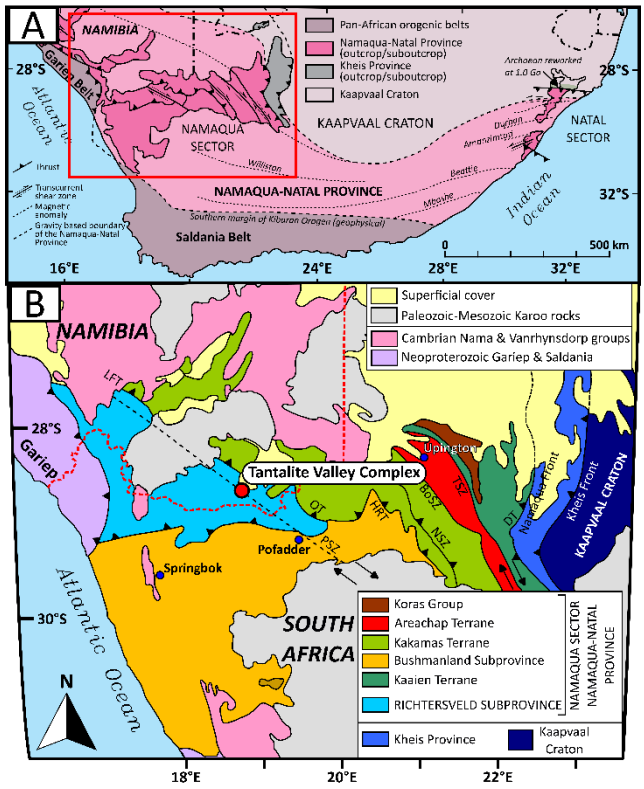

Figure 1. A) Location of the Namaqua Natal Metamorphic belt. B) The Namaqua Sector of the Namaqua Natal Metamorphic Belt. Modified from Macey et al. (2017).

2 Regional and local geology

The Namaqua Natal Metamorphic Province (NNMP) displayed in Figure 1 is a 400 km wide tectono-metamorphic belt bounding the southern and western margins of the Kaapvaal craton (Thomas et al. 1994; Cornell et al. 2006). The province is composed of two sectors, the Namaqua and the Natal sectors in the west and east respectively with the Namaqua sector having five distinct subdivisions, namely; the Richtersveld subprovince, the Bushmanland subprovince, and the Kakamas, Areachap and Kaaien terranes (Thomas et al. 1994; Cornell et al. 2006).

The Tantalite Valley Complex (TVC) is a mafic – ultramafic complex that intruded at 1212 ± 11 Ma into host rocks of the Richtersveld subprovince in the Namaqua-Natal Metamorphic Province (Moore et al. 1979; Macey et al. 2017; Figure 1). The host rocks have experienced numerous metamorphic and deformation events associated with the Orange River and Namaquan orogenies. The Orange River Group host rocks underwent deformation during the Namaquan Orogeny and now form part of the Namaqualand Gneiss Complex (von Backstrom

1976; Schreiber 2016). The approximately 9 x 3 km complex is found within the Pofadder Shear Zone, a dextral shear zone that stretches from the northeast of Luderitz in Namibia to the northeast of Pofadder in South Africa for a distance of 500 km (Kartun 1979). The complex consists of variably altered lithologies of norite, gabbronorite, olivine metagabbro, metagabbro, metagabbronorite, metatroctolite and ultramafic rocks such as dunite, harzburgite, lherzolite, (olivine) websterite and orthopyroxenite along with a thin contact hornfels zone (± 50 m) best seen along the complex's south-eastern and eastern border (von Backstrom 1976; Moore et al. 1979; Schreiber 2016).

3 Methodology

3.1 SEM analysis

Eleven well mineralized polished mounts were selected based on promising assay results and optical microscopy and were then analysed using SEM to ascertain the compositions of the "high contrast minerals" which includes those belonging to the Platinum Group Minerals (PGM).

SEM Energy Dispersive Spectrometer (SEM-EDS) analysis and elemental mapping was accomplished using a Zeiss EVO® MA15 Scanning Electron Microscope. The system is designed to perform high-resolution imaging concurrently with quantitative analysis, with errors ranging from ± 0.6 to 0.01 wt% on the major elements using EDS.

Platinum group minerals were identified with backscattered electron images, and phase compositions were quantified by EDS analysis using an Oxford Instruments® X-Max 20mm^2 detector and Oxford INCA software. Beam conditions during the quantitative analyses were 20 kV and approximately 1.0 A, with a working distance of 8.5 mm and a specimen beam current of - 20.00 nA. For mineral analyses counting time was 10 seconds live-time. Internal Astimex Scientific mineral standards were used for standardization and verification of the analyses. All major elements are below 5% uncertainty of their certified compositions. Pure Co was used periodically to correct for detector drift.

3.2 LA-ICP-MS

Bulk rock chemistry and LA-ICP-MS was undertaken on a subset of polished mounts and crushed country rock samples. The LA-ICP-MS set up follows guidelines set out by Eggins (2003). The methods employed here includes a resolution 193 nm Excimer laser coupled to an Agilent 7700 Q ICP-MS housed at the Central Analytical Facility (CAF), Stellenbosch University. The ICP-MS was optimized for low oxide ratios (less than 0.3%) and sensitivity by ablating a line on NIST612 whilst tuning both the laser parameters and the ICP. Ablation was performed in an atmosphere of Helium gas with a flow rate of 0.45L/min and then mixed with Argon with a flow rate of 1L/min and Nitrogen (0.003L/min) just before introduction into the ICP Plasma. A background acquisition time of 20 seconds was used with an ablation time of 45 seconds followed by a washout time of 25 seconds. Uncertainty for major elements is typically below 6% of their certified compositions. A total of 80 spots were selected for in-situ LA-ICP-MS from four polished mounts spread out across pyrite, pentlandite and pyrrhotite.

3.3 Secondary Ion Mass Spectrometry (SIMS) analysis

Three samples were sent for SIMS analysis at the Centre for Microscopy, Characterisation, and Analysis (CMCA) at the University of Western Australia for triple sulphur isotope analysis (^{33}S, ^{34}S, ^{36}S). The phases tested were pentlandite, pyrrhotite and pyrite for a total of 89 spots. The analysis protocol uses a CAMECA IMS1280 large-geometry ion microprobe with matrix-matched standards (LaFlamme et al. 2016) used to correct for instrumental mass fractionation. The matrix-matched standards are as follows: Sierra pyrite (δ^{34}S = 2.17 ± 0.28‰; Δ^{33}S = -0.02 ± 0.01‰; Alexo pyrrhotite (δ^{34}S = 5.23 ± 0.40‰; Δ^{33}S = -0.96 ± 0.04‰); VMSO pentlandite (δ^{34}S = 3.22 ± 0.51‰; Δ^{33}S = 0.0 ± 0.02‰) (LaFlamme et al. 2016). Uncertainty for isotope concentrations is typically below 6% of their certified compositions.

4 Sulphide and PGM paragenesis

Analysis of all polished mounts made from orthopyroxenite obtained from drill core reveals a primary pristine assemblage of sulphide disseminations with a largely interstitial/intergranular texture or in some rare instances as blebs of magmatic sulphides. The primary magmatic assemblage consists of pentlandite-pyrrhotite-chalcopyrite (Figure 2) with pentlandite having the greatest modal proportion in most cases followed by pyrrhotite and finally chalcopyrite. However, their proportions do vary considerably across drill core samples. Often seen under the microscope is a border of pentlandite separating the chalcopyrite and pyrrhotite indicating it to be peritectic in nature, pentlandite can infrequently be found as exsolved pentlandite flames within pyrrhotite grains. Alteration of the above pristine assemblage within orthopyroxenite manifests as an overprint in which primary pyrrhotite (pyrrhotite$_1$) (and in some instances pentlandite) is replaced by pyrite$_1$ due to late-stage hydrothermal fluids. Pyrite occurs as large euhedral grains with a hexagonal habit but also occurs as anhedral linear arrays within pyrrhotite$_1$ marking the plane of fluid ingress. Alteration further manifests in the gangue silicate assemblage in which amphibole and micas have recrystallized as pyroxene pseudomorphs (not to completion) and overgrowths. Following this, pyrite$_1$ associated with pentlandite and chalcopyrite and the first replacement assemblage is occasionally altered to pyrrhotite$_2$. The two pyrrhotite populations appear the same, however, under cross polarised light, the

primary pyrrhotite$_1$ displays uniform "extinction" within grain boundaries whilst the overprinting pyrrhotite$_2$ can be seen to have smaller euhedral polygonal granoblastic mosaic textured pyrrhotite crystals with a large number of triple junctions.

Analysis under the SEM revealed a number of high contrast minerals of varying compositions. These high contrast minerals are found largely as inclusions/clusters in pentlandite and to a lesser degree in chalcopyrite, even less so in pyrrhotite and pyrite. In some instances, PGMs are found away from sulphides completely, and spatially associated with silicates as opposed to sulphides. Some mineral phases that were found include Hessite (Ag_2Te), Electrum (gold-silver alloy), Merenskyite $(Pt,Pd)(Te,Bi)_2$, Moncheite $Pt(Te,Bi)_2$ and Paolovite (Pd_2Sn).

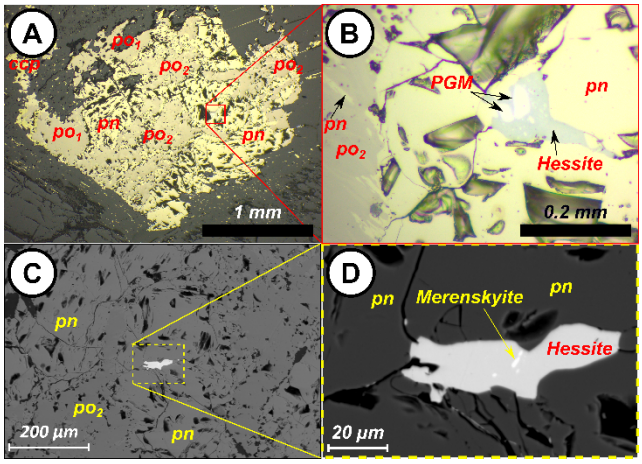

Figure 2. Reflected light microscopy as well as backscattered electron photomicrographs taken from sample D-07 which is particularly well-endowed. A) Pristine sulphide assemblage with overprinting pyrrhotite$_2$. B) Enlarged reflected light image of the PGMs and Hessite encircled in (A). C) Backscattered electron photomicrograph with the area of interest enclosed in yellow. D) Enlarged backscattered electron photomicrograph of the site of interest in (C) showing hessite with inclusions of merenskyite. Abbreviations; pn = pentlandite, po = pyrrhotite, ccp = chalcopyrite.

5 Source of sulphur and degree of silicate melt interaction

Sulphur selenium ratios coupled with multiple sulphur isotope ratios obtained from SIMS analysis (Figure 3), suggest that the sulphur in the system was derived from the mantle. Samples plotting slightly away from the mantle arrays have been the recipients of syn- to post magmatic hydrothermal alteration as well as weathering.

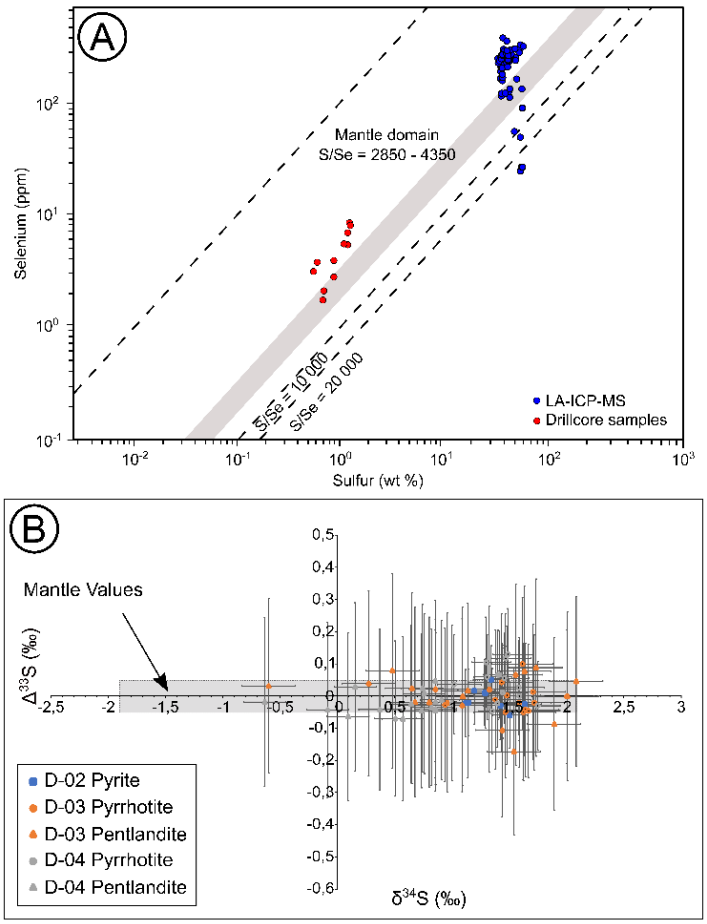

Figure 3. (A) Whole rock and in-situ LA-ICP-MS sulphur versus selenium plot. Modified from Queffurus and Barnes (2015). Mantle values determined by Eckstrand and Hulbert (1987). (B) Multiple sulphur isotope plot of pyrite, pyrrhotite and pentlandite in three different samples, the grey block in the centre represents sulphur isotope concentrations from the mantle as determined by Lesher (2017) for $\delta^{34}S$.

The R-Factor was computed using bulk rock samples from the igneous margin of the TVC as proxies for the parental melt composition. Their assay values for Co, Ni, Cu and Pd were then compared with computed values of 100% sulphides taken from the well-endowed pyroxenites to determine the R-Factor. Unfortunately, the results proved inconclusive due to alteration and metamorphism. As such, several semi-quantitative approaches were applied wherein the complex was compared to various other similar deposits in an effort to gauge its relative R-factor. The results indicate the systems R-Factor value lies between 1000 and 3000.

6 Conclusion

Sulphide saturation has occurred within the TVC resulting in the development of a relatively small fraction of sulphide melt that has preferentially concentrated base-, semi-, and precious metals within ultramafic layers and forming minor amounts

(< 2%) of pentlandite, pyrrhotite, chalcopyrite and pyrite. Based on in-situ multiple sulphur isotope analyses and S/Se values, sulphur saturation did not occur as a result of crustal assimilation of sulphur rich crustal rocks. Instead, sulphur saturation occurred following substantial degrees of fractional crystallization and occurred when orthopyroxene began crystallizing which marks a large decrease in the solubility of sulphur (see Robb 2005). The overprinting sulphides have not sourced sulphur from another reservoir but rather the magma itself, suggesting that they are likely related to syn- to early post-magmatic hydrothermal fluids.

Typically, magmatic sulphide deposits have very small footprints making them easy to miss in the field and through drilling especially if the igneous stratigraphy is poorly constrained and further complicated by structural features. However, the lack of crustal contamination will mean difficulty in obtaining substantial degrees of sulphur saturation or indeed supersaturation needed to generate a massive sulphide deposit. R-factor determinations place this value at approximately 3 000 indicating the TVC to potentially host a sulphide poor PGE deposit should the immiscible sulphide fraction have concentrated within a discrete reef horizon. These findings underpin the prospectivity of the TVC and the need for further exploration.

Acknowledgements

The author would like to thank Orange River Pegmatite (Pty) Ltd for their continued financial support and generosity throughout the course of the study. Our gratitude must also be extended to the staff at the Stellenbosch University Central Analytical Facility (CAF) for their expertise.

References

Cornell, D. H., Thomas, R. J., Moen, H. F. G., Reid, D. L., Moore, J. M., & Gibson, R. L. (2006). The Namaqua-Natal Province. In *Geology of South Africa* (pp. 325–379).

Eckstrand, O. R., & Hulbert, L. J. (1987). Selenium and the source of sulphur in magmatic nickel and platinum deposits (abs.). In *Geological Association of Canada-Minerological Association Canada Program with Abstracts* (p. 40).

Eggins, S. (2003). Laser Ablation ICP-MS Analysis of geological Materials Prepared as Lithium Borate Glasses. *Geostandards and Geoanalytical Research*, *27*, 147–162.

Kartun, K. G. (1979). *The Geology of the Tantalite Valley Mafic-Ultramafic Complex and the Kumkum Metamorphic-Igneous Massif near Warmbad, South West Africa (Namibia)*. University of Cape Town.

Laflamme, C., Martin, L., Jeon, H., Reddy, S. M., Selvaraja, V., Caruso, S., Hao, T., Roberts, M. P., Voute, F., Hagemann, S., Wacey, D., Littman, S., Wing, B., Fiorentini, M., & Kilburn, M. R. (2016). In situ multiple sulfur isotope analysis by SIMS of pyrite, chalcopyrite, pyrrhotite =, and pentlandite to refine magmatic ore genetic models. *Chemical Geology*, *444*, 1–15. https://doi.org/10.1016/j.chemgeo.2016.09.032

Lesher, C. M. (2017). Roles of xenomelts, xenoliths, xenocrysts, xenovolatiles, residues, and skarns in the genesis, transport, and localization of magmatic Fe-Ni-Cu-PGE sulphides and chromite. *Ore Geology Reviews*, *90*, 465–484.

Macey, P. H., Thomas, R. J., Minnaar, H. M., Gresse, P. G., Lambert, C. W., Groenewald, C. A., Miller, J. A., Indongo, J., Angombe, M., Shifotoka, G., Frei, D., Diener, J. F. A., Kisters, A. F. M., Dhansay, T., Smith, H., Doggart, S., Le Roux, P., Hartnady, M. I., & Tinguely, C. (2017). Origin and evolution of the ~1.9 Ga Richtersveld Magmatic Arc, SW Africa. *Precambrian Research*, *292*, 417–451.

Moore, A. C., Kartun, K. G., & Waters, D. J. (1979). Metamorphic history of the Aureole associated with the Tantalite Valley Complex, South West Africa/Namibia. *Transactions of the Geological Society of South Africa*, *82*, 67–80.

Queffurus, M., & Barnes, S. J. (2015). A review of sulphur to selenium ratios in magmatic nickel-copper and platinum-group element deposits. *Ore Geology Reviews*, *69*, 301–324.

Robb, L. (2005). Introduction to ore-forming processes. In *Blackwell Publishing*.

Schreiber, U. M. (2016). *Ministry of Mines and Energy The Geology of Area 2818*.

Thomas, R. J., Cornell, D. H., Moore, J. M., & Jacobs, J. (1994). Crustal evolution of the Namaqua-Natal Metamorphic Province, southern Africa. *South African Journal of Geology*, *97*(1), 8–14.

von Backstrom, J. W. (1976). The Geology and Mineral Deposits of Tantalite Valley, Warmbad District, South West Africa. *Atomic Energy Board, Pelindaba, Pretoria*, *April*, 27.

A new look to the high-PGE chromitites from the Cabo Ortegal Complex (NW Spain)

Matías A. García-Tudela[1], Joaquín A. Proenza[2], Júlia Farré-de-Pablo[2], Thomas H. Aiglsperger[1], Núria Pujol-Solà[2,3] José María González-Jiménez[4]

[1]Department of Civil Engineering and Natural Resources, Luleå University of Technology, SE 97187, Luleå, Sweden
[2]Departament de Mineralogia, Petrologia i Geologia Aplicada, Facultat de Ciències de la Terra, Universitat de Barcelona, Carrer Martí i Franquès, s/n, 08028 Barcelona, Spain
[3]Departamento de Mineralogía y Petrología, Facultad de Ciencias, Universidad de Granada, Av. Fuentenueva s/n, 18071 Granada, Spain
[4]Instituto Andaluz de Ciencias de la Tierra (CSIC-UGR), Avda. de las Palmeras 4, E-18100 Armilla, Granada, Spain

Abstract. The ultramafic rocks of the Herbeira massif in the Cabo Ortegal Complex host chromitite bodies. On the basis of their morphology, host rocks and unaltered chromite cores compositions, they can be grouped into two types: Type-I chromitites, which are massive pods in dunites with Cr# values [Cr/(Cr+Al) atomic ratio] between 0.60-0.63; and Type-II chromitites, which are massive bands in dunites and pyroxenites with Cr# values between 0.80-0.82. Parental melt composition suggests that Type-I chromitites crystallized from melts akin to fore-arc basalt, which probably originated in a mantle wedge during a subduction initiation event, and Type-II chromitites originated from a boninitic parental melt once the subduction zone already developed. Both chromitite types exhibit platinum-group element (PGE) contents exceeding 2,000 ppb and are enriched in PPGE (Rh, Pt, Pd) relative to IPGE (Os, Ir, Ru). Abundant platinum-group minerals (PGM) are found at the edges of chromite grains or embedded by the interstitial serpentinized groundmass. These PGM are associated with base-metal sulfides (mainly pentlandite). The PGE distribution patterns and PGM association with base-metal sulfides suggest that PGEs were concentrated by immiscible sulfide melt. Additionally post-magmatic processes altered the primary PGM, promoting local remobilization of Pt and Pd.

1 Introduction

The high-Cr ophiolitic chromitites of the Herbeira massif in the Cabo Ortegal Complex (NW Spain) reportedly have platinum-group element (PGE) contents up to 13,000 ppb (Moreno et al. 2001), which are higher than those typical of high-Cr ophiolitic chromitites (< 1,000 ppb whole-rock PGE concentrations; Farré-de-Pablo et al. 2020 and references therein).

Moreno et al. (2001) interpreted the ultramafic rocks of the Herbeira massif as a mafic-ultramafic cumulate sequence (above the Moho) characteristic of a magmatic arc-root. According to these authors, the origin of the high-Cr and PGE-rich chromitites from the Herbeira massif was linked to successive injections of Cr- and PGE-rich magmas. However, more recent research interpreted the ultramafic sequence as a part of the mantle, where the interaction between melts and a refractory harzburgite in a sub-arc mantle environment formed chromitites, dunites and pyroxenites (Tilhac et al. 2016, 2020). Therefore, the origin of these chromitites, together with their PGE enrichment, remains unclear.

In this contribution, we present and discuss new petrographic, mineralogical and geochemical data for the chromitites of the Herbeira massif. These new insights, combined with previous knowledge, will help to unravel the origin of these chromitites and understand their enrichment in PGE.

2 Geological setting

The Cabo Ortegal Complex (Fig. 1a) is part of the European Variscan Belt and consists of mafic and ultramafic mantellic rocks and metamorphic rocks (Arenas et al. 2019). The ultramafic rocks of the Cabo Ortegal Complex are found in three massifs: Limo, Herbeira and Uzal (Fig. 1b). All these massifs consist of harzburgites, dunites, and pyroxenites, with subordinate wehrlites and lherzolites (Arenas et al. 2019).

According to Arenas et al. (2019), radiometric age data of ultramafic rocks suggest: 1) the partial melting stages that led to later injections of acidic and basic magma into the ultramafic rocks occurred at 395 Ma, 2) the formation of a garnet-clinopyroxene association (800°C, 16.5 kbar) at 390-395 Ma, and 3) an amphibolitization stage at 380 Ma. The origin of the ultramafic rocks has been established less precisely, at around 500 Ma. The pyroxenites have been interpreted as products of melt–peridotite interaction in a suprasubduction mantle around 459–515 Ma ago (Santos et al. 2002; Tilhac et al. 2017). The P-T conditions of peak

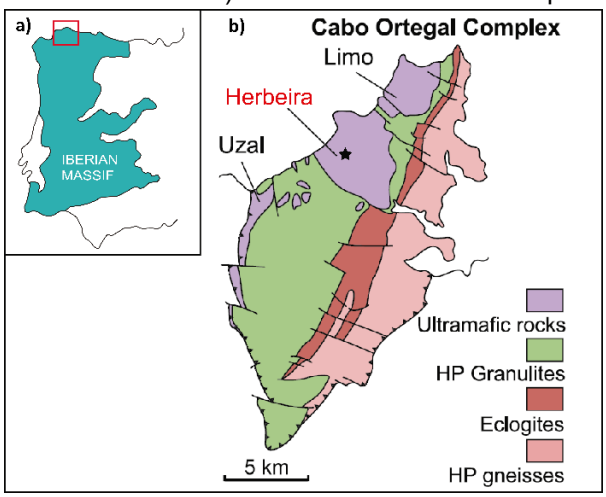

Figure 6. *Geological map of the Herbeira massif of the Cabo Ortegal Complex. The black star indicates the location of the samples. Modified from Tilhac et al. (2020).*

metamorphism of 1.6–1.8 GPa, 780– 800 ºC have been determined in the ultramafic rocks, recorded by undeformed garnet coronas around spinel (Girardeau and Ibarguchi 1991; Tilhac et al. 2016).

The main study area is located at the Herbeira massif (Fig. 1b). The massif is divided into an eastern and a western domain separated by the Herbeira Trans-Fault (Moreno et al. 2001). According to Tilhac et al. (2020), the eastern domain comprises harzburgites and minor pyroxenites, dunites, and chromitites. Meanwhile, the western domain is composed of dunites and chromitites, pyroxenites interlayered with dunites, harzburgites, and local chromitites. The chromitites of this study occur in the western domain of the Herbeira massif. They are massive podiform bodies hosted in dunites and massive bands hosted in dunites with minor pyroxenites layers.

3 Samples and analytical methods

The studied samples include massive chromitites from pods and bands. In this study, the massive chromitites from pods will be referred as Type-I chromitites and the massive chromitites in bands will be referred to as Type-II chromitites.

The mineral chemistry of chromite from both types of chromitites in terms of major and minor elements was analyzed using a JEOL JXA-8230 electron microprobe (EMP) at the Centres Científics i Tecnològics de la Universitat de Barcelona (CCiTUB). The analytical conditions were 15 kV accelerating voltage, 10-20 nA beam current with spot diameter 1-5 µm, and 20s count time. The calibration standards used were: Cr_2O_3 (Cr, PET, Kα), corundum (Al, TAP, Kα), rutile (Ti, PET, Kα), periclase (Mg, TAP, Kα), hematite (Fe, LIF, Kα), rhodonite (Mn, LIF, Kα), NiO (Ni, LIF, Kα), and metallic V (PET, Kα).

Whole-rock PGE analyses were performed on 2 chromitite samples (1 Type-I and 1 Type-II chromitites) at Genalysis Ltd (Perth, Western Australia) after nickel sulfide fire assay collection, following the method described by Chan and Finch (2001).

Hydroseparation was performed at the Laboratories for Quantitative Target Mineralogy (QanTmin) of the Luleå University of Technology; the resulting concentrates were mounted as polished monolayers on resin blocks and analyzed by field emission scanning electron microscope (FE-SEM), using a Zeiss Sigma 300 VP SEM at the same institution.

4 Chromite mineral chemistry

The primary composition (unaltered chromite core) of chromite varies according to the type of chromitite (Fig. 2a-b). Chromite from Type-I chromitites has Cr# values [Cr/(Cr+Al) atomic ratio] ranging from 0.60 to 0.63, TiO_2 contents between 0.08 and 0.29 wt.%, and Mg# values [Mg/(Mg+Fe^{2+}) atomic ratio] between 0.54 and 0.57. The chromite from Type-II chromitites has Cr# values ranging from 0.80 to 0.82, TiO_2 contents between 0.05 and 0.15 wt.%, and Mg# values between 0.42 and 0.44. Both types of chromitites display slightly high Fe_2O_3 contents: Type-I chromitites range between 5.76 and 6.89 wt.% and Type-II chromitites between 7.32 and 8.06 wt.%.

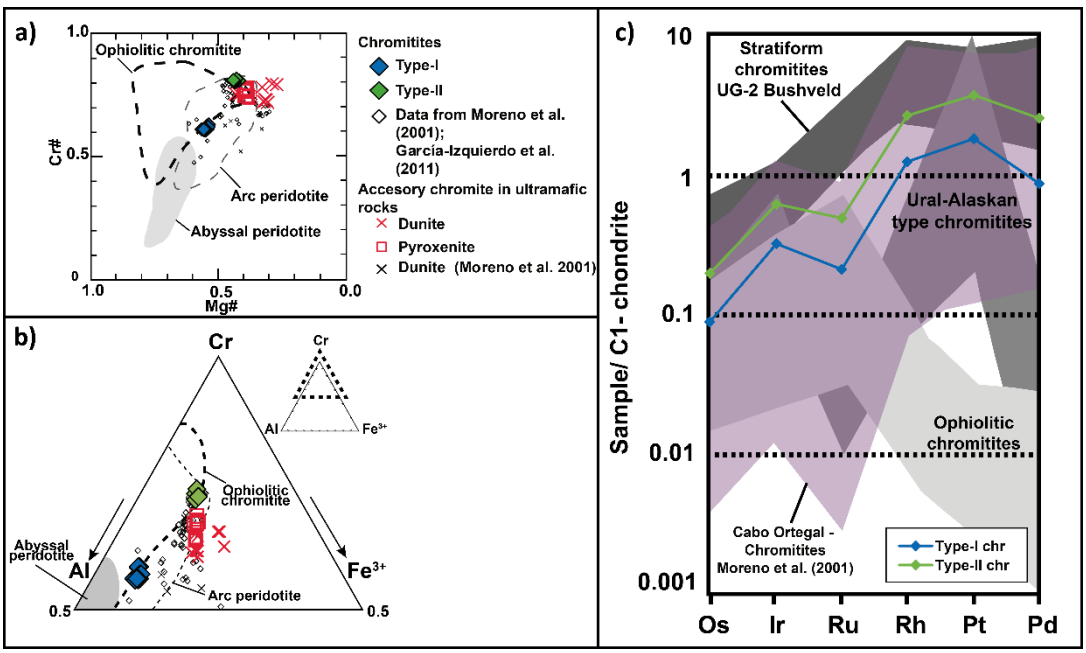

Figure 2. a-b) Chemistry of chromite from chromitites of the Herbeira massif compared with different tectonic settings. a) Mg# versus Cr# values. b) Al-Cr-Fe^{3+} ternary diagram. Data sources of chromite from different tectonic settings are from Miura et al. (2018). c) C1 chondrite normalized (Naldrett and Duke 1980) PGE contents of the studied chromitites. Data for ophiolitic chromitites, Ural-Alaskan-type complexes and layered UG-2 Bushveld chromitites taken from González-Jiménez et al. (2015). Data for Cabo Ortegal chromitites are from Moreno et al. (2001).

5 PGE geochemistry and PGM mineralogy

The bulk-rock PGE content of the Type-I chromitites is 2,460 ppb, and the bulk-rock PGE content of Type-II chromitites is 3,600 ppb. These values are higher than the average values for high-Cr ophiolitic chromitites (< 1,000 ppb total PGE; Farré-de-Pablo et al. 2020 and references therein). Chondrite-normalized (Naldrett and Duke 1980) PGE patterns (Fig. 2c) for both types of chromitites show enrichment in Pd-group PGE (PPGE: Rh, Pt and Pd) relative to Ir-group PGE (IPGE: Os, Ir and Ru), defining a positive slope from Ru to Pt and a negative slope between Pt and Pd.

The PGM assemblage observed in situ and in hydroseparated concentrates consists of Rh-Ir-Pt-bearing arsenides and sulfarsenides, Pt-Ir-Pd-base-metal- bearing alloys, and unidentified phases of Pt-Pd-S and Pt-Pd-Fe. In situ observations on thin sections from both types of chromitites reveal that PGM occur as inclusions on the edges of chromite, in fractures along chromite and in the interstitial silicate matrix (Fig. 3a-b). The PGMs located on the edges of chromite are composite grains of Rh-Ir-Pt-bearing sulfarsenides with Ir-Pt-Fe, Pt-Pd sulfides with Pt-Pd-Fe (Fig. 3a), and Ni-Fe sulfide (pentlandite), and Pt-Pd-As with Ni-Fe and Cu-Fe sulfides. The PGMs located in fractures of chromite grains and in the interstitial silicate matrix usually form single grains of Pt-Pd sulfides (Fig. 3b), Pt arsenides and Pt-Fe-Ni sulfides. The PGMs observed in hydroseparated concentrates show that Pt-Fe-Cu(-Ni) alloys occur as single irregular grains with sizes up to 20 µm. Each show porous textures (Fig. 3c). Irregular shaped Pt-Pd-Cu alloys occur with Ni-Fe sulfides. Hollingworthite (RhAsS), irarsite (IrAsS) and platarsite (PtAsS) appear as single allotriomorphic to subidiomorphic grains (Fig. 3d). Sperrylite ($PtAs_2$) occurs as allotriomorphic to idiomorphic grains with sizes up to 50 µm. Zaccariniite (RhNiAs) appears as composite grains associated with Ir-Fe-Ni and Pt-Fe-Cu alloys.

6 Discussion and conclusions

The chromite from the studied chromitite samples systematically have high Cr# values >0.6 (Type-I: 0.60-0.63 and Type-II: 0.80- 0.82) (Fig. 2a). All of them show compositions typical of chromitites hosted in the mantle section of ophiolites, although they have relatively higher Fe_2O_3 contents (5.76-8.06 wt.%; Fig. 2b). We estimated the composition of the melts in equilibrium with the chromite from the studied chromitites, and hence their parental melts, using the Al_2O_3 and the TiO_2 contents of chromite from both types of chromitites according to the approach of Kamenetsky et al. (2001) modified by González-Jiménez et al. (2020). The calculated composition of the parental melt for Type-I chromitites had Al_2O_3 contents between 14.29 and 14.58 wt.%, TiO_2 from 0.15-0.76 wt.%. and FeO/MgO ratio between 1.19 and 1.31. The Al_2O_3 content and FeO/MgO ratio are similar to MORB (e.g., Gale et al. 2013), but the calculated TiO_2 content for the melt is too low (typical MORB 1.68 wt% TiO_2; Gale et al. 2013). Low Ti content in MORB-like melts and low Ti/V ratio (~10-20) are characteristic of fore-arc basalts (Reagan et al. 2010), which are the first products when intra-oceanic subduction begins. On the other hand, the parental melt composition for Type-II chromitites had Al_2O_3 contents between 9.91 and 10.39 wt.%, TiO_2 from 0.15 to 0.25 wt.% and FeO/MgO ratio between 1.57 and 1.74. This composition resembles those from boninitic magmas (e.g., Hickey and Frey 1982).

The two types of chromitites exhibit PGE contents exceeding 2,000 ppb and are enriched in PPGE (Rh, Pt, Pd) relative to IPGE (Os, Ir, Ru) (Fig. 2c). This suggests that the parental melts of both types of chromitites were enriched in PGE. The PPGE enrichment resembles that of the Type II chromitites (especially Type IIA) described in González-Jiménez et al. (2014a, b). According to these authors and references therein, the PPGE enrichment of Type II chromitites may be related to

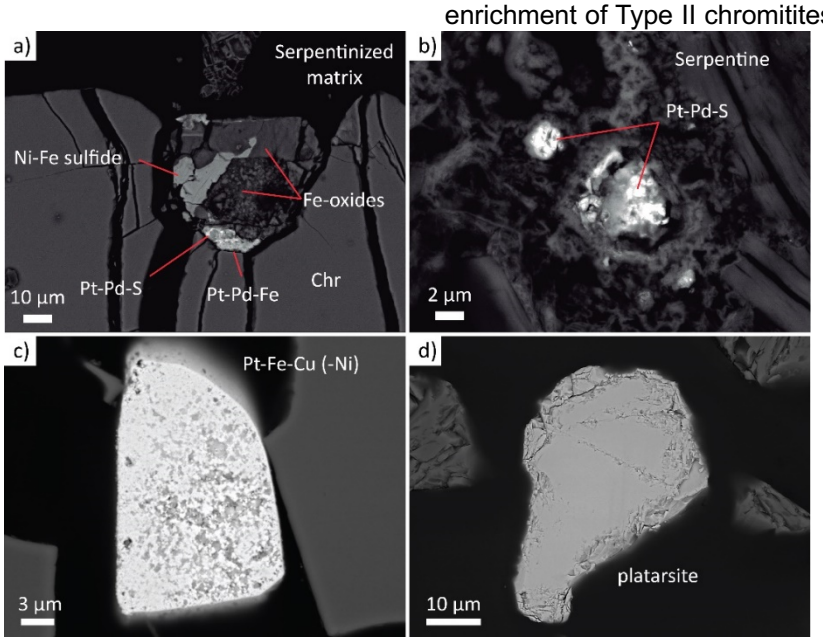

Figure 3. *a) Pt-Pd-S and Pt-Pd-Fe with Ni-Fe sulfide and Fe-oxides on the edge of a chromite grain from a Type-II chromitite. b) Pt-Pd-S grains enclosed by fibrous serpentine in a Type-I chromitite. c) Pt-Fe-Cu (-Ni) alloy grain with porous texture. d) Allotriomorphic platarsite grain.*

the PGE concentration in sulfide melts eventually segregated by immiscibility from evolving volatile-rich small volume melts. This is consistent with observation that PGMs and PGM-bearing sulfides are systematically located at the silicate matrix, thus evidencing that segregation of sulfide melt probably took place after the chromite crystals precipitated. Additionally, sulfide segregation could be favored by decreasing S and volatile solubility in the magma as a result of increasing polymerization degree by differentiation processes that resulted in Si-richer melts of boninitic affinity parental to the pyroxenites of the Herbeira massif too (Tilhac et al. 2016).

Moreover, the observation of Pt-Fe-Cu(-Ni) alloys with porous textures (Fig. 3c) suggest that they were formed by post-magmatic processes as a result of alteration of PGE-rich base metal sulfides or pre-existing PGM. Their location at the edge of chromite or interstitial matrix favored interaction with late metamorphic fluids, whereas porous textures suggest the accumulation of small nanoparticles of Pt, Fe, Cu and Ni precipitated from hydrothermal fluids (Farré-de-Pablo et al. 2022). The presence of zaccariniite with Ir-Fe-Ni alloys (probably garutiite) has also been interpreted to form as secondary minerals due to alteration processes (e.g., serpentinization) (McDonald et al. 2010; Vymazalova et al. 2012). Post-magmatic processes can locally remobilize PGE, especially Pt and Pd as observed in the studied chromitites (Fig. 2c). This can be due to the fact that Pt and specially Pd are relatively mobile during hydrothermal alteration (Barnes and Liu 2012). The PGE remobilization could be related to the percolation of hydrated fluids during amphibolite facies metamorphism (~8 kbar, 500°C; Tilhac et al. 2016) that affected chromitites and ultramafic rocks of the Cabo Ortegal Complex.

Acknowledgements

This research was financially supported by the Spanish Projects CGL2015–65824, RTI2018-099157-A-I00, PID2019-105625RB-C2.

References

Arenas R, Gil Ibarguchi JI, Fernández-Suárez J, et al (2019) El Complejo de Cabo Ortegal: los terrenos alóctonos del NW de Iberia y los episodios iniciales del ensamblado de Pangea. Concello de Cariño

Barnes SJ, Liu W (2012) Pt and Pd mobility in hydrothermal fluids: Evidence from komatiites and from thermodynamic modelling. Ore Geology Reviews 44:49–58.

Chan TK, Finch IJ (2001) Determination of platinum-group elements and gold by inductively coupled plasma mass spectrometry. In: Australian Platinum Conference. Perth, Western Australia, pp 1–9

Farré-de-Pablo J, Proenza JA, González-Jiménez JM, et al (2020) Ophiolite hosted chromitite formed by supra-subduction zone peridotite –plume interaction. Geoscience Frontiers 11:2083–2102.

Farré-de-Pablo J, Proenza JA, González-Jiménez JM, et al (2022) Low-temperature hydrothermal Pt mineralization in uvarovite-bearing ophiolitic chromitites from the Dominican Republic. Miner Deposita 57:955–976.

Gale A, Dalton CA, Langmuir CH, et al (2013) The mean composition of ocean ridge basalts. Geochemistry, Geophysics, Geosystems 14:489–518.

García Izquierdo B, Capote del Villar R, Lunar R, et al (2011) Evolución geodinámica y procesos mantélicos en el Macizo de Herbeira, Complejo de Cabo Ortegal (NO de la Península Ibérica). Instituto Universitario de Geología “Isidro Parga Pondal”, Área de Xeoloxía e Minería do Seminario de Estudos Galegos

Girardeau J, Ibarguchi JIG (1991) Pyroxenite-Rich Peridotites of the Cabo Ortegal Complex (Northwestern Spain): Evidence for Large-Scale Upper-Mantle Heterogeneity. Journal of Petrology Special_Volume:135–154.

González-Jiménez J, Mondal S, Ghosh B, et al (2020) Re-Os Isotope Systematics of Sulfides in Chromitites and Host Lherzolites of the Andaman Ophiolite, India. Minerals 10:686.

González-Jiménez JM, Griffin WL, Gervilla F, et al (2014a) Chromitites in ophiolites: How, where, when, why? Part I. A review and new ideas on the origin and significance of platinum-group minerals. Lithos 189:127–139.

González-Jiménez JM, Griffin WL, Proenza JA, et al (2014b) Chromitites in ophiolites: How, where, when, why? Part II. The crystallization of chromitites. Lithos 189:140–158.

González-Jiménez JM, Locmelis M, Belousova E, et al (2015) Genesis and tectonic implications of podiform chromitites in the metamorphosed ultramafic massif of Dobromirtsi (Bulgaria). Gondwana Research 27:555–574.

Hickey RL, Frey FA (1982) Geochemical characteristics of boninite series volcanics: implications for their source. Geochimica et Cosmochimica Acta 46:2099–2115.

Kamenetsky VS, Crawford AJ, Meffre S (2001) Factors Controlling Chemistry of Magmatic Spinel: an Empirical Study of Associated Olivine, Cr-spinel and Melt Inclusions from Primitive Rocks. J Petrology 42:655–671.

McDonald AM, Proenza JA, Zaccarini F, et al (2010) Garutiite, (Ni,Fe,Ir), a new hexagonal polymorph of native Ni from Loma Peguera, Dominican Republic. ejm 22:293–304.

Miura M, Arai S, Mizukami T, et al (2018) Petrology of Chromitites in the Higashi-Akaishi Ultrahigh-Pressure (UHP) Peridotite Complex, Japan: Toward Understanding of General Features of the UHP Chromitites. Minerals 8:525.

Moreno T, Gibbons W, Prichard HM, Lunar R (2001) Platiniferous chromitite and the tectonic setting of ultramafic rocks in Cabo Ortegal, NW Spain. Journal of the Geological Society 158:601–614.

Naldrett AJ, Duke JM (1980) Platinum metals magmatic sulfide ores. Science 208:1417–1424

Reagan MK, Ishizuka O, Stern RJ, et al (2010) Fore-arc basalts and subduction initiation in the Izu-Bonin-Mariana system. Geochemistry, Geophysics, Geosystems 11:.

Santos JF, Schärer U, Gil Ibarguchi JI, Girardeau J (2002) Genesis of Pyroxenite-rich Peridotite at Cabo Ortegal (NW Spain): Geochemical and Pb–Sr–Nd Isotope Data. Journal of Petrology 43:17–43.

Tilhac R, Ceuleneer G, Griffin WL, et al (2016) Primitive Arc Magmatism and Delamination: Petrology and Geochemistry of Pyroxenites from the Cabo Ortegal Complex, Spain. J Petrology 57:1921–1954.

Tilhac R, Grégoire M, O’Reilly SY, et al (2017) Sources and timing of pyroxenite formation in the sub-arc mantle: Case study of the Cabo Ortegal Complex, Spain. Earth and Planetary Science Letters 474:490–502.

Tilhac R, Oliveira B, Griffin WL, et al (2020) Reworking of old continental lithosphere: Unradiogenic Os and decoupled Hf Nd isotopes in sub-arc mantle pyroxenites. Lithos 354–355:105346.

Vymazalova A, Laufek F, Drabek M, et al (2012) Zaccariniite, RhNiAs, a new platinum-group mineral from Loma Peguera, Dominican Republic. The Canadian Mineralogist 50:1321–1329.

Characterization of the UG2 Reef split-facies types, Eastern Bushveld Complex, South Africa: A mineralogical perspective.

Caroline Hlongwani[1], Karel S. Viljoen[1], Derek H. Rose[1,2], Lauren C. Blignaut[3]
[1]University of Johannesburg, South Africa
[2]Mintek, Randburg, South Africa
[3]Kings Christian Collegiate, Oakville, Canada

Abstract. The Rustenburg Layered Suite of the Bushveld Complex has been extensively exploited for platinum group elements (PGEs), mainly from the Merensky and UG2 Reefs. An exploration drilling programme on the Booysendal Platinum producing Mine on the Eastern Limb of the Bushveld Complex revealed the occurrence of the UG2 Reef split-facies. In comparison to the normal UG2 reef (where the chromitite seam is not separated by pyroxenite), the split reef facies is defined by the splitting of the chromitite layers into multiple layers that are separated by pyroxenite middlings. This is anticipated to pose new challenges during metallurgical processing of the ore. To fully comprehend the mineralogical and metallurgical variations of the UG2 Reef split-facies types, geometallurgical test work was carried out on drill core samples collected from the mine. This was done to determine the bulk modal mineralogy, milling performance, mineral liberation and the flotation response of the various UG2 Reef split-facies types identified. Preliminary results of the study are presented and discussed in this paper.

1 Introduction

Northam Platinum's Booysendal Mine is located on the Eastern Limb of the Bushveld Complex within the Limpopo and Mpumalanga Provinces, in South Africa. It contains both the Merensky and Upper Group 2 (UG2) Reefs and covers a strike length of 14.5 km. The mining operation is divided into the North UG2 mine, North Merensky mine and the newly developed South mine project. Ongoing drilling has revealed that the UG2 reef occurs in several facies types, this includes the normal UG2 (uniform chromitite layer divided into the Upper Group 2 Leader, UL and Upper Group 2 Main member, UM) and the split UG2 Reef (where the chromitite seams are interlayered with pyroxenite units). The UG2 Reef split-facies occurs from the north to the southern portions of the mine premises, with the boreholes investigated in the current study drilled from the north to the central part of the mining right area (Figure 1).

Because the processing behaviour of any ore-type is underpinned by its mineralogical and textural characteristics, an understanding of the various UG2 split reef facies-types is essential to optimize recovery during ore processing. Hence an investigation of the mineralogy and the petrography of the UG2 Reef split-facies types was carried out. A challenge faced by the mine geologists is that the demarcation between the UL and UM units has not always been evident on a mesoscopic scale, and chemical assays data (platinum (Pt)/palladium (Pd) ratio) is used to distinguish the two units. McCall (2016) indicated that the geological contact between the UL and UM units could in fact be marked by the sudden appearance of clinopyroxene oikocrysts from the UL, gradationally moving into the lower UM unit.

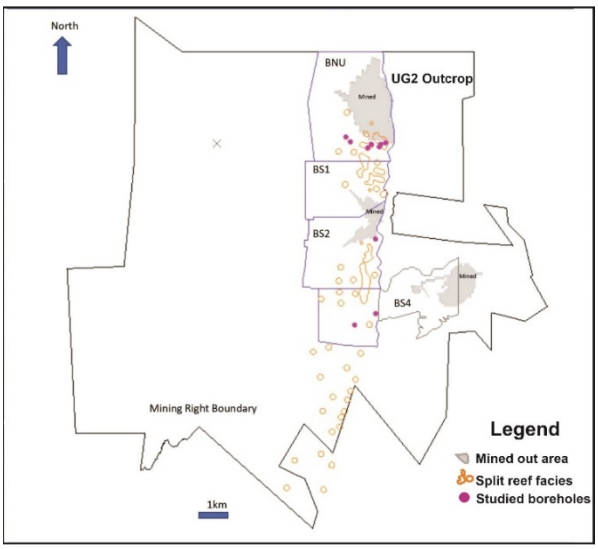

Figure 1. Aerial view of Booysendal Mine, showing the mined-out areas, the split reef and collar position of the studied boreholes (pink circles).

A comparison to previous studies (Dzvinamurungu et al 2013; McCall 2016) is made in the current study and the results are discussed later. Though this is not the first geometallurgical characterization project conducted on a mining operation in the Eastern Bushveld Complex, most of the previous studies however, only considered the Merensky Reef, or the normal UG2 Reef or both (Dzvinamurungu et al 2013; McCall 2016). It was the study by Rose et al. (2018) that investigated the UG2 Reef split-facies at Two Rivers Mine but no such study has been conducted at Booysendal Mine. The results of this study are brought into the discussion of this paper.

For the current study, much emphasis has been placed on the characterization of feed samples (hereby referred to as composite samples) by mineralogical, chemical, and petrographical methods. From the boreholes studied (Figure 1), and based on the UL and UM lithological

proportions, 3 UG2 Reef split-facies types were identified. These were further classified based on qualitative and semi quantitative mineralogical and textural data before any benchtop processing test work was conducted. Characterization of materials (especially feed samples) complemented by benchtop test work results allows for mining operations to build predictive process models by establishing a link between variability in material primary properties and variability resulting from processing (Lotter et al. 2011).

2 Methodology

Seventeen boreholes were logged, thin sections cut, prepared, and studied under optical and scanning electron microscopy fitted with energy dispersive spectrometers (SEM-EDS). Some aliquots were sent to Intertek in Australia for chemical assays (NiS fire assay with inductively coupled plasma-mass spectrometry (ICP-MS) finish; as well as sodium peroxide fusion/inductively coupled plasma-optical emission spectrometry (ICP-OES). The results of the Pt/Pd ratio and 4E PGE grade were used to draw a clear demarcation of the UL versus UM chromitite layers within the split reef-facies. Based on the chemistry, 3 UG2 Reef split-facies types were identified, and composite samples created from the seventeen boreholes and each borehole classified under a specific facies-type. In total, 8 composite samples were defined, and each simulates a possible mining cut that the mine can exploit during production. These composite samples were analysed for bulk mineralogy using X-ray diffraction (XRD) while employing the Rietveldt Refinement method.

3 Lithology, Petrography and Mineralogy

The mining cut varies across the split reef borehole intersections studied. According to mine terminology, the mining cut is stratigraphically divided into the hanging wall, main ore zone and footwall. The hanging wall comprises the following: pyroxenitic units (UP4 and UP1), chromitite stringer (UT3, ca. 1cm), pegmatoidal pyroxenite (UPEG, up to 27cm), and a 20 cm thick chromitite band (UT2). The main ore zone comprises chromitite layers commonly referred to as the leader seam (UL) and main seam (UM). These are parted or separated by a single or multi-pyroxenite unit(s) referred to as (UP which can range between 16 to 600 cm in thickness). The footwall comprises anorthosite, norite or pegmatoidal pyroxenite (UF). Generally, the mining cut starts from the UT3 stringer down to 40 cm into the footwall lithology.

Based on the lithological proportions of the UL and UM seams, mineralogical associations, textural features, and geochemical characteristics, three facies- types are identified and described as facies-type 1, where the UM and UL is separated by a pyroxenite unit (Figure 2), facies-type 2, where the UL remains uniform and directly overlies the UM, which in turn is split by a pyroxenite unit into two layers (Figure 3). The UL and UM in this facies type are distinguished by the change in chemistry, Pd/Pt ratio. Facies-type 3, where the UL and UM seams are collectively split into four or even five layers (Figure 4). Furthermore, 8 composite samples representing 8 mining cuts were collected from the three identified facies-types. The UG2 Reef split-facies types are described in detail subsequently.

Microscopic studies revealed no significant textural variations within the different UG2 Reef split-facies types studied, however, some common mineralogical similarities are noted in the same stratigraphic units across the 3 facies-types. Plagioclase and orthopyroxene occur interstitial to chromite (within the chromitite layers) (Figure 5a). While platinum group minerals (PGMs) seem to occur either as enveloped constituents within the chromite grains (Figure 5b) or at their margins, Base Metal Sulphides (BMS) are restricted to the margins of the chromite grains (Figures 5c, d).

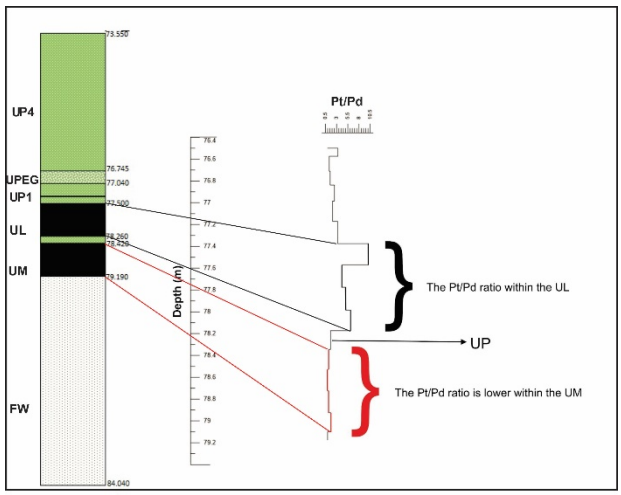

Figure 2. Lithology log of borehole BUT008D1, example of facies-type 1 split reef (right). Chemostratigraphic diagram showing the Pt/Pd variation across different chromitite seams (left). Logs not drawn to the same scale.

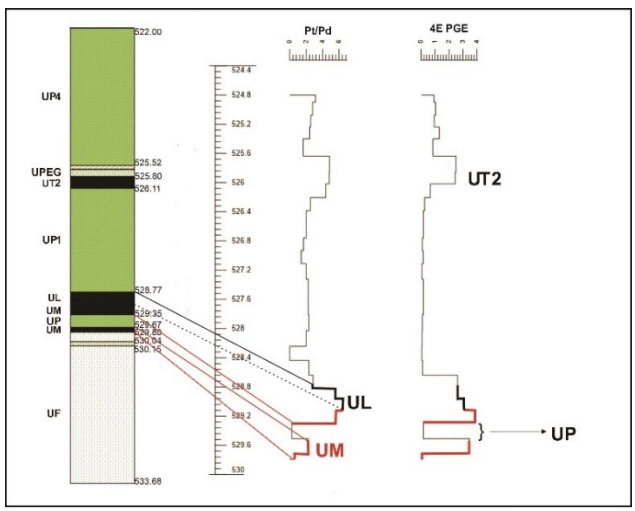

Figure 3. Lithology log of borehole BYS156D1, example of facies-type 2 split reef (right). Chemostratigraphic diagram showing the Pt/Pd and 4E grade variation across different chromitite seams (left). Logs not drawn to the same scale.

The UL typically shows a prominent association of apatite with chromite grains, an occurrence which is only seen in the UL and not the UM (Figure 6a). Platinum group elements-sulphides (PGE-sulphides) such as PtPdS (most likely braggite) and PtS (most likely cooperite) are commonly found in the UL and UM seams (although not described quantitatively here) and generally associated with chalcopyrite and/or pentlandite (Figure 5d). The pyroxenite parting may or may not show specks of BMS on disseminated chromite grains. The pyroxenite is composed of plagioclase, orthopyroxene with exsolution lamellae of clinopyroxene (Figure 6b), with quartz occasionally observed. The footwall lithologies such as norite, anorthosite and/or pegmatoidal pyroxenite may show association with disseminated chromite grains but seem completely devoid of any BMS.

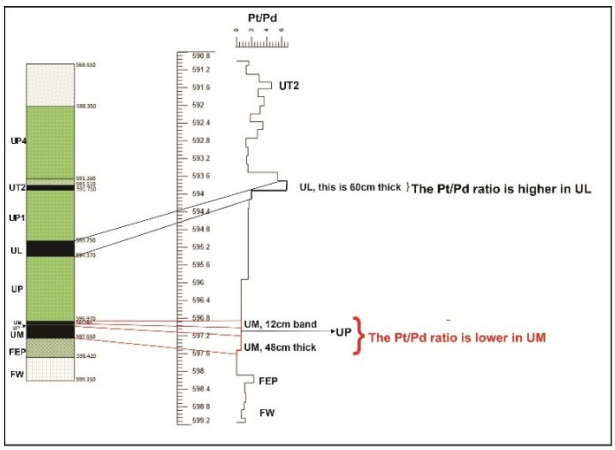

Figure 4. Lithology log of borehole BYS153D1, example of facies-type 3 split reef (right). Chemostratigraphic diagram showing the Pt/Pd variation across different chromitite seams (left). Logs not drawn to the same scale.

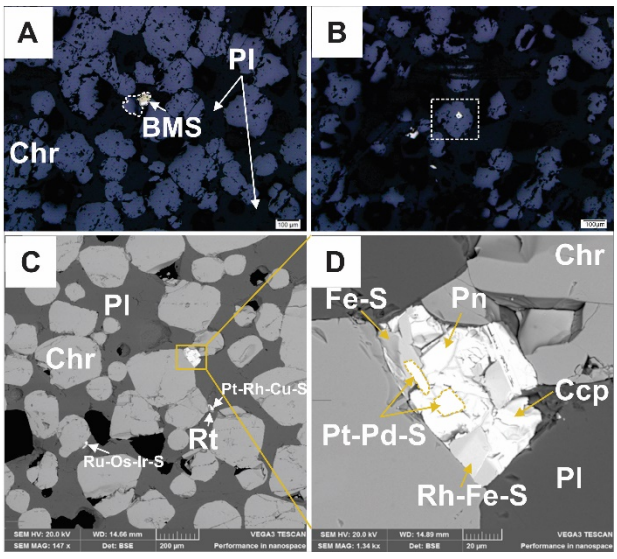

Figure 5. Photomicrographs of various sulphides-gangue mineral textures and association within the chromitite seam (UM). (A) Base metal sulphides (BMS) exsolution in chromite (Chr) grains or (B) interlocked within chromite (Chr) grains or (C) at the interface of chromite (Chr) and plagioclase (Pl). Other mineral associations noted include rutile (Rt) and PGMs alongside the Chr grain margins. (D) Shows a composite grain bounded by chromite (Chr) and plagioclase (Pl) grains.

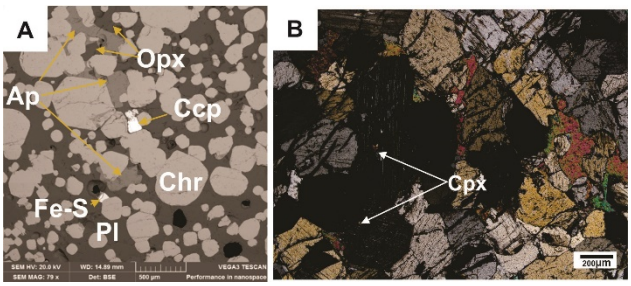

Figure 6. Photomicrographs of (A) mineral associations between apatite (Ap), orthopyroxene (Opx), plagioclase (Pl), and chalcopyrite (Cp) within the UL chromitite seam. (B) shows clinopyroxene (Cpx) exsolution in orthopyroxene (Opx), generally observed within the UP unit.

4 Milling Performance

Milling tests were conducted on 8 composite samples from the three facies types. The milling tests results are presented in the milling curve below (Figure 7) from which the times were then determined. From the three facies types, facies-type 3 composites i.e., UMC and ULT210CUT requires the longest milling times (43 mins) in comparison to LMC, to reach the target grind (70 wt% passing 75µm). Facies-type 2 composite, however, compares relatively well with Facies-type 1 composite LMC, both requiring approximately 40 minutes of milling to reach the target grind. Composite UMC_UT2 of facies-type 1 shows the most milling efficiency with just 37 minutes required to reach the target grind. Lastly, composite UMC of facies-type 1 requires a similar amount of milling time as facies-type 3 LMC composite, at roughly 42 minutes.

5 Discussion and Conclusion

Distinct classification of the various UG2 Reef split-facies types was achieved with respect to the lithological proportions of the UL and UM chromitite seams and to some extent mineralogical characteristics. While the demarcation between the UL and UM seams is remarkably difficult to spot on a mesoscopic scale, the chemistry of the platinum and palladium shows a trend between the two seams, with decreasing Pt/Pd ratio from the UL into the UM seams. This geochemical signature is consistent throughout the boreholes investigated. While McCall (2016) reported that the geological contact between the UL and UM seams is marked by

the sudden appearance of clinopyroxene oikocrysts, these have been noted to occur randomly and not consistently on the geological contact of the UL and UM seams within the drill core investigated. From bench-top milling tests, it is evident that some composites or mining cuts i.e. facies-type 1 UMC_UT2, LMC and facies-type 2 ULT210CUT are the most desirable as they require less milling time ca. 40 minutes) to achieve a target grind of 70wt% passing 75 µm. A study from Rose et al (2018) shows that the UG2 split reef at Two Rivers Mine, north of the current study area (referring to sample S7D) has low PGE grade and poor recoveries. This, however, was only the UG2 Reef split-facies types, there is also the multiple reef split facies which would be equivalent to the Facies-type 3 in the current study, which would most likely have an even lower performance relative to the other two UG2 Reef split-facies types, also judging by the milling times determined in the current study.

The results reported here for the milling times of the UG2 Reef split-facies types contrast with those of the normal UG2 reef, which is reportedly between 27 to 31 minutes to achieve a coarser grind of 60 wt% passing 75µm (Rose et al 2018). The milling times as determined in this study, however, are comparable to those reported by Dzvinamurungu et al (2013) for the Merensky reef in the western limb of the Bushveld Complex, which ranges between 33 to 41 minutes. The differences between the milling times of the normal UG2 and the UG2 split reef facies-types can be attributed to ore mineralogy. The amount of primary silicates such as plagioclase and orthopyroxene in the ore has a direct influence in the amount of energy and time required to reach a specific target grind (Dzvinamurungu et al 2013).

Though the UG2 Reef split-facies types have not been quantitatively described as yet, it would be interesting to see if there is a link between the varied milling performance to the ore mineralogy (or even ore texture) across the facies-types identified, through data to be acquired with the Mineral Liberation Analyzer (MLA).

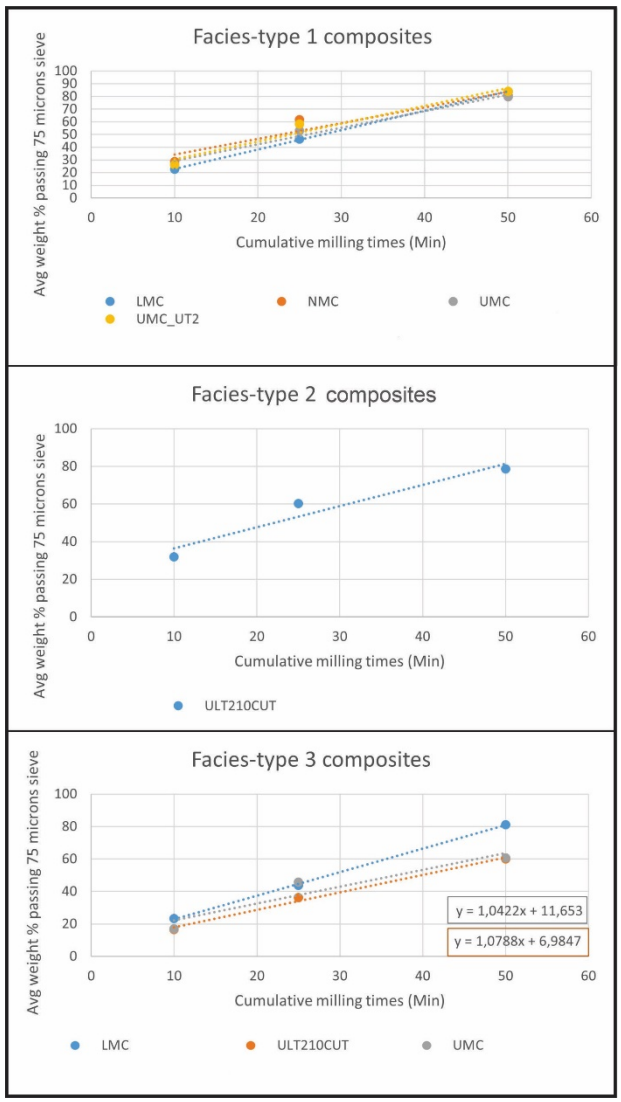

Figure 7. Milling curves of the three facies-types identified. Curves are plotted from average values of two composite samples milled per facies-type.

Acknowledgements

This study would not have been made possible without the initiative of senior management personnel (Dennis Hoffmann, Meshack Mqadi and Arnold Hartzenberg) whose assistance, cooperation and support allowed this study to occur. The staff at the mine (Given, Sipho, Karabo and Tebogo) are thanked for assisting with access to the drill core, core cutting and sample packaging. Funding for this study came from the research grant from the National Research Fund (NRF), and a Department of Science and Innovation (DSI) Geometallurgy Chair grant to Prof. K.S. Viljoen. Additional funding was provided by DHET University Capacity Development Grant (UCDG) administered under the Strategic Initiatives and Administration (SIA) at the University of Johannesburg.

References

Dzvinamurungu T, Viljoen KS, Knoper MW, Mulaba-Bafubiandi A (2013) Geometallurgical characterisation of Merensky Reef and UG2 at the Marikana Mine, Bushveld Complex, South Africa. Miner.Eng 52: 74-81.

Lotter NO, Kormos LJ, Oliveira J, Fragomeni D, Whiteman E (2011) Modern process mineralogy: two case studies. Miner Eng 24: 638–650.

McCall MJ (2016) Mineralogical and geochemical variations in the UG2 reef at Booysendal and Zondereinde mines, with implications for beneficiation of PGM. Unpublished MSc Dissertation. Stellenbosch University.

Rose DH, Viljoen KS, Mulaba-Bafubiandi A (2018) A mineralogical perspective on the recovery of platinum group elements from the Merensky Reef and UG2 at Two Rivers Platinum mine on the Eastern limb of the Bushveld Complex in South Africa. Mineral. Petrol 112: 881-902.

Towards a genetic model for the unusual Cu-Au-Te(-PGE) sulfide and Ni sulfide deposits of the Curaçá Valley, Brazil

David Holwell[1], Daryl Blanks[1], John Thompson[2], Filipe Porto[3], Eduardo Oliviera[3], Francisco Tomazoni[4], Anderson Lima[4], Rafael D'Altro[4], Pablo Graia[4] and Taila Sant'Ana[4]
[1]Centre for Sustainable Resource Extraction, University of Leicester, UK
[2]PetraScience Consultants, Vancouver, Canada
[3]Ero Copper, Vancouver, Canada
[4]Ero Caraiba, Brazil

Abstract. The Curaçá Valley, Brazil, contains a number of dominantly Cu-rich sulfide deposits hosted by orthopyroxene rich mafic and ultramafic rocks emplaced into the lower crust. The deposits are dominated by chalcopyrite-bornite with elevated Au and Te, and a strong association with abundant phlogopite. Textural evidence indicates emplacement of these sulfides as a migrating Cu-rich sulfide liquid enriched with volatiles. In addition, the Curaçá Valley contains some Ni-rich deposits in identical host rocks, but with interstitial and net textured pyrrhotite-pentlandite-pyrite, with very little Cu, Au and Te. We propose that the Curaçá Valley deposits, and those of the potentially analogous O'okiep district in South Africa, formed from low degree partial melting of a metasomatically enriched mantle source in a collisional setting. Sulfides within the resultant hydrous, alkaline ultramafic rocks were able to fractionate, with Ni sulfides trapped in some bodies, and the Cu-Au-Te sulfide liquid able to migrate through the plumbing system on a district scale at lower crustal temperatures over considerable time. As such, these deposits represent a distinct class of orogenic, lower crustal magmatic sulfide deposits that display sulfide liquid fractionation on a district scale.

1 Magmatic Ni-Cu-PGE sulfide systems

The majority of large magmatic Ni-Cu-PGE sulfide deposits are hosted within mafic-ultramafic complexes thought to have been derived from high degree mantle melts (>15 % partial melting) in rift and/or plume settings. They are typically grouped into three categories: Ni-dominant deposits hosted by komatiites; Ni-Cu-dominant deposits hosted by ultramafic-mafic intrusions such as chonoliths, pipes and conduits; and PGE-dominant reef deposits in layered ultramafic-mafic complexes (e.g. Barnes et al. 2016).

Spatially, the Ni-Cu-dominant deposits are associated with craton margins, (e.g. Noril'sk, Voisey's Bay, Thompson Nickel Belt, Raglan, (e.g. Begg et al. 2010; Maier and Groves 2011); whereas the more PGE-rich layered intrusions are generally found in intracratonic settings (e.g. Bushveld Complex).

Additionally, magmatic sulfide deposits located within collisional settings are being increasingly recognised such as the Finnish Nickel Belt, the Central Asian Orogenic Belt in central China, Aguablanca in Spain, and Älgliden in Sweden.

Furthermore, generally smaller accumulations and occurrences of magmatic sulfides have been recorded in alkaline and hydrous ultramafic intrusions from the lower to mid crust, such as Valmaggia, Italy, Mordor, Australia and Sron Gharb, Scotland (Holwell et al. 2019). These occurrences and deposits are thought to have formed from low degree (<10%) partial melts and have a characteristically elevated Cu-Au-Te signature compared to deposits formed from higher degree melting. In addition, these deposits are almost always associated with magmatic carbonate (Blanks et al. 2020; Holwell and Blanks 2021) and most likely formed in post subduction/collisional regimes.

1.1 Curaçá/O'okiep style deposits

The dominantly Cu-sulfide ores of the Curaçá Valley, Brazil, and those of the O'okiep district, South Africa, form an unusual subgroup of intrusion-related sulfide deposits. They are located in small, hydrous mafic-ultramafic intrusions emplaced into the lower-mid crust around peak metamorphic conditions (Oliviera and Tarney 1995; Robb et al 1999). The metallogeny of both districts is dominated Cu-sulfide deposits with abundant bornite, chalcopyrite with magnetite and hydrous silicates. They both have high Cu/Ni and Au/PGE ratios and have abundant telluride minerals. Both districts have some Ni-dominant deposits in isolated intrusions such that over the districts, there are some intrusions that host Ni sulfide deposits and some that host Cu sulfide deposits.

The recognition of the alkaline metallogenic signature (Holwell et al. 2019; Blanks et al. 2020) raises the question as to whether these deposits are Cu-Au-Te rich due to them having a collisional/post-collisional alkaline affinity, and thus represent some of the most economic concentrations of sulfide in such settings.

However, the depth at which they were emplaced (~20+ km) also raises the possibility that they existed for some time in a temperature window, or 'Goldilock's zone' where Ni sulfide is solid and Cu sulfide is liquid and able to move (Holwell et al. 2022). As such, we also explore the possibility that the Ni and Cu deposits may have had a common sulfide source, that was able to fractionate over considerable distances.

2 The Curaca Valley deposits

2.1 Copper deposits

Copper deposits of the Curaçá Valley, São Francisco Craton, Brazil, such as those at the Pilar mine are located within lozenge shaped, dominantly ultramafic units, emplaced around 2.05Ga. These often follow tight fold structures within the host rock gneisses, which display much higher degrees of deformation showing the intrusion to be late to post tectonic. They are dominated by orthopyroxene rich lithologies devoid of olivine.

The ores are largely chalcopyrite and bornite, with some pyrrhotite, and some rare pentlandite. Associated with the Cu sulfides is abundant phlogopite, some magnetite, Cr-spinel, and rarer apatite and carbonate. Accessory ore minerals include a range of tellurides, mostly melonite ($NiTe_2$), and tellurides of Au, Ag, Pt, Pd and Pb.

The sulfides occur as massive accumulations, typically as veins or breccia fills, with these textural evidence suggesting injection of Cu sulfide into the host rocks, along with some interstitial and net-textured accumulations.

2.2 Nickel deposits

Newly discovered Ni sulfide deposits of the Umburana system in the Curaçá Valley are hosted within orthopyroxene dominant ultramafic intrusions very similar to those that host the Cu ores. The ores are made up of disseminated interstitial, net textured and patchy to massive sulfides made up of pyrrhotite, pentlandite loops and flames, and some euhedral pyrite. Chalcopyrite is rare, but where present forms veins and disseminated patches at the edges or away from the margins of the Ni sulfide accumulations. PGE and Te contents are very low. Some carbonate is present with the sulfide, especially where they are present in more vein like textures.

3 Possible genetic models

3.1 An alkaline system

The characteristics of low degree partial melts are that they are alkaline, typically somewhat hydrous and form in low volumes compared to basaltic magmas derived from higher degrees of partial melt. Whilst the alkaline nature of magmatic rocks can be mimicked by the effects of crustal contamination, metallogenically, mineralisation in such settings is characteristically Cu-Au-Te rich. In particular, the enrichment of Te seems to be an entirely mantle character, with Te enrichments in metasomatized mantle rocks (Blanks et al 2020), and a consistent enrichment in alkaline deposits throughout the lithosphere (Holwell et al. 2019).

The Cu-Au-Te signature of the Curaçá Cu deposits, with abundant hydrous phases, particularly phlogopite, would be supportive of an alkaline interpretation. The question is how do the Ni deposits fit this model? As currently known and explored,, there are many more Cu occurrences identified in the Valley than Ni ones, and if the district is taken as a whole, then the overall metallogenic signature is still Cu-Au-Te dominant with some Ni and PGE. However, the complete lack of IPGE in both styles of deposit would be consistent with a low degree of partial melting that did not melt all sulfide in the mantle, thus allowing the IPGE to remain in mantle restite.

As such, an alkaline affinity does work when assessing the Curaçá Valley as a whole, but it also implies that the sulfides in each individual intrusion may not represent the parental sulfide composition. This can be explained by large scale sulfide liquid fractionation.

3.2 District scale sulfide liquid fractionation

Sulfide liquid fractionation initially produces a crystalline monosulfide solid solution (mss) phase at high temperatures (>1000°C), into which Ni, Co and IPGE and Rh will partition, with Cu, Au, Pt, Pd and semi metals like Te remaining as a liquid (Holwell and McDonald 2010). This allows for the possibility, especially at lower crustal depths where the temperatures of any intrusions will remain hotter for longer, that Cu-Au-Te-(Pt-Pd) sulfide migrated away from the Ni sulfides (Holwell et al. 2022) before crystallising to Cu sulfides like intermediate solid solution (iss).

The general Cu-Au-Te(+Pd) signature of the Cu ores from the Curaçá Valley are entirely consistent with an iss signature, but it would imply sulfide liquid fractionation within the magmatic plumbing system on a district scale of km to tens of km. Whilst this may seem extreme, the process is clearly scalable from the mm to cm scale seen in many sulfide blebs and patches (e.g. Blanks et al. 2022) up to deposit scale such as the Cu-rich veins at Sudbury.

Textural differences are striking, with the Ni ores having sulfides as disseminations, interstitial patches and net textured and massive sulfides representative of sulfide coexisting with silicate minerals. The Cu ores in stark contrast commonly show textures indicative of migrating Cu sulfide liquid, intruding as veins and breccia fills along with net-textures and insterstitial sulfides.

The importance of phlogopite and other volatile-rich mineral phases with the Cu sulfide would also be consistent with a fractionated, volatile-rich sulfide liquid migrating significant distance,

4 Global analogue: O'okiep district

The O'okiep district in South Africa represents a remarkably analogous ore district to the Curaçá Valley albeit of a different age (~1000 Ma). Similarities between the regions include: (1) emplacement in a collisional setting; (2) lower crustal, hot conditions on emplacement ~800-900°C;

(3) tens to hundreds of individual, small (typically <100 m thick and 1000 m long) mafic-ultramafic bodies within the district; (4) mostly Cu-dominant (chalcopyrite-bornite) ores, with some Ni-rich deposits; (5) massive sulfide accumulations and veins with associated magnetite; (6) very low S/Se ratios; (7) abundant volatile phases in the associated ultramafic rocks such as phlogopite.

As such, we consider both these districts to have formed in similar ways and may represent 'typical' conditions of magmatic sulfide genesis in the lower crust from low degree partial melts of metasomatically enriched mantle lithosphere.

Acknowledgements

The staff and management at Ero Copper are thanked for financial and logistical support. Wolf Maier is thanked for access to samples from the O'okiep district.

References

Barnes SJ, Cruden AR, Arndt N, Saumur BM (2016) The mineral system approach applied to magmatic Ni–Cu–PGE sulphide deposits. Ore Geol Rev 76:296–316

Begg GC, Hronsky JA, Arndt NT, et al (2010) Lithospheric, cratonic, and geodynamic setting of Ni-Cu-PGE sulfide deposits. Econ Geol 105:1057–1070

Blanks DE, Holwell DA, Fiorentini ML, et al (2020) Fluxing of mantle carbon as a physical agent for metallogenic fertilization of the crust. Nat Commun 11:1–11

Holwell DA, Blanks DE (2021) Emplacement of magmatic Cu-Au-Te (-Ni-PGE) sulfide blebs in alkaline mafic rocks of the Mordor Complex, Northern Territory, Australia. Miner Deposita 56:789–803

Holwell DA, Fiorentini M, McDonald I, et al (2019) A metasomatized lithospheric mantle control on the metallogenic signature of post-subduction magmatism. Nat Commun 10:1–10

Holwell DA, Fiorentini ML, Knott TR, et al (2022) Mobilisation of deep crustal sulfide melts as a first order control on upper lithospheric metallogeny. Nat Commun 13:1–12

Maier WD, Groves DI (2011) Temporal and spatial controls on the formation of magmatic PGE and Ni–Cu deposits. Miner Deposita 46:841–857

Oliveira EP, Tarney J (1995) Genesis of the Precambrian copper-rich Caraiba hypersthenite-norite complex, Brazil. Miner Deposita 30:351–373

Robb LJ, Armstrong RA, Waters DJ (1999) The history of granulite-facies metamorphism and crustal growth from single zircon U–Pb geochronology: Namaqualand, South Africa. J Petrol 40:1747–1770

The importance of volatiles in the formation of magmatic sulphide ore deposits: experimental constraints

Giada IACONO-MARZIANO[1], Margaux LE VAILLANT[2], Stephen J. BARNES[2]
[1] Institut des Sciences de la Terre d'Orléans, UMR 7327 CNRS-Université d'Orléans-BRGM, 45071 Orléans, France
[2]CSIRO, Mineral Resources, Kensington, WA 6151, Australia

Abstract. Research studies provide growing evidence for the presence of fluids within magmatic mineral systems of mafic-ultramafic composition, despite these ore-forming magmas generally being considered as volatile-poor. Here we summarise the results of two experimental studies that clarify the role of volatiles in the formation of magmatic sulphide ore deposits in mafic-ultramafic magmas: (i) interaction experiments simulating magmatic assimilation of sulfate and/or organic compounds (Iacono-Marziano et al. 2017); (ii) a more recent experimental study shedding light on previously unnoticed physical processes ensuing from the association between sulphide melt and fluid phase (Iacono-Marziano et al. 2022). The silicate melt composition used for both studies is similar to the parental melt of the Noril'sk-Talnakh ore-bearing intrusions in Polar Siberia, and the starting materials of the experiments were samples from the Noril'sk region. Moreover, the experiments were conducted at magmatic conditions relevant to the emplacement pressures and temperatures of the Noril'sk-Talnakh intrusions. Experimental findings are therefore directly applicable to these world-class ores, suggesting that volatiles may have played a crucial role in their formation. Several other magmatic sulphide ores present evidence of the occurrence of a fluid phase during ore formation; hence the mechanisms illustrated by the experiments are likely to be more common than currently considered.

1 Triggering sulphide saturation

The addition of external sulphur to fertile magmas is one of the most common ore-forming processes invoked for magmatic sulphide deposits (e.g., Naldrett 2004). Sulphur can be introduced into the magma by several process: those that have been experimentally documented are anhydrite dissolution (Iacono-Marziano et al. 2017), black shale devolatilization (Virtanen et al. 2021), and black shale assimilation (Deegan et al. 2022). Our experiments at magmatic conditions (1200°C, 80 MPa) show that anhydrite assimilation in the presence of a reducing agent, i.e., organic matter-rich rocks such as coal, is extremely efficient in producing sulphide supersaturation in the magma (Iacono-Marziano et al. 2017).

2 Accumulation of the sulphide melt

The association between the sulphide melt and the fluid phase has been shown to allow the upward transfer of the sulphide melt (Mungall et al. 2015). Our recent experimental results illustrate another physical process that occurs when the proportion of fluid phase in the magma is low: the sulphide-fluid association favours the accumulation of the sulphide liquid, by facilitating the coalescence of the sulphide droplets that are attached to the same fluid bubble (Iacono-Marziano et al. 2022). This consents the accumulation of the sulphide melt in the upper part of the experimental samples (Fig. 1).

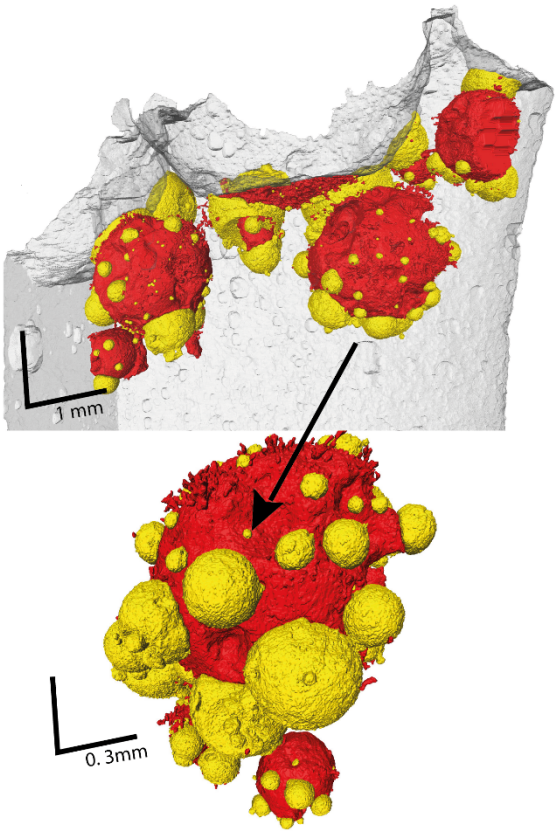

Figure 1. High-resolution X-ray computed tomography rendering of a representative experimental sample showing 3D distribution of sulphide droplets in yellow and fluid bubbles in red (the silicate glass is in grey). The upper image shows a general view of the upper part of the experimental sample, whereas the lower image shows a detail of sulphide-fluid associations, with several sulphide droplets attached to the same fluid bubble. Modified from Iacono-Marziano et al. (2022).

Coalescence of sulphide droplets may be facilitated by the lowering of their interfacial tension induced by the bubble. However, the main driver for coalescence to occur is likely to be the fact that connection to the bubbles keeps the droplets in contact for a long enough time to allow drainage of the melt film between them, as opposed to the situation in a flowing magma where adjacent

droplets are sheared apart before the melt film has time to drain (Robertson et al. 2015). This process may enable sulphide droplets coalescence and deposition in flowing magma, which otherwise have been shown to be unlikely processes (Robertson et al. 2015).

3 Metal enrichment of the sulphide melt

Experimental results indicate that sulphur degassing to the fluid phase increases with increasing proportion of fluid phase, concurrently reducing sulphide melt stability. Consequently, the sulphide melt is consumed and its metal content augments, due to the preferential partitioning of metals into the sulphide melt (Iacono-Marziano et al. 2022). Experimental samples with increasing fluid contents present increasingly Ni- and Cu-rich sulphide melts, illustrating how the metal enrichment of the sulphide melt can be attained by sulphur degassing (Fig. 2). Sulphide upgrading can therefore be achieved by magma degassing.

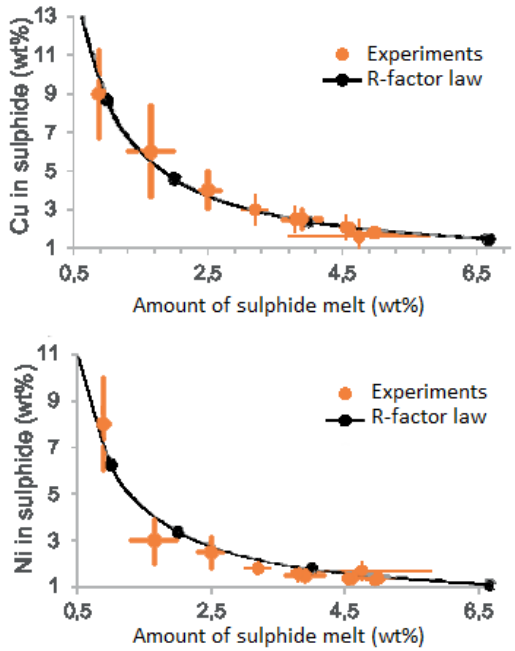

Figure 2. Cu and Ni content of the sulphide melt versus its amount in experimental samples (orange dots) and in theoretical calculations (black line) using the R-factor law of Campbell & Naldrett (1979). Modified from Iacono-Marziano et al. (2022).

4 PGM formation by desulphurisation

Extensive sulphur degassing may completely consume the sulphide melt and form platinum-group minerals (PGMs) at relatively high temperatures (1150°C in the experiments of Iacono-Marziano et al. 2022). Platinum-group mineral formation in the experimental samples (Fig. 3) occurs by desulphurisation of the sulphide melt, while Ni and Cu are partitioned between the silicate melt and the fluid phase. This suggests an unconventional mechanism of PGM formation at temperatures higher than those typical of sulphide melt crystallization.

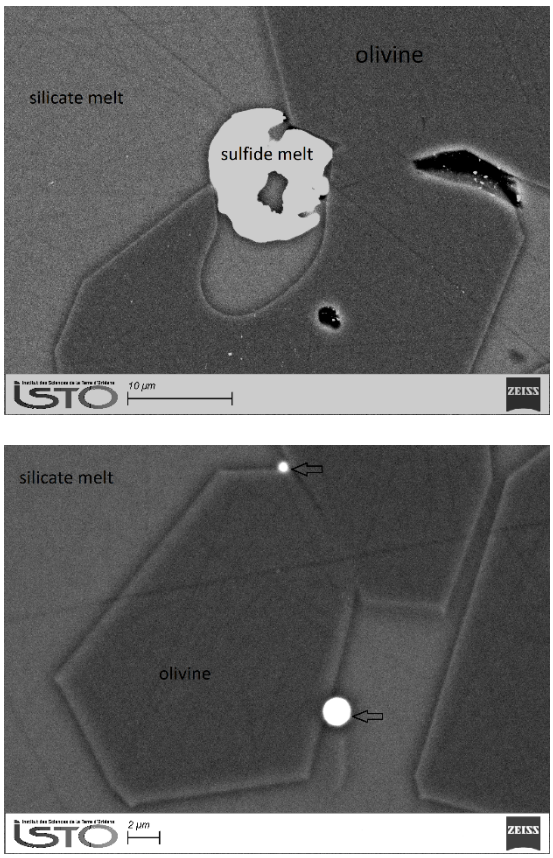

Figure 3. BSE images of an experimental sample with a high proportion of fluid phase (2.2 wt.%), which experienced extensive sulphur degassing. The upper image shows a partially corroded sulphide bleb observed in the upper part of the sample. The lower image shows the Pt-rich, Fe-S-Ni-Cu bearing phase (indicated by the arrows) that commonly occurs at the interface between the olivine and the silicate melt.

5 Application to Noril'sk-Talnakh ores

The experimental results presented above illustrate how the occurrence of a fluid phase in a mafic-ultramafic magma may represent a significant boost for magmatic sulphide ore-forming processes: sulphide melt accumulation, tenor increase, and crystallization of PGMs are indeed key processes in the formation of magmatic Ni-Cu-Co-PGE ore deposits. We use the world-class Noril'sk-Talnakh ore deposits, in Polar Siberia as a case study.

Noril'sk-Talnakh ores are hosted in mafic-ultramafic subvolcanic ribbon-shaped intrusions. Extensive interaction of the ore-forming magmas with evaporitic and carbonaceous rocks has been proposed to be at the origin of the mineralisation and the coexisting abundant fluid phase (e.g. Iacono-Marziano et al. 2017).

The three main ore types are described in ore-bearing intrusions: (i) massive sulphides in the lower

part of the intrusion and largely in the country rocks; (ii) disseminated sulphides (also called globular ores) inside picritic and taxitic rocks, also in the lower part of the intrusion; (iii) low-sulphide PGE ores in the upper part of the intrusion (e.g. Naldrett 2004; Le Vaillant et al. 2017; Schoneveld et al. 2020).

In the second and third ore-types subspherical structures within the crystalline framework have been interpreted as fluid bubbles filled with late magmatic phases or hydrothermal minerals (e.g. Le Vaillant et al. 2017; Schoneveld et al. 2020). In the lower part of the intrusion, these structures are systematically associated with sulphide minerals suggesting they represent sulphide-fluid associations preserved in the olivine-rich magmatic rocks (Le Vaillant et al. 2017). In the upper part of the intrusion, these subspherical structures are even more common and generally contain lower amounts of sulphide minerals but abundant PGMs (Schoneveld et al. 2020), suggesting higher extents of sulphur degassing and sulphide dissolution. On the contrary, massive sulphides are proposed to have experienced low extents of sulphur degassing, attested by the lower metal contents with respect to disseminated sulphides (Iacono-Marziano et al. 2022).

Ore type distribution in Noril'sk-Talnakh intrusions therefore strongly suggests an increasing extent of degassing from the bottom toward the top of the intrusions, implying increasing sulphide melt consumption and metal enrichment. Although a role for volatiles is less clear in other magmatic sulphide deposits, an increasing number of examples of sulphide-fluid associations is reported, as summarised in Iacono-Marziano et al. (2022). This suggests that the role of volatiles in the formation of magmatic sulphide deposits should be re-evaluated.

Acknowledgements

This research received funding from the French agency for research (ANR project #12-JS06-0009-01), the "Equipement d'Excellence" Planex of the University of Orléans (France), and the programme TelluS of the Institut National des Sciences de l'Univers, CNRS.

References

Campbell, I.H., and Naldrett, A.J. (1979): The influence of silicate:sulphide ratios on the geochemistry of magmatic sulphides, Economic Geology, v. 74, p. 1503–1506.

Deegan, F.M., Bédard, J.H., Grasby, S.E., Dewing, K., Geiger H., Misiti, V., Capriolo, M., Callegaro, S., Svensen, H.H., Yakymchuk, C., Aradi, L.E., Freda, C., and Troll, V.R. (2022): Magma-shale interaction in Large Igneous Provinces: Implications for climate warming and sulfide genesis, Journal of Petrology, v. 63, p.1-10.

Iacono-Marziano, G., Ferraina, C., Gaillard, F., Di Carlo, I., and Arndt, N.T. (2017): Assimilation of sulfate and carbonaceous rocks: experimental study, thermodynamic modeling and application to the Noril'sk-Talnakh region (Russia), Ore Geology Reviews, v. 90, p. 399–413.

Iacono-Marziano, G., Le Vaillant, M., Godel B.M., Barnes, S.J., and Arbaret, L. (2022): The critical role of magma degassing in sulphide melt mobility and metal enrichment, Nature Communications, v. 13, 2359.

Le Vaillant, M., Barnes, S.J., Mungall, J.E., and Mungall, E.L. (2017): Role of degassing of the Noril'sk nickel deposits in the Permian-Triassic mass extinction event. Proceedings of the National Academy of Sciences, v. 114, p. 2485–2490.

Mungall, J.E., Brenan, J.M., Godel, B., Barnes, S.J., and Gaillard, F. (2015): Transport of metals and sulphur in magmas by flotation of sulphide melt on vapor bubbles, Nature Geoscience, v. 8, p. 216–219.

Naldrett, A.J. (2004): Magmatic Sulphide Deposits: Geology, Geochemistry and Exploration, Springer Berlin, 728 p.

Robertson, J.C., Barnes, S.J., and Le Vaillant, M. (2015): Dynamics of magmatic sulphide droplets during transport in silicate melts and implications for magmatic sulphide ore formation, Journal of Petrology, v. 56, p. 2445-2472.

Schoneveld, L., Barnes, S.J., Godel, B., Le Vaillant, M., Yudovskaya, M.A., Kamenetsky, V., and Sluzhenikin, S.F. (2020): Oxide-sulphide-melt-bubble interactions in spinel-rich taxitic rocks of the Norilsk-Talnakh intrusions, polar Siberia, Economic Geology, v. 115, p.1305–1320.

Virtanen, V.J., Heinonen, J.S., Molnar, F., Schmidt, M.W., Marxer, F., Skyttä, P., Kueter, N., and Moslova, K. (2021): Fluids as primary carriers of sulphur and copper in magmatic assimilation, Nature Communications, v. 12, 6609.

Cobalt–nickel–copper arsenides, sulfarsenides and sulfides of Bou Azzer (Anti-Atlas – Morocco): Lithological and structural controls

Marieme Jabbour[1], Zoubair ELOuad[2], Mohamed Ez-Zghoudy[1], Mustapha Souhassou[2], Younes Moundi[3], Nicolas Saintilan[4], Said Ilmen[5], Amine Bajddi[3], Lhou Maacha[3], Faouziya Haissen[6], Mohamed Zouhair[3], Moha Ikenne[1]
[1] Laboratory of Applied Geology and Geo-Environment, Ibnou Zohr University, Agadir, Morocco.
[2] Laboratory of Geo-Bio-Environmental Engineering and Innovation, Research, Ibnou Zohr University, Taroudant, Morocco.
[3] MANAGEM Group, Twin Center, Tour A, BP 5199, Casablanca. Morocco
[4] Institute of Geochemistry and Petrology, Department of Earth Sciences, ETH Zurich. Zürich, Switzerland
[5] CAG2M, Polydisciplinary Faculty of Ouarzazate, Ibnou Zohr University, BP 638, 45000 Ouarzazate, Morocco
[6]Department of Geology Faculty of Sciences Ben M'sik, Hassan II University of Casablanca Morocco.

Abstract. The Bou Azzer–El Graara inlier is famous by its Co-Ni deposit associated to a Neoproterozoic ophiolitic complex. This paper aims to present results from three sectors, the Bou-Froukh, the Aghbar, and the Ait Ahmane deposits. Geological investigations (Leblanc, 1975; Saquaque, 1989) and recent radiometric data (Admou 2013) allow recognizing three major formations in the Bou Azzer Inlier: The Bou Azzer group; the Tiddiline Fm., and the Ouarzazate group. These Neoproterozoic formations have undergone the Pan-African events which take place in two episodes. The B1 phase is materialized by the development of a general NW-SE flow cleavage recorded in the Bou Azzer group, whereas the B2 phase is characterized by a fracture cleavage expressed in the Tiddiline Fm. , along with a network of reverse faults and sinistral strike-slip faults crossing the entire region, they are considered to be inherited from the B1 phase and then replayed in the form of sinistral strike-slip faults during the B2 phase, and staked by quartz- carbonate lenses, making them vents for mineralizing fluids. These faults played a significant role in the Bou Azzer district's mineralization by enabling the emplacement of arsenides vein mineralization. The mineralization primarily consists of triarsenides, sulfoarsenides, and sulfides, hosted by quartz and quartz-carbonate veins.

1 Introduction

The Bou Azzer - El Graara inlier (BEI) is famous by its Neoproterozoic ophiolitic complex and its Co-Ni arsenides deposits. It plays a key role in the understanding of geological and geodynamics history of the Anti-Atlas Panafrican belt. This work aims to present new results of three different Co-Ni ore deposits: The Bou-Froukh, Aghbar, and Ait Ahmane deposits. The lithological assemblages in the area are categorized into three primary groups: The Bou Azzer group (serpentinized peridotites, metabasitesand the associated quartz-diorites), the Tiddiline Fm., (detrital and volcani-sedimentary facies), and the Ouarzazate group (volcanic and pyroclastic rocks). These Neoproterozoic terrains have undergone the Panafrican events marked by two deformation phases. The one, B1, is distinguished by a general NW-SE flow cleavage, observed in the Bou Azzer group, whereas the second phase, B2, is defined by a fracture cleavage recorded in the Tiddiline Fm.

Additionally, a network of reverse faults and sinistral strike-slip faults that cut across the entire area is believed to be inherited from the B1 phase and replayed as sinistral strike-slip faults during the B2 phase. These structures were the vents of the mineralizing fluids, particularly Co, Ni, As, Au, and Ag, which have been deposited as triarsenides, sulfoarsenides, and sulfides, primarily hosted by quartz and quartz-carbonate veins. Our investigations aim to provide detailed lithological and structural features from the three deposits help understanding the factors that control the Co- bearing arsenides mineralization within the entire Bou Azzer –El Graara inlier.

2 Geological setting

The BEI is composed of a Neoproterozoic basement consisting of gneiss, amphibolites, serpentinites and mafic rocks, quartz diorites, overlain by volcanic-sedimentary cover represented by Ouarzazate group, divided into two groups: the terrigenous serie of the Tiddiline attributed to the Lower Ediacaran, and the Upper Ediacaran serie of the Ouarzazate Group. These latter are stratigraphically overlain by the early Cambrian series commonly known as the Adoudounian series (Figure 1).

The Aghbar area, located in the central part of the BEI, it is composed of serpentinites representing the Cryogenian ophiolite mantle covered by late Ediacaran volcanic and volcaniclastic rocks, overlain continuously by the lower Cambrian series formed mainly by dolomites and andesites.

The Bou-Froukh sector represents the western end of the BEI. It is composed of Cryogenian formations consisting of serpentinites, mafic rocks, intrusive quartz-diorites, the Tiddiline Fm., to the north, Ediacarian volcanic rocks, and the Adoudounian volcani-sedimentary cover.

The Ait Ahmane area is located in the eastern side of the inlier; it is characterized by the predominance of the ophiolitic rocks and the associated quartz-diorite intrusions (Ikenne et al. 2023). This area is characterized by a NNW-SSE oriented band arrangement of the different terrains

that comprise it, with the serpentinite massifs, gabbro band, and quartz-diorite band arranged from north to south. The quartz diorite band is intersected by veins of quartz, and quartz-carbonate, which serve as the host for cobalt mineralization.

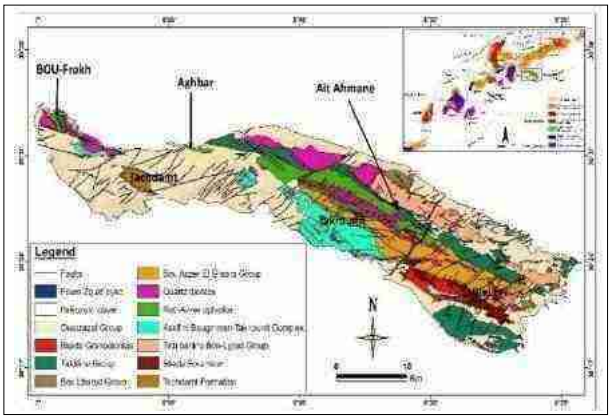

Figure 1. Geological map of the Bou Azzer - El Graara inlier (modified after Leblanc, 1980)

3 Structural data

Leblanc (1975) and Saquaque et al. (1989) highlighted the main events of the Pan-African orogeny in the BEI. They recognized two tectonic phases.

The first one, called phase B1 is a tangential phase that developed a NW-SE metamorphic schistosity in a low grade environment. This phase would have taken place during the obduction of the Bou Azzer ophiolitic complex on the northern border of the West African craton following a shortening in the NE-SW direction (Saquaque et al. 1989). The second, phase B2, is responsible for a fracture cleavage. this second event have also accompaniedby major sinistral strike-slip faults and reverse faults that take up the inherited faults from phase B1, withan average compression direction of N20° to N35° (Figure 2) (Leblanc et Lancelot, 1980; Azizi et al. 1990; Azizi, 1990; Ez-Zghoudy et al., 2023).

In these three studied deposits (Aghbar, Ait Ahmane and Bou Froukh); we identified three main families of structures:

- The E-W to WNW-ESE faults family, associated with major geological events considered as inherited from the B1 phase.
- The ENE-WSW family, recognized mainly in the central and western studied sectors. It consists of reverse faults related to the B2 phase.
- The NNE-SSW to NE-SW family, important because it regularly contains mineralization, is supposed to be related to the Hercynian orogeny (Maacha, 2013) or reactivated during the Hercynian period.

Figure 2. (A) Intra-dioritic quartz-carbonate emplacement, (B) sigmoidal tectonic structure, (C) reverse fault with quartz filling, (D) Fault mirror showing striations and pullout surfaces, (E) S1 flow cleavage across serpentinites, (F) Streaks indicating strike-slip movement (pitch between 5° and 30°).

4 Petrographic study

The three studied deposits are characterized by a large lithological diversity, and several petrographic facies have been mapped and described in these areas. The serpentinites are the predominant rocks in the tree areas; they are the result of the hydration and alteration of the ultramafic rocks that represent the mantle part of the ophiolite (Leblanc, 1980). These serpentinites host several kinds of dykes. The quartz diorites represent the latest element associated with the ophiolitic complex in the BEI terrains, they are anterior or synchronous to the B1 tectonic phase, during which they were tectonized (Leblanc 1981, Ikenne et al.2023).

The formations that post-date the major Pan-African B1 phase are assigned to the Ediacaran age.

During this period, two sedimentary formations were unconformably deposited on the ophiolitic complex and the associated rocks (Leblanc 1980):

- The Tiddiline Fm., which corresponds to detrital (mollasse and arkose) and volcani-detrital (greywackes) facies.
- The Ambed Fm., which is a silici-carbonates shell linked to a meteoric alteration. It constituted the receptacle of mineralizations (Maacha et al. 2011).

After the Pan-African stress, the Bou Azzer domain is exposed to a transtensive regime synchronous with the deposition of the Ouarzazate Fm. (Azizi et al. 1990). This regime favored the development of a system of horsts and grabens associated with the rise of serpentinite domes, alternating with depressions with Ediacaran deposits (Maacha et al. 2011). In the study area and based on the microscopic study, these deposits are represented by andesites, volcanic breccia, and pyroclastic rocks (Figure3).

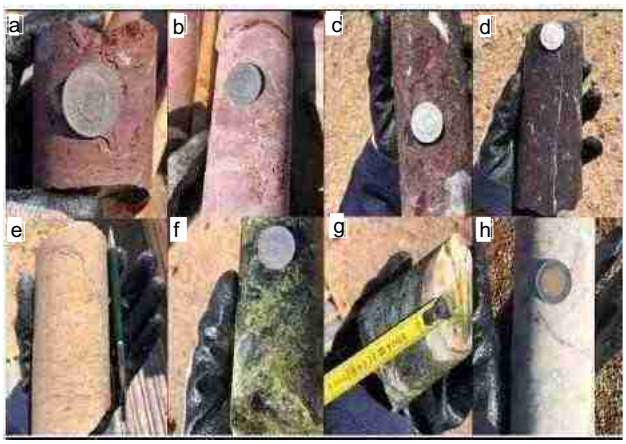

Figure 3. a- Sandstone/ b- Dolomite/ c-Conglomerate/ d- Andesite/ e- Dacite/ f,g- Serpentinite/ h- quartzo-carbonate veins.

5 Co-Ni-Cu mineralization

In all deposits of the Bou Azzer district, mineralized bodies are generally located along major Pan- African faults, and they are spatially and genetically associated with serpentinites (Leblanc. 1975, Maacha et al. 2011, Ikenne et al. 2021, Ez- Zghoudy et al. 2023). The mineralizations consist mainly of cobalt and nickel arsenides which are formed in a polyphase metallogenic system, whose ultimate stage corresponds to a mixing between exogenous fluids enriched in Co, Ni and As chlorides leached from serpentinites, and a volcanogenic fluid carrying selenium, molybdenum, bismuth, and gold (Maacha et al. 1998).

The studied areas contain several mineralized bodies in form of veins and/or lenses of different sizes. These bodies are located along sinistral faults attributed to the B2 Pan-African phase (Maacha et al. 2011). The lenses and veins are composed of quartz-carbonate facies with a late paragenesis of chalcopyrite and malachite (Figure 4).

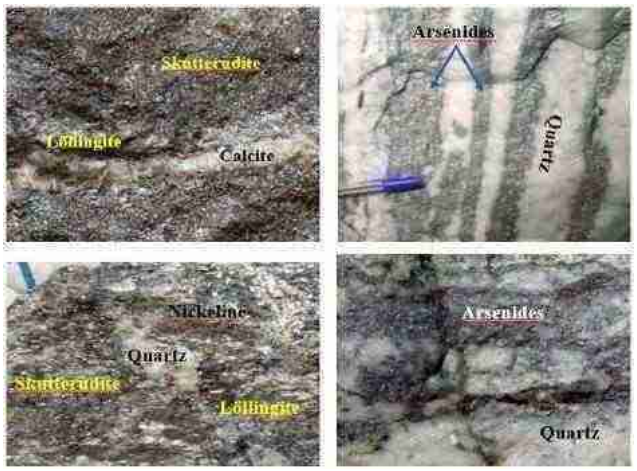

Figure 4. Macroscopic aspects of the mineralization in the Bou Azzer ore deposits.

Morphologically, the main deposits are developed either within the serpentinite or mainly along the contact between the serpentinite and quartz-diorite rocks.

Microscopic examination of these mineralizations shows a predominance of a mineralization consisting of triarsenides (skutterudite), biarsenides (safflorite, löllingite) monoarsenides (nickeline), sulfoarsenides (arsenopyrite), with little sulfides (chalcopyrite, galena) (Figure 5), accompanied by various generations of intercalated calcite, dolomite and quartz. Gold and silver assemblages include mainly native gold and electrum, polybasite, proustite, xanthoconite, argyrodite, stromeyerite and freibergite.

Optical investigations and textural relationships indicate three hydrothermal stages characterized by mineral assemblages of pre-arsenide gold stage I, stage II (Co, Ni, Fe)-arsenide and sulfarsenide, and stage III epithermal sulfide-sulfosalt ± Au ± Ag; a post-ore supergene stage IV is characterized by secondary Co minerals (erythrite, roselite, talmessite) (Bouabdellah et al. 2016).

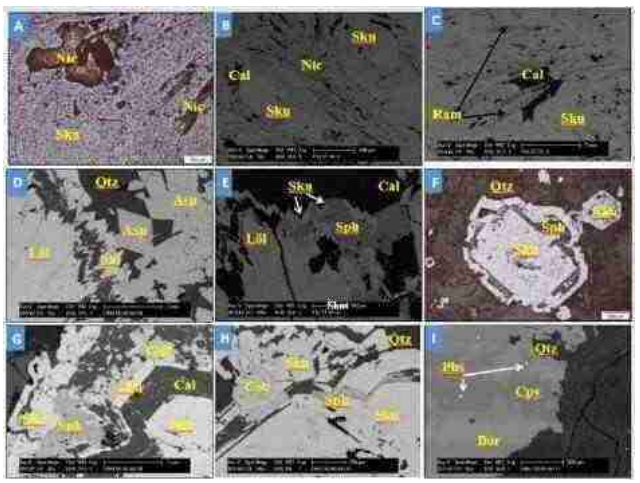

Figure 5. Black scattered images of contact mineralization hosted in calcitic lenses located between serpentinites and quartz diorite. Abbreviations (Nic. Nickeline; Sku. Skutterudite; Ram. Rammelsbergite; Qrz. Quartz; Saf. Saffllorite; Löl. Löllingite; Asp. Arsenopyrite; Sph. Sphalerite; Pbs. Galena; Bor.

Bornite; Cpy. Chalcopyrite; Cob. Cobaltite; Gdf. Gersdorffite; Cal. Calcite).

The second type, vein mineralization, consists of mineralized veins that have a banded texture and intersect either quartz diorites or Ediacaran lavas (Figure 6).

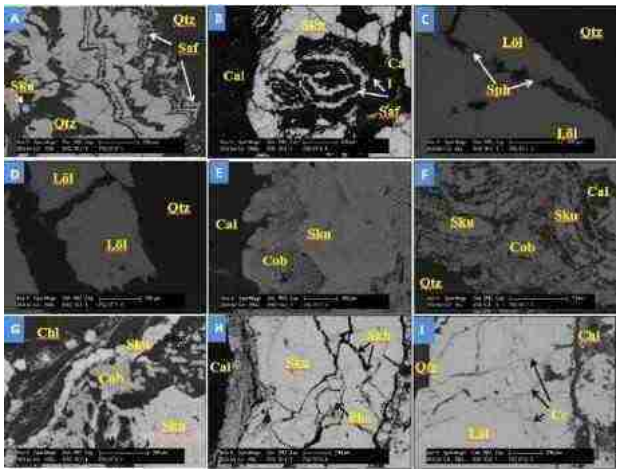

Figure 6. SEM phtomicrographs showing mineral association and mineral textures of the studied veins. Abbreviations (Nic. Nickeline; Sku. Skutterudite; Ram. Rammelsbergite; Qrz. Quartz; Saf. Safflorite; Löl. Löllingite; Asp. Arsenopyrite; Sph. Sphalerite; Pbs. Galena; Bor. Bornite; Cpy. Chalcopyrite; Cob. Cobaltite; Gdf. Gersdorffite; Cal. Calcite).

6 Conclusion

In conclusion, our field investigations in the BEI have revealed that the mineralization in the Aghbar, Ait Ahmane, and Bou-Froukh deposits is controlled by three families of tectonic structures. These structures include an E-W to WNW-ESE trending family inherited from the Pan-African B1 phase, an ENE-WSW trending family of faults related to the Pan-African B2 phase, and an NNESSW to NE-SW trending family related to the Hercynian orogeny. We have redefined two main types of mineralization in these deposits: i) so- called "contact ore bodies with massive lenses structurally controlled by the Pan-African faults and which occur either within serpentinite or mainly along its contact with Cryogenian quartz- diorite (Bou-Froukh and Ait Ahmane) or with Ediacaran volcanic rocks (Aghbar); and ii) the vein systems, which cut the different lithologies and are controlled by an NNE-SSW to NE-SW family, correspond to a reactivation of tension gashes as reverse faults during a shortening phase, probably of Hercynian age. These veins are only mineralized along segments of about 40 m from the contact of the serpentinite massif. The mineralization consists mainly of Co-Ni-Fe-bearing arsenides, sulfarsenides, sulfides, and native elements (Bi, Au), with gangue minerals chiefly represented by quartz, calcite, dolomite, and chlorite.

References

Admou H, Fekkak A., Razin P, Egal E, Youbi N, Soulaimani A, Blein O, Baudin T, Chèvremont P, (2013) Notes et Mémoires du Service Géologique Maroc. N°533. Carte Géologique Maroc (1/50 000). Feuille Aït AAhmane.

Azizi-Samir MR (1990) Géologie du Précambrien terminal (III) et traitement statistique des données géochimiques de prospection, dans la boutonnière de Bou Azzer - El Graara (Anti-Atlas, Maroc). Thèse. Université Joseph Fourier, Grenoble I. 280 p.

Azizi-Samir MR, Ferrandini, J, Tane J.L (1990). Tectonique et volcanisme tardi-Panafricains (580-560 Ma) dans l'Anti-Atlas Central (Maroc) : interprétation géodynamique l'échelle du NW de l'Afrique. J Afri Earth Sci 10:549-563.

Bouabdellah M, Maacha L, Levresse G, Saddiqi O (2016) The Bou Azzer Co–Ni–Fe–As(±Au ± Ag) District of Central Anti-Atlas (Morocco): A Long-Lived Late Hercynian to Triassic Magmatic-Hydrothermal to Low- Sulphidation Epithermal System. In: Bouabdellah, M., Slack, J. (eds) Mineral Deposits of North Africa. Mineral Resource Reviews. Springer, Cham. https://doi.org/10.1007/978-3-319-31733-5_8.

Ez-Zghoudy M, Ikenne M, Souhassou M, Belfoul MA, Gouiza M, Ilmen S, Ousbih M, Karfal, A, Maacha L, Zouhair M (2023) Structural controls on the Co and Ni-bearing arsenides from the Bou Azzer mine (Case of Aït Ahmane F53 vein deposit): Implications for mineral exploration. J Afri Earth Sci 104929. https://doi.org/10.1016/j.jafrearsci.2023.104929.

Ikenne ., Souhassou M, Saintilan N.J, Karfal A, Hassani AE, Moundi Y, Ousbih M, Ezzghoudi M, Zouhir M, Maacha L (2021) Cobalt–nickel–copper arsenide, sulfarsenide and sulfide mineralization in the Bou Azzer window, Anti- Atlas, Morocco: one century of multi-disciplinary and geological investigations, mineral exploration and mining. Geol Soc, London, Special Pub 502: 45-66.

Ikenne M, Souhassou M, Cousens B, Montero PF, Bea F, Askour F, Haissen F, Beraaouz EH, Ernst RE, Bajddi A, Ilmen S, Belkacim S, Toummite A (2023) Zircon U-Pb geochronology and Sm-Nd and Rb-Sr isotope systematics of Neoproterozoic Granitoïds from Bou Azzer (Anti-Atlas - Morocco): the obduction trigger of the Central Anti-Atlas Terrane. J Afr Earth Sci 104900. https://doi.org/10.1016/j.jafrearsci.2023.104900.

Leblanc M (1975) Ophiolites précambriennes et gris arséniés de cobalt (Bou Azzer, Maroc).Ph.D. Thesis Université de Paris VI, 329 p

Leblanc M, Lancelot JR (1980) Interprétationgéodynamique du domaine pan-africain (Précambrienterminal) de l'Anti-Atlas (Maroc) à partir de données géologiques et géochronologiques. Can J Earth Sci 17 : 142–155.

Maacha L (2013) Études métallogéniques et géophysiques des minéralisations cobaltifères et cuprifères de Bou-Azzer El Graara, Anti- Atlas Maroc. Les minéralisations de cuivre de la plateforme de Bleida. Ph.D. Thesis, Université Cadi Ayyad, Marrakech, 748p.

Maacha L, Alansari A, Saquaque A, Soulaimani A (2011) The Bou Azzer Cobalt-Nickel-Arsenic district. In: Les principales mines du Maroc, Michard, A., Saddiqi, O., Chalouan, A., Rjimati, C., Mouttaqi, A. (Eds.). Nouveaux Guides Géologiques et Miniers du Maroc, pp. 91-97.

Maacha L, Azizi-Samir R, Bouchta R (1998) Gisements cobaltifères du district de Bou Azzer (Anti-Atlas) : structure, minéralogie et conditions de genèse. Chron Rech Min 531–532 :65–75.

Saquaque A, Admou H, , Karson J, Hefferan K, Reuber I, (1989) Precambrian accretionary tectonics in the Bou Azzer-El Graara region, Anti-Atlas, Morocco. Geology 17:1107-1110.

PROSPECTS ON PLATINOIDS OF THE MAFIC-ULTRAMAFIC BELT OF THE SULTANUVAIS MOUNTAINS (UZBEKISTAN)

Jurabekov N.J.[1], Khaydarova A.B.[1], Khalmatov R.A.[1] Kholikov A.B.[2]
[1] University of Geological Sciences, Tashkent, Uzbekistan
[2] Institute of Mineral Resources,Tashkent, Uzbekist

Abstract. Mafic-ultramafic belts, tracing zones of deep faults, and suture zones have been discovered in Uzbekistan. Within their limits, in the mountains of Sultanuvais, Bukantau, Tamdytau, Nurata, and Chakylkalyan, studies have been conducted to detect platinum group metals (PGM). The article discusses the prospects for the platinoids of the Tebinbulak intrusion, which is located in the core of a synclinal fold of siliceous rocks. It is an ethmoid-like body (ellipsoid in plan) measuring 4.5x1.8 km, slightly asymmetrical, extending from south to north. The composition of the intrusion is dominated by ultrabasic rocks: peridotites (verlites, schliregeimites), pyroxenites, hornblendites; there are also in some degree mafic rocks. Two promising areas for platinum metals have been identified. Further research is required for an objective assessment of high-category resources.

1 Introduction

The economic significance of platinum group metals (PGM) – ruthenium, rhodium, palladium, osmium, iridium, and platinum – is determined primarily by valuable physical and chemical properties: heat resistance, corrosion and acid resistance, refractory, etc.

The main consumer of platinoids is the modern chemical industry, which uses them as catalysts in the production of nitric and other acids, in hydrogenation reactions of various compounds. The oil refining, automotive, electrical engineering, and jewelry industries are also important areas of application; a small part is used in medicine (surgical instruments, dentures, etc.).

There has been a trend of rapid growth in the consumption of platinoids in the automotive industry in the manufacture of filter-neutralizers of exhaust gases of cars.

The Republic of Uzbekistan does not have its own deposits of platinum metals, and its needs were covered by imports from abroad. However, in the Navoi Mining and Metallurgical Combine (NGMC) in 1980, a technology for extracting palladium from Muruntau ores was developed and implemented.

The Tebinbulak intrusive massif is located at the northwestern end of the Sultanuvais Mountains and includes the Aktau and Jamansai intrusions which are usually considered as large allochthonous blocks juxtaposed with the surrounding schists in a tectonic mélange.The host rocks are represented by metamorphosed Devonian formations (siliceous shales, siltstones, sandstones), forming a synclinal fold, in the core of which the Tebinbulak intrusive massif is located. It is a somewhat asymmetrical, elongated from south to north ethmolith-like body (ellipsoid in plan) measuring 4.5x1.8 km. The composition of the intrusive is dominated by ultrabasic rocks: peridotites (verlites, schliregeimites), pyroxenites, tebinites, hornblendites; there are also mafic rocks - hornblendite gabbro with sections of pyroxene gabbro and gabbro-syenites, gabbro-diorites. This intrusion is promising for the detection of industrial objects of platinum group metals.

2 Methodology

This study summarizes published and archival materials on platinoids of the Tebinbulak intrusion. Field studies sampled the rocks of the intrusive complex in order to determine the industrial significance of the platinoids. The analytical and mineralogical determinations done by the following techniques: primary analytical determination of a wide range of chemical elements by semi-quantitative spectral methods, quantitative determination of concentrations of the main useful components (gold, silver, platinoids, tungsten, etc.) by atomic absorption, quantitative microprobe (Jeol JSM5910LV - Japan) determination by EPMA and elemental determination by ICP (inductively coupled plasma) - mass spectrometric (Elan-G100DRS - USA). All the methods were carried out in the laboratory "Physical-Chemical Research Methods" of SI "IMR", the Institute of Geology and Geophysics of the Academy of Sciences of the Republic of Uzbekistan and the Central Laboratory of the State Committee of Geology of the Republic of Uzbekistan.

3 Discussions of the results

The majority of analysed samples from the Tebinbulak complex, presented by peridotites, pyroxenites and hornblendites with subordinate gabbro and gabbro-diorites.

The average chemical compositions of the main rocks of the Tebinbulak massif are given in Table 1.

Table 1. Chemical composition of rocks of the Tebinbulak massif, weight %

Component	Peridotites (3 an.)	Pyroxenites (8 an.)	Hornblendite (10 an.)	Gabbro (all) (14 an.)
SiO2	42,68	48,64	39,2	42,42
Al2O3	2,55	4,24	11,2	17,92
Fe2O3	6,39	4,22	7,47	6,28
FeO	4,91	4,60	9,93	6,37
MgO	26,97	14,86	11,35	5,89
CaO	8,96	19,60	13,3	13,23
Cr2O3	0,061	0,026	0,015	0,037
NiO	0,007	0,003	0,0014	0,012
CoO	0,001	0,002	0,0016	0,002
CuO	-	-	0,003	0,005
V2O5	0,017	0,0125	0,09	0,02
The amount	92,546	96,2035	92,561	92,186

Ultramafic bodies are exposed mainly in the northern parts of the western and eastern half of the Sultanuizdag ridge. Ten large and a significant number of small lenticular bodies of serpentinites are distinguished. A much smaller volume of ultramafic rocks is exposed in the middle reaches of the Kohrali, Sultan-bobo, Uzunbulak, and Kazgansayas. Several small audited bodies were found in the zone of the Urusai fault. The main mass of serpentinites is located in the form of two bands. The first is traced in the northern part of the ridge and lies among the effusive rocks of the Jamansai formation. Sometimes they come into contact with gabbro amphibolites. The second band is located south of the first, these bodies form interformational lenses by contact with terrigenous-sedimentary and sedimentary-effusive rocks of the Jamansai formation. The total area of Ultramafic bodies is 22 km^2.

The contacts of serpentinites with host rocks are predominantly tectonic and sub-consistent. Ultramafites are characterized by a rather monotonous composition and are represented by serpentinites. Dunites, peridotites, and pyroxenites are poorly expressed; they occur in the form of shlierens in serpentinites.

The objects of the Tebinbulak ore field of Sultanuvais Mountain belong to the titanomagnetite platinum-gold ore formation. They correspond to the riftogenic regime (D-C) with the manifestation of picrite-gabbro-diabase-alkali-olivine-basalt association of formations. Magmatism manifested itself within the long-lived regional Bukantau-South Ferghana zone of deep faults.

The Tebinbulak gabbro-pyroxenite massif is ore-containing and is located in the zone of the submeridional Urusai deep fault, in the core of the synclinal fold among the Lower Devonian rocks (siliceous, shale, sandstones, siltstones) and is a plate-like body. In the near-contact parts of it, the host rocks have been transformed into the plagioclase-micaceous cornea, marbled, scarred limestones (Figure 2).

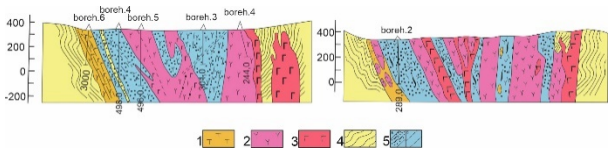

Figure 1. Geological sections of the Tebinbulak intrusive (based on the materials of the Tebinbulak exploration party): Symbols: 1 - peridotites; 2 - pyroxenites; 3 - hornblendites; 4 - ore-bearing Lower Devonian greenstone shales; 5 - zones (areas) of veined-interspersed titanomagnetite mineralization: a - traced; b - isolated from geophysical data.

The composition of the intrusive is dominated by ultrabasic rocks, the most common being hornblendites, pyroxenites, and peridotites. The maximum amount of titanomagnetite is noted in hornblendites and pyroxenites (up to 8.4-10%), where ilmenite and pyrite are present. Gabbroic rocks are represented by hornblendite essexite gabbro, gabbro-monzonites, and gabbro-diorite veins. In gabbro, concentrations of titanomagnetite and ilmenite reach 5.5%. Sphene (up to 1%), apatite, zircon, and rutile are also noted. The third group is the youngest dykes of syenites, leucosienites. The rocks are characterized by increased alkalinity, ferruginousness, and titanicity (maximum in pyroxenites, hornblendites) and are differentiated from basaltic magma. The age of the intrusion according to geological data and the absolute age of potassium-argon 313±8 million years corresponds to C_{1-2}.

Titanomagnetite mineralization with platinum and gold in ultrabasic rock differences extends in a sub-meridional direction near the western contact of the intrusion in the form of a 2.5 km long strip with a width of 100-400m and is traced to a depth of 500m. Mineralization is represented by two associations - titanomagnetite and platinum-gold sulfide. Titanomagnetite mineralization develops in the form of inclusions, and veins of densely interspersed and massive addition, schlieren secretions. 90-95% of the ores consist of magnetite. Its exsolution structures with ilmenite are characteristic, and spinel, hematite, and sphene are also present. The impurities are V, Cr, Mn, Ni, Co (Figure 3).

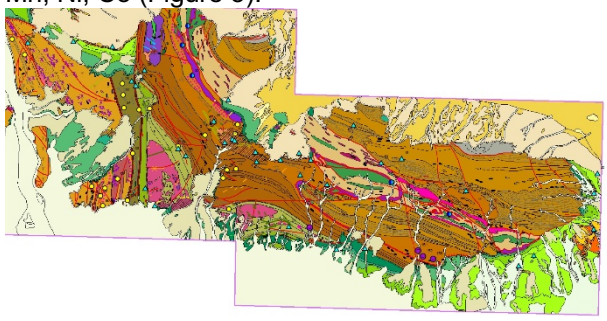

Figure 2. Geological map of the Sultanuvais Mountains in GIS format.

Gold and platinoids are found both in host rocks and in titanomagnetite ores. Their distribution is

extremely uneven and the content increases significantly in the sulfide association. Sulfide paragenesis is represented by chalcopyrite, pyrite, bornite, arsenopyrite, and arsenopyrite. The gold content in pyroxenites, hornblendites, and peridotites averages 0.021 ppm (0.01-0.023), which is five times higher for ultrabasics. There is a positive correlation between gold and platinoid contents. Gold is mainly finely dispersed and pulverized (0.01-0.1mm) high-grade. Gold telluride (Montreuil) has also been found. Gold concentrators are pyrite (up to 1.8 c/u) chalcopyrite (up to 0.5 ppm), its carriers are titanomagnetite (up to 0.7 c/u), hornblendites (up to 0.24 ppm) (Figure 4).

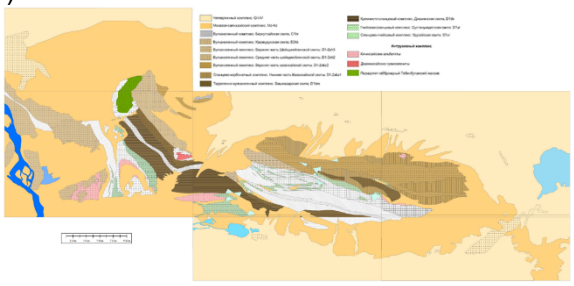

Figure 3. Map of the structural and material complexes of the Sultanuvais mountains.

Platinum and palladium predominate among platinoids, rhodium, traces of ruthenium, and iridium are noted. Peridotites, hornblendites contain PGM close to clarke, and in pyroxenites and gabbro it is 1.5 times higher than clarke.

The maximum amount of palladium (up to 0.06 ppm) is found in pyroxenites, tebinites. The content increases sharply in the presence of sulfide mineralization (the amount of platinoids is up to 1.45 ppm).

According to A.B. Khalikov, more than 25 anomalies with the content of platinum group metals up to 7.73 ppm were detected in the Tebinbulak massif in areas of ferruginization. Sulfides concentrate up to 99.2% of platinum metals with a platinum content from 0.4 to 25 ppm and palladium from 0.24 to 22 ppm. The ratio of palladium to platinum ranges from 0.2-6.7. The main concentrators of platinoids are pyrite (0.64-47 c/u) and chalcopyrite (1.88-4.5 ppm). Platinoids are also present in titanomagnetite (0.01-0.16 ppm), hornblendites (up to 0.24 ppm), pyroxene. Micro inclusions of platinum minerals - cuprite, polyxene, sperrilite - have been found in rocks and sulfides (V.V. Baranov, 1978).

In general, titanomagnetite mineralization with platinum and gold, located in the differentiated gabbro-pyroxenite massif, belongs to the magmatic and late magmatic types. The processes of late magmatic amphibolitization and postmagmatic serpentinization played an important role in the redistribution of ore components. According to the material composition and the nature of the distribution of the main components of the Tebinbulak ore, they are compared with the largest Ural Kachkanar deposit with good reason.

Figure 5 shows histograms of statistical calculations of spectral analysis of rocks of Tebinbulak ore field. Concentrations of most chemical elements: Sb-52.4; Au-39.4; Ta-24.5; Ba-1.4; As-14.7; W-4.6; Cu-9.4; Co-3.6; Cd-3.5; Bi-3.3– V-2.9; Cr-2.9; Mn-2.7; Ni-1.6; Ga-1.5; Ag–1.2; Pb-0.9

Correlations of elements by spectral analysis are shown for the most significant correlations - 84 samples with a critical value of the correlation coefficient for 5% of the significance level of Pk-0.212. noted with Cr, W, Ag, Cd, Sn, Ti, V, Ni, Mn, Co, Pb, Ba, Ga, Cu, Mo, Sb, Ni, As.

According to mass spectrometric analysis, the reduced average content of many elements, including the traditional satellites of gold - As, Ag (24.1 and 0.55 ppm, respectively). And also, the low maximum value–As-249 ppm (0.025%), raises the question of the possibility of its use as an indicator of gold mineralization. Accordingly, for the Tebinbulak expedition, the concentration of most chemical elements was obtained, (concentrations Re-495.1; Se-157.8; Pt-129.2; Te-67.9; Au-25; Pd-19; Si-18.5; As-14.2; Sb-8.7; Ag-7.9; Mo-4.4; Ir-3.2; Ni-3.1; Ca-2.8; Va-2.7; P-2.7; V-2.4; B-2.3; Sr-1.7; Mn-1.6; Fe-1,5; Co-1,4; Ti-1,2; U-1,1; Sc-1,1; Mg-1; W-0,9; Pb-0,9; Cr-0,9; Bi-0,8; Ru-0,6; Rh-0,2; Os-0,02). Normalized according to A.P. Vinogradov. The analysis was performed in Excel and Statistica.

To compare the concentrationsaccording to the regional background with the concentrations according to A.P. Vinogradov (granite-metamorphic shell), c/u. Accordingly, the concentration of most chemical elements by regional background was obtained, (concentrations Pd-72.3; Pt-25.8; Ti-7.8; P-7.6; As-6.3; Re-6.2; V-5.2; Sr-4.8; Ir-4.1; Mg-3.5; Cr-3.4; Co-3.2; Va-3.2; Pb-2.9; Sb-2.3; W-2.3; Sc-2.1; Au-2; Ni-1.8; Mn-1.8; Mo-1.8; Bi-1.7; Rh-1.4; Ag-1.4; Fe-1.3; Ru-1.2; Te-1.1; U-1; B-1; Os-0.9; Ca-0.9; Se-0.9; Si-0.9).

Correlations of elements by mass spectrometric analysis are shown. The most significant correlations - 34 samples with a critical value of the correlation coefficient for 5% of the significance level Rk-0.330) are noted with Fe, V, Pb, Va, Ti, P, V, Mg, Sc, Mn, Co, Ca, Te, Mo, Bi, As, B, Cr, U, Se, Ag, Pt, Rh, Pd, Os, Ru, Au, Ir, Re, Sb, Sr, Si, W, Ni.

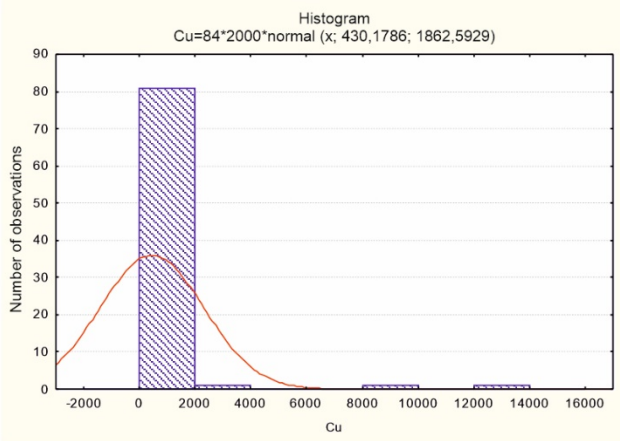

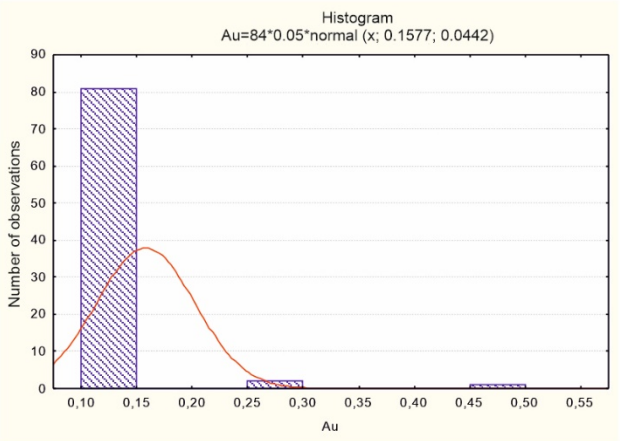

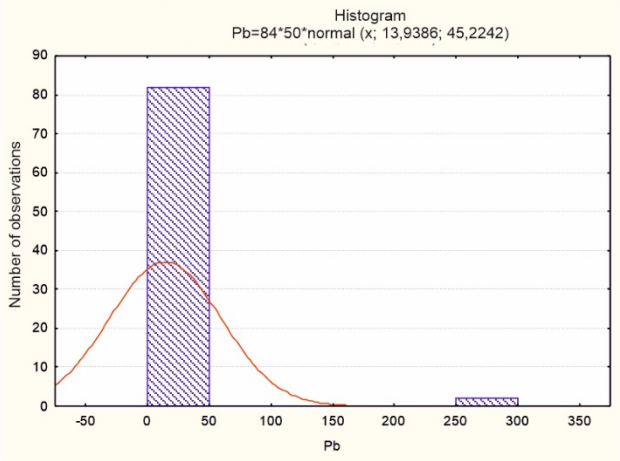

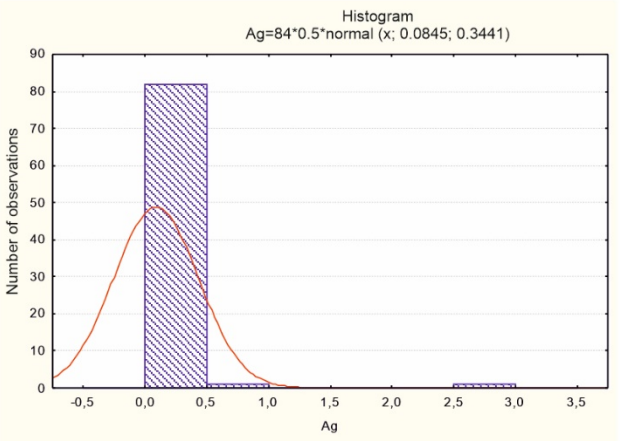

Figure 5. Histograms of the distribution of the contents ofchemical elements in the Tebinbulak ore field.

4 Conclusion

The research results show that in the Sultanuvais mountains, it is possible to expand the mineral resource base of Uzbekistan at the expense of platinum group metals (MPG). The most optimal way to implement these tasks is a detailed study of the areas promising for the MPG.

For a study with the involvement of foreign and domestic investments, 2e areas in the Tebinbulak intrusive massif of the Sultanuvais Mountains are proposed: mineralized zone №Tb-1, mineralized zone №Tb-2 with general forecast resources of platinoids.

References

Akhunjanov R., Zenkova S.O., Karimova F.B. Distinctive features of ultrabasite-basite intrusives of various ore bearing (Western Tien Shan). // Geology and Mineral resources. -2015. - No. 3. – pp.11-26.

Babadzhanov A.A. "Platinum bearing of skarnovo-rare-metal deposits of Western Uzbekistan" (final), - Tashkent, IGiG, 2014

Dalimov T.N., Ganiev I.N. Evolution and types of magmatism of the Western Tien Shan. Tashkent, University, 2010. - 227 p.

Kustarnikova A.A., Usmanov A.I., Babadzhanov A.A., Mansurov M.M., Maripova S.T., Mikhailova Yu.V., Musaev A.M., Smirnova S.K., Turesebekov A.H. – Metallogeny of gold and copper of Uzbekistan. - Institute of Geology and Geophysics named after H.M.Abdullayev. – T., 2012. – 410 p.

Kholikov A.B. Platinum bearing of Sultanuvais mountains // Materials of the International Scientific and Technical Committee / Integration of science and practice as a mechanism for effective development of the geological industry of the Republic of Uzbekistan. - Tashkent, 2014. - pp. 328-331.

Kholikov A.B. Mafit-ultramafic formations of the Western Tien Shan and their platinum bearing // Materials of the International Scientific and Technical Committee / Integration of science and practice as a mechanism for effective development of the geological industry of the Republic of Uzbekistan. - Tashkent, 2022. - pp. 332-337.

Nikitina O.N., Tukhtabayev T.M., etc. "Drawing up a geological map of the Sultanuvais mountains m-a 1:50000 within the sheets to 41-61-B, D; 62-A, B, D; 74-A, B" for 2004-2007. Pos. Eshonguzar, 2007

Artikov T.K., Dementeenko L.I., Nikitina O.N., etc. Geological structure and minerals of the eastern part of the Sultanuvais Mountains. Report on the implementation of GS, GDP1:50000 scale and medium-scale GC of the pre-Mesozoic foundation within the sheets to 41-62- C, D; 74-A, B gor Sultanuvais for 1998-2003. Pos. Eshonguzar, 2003

Insights into genesis of Pt-Fe minerals, laurite and kashinite from clinopyroxenite-dunite massifs: evidence from compositional and Cu-S isotope data

Kreshimir N. Malitch[1], Inna Yu. Badanina[1], Natalia G. Soloshenko[1], Sergey L. Votyakov[1], Tatiana A. Velivetskaya[2], Alexander V. Ignatiev[2]
[1]Institute of Geology and Geochemistry, Ural Branch RAS, Ekaterinburg, Russia
[2]Far East Geological Institute, Far East Branch RAS, Vladivostok, Russia

Abstract. To provide new insights into the origin of platinum-group minerals (PGM), this study presents the mineral chemistry and Cu-isotopic data for primary and secondary Pt-Fe minerals, and in-situ S-isotope data for Ru-Os sulfides and kashinite from chromitites and placer deposits of the Nizhny Tagil and Svetly Bor clinopyroxenite-dunite massifs (Middle Urals) and the Guli clinopyroxenite-dunite massif (Polar Siberia). Collectively the studied samples of primary high-temperature ferroan platinum (Pt_2Fe) and isoferroplatinum (Pt_3Fe) have an overall $\delta^{65}Cu$ range from –0.37 to 0.31‰. Secondary low-temperature PGM represented by the tetraferroplatinum (PtFe) – tulameenite ($PtFe_{0.5}Cu_{0.5}$) solid solutions series have the $\delta^{65}Cu$ values ranging from –1.15 to –0.72‰. The lighter Cu-isotopic composition of secondary Pt-Fe minerals compared to that of primary Pt-Fe minerals ($\delta^{65}Cu$ = –1.01 ± 0.17‰, n = 8 and $\delta^{65}Cu$ = 0.07 ± 0.43‰, n = 14, respectively) is consistent with a secondary nature of isotopic variations, due to evolved composition of the ore-forming fluid during the low-temperature formation of the tetraferroplatinum – tulameenite series. The sulfur isotope results reveal a restricted range of chondritic $\delta^{34}S$ values for laurite (RuS_2) and Rh-bearing kashinite $(Ir,Rh)_2S_3$ ($\delta^{34}S$ = –0.15 ± 0.24‰, n = 4 and $\delta^{34}S$ = –0.23 ± 0.45‰, n = 7, respectively) implying that sulfur derived from a common near-chondritic source.

1 Introduction

A significant number of zoned clinopyroxenite-dunite massifs are located in Russia (the Urals, Eastern Siberia, and the Far East). They are characterized by the presence of dunites, clinopyroxenites and platinum placer deposits. Despite numerous studies of zoned-type ultramafic massifs, the origin of these massifs and of the associated platinum mineralization remains unresolved. Understanding the main events of platinum-metal ore formation is impossible without analyzing the sources and behavior of the main ore-forming components, namely platinum, osmium, sulfur and copper. In contrast to the Re-Os isotope data (Tessalina et al. 2015; Malitch et al. 2020), which previously allowed characterization of distinct sources of platinum-group elements (PGE) and the multi-stage nature of PGE mineralization, the isotopic systematics of platinum, sulfur and copper for platinum-group mienrals (PGM) from this type of geological setting still remains poorly defined. Sulfur isotope data have been restricted to Ru-Os sulfides from the Guli massif (Malitch et al. 2022).

To gain further insights into the genesis of PGM, we have carried out a combined study of primary and secondary Pt-Fe minerals, laurite and kashinite from chromitites and placer deposits of the Nizhny Tagil and Svetly Bor clinopyroxenite-dunite massifs in Middle Urals and the Guli clinopyroxenite-dunite massif in Polar Siberia. We integrate (1) electron microprobe analyses of PGM, (2) in-situ sulfur isotope analyses of laurite and kashinite using a femtosecond laser ablation GC-IRMS at high spatial resolution, and (3) copper isotope analyses using an MC ICP-MS and sample-standard bracketing technique.

2 Geological background and samples

The Nizhny Tagil and Svetly Bor zoned clinopyroxenite-dunite massifs form part of the Platinum Belt of the Urals, which is located along the 60th meridian for more than 900 km. These massifs are famous for platinum deposits; over 330 tonnes of platinum have been mined from associated placer and lode deposits in the past. The most common PGM that occur in bedrocks and placer platinum deposits are Pt-Fe minerals, among which high-temperature ferroan platinum (Pt_2Fe) and isoferroplatinum (Pt_3Fe) dominate over subordinate Os-Ir alloys, Ru-Os sulfides of the laurite–erlichmanite series (RuS_2-OsS_2), Ir-Rh sulfides of the kashinite–bowieite series (Ir_2S_3-Rh_2S_3) and Ir-Rh thioshpinels of the cuproiridsite–cuprorhodsite–ferrorhodsite series ($CuIr_2S4$-$CuRh_2S_4$-$FeRh_2S_4$) (Malitch et al. 2017). Secondary low-temperature PGM assemblages, associated with serpentinization, are represented by the tetraferroplatinum (PtFe) – tulameenite ($PtFe_{0.5}Cu_{0.5}$) – ferronickelplatinum ($PtFe_{0.5}Ni_{0.5}$) solid solutions series and Pt-Cu minerals.

The Guli ultramafic massif, located in the Maimecha-Kotui province Province in northern part of Siberian Craton, is remarkable for its considerable size (about 600 km^2, Malitch and Lopatin 1997). The ultramafic rock assemblage of the Guli massif and its significant potential for placer PGM accumulations make it typical of zoned massifs of the Uralian-Alaskan-Aldan type, whereas the huge size of the ultramafic complex, its shape, the lack of concentrically zoned structure, and the common occurrence of refractory Ir-, Os-, and Ru-rich PGM in chromitite and placer deposits are features more consistent to those of ophiolite massifs (Malitch and Lopatin 1997).

Platinum-group minerals selected for this study were obtained from vein-disseminated chromitite segregations confined to the marginal areas of coarse-grained dunite in the central parts of the Nizhny Tagil (i.e., Krutoy Log and Alexandrovsk Log deposits (Figure 1a, b) and Svetly Bor massifs, and Quaternary deposits of the upper part of the Ingaringda River located within the Guli massif. In total, 19 samples of Pt-Fe minerals from primary (11 samples) and secondary (8 samples) PGM were analyzed (Figure 1c-g). Laurite and kashinite studied are invariably associated with isoferroplatinum of the Svetly Bor massif (Figure 2).

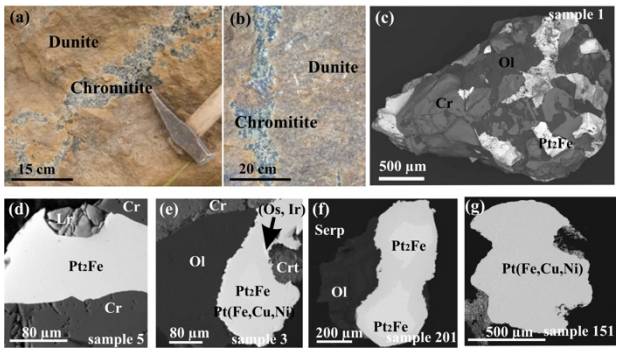

Figure 1. Morphological features of: (**a**, **b**) vein-disseminated chromitites and (**c**) Pt-Fe minerals associated with chromite (Cr) and olivine (Ol) from the Krutoy Log deposit of the Nizhny Tagil massif. Back-scattered images of PGM assemblages from chromitites of the Krutoy Log (**d**, **e**, **g**) and Alexandrovsk Log (**f**) PGE deposits. Pt_2Fe – ferroan platinum, Lr – laurite, (Os, Ir) – iridian osmium, Pt(Fe,Cu,Ni) – minerals of the tetraferroplatinum–tulameenite series, Cr – chromite, Ol – olivine and Serp – serpentine.

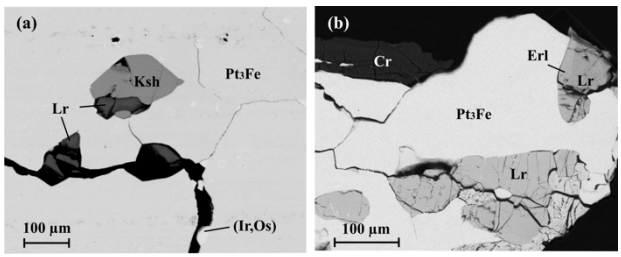

Figure 2. Back-scattered images of PGM assemblages from the Svetly Bor massif. Pt_3Fe – isoferroplatinum, Lr – laurite, Erl – erlichmanite, Ksh – kashinite, (Ir,Os) – osmian iridium, Cr – chromite.

3 Analytical methods

Electron microprobe analyses of PGM were carried out at Common Use Center "Geoanalyst" of the Institute of Geology and Geochemistry, UB RAS, Ekaterinburg, using a CAMECA SX-100 equipped with five WDS spectrometers. Quantitative WDS analyses were performed at 25 kV accelerating voltage and 20 nA sample current, with a beam diameter of ~1 μm. The following X-ray lines and standards have been used: RuLα, RhLα, PdLβ, OsMα, IrLα, PtLα, NiKα (all native element standards); FeKα, CuKα, SKα (all chalcopyrite); AsLα (sperrylite). Corrections were performed for the interferences involving Ru-Rh, Ru-Pd and Ir-Cu.

Eleven S-isotope analyses were subsequently performed at Laboratory of Stable Isotope within Common Use Center of the Far East Geological Institute, Far Eastern Branch of the Russian Academy of Sciences (Vladivostok, Russia). Sample preparation for mass spectrometric isotope analysis of sulfur was carried using a femtosecond laser ablation system NWR Femto in combination with a reactor for sulfide aerosol conversion into SF_6 gas, a cryogenic and chromatographic purification system, and an isotope ratio mass spectrometer (FsLA-GC-IRMS) (Ignatiev et al. 2018; Velivetskaya et al. 2019). Isotope ratio of sulfur were measured using a MAT-253 mass spectrometer (Thermo Fisher Scientific, Germany) equipped with a Faraday cup for simultaneous measurements of the ion currents at m/z 127 ($^{32}SF_5^+$) and 129 ($^{34}SF_5^+$). The measurements were carried out relative to the laboratory working standard, calibrated to the international standards IAEA-S-1, IAEA-S-2 and IAEA-S-3. The sulfur isotope composition in the sample was calculated as $\delta^{34}S=[(^{34}S/^{32}S)_{sample}–(^{34}S/^{32}S)_{std}]/(^{34}S/^{32}S)_{std}*10^3$ and expressed in ‰ with respect to reference standard VCDT (Vienna Canyon Diablo Troilite). Average accuracy of $\delta^{34}S$ analyses was better than 0.2‰ (2σ). Further details of analytical methods are presented elsewhere (Ignatiev et al. 2018).

The method for determining $\delta^{65}Cu$ included the selective chromatographic separation of Cu from a solution of the studied Pt-Fe mineral sample, followed by determination of the $^{65}Cu/^{63}Cu$ isotope ratio using a Neptune Plus multiple-collector inductively coupled plasma mass-spectrometer (Thermo Fisher). A detailed description of the technique is presented by Okuneva et al (2022); digestion and chromatographic separation were carried out in a clean room unit (class 1000, ISO 6) and laminar flow cabinets (class 100, ISO 5). The decomposition stage of Pt-Fe minerals (0.00n mg) included their dissolution in concentrated nitric acid. For chromatographic isolation of pure Cu fraction, AG MP-1 ion-exchange resin (Bio-Rad inc., USA) was used (Maréchal and Albarède 2002); the analyte isolation scheme was detailed in Okuneva et al (2022). The $^{65}Cu/^{63}Cu$ isotope ratios in the analytical copper fraction were measured by sample-standard bracketing technique using a Neptune Plus mass-spectrometer. Measurement sequence was as follows: blank experiment (3% HNO_3 solution) → NIST SRM 976 Cu standard → the studied PGM sample (3% nitric acid solution of the mineral) → NIST SRM 976 Cu standard. Each single measurement of the Cu-isotopic composition consisted of 60 cycles collected at 8-second integrations followed by a baseline measurement for 30 seconds. The copper isotope composition of the sample was calculated as $\delta^{65}Cu=[(^{65}Cu/^{63}Cu)_{sample}/(^{65}Cu/^{63}Cu)_{std} – 1)]\times1000$; the measurement accuracy was ±0.14‰ (2σ).

4 Compositional features of PGM

The majority of the PGM from chromitites and placer deposits of the Nizhny Tagil and Svetly Bor massifs are represented by high temperature ferroan platinum and isoferroplatinum that have compositions close to Pt_2Fe and Pt_3Fe, respectively (where Pt equals to the sum of PGE, at %, Fe is Σ Fe, Cu, Ni, at %). These Pt-Fe minerals are commonly replaced by intermediate members of the tetraferroplatinum (PtFe)–tulameenite ($PtFe_{0.5}Cu_{0.5}$) series and tulameenite ($PtFe_{0.5}Cu_{0.5}$) (Figure 3). Chemically, ferroan platinum and isoferroplatinum carry notable trace concentrations of Ir (up to 4.6 wt. %), besides smaller quantities of Cu (0.4–1.4 wt.%), Ni (0.3–0.4 wt.%), Rh (0.8–1.1 wt.%) and Os (0.3–0.4 wt.%). Copper content in minerals of the tetraferroplatinum (PtFe)–tulameenite ($PtFe_{0.5}Cu_{0.5}$) solid solution series varies within 6.8–11.3 wt.%, reaching 12.3 wt.% in tulameenite. The Pt-Fe minerals from the Nizhny Tagil and Svetly Bor massifs host various inclusions: Ru-Os sulfides of the laurite–erlichmanite series (Figures 1d, 2, 4a, 4b), Ir-Rh sulfides of the kashinite (Ir_2S_3)–bowieite (Rh_2S_3) series (Figures 2a, 4c), Ir-Rh-Pt thiospinels of the cuproiridsite ($CuIr_2S_4$) –cuprorhodsite ($CuRh_2S_4$) – malanite ($CuPt_2S_4$) series (Figure 4d), and Os-Ir(-Ru) alloys (Figures 1e, 2a). Compositional features of Pt-Fe minerals from the Guli massif, including a similar set of PGM inclusions, were characterized in detail by Malitch and Thalhammer (2002).

A common occurrence of inclusions of laurite, kashinite, iridian osmium and osmian iridium in Pt-Fe minerals and the equilibrium phase relations of Os-Ir alloys, deduced from the binary system Os–Ir (Massalski 1993), are indicative of their high-temperature origin. The presence of reaction rims composed of minerals of the tetraferroplatinum (PtFe) – tulameenite ($PtFe_{0.5}Cu_{0.5}$) series, which replace high-temperature ferroan platinum and isoferroplatinum, is indicative of their secondary origin. Most researchers associate the formation of this low-temperature PGM assemblage with serpentinization of ultramafic rocks (Betekhtin 1991).

5 Copper and sulfur isotope data

5.1 Copper isotopic compositions

All the samples of primary Pt-Fe minerals have $\delta^{65}Cu$ values ranging from –0.37 to 0.31‰ (Figure 5). They have a mean $\delta^{65}Cu$ value of 0.07‰, and a standard deviation of 0.43‰ (n=14). We note the pronounced similarity in $\delta^{65}Cu$ values for samples of isoferroplatinum from the Svetly Bor massif, ferroan platinum from the Nizhny Tagil massif, which are close to those for samples of ferroan platinum from the Guli massif (Figure 5). Minerals of the tetraferroplatinum (PtFe) – tulameenite ($PtFe_{0.5}Cu_{0.5}$) solid solution series are characterized by lighter Cu-isotopic compositions ($\delta^{65}Cu$ values range from –1.15 to –0.72‰; Figure 5), with a mean value of –1.01‰ and a standard deviation of 0.17‰ (n=8).

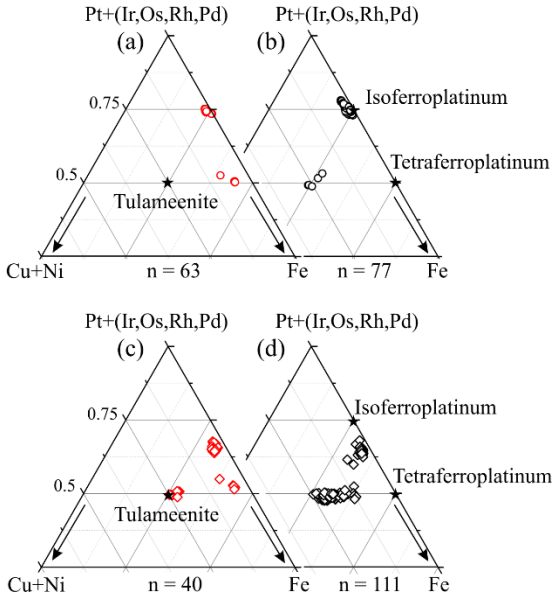

Figure 3. Chemical composition of Pt-Fe minerals from placers (**a**) and chromitites (**b**) of the Svetly Bor massif, placers (**c**) and chromitites (**d**) of the Nizhny Tagil massif in the ternary diagram Pt + (Ir, Os, Rh, Pd) – Cu+Ni – Fe, at.%. Asterisks indicate minerals of the Pt-Fe system.

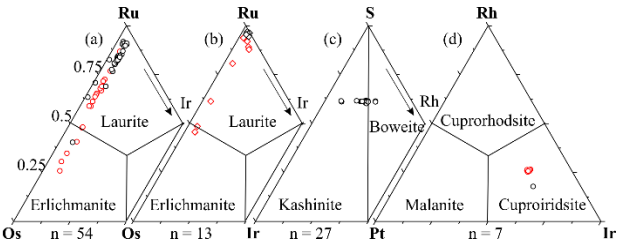

Figure 4. Chemical compositions (at. %) of Ru-Os sulfides in coordinates Ru–Os–Ir (**a**, **b**), Ir-Rh sulfides in coordinates S–Ir–Rh (**c**), and Ir-Rh-Pt thiospinels in coordinates Rh–Pt–Ir (**d**) from placer deposits (open circles in red) and chromitites (open circles in black) from the Svetly Bor, placer deposits (open diamonds in red) and chromitites (open diamonds in black) from the Nizhny Tagil massifs.

It has been shown (Graham et al. 2004) that redox reactions play an important role in the fractionation of Cu isotopes at low temperatures. For example, variations in the Cu-isotopic composition in primary and secondary Cu-bearing minerals may be due to fractionation between different complex species in solution (Maréchal and Albarède 2002) or associated with the influence of isotopically different fluids during hydrothermal processes (Graham et al. 2004). In this context, the lighter Cu-isotopic composition in secondary Cu-bearing PGM compared to that in ferroan platinum ($\delta^{65}Cu$ = –1.01 ± 0.17‰, n = 8 and $\delta^{65}Cu$ = 0.07 ± 0.43‰, n = 14, respectively) is consistent with the secondary nature of isotopic variations, likely due to evolved composition of the ore-forming fluid during the low-temperature formation of the tetraferroplatinum (PtFe) – tulameenite ($PtFe_{0.5}Cu_{0.5}$) solid solution series.

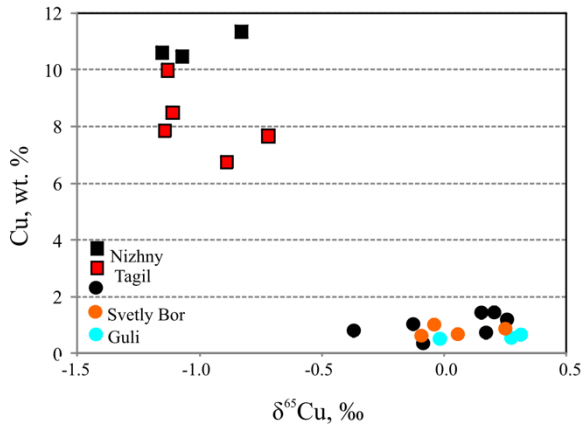

Figure 5. Copper isotope data for Pt-Fe minerals from the Krutoy Log and Alexandrovsky Log deposits of the Nizhny Tagil massif (symbols in black and red color, respectively), Svetly Bor and Guli massifs. Ferroan platinum (black and blue circles), isoferroplatinum (orange circles), minerals of the tetraferroplatinum–tulameenite solid solution series (squares).

5.2 Sulfur isotopic compositions

The $\delta^{34}S$ values in laurite and Rh-bearing kashinite forming part of polymineralic assemblage with isoferroplatinum show a relatively narrow range from –0.8 to 0.4‰. Laurite (Ru#=85-91) have $\delta^{34}S$ values of –0.4–0.00‰ (Figure 6), with a mean of –0.15‰ and a standard deviation of 0.24‰ (n=4), which are similar to Rh-bearing kashinite with $\delta^{34}S$ values ranging from –0.8 to 0.4‰ (a mean value of 0.23‰ and a standard deviation of 0.45‰, n=7). The sulfur isotope signatures of the studied PGM are similar to those of Ru-Os sulfides from the Guli massif (Figure 6). They are indicative of a subchondritic source of sulfur. The deep source of sulfur is consistent with the osmium isotope data obtained for Ru-Os sulfides and Os-Ir alloys from the Nizhny Tagil and Guli massifs (Malitch et al. 2011; Tessalina et al. 2015), implying that HSE and S derived from a near-chondritic source.

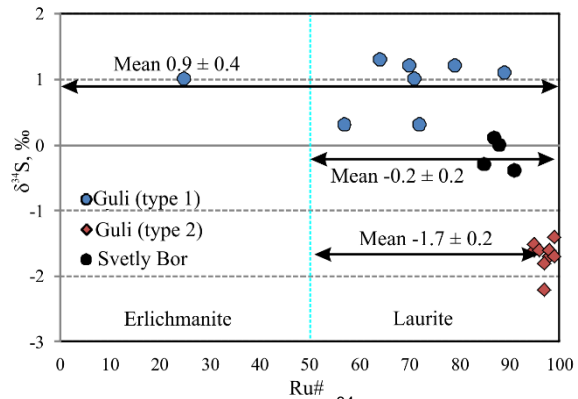

Figure 6. Sulfur isotope data ($\delta^{34}S$, ‰) for Ru-Os sulfides from the Svetly Bor (this study) and Guli (Malitch et al. 2022) massifs.

Acknowledgements

The authors are grateful to T.G. Okuneva, S.V. Karpova and A.R. Sidoruk for valuable analytical assistance, and to Dr. W.D. Smith for useful suggestions and editorial input. This study was financed by the Russian Science Foundation (https://rscf.ru/en/project/22-27-00140/).

References

Betekhtin AG (1935) Platinum and other platinum-group minerals. USSR Academy of Sciences, Moscow, 148 p. [in Russian].

Graham S, Pearson N, Jackson S, Griffin W, O'Reilly SY (2004) Tracing Cu and Fe from source to porphyry: in situ determination of Cu and Fe isotope ratios in sulfides from the Grasberg Cu-Au deposit. Chemical Geology 207: 147–169.

Ignatiev AV, Velivetskaya TA, Budnitskiy SY, Yakovenko VV, Vysotskiy SV, Levitskii VI (2018) Precision analysis of multisulfur isotopes in sulfides by femtosecond laser ablation GC-IRMS at high spatial resolution. Chemical Geology 493: 316–326.

Malitch KN, Lopatin GG (1997) New data on the metallogeny of the unique Guli clinopyroxenite-dunite massif, northern Siberia, Russia. Geology of Ore Deposits 39: 209–218.

Malitch KN, Thalhammer OAR (2002) Pt-Fe nuggets derived from clinopyroxenite-dunite massifs, Russia: a structural, compositional and osmium-isotope study. Can. Mineral. 40: 395–418.

Malitch KN, Efimov AA, Badanina IYu (2011) Contrasting platinum-group mineral from chromitites of the Nizhny Tagil and Guli massifs (Russia): implications for composition, sources and age. Doklady Earth Sciences 441: 1514–1518.

Malitch KN, Stepanov SYu, Badanina IYu, Khiller VV (2017) Bedrock platinum-group element mineralization of zonal clinopyroxenite-dunite massifs of the Middle Urals. Doklady Earth Sciences 476: 1147–1151.

Malitch KN, Puchtel IS, Belousova EA, Badanina IYu (2020) Contrasting platinum-group mineral assemblages of the Kondyor massif (Russia): Implications for the sources of HSE in zoned-type ultramafic massifs. Lithos 376–377: 105800. https://doi.org/10.1016/j.lithos.2020.105800

Malitch KN, Kogarko LN, Badanina IYu, Velivetskaya TA, Ignatiev A.V. (2022) Sulfur isotope composition of Ru-Os sulfides from the Guli massif, Maimecha-Kotui province, Russia: first results. Doklady Earth Sciences 507: 1012–1018. https://doi.org/10.1134/S1028334X22600955

Maréchal C, Albarède F. (2002) Ion-exchange fractionation of copper and zinc isotopes. Geochimica et Cosmochimica Acta 66: 1499–1509.

Massalski TB (1993) (ed) Binary alloy phase diagrams. Amer Soc Metals, Metals Park, Ohio, 2224 pp.

Okuneva TG, Karpova SV, Streletskaya MV, Soloshenko NG, Kiseleva DV (2022) The method for Cu and Zn isotope ratio determination by MC ICP-MS using the AG MP-1 resin. Geodynamics & Tectonophysics 13: 2s. https://doi.org/10.5800/GT-2022-13-2s-0615

Tessalina SG, Malitch KN, Augé T, Puchkov VN, Belousova E, McInnes BIA (2015) Origin of the Nizhny Tagil clinopyroxenite-dunite massif (Uralian Platinum Belt, Russia): insights from PGE and Os isotope systematics. J. Petrol. 56: 2297–2318.

The Ni-Cu-Co mineralisation of the Espedalen Complex, southern Norway: constraints for the distribution of magmatic sulphides within an anorthosite intrusion

Eduardo Mansur[1], Trond Slagstad[1], Jan Sverre Sandstad[1], Sarah Dare[2]
[1]Geological Survey of Norway, PO Box 6315 Torgarden, Trondheim, 7491, Norway
[2]Département de Sciences Appliquées, Université du Québec à Chicoutimi, QC G7H 2B1, Canada

Abstract. The Espedalen Complex, south-central Norway, comprises three main suites (jotunite, charnockite and augengneiss; main anorthosite–ultramafic–norite; and gabbronorite suites) formed between 1520 and 1510 Ma. Several Ni-Cu-Co sulphide occurrences are hosted within the anorthosite-ultramafic-norite suite. Most of the Ni-Cu-Co sulphide occurrences are hosted within anorthosites and norites but spatial association with ultramafic rocks is common. In some cases, the mineralization occurs as predominantly undeformed disseminated sulphides, interstitial to cumulus silicates (olivine, orthopyroxene and plagioclase), whereas in other cases, net-textured and massive sulphide lenses (few-meters thick) are constrained to shear zones. The sulphide assemblage consists mainly of pyrrhotite, followed by pentlandite and chalcopyrite. Primary sulphide assemblages yield Ni and Cu tenors from 4 to 9% and 2 to 4%, respectively. The platinum-group element (PGE) contents are low in the Espedalen Complex, with tenors mostly below 0.5 ppm. Sulphide ore composition can be modelled by variable R-factor (mass ratio of silicate to sulphide liquids) regimes of around 500-1000, and slightly different parental magmas. The Espedalen Complex represents a fertile area with potential for the discovery of new Ni-Cu-Co mineralisation with relatively high Ni and Cu tenors, but low PGE.

1 Introduction and Geological Setting

The Espedalen Complex occurs in the eastern portion of the Jotun–Valdres Nappe Complex, southern Norway (Fig. 1A). It comprises three main suites (jotunite, charnockite and augengneiss; main anorthosite–ultramafic–norite; and gabbronorite suites) that formed between 1520 and 1510 Ma. The complex hosts significant Ni-Cu-Co mineralisation associated with the anorthosite-ultramafic-norite suite, but these have not been systematically investigated. More than 15 mineralised sites were discovered during old mining activities and recent exploration. The largest sites comprise the Dalen and Stormyra deposits, which host 5.3 Mt @ 0.29% Ni, 0.12% Cu and 0.02% Co, and 1.01 Mt @ 1.09% Ni, 0.48% Cu and 0.04%, respectively. This study provides the first systematic characterization of the different Ni-Cu-Co mineralisation from the Espedalen Complex. We combine field work with whole rock and sulphide geochemistry from different mineralisation sites. Our dataset also includes samples and assay results from 165 drill cores.

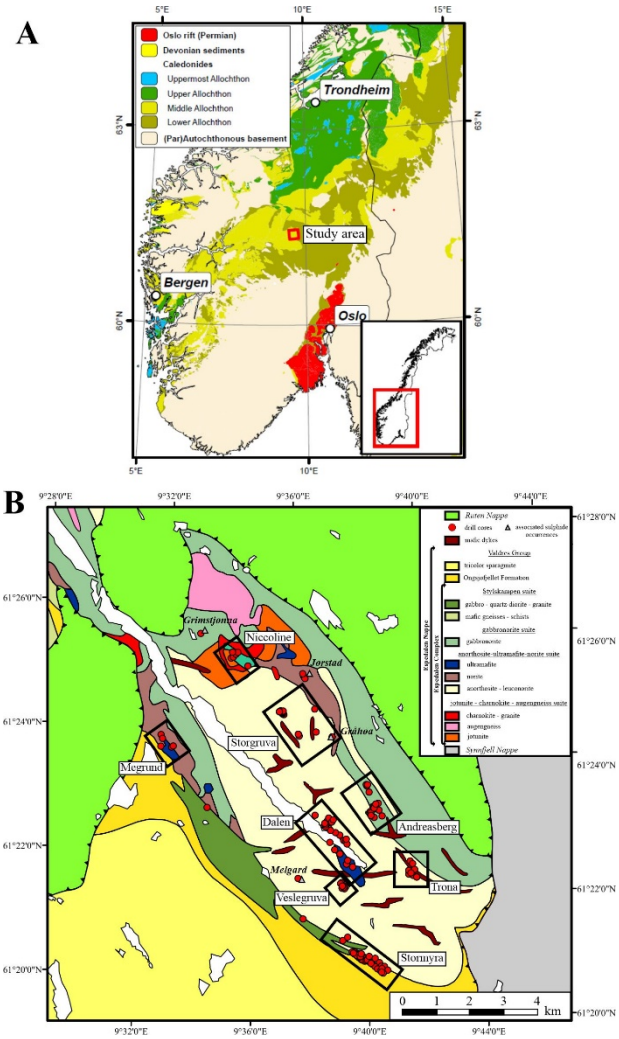

Figure 1. A – Simplified tectonic map of central-south Norway showing the main lithotectonic units. B - Geological map of the surrounding region of the Espedalen Complex and drill hole locations, with highlighted areas (black boxes) for the main magmatic Ni-Cu-Co sulphide occurrences and minor associated occurrences. The map is partially modified from Corfu and Heim (2014).

2 Ni-Cu-Co sulphide mineralisation

Most of the Ni-Cu-Co sulphide mineralisation in the Espedalen Complex is hosted by rocks of the anorthosite-ultramafic-norite suite (Fig. 1B). These areas are commonly marked by old mining excavations, which can vary from pits, only a few metres deep, to excavations that extend to hundreds of metres. However, important resources

that do not crop out were recently discovered by drilling (e.g., Stormyra), and thus, no previous mining activity is observed in these regions. In the areas where previous activity allows for better-exposed ore, the sulphide mineralisation normally defines 50 cm to 2 m-wide zones with variable sulphide contents depending on the location (Fig. 2A). These are commonly deformed and hosted within shear zones, suggesting the displacement and eventual fragmentation of original sulphide bodies (Fig. 2B). In these cases, the host rocks, which vary from anorthosite to melanorite, also display variable degrees of deformation (Fig. 2C). Although Ni-Cu-Co mineralisation is typically hosted by anorthositic to noritic rocks, several occurrences also display a close spatial relation to, or are hosted within, ultramafic cumulates. These medium-grained olivine-orthopyroxenites have preserved their cumulus texture which is commonly poikilitic defined by subrounded olivine crystals enclosed within orthopyroxene oikocrysts (Fig. 2D).

Some of the sulphide occurrences from the Espedalen Complex are associated with shear zones that seem to dislocate the ore bodies from their initial portion within the intrusion. The mineralisation varies from disseminated (Fig. 2D), net-textured (Fig. 2E) and massive sulphides (Fig. 2F). In addition, several zones with locally remobilised sulphides are observed at most occurrences, which are not limited to those hosted within shear zones but also found in less deformed ore bodies. These zones vary from a few metres to several centimetres in scale and consist of deformed rocks with thin sulphide veinlets (Fig. 2G). The secondary mineralogy of the host rocks allows some assessment of the protolith, with ultramafic protoliths normally yielding a chlorite and talc-dominated schist, whereas noritic protoliths yield chlorite, epidote and plagioclase assemblages. We use the terms ‘primary sulphides’ and ‘remobilised sulphides’ to distinguish sulphide occurrences with predominantly magmatic textures, from these thin sulphide veinlets indicating local remobilization, respectively. However, the term ‘remobilised sulphides’ does not refer to the major scale dislocation and/or disruption of some of the sulphide ore bodies within shear zones.

3 Sulphide petrography

The petrographic characteristics of primary and remobilised sulphide ores from the various localities are comparable to each other and thus, these are not individually described to avoid repetition. In disseminated ores, the sulphide assemblage consists mainly of pyrrhotite, followed by pentlandite and minor chalcopyrite, and is interstitial to silicates (Fig. 3A). The presence of magnetite is common and normally occurs as anhedral grains included within pyrrhotite and pentlandite, but small sulphide inclusions in magnetite are also observed. The semi-massive to massive sulphide ores from different localities are also dominated by pyrrhotite and pentlandite with only minor chalcopyrite.

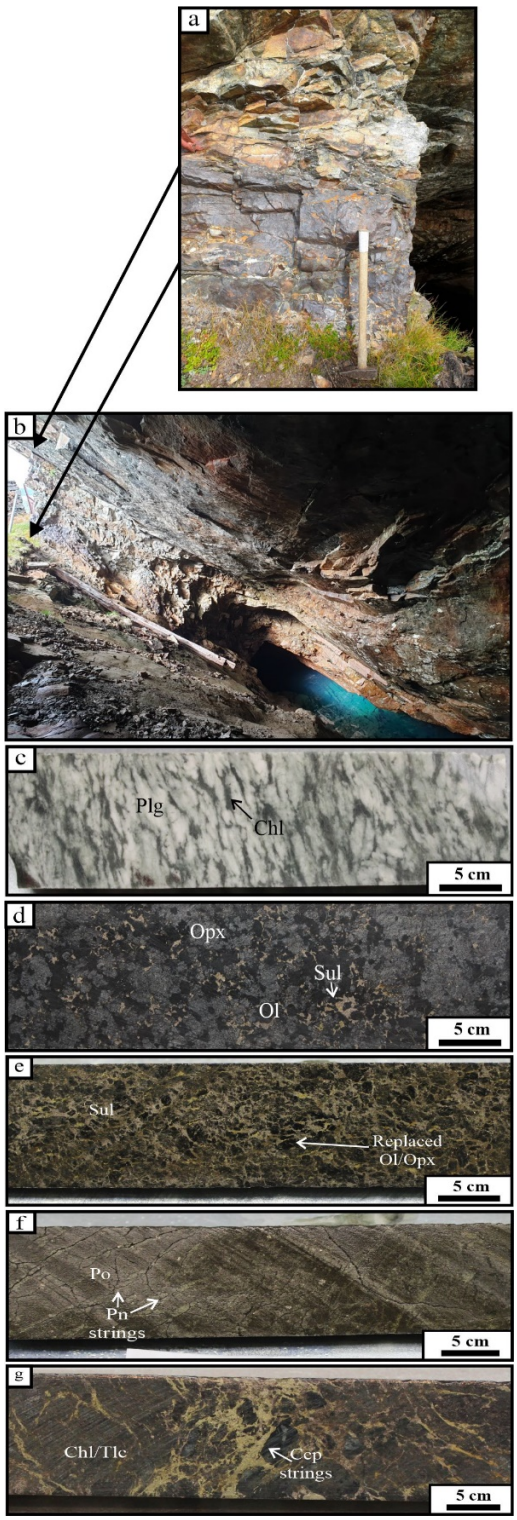

Figure 2. A – Oxidation in outcropping sulphide occurrences partially extracted by previous mining activities. B - Semi-massive sulphide body shown in (A) hosted within a shear zone. C - Deformed anorthosite to leuconorite with strong foliation. D- Medium-grained olivine-orthopyroxenite with poikilitic texture and interstitial sulphides. E - Net-texture sulphide with angular fragments of altered olivine and orthopyroxene. F - Massive sulphide with abundant pyrrhotite and the occurrence of pentlandite strings. G - Chalcopyrite stringers within chlorite-talc schist which represent a transformed ultramafic protolith. Abbreviations: Ccp – chalcopyrite; Chl – chlorite; Ol –

olivine; Opx – orthopyroxene; Plg – plagioclase; Pn – pentlandite; Po – pyrrhotite; Sul – sulphides; Tlc – talc.

Pentlandite normally displays granular texture of individual grains included within pyrrhotite, but in some cases also defines an intergrown mass with pyrrhotite (Fig. 3B).

Secondary alteration and recrystallisation are not ubiquitous features in most primary sulphide occurrences from the Espedalen Complex but are important factors at the Stormyra deposit. Different from other localities, the sulphide assemblage from the Stormyra deposit is marked by variable, but commonly abundant (more than 20%) pyrite. The pyrite grains are predominantly observed in semi-massive and massive ores where they are mostly included within pyrrhotite-dominated masses, but occurrence within chalcopyrite-dominated and even pentlandite-rich portions is also observed. The pyrite grains are mostly subrounded and seem to have grown from the pyrrhotite-pentlandite-chalcopyrite assemblage during post-magmatic alteration (Fig. 3C). Finally, the remobilised sulphide assemblages are dominated by chalcopyrite, mostly associated with secondary silicates (e.g., chlorite and talc), and display ductile structures. The occurrence of anhedral pyrite grains, and less commonly magnetite, within the chalcopyrite in remobilised sulphides domains is recurrent.

4 Sulphide geochemistry

The samples from the different Ni-Cu-Co sulphide mineralisation display very variable sulphide proportions, which result in a wide range of S values ranging from 0.1 to 35 wt.%. The range comprises variations from disseminated, net-textured and massive sulphide ores, respectively, but the values display a continuous trend, suggesting a gradual change in sulphide contents. There is a positive correlation between S and Ni (Fig. 4A), Cu (Fig. 4B) and Co (Fig. 4C) in both primary and remobilised sulphides. However, for all these elements, the concentrations are higher in the former relative to the latter at a given S concentration. For instance, Ni, Cu and Co concentrations in primary sulphides broadly range from 0.05 to 8 wt. %, <0.01 to 4 wt. % and <100 to 3000 ppm, respectively, but from <0.01 to 2 wt. %, <0.01 to 1 wt. % and <100 to 2000 ppm in remobilised sulphides, respectively.

There is also a broad correlation between S and PGE in primary sulphides, which supports their control dominantly by the presence of sulphide minerals (illustrated by Pd in Fig. 4D). However, the concentrations of all PGE are very low and close to detection limits (e.g. horizontal alignments in the plots from 4D), which introduces much scattering in the exploration geochemistry dataset. We have calculated the metal tenors (i.e., concentration of metals in 100% sulphides) for primary and remobilised sulphides from different localities (following Barnes et al., 2011). A distinct feature of the mineralisation in the area is that Ni (Fig. 4E) and Cu (Fig. 4F) tenors from primary sulphides are greater than those from remobilised sulphides.

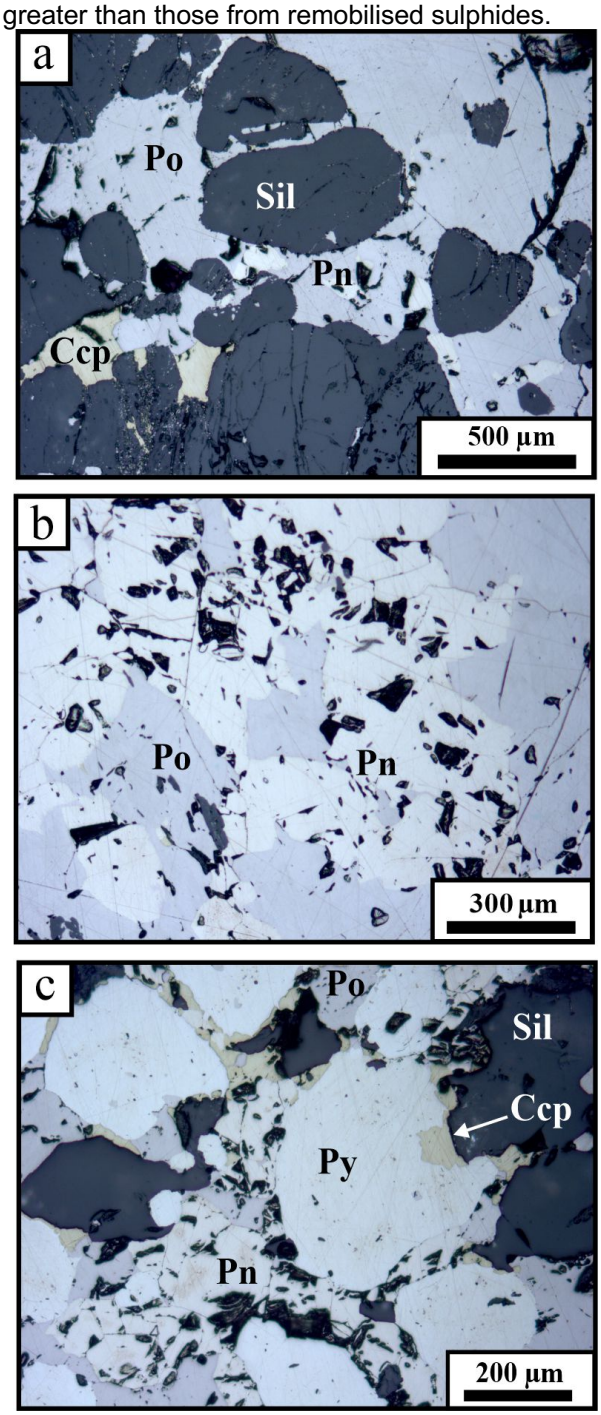

Figure 3. A – Disseminated sulphides comprising pyrrhotite, pentlandite and minor chalcopyrite, interstitial to olivine and orthopyroxene. B - Abundant granular pentlandite enclosed within pyrrhotite. C - Anhedral pyrite crystals enclosed within pyrrhotite and minor pentlandite and chalcopyrite masses. Abbreviations: Ccp – chalcopyrite; Pn – pentlandite; Po – pyrrhotite; Py – pyrite; Sil – silicates.

Moreover, primary sulphides from Stormyra and other minor occurrences display greater tenors relative to the primary sulphides from other locations. For instance, median Ni and Cu tenors vary from 7 to 8.5% and 3 to 3.5% in primary sulphides from Stormyra, Andreasberg and Megrund, followed by 4 to 5.5% and 1.6 to 3% in primary sulphides from other localities, and from 0.3

to 2% and 0.25 to 1.5% in remobilised sulphides, respectively (Fig. 4E and 4F).

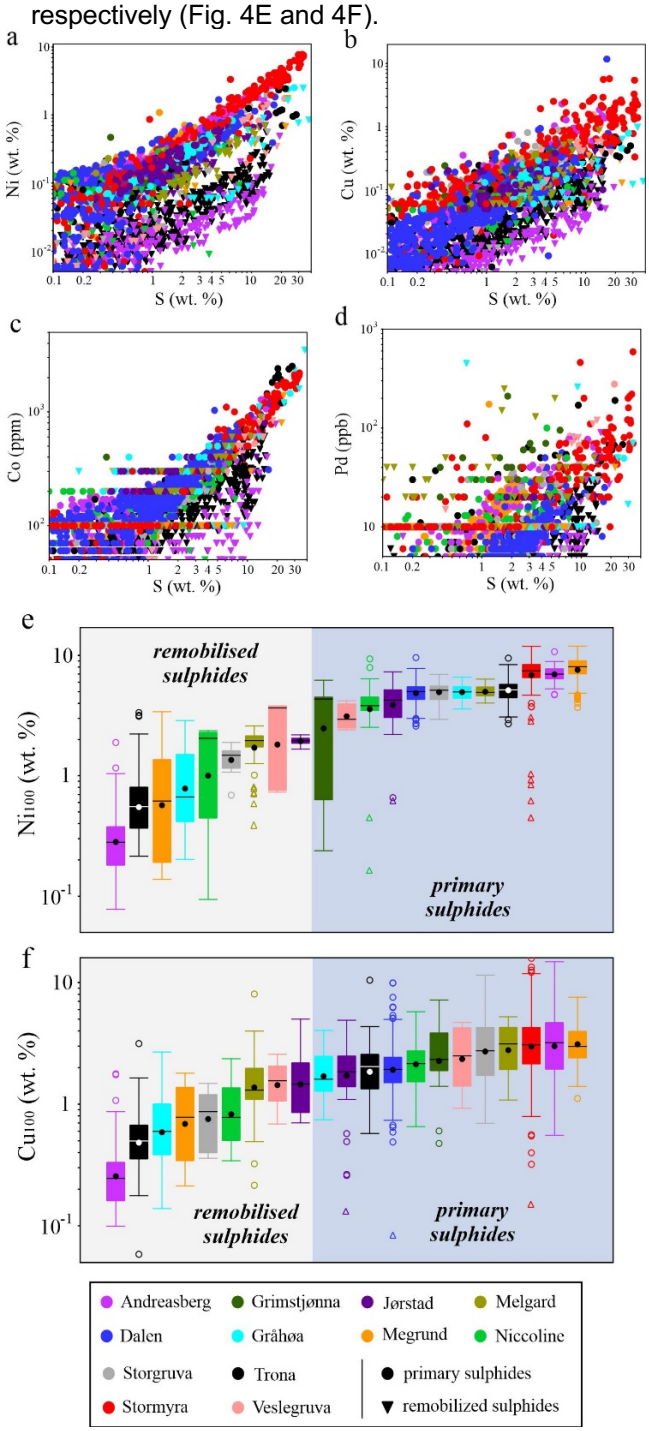

Figure 4. Binary plots of (a) Ni, (b) Cu, (c) Co and (d) Pd, versus S and box and whisker diagrams of (e) Ni and (f) Cu tenors in primary and remobilised sulphides.

5 Interpretations and conclusions

The variations in metal tenors are interpreted to reflect a combination of slightly different, but invariably PGE-depleted, parental magmas and variable R-factor regimes (R-factor varying from 300 to 700; Campbell and Naldrett, 1979) during ore formation (e.g. Lightfoot et al., 2012). The PGE-depleted parental magmas that formed the different sulphide mineralisation of the Espedalen Complex can be modelled as the product of 15% mantle melting (Barnes and Lightfoot, 2005) followed by approximately 2% crystallisation with sulphide removal under cotectic proportions. Moreover, redistribution of magmatic sulphides during post-magmatic deformation and alteration of the Espedalen Complex seems to have taken place at major and local scales. Large-scale displacement has no major geochemical impact, whereas local remobilisation, associated with centimetre-scale local shear zones, formed sulphide veinlets with lower metal tenors (Holwell et al., 2017; Mansur et al., 2021). Overall, the Espedalen Complex, and eventual extensions, offers large potential for further discoveries of magmatic sulphide deposits. We suggest that properly assessing if other geological domains, previously assigned to the Jotun Nappe, are correlated or not with the Espedalen Complex is essential for further expanding this prospective area. If correlated to the Espedalen Complex, these terrains could represent potential targets for Ni-Cu-Co deposits, but not for PGE deposits.

Acknowledgements

Part of the analyses for this study were performed in the Norwegian Laboratory for Mineral and Materials Characterisation (MiMaC) NGU node, supported by the Research Council of Norway project number 269842/F50.

References

Barnes S-J, Lightfoot PC (2005) Formation of magmatic nickel sulfide ore deposits and processes affecting their copper and platinum group element contents. Econ Geol 100th Anniversary: 179–213

Barnes SJ, Osborne GA, Cook D, Barnes L, Maier WD, Godel B (2011) The Santa Rita nickel sulfide deposit in the Fazenda Mirabela intrusion, Bahia, Brazil: geology, sulfide geochemistry, and genesis. Econ Geol 106(7):1083–1110

Campbell IH, Naldrett AJ (1979) The influence of silicate: sulfide ratios on the geochemistry of magmatic sulfides. Econ Geol 74(6):1503– 1506

Corfu F, Heim M (2014) Geology and U–Pb geochronology of the Espedalen Complex, southern Norway, and its position in the Caledonian nappe systems. Geol Soc Lond, Spec Publ 390(1): 223-239

Holwell DA, Adeyemi Z, Ward LA, Smith DJ, Graham SD, McDonald I, Smith, JW (2017) Low temperature alteration of magmatic Ni-Cu-PGE sulfides as a source for hydrothermal Ni and PGE ores: A quantitative approach using automated mineralogy. Ore Geol Rev 91: 718-740

Lightfoot PC, Keays RR, Evans-Lamswood D, Wheeler R (2012) S saturation history of Nain Plutonic Suite mafic intrusions: origin of the Voisey's Bay Ni–Cu–Co sulfide deposit, Labrador, Canada. Mineral Deposita 47: 23-50

Mansur E, Barnes SJ, Ferreira Filho CF (2021) The effects of post-cumulus alteration on the distribution of chalcophile elements in magmatic sulfide deposits and implications for the formation of low-S-high-PGE zones: The Luanga deposit, Carajas mineral province, Brazil. Can Mineral 59(6): 1453-1484

Ni-Cu sulphide deposits in Sweden – general characteristics, genetic aspects and economic potential

Olof Martinsson
Luleå University of Technology, Sweden

Abstract. Several different types of Ni-Cu sulphide deposits have been discovered in Sweden during the last 150 years of exploration and several of them have also been mined in small scale. These deposits share most characteristics with typical magmatic Ni-Cu deposits worldwide but could be divided into at least five different types based on character of host rock and origin of mineralization. Those are deposits related to peridotite sills, mafic dykes, mafic plutons, layered mafic intrusions and serpentinites. In general, the metal composition is related to magma composition with those hosted by ultramafic rocks being more Ni-dominated. Most of the deposits are formed in an arc setting but those related to ultramafic rocks might have formed during events of extension. The economic potential of the known nickel deposits is restricted as most deposits are small in size and/or low grade. However, as several of these deposits are suggested to be part of larger magmatic systems further research and exploration could maybe result in more significant discoveries.

1 Introduction

Sweden is an important mining district in EU with production of mainly Fe, Zn, Cu, Pb, Au, and Ag. Although nickel was discovered from the Co-mine at Los in Sweden 1751 only very limited mining of nickel has occurred. Small scale mining occurred mainly in the 19th century in south Sweden with Kleva as the most important example. In mid 1900s the Lainejaure mine produced 0.1 Mt of ore with 2% Ni and 1% Cu (Grip 1961). Extensive exploration for nickel was done during the later part of the 1900s by Boliden, Swedish Geological Survey, and Swedish Geological AB. This resulted in the discovery of several deposits in the “Nickelbelt” in the eastern part of the Västerbotten County but also in some other areas.

The Ni-deposits are related to ultramafic and mafic intrusive rocks but with slightly different character depending on type of host rock and local geological environment. This paper will give the general characteristics of Ni-deposits occurring in different geological settings and with implications for genetic aspect of mineralization and exploration.

2 Geological setting

The Precambrian part of Sweden belongs to the Baltic shield formed during several orogenic events spanning from 3.0 to 0.9 Ga and including rifting, subduction and collision episodes. To an Archean nucleus several geological sub-provinces has been added and include the 2.5-1.95 Ga Karelian, 1.95-1.86 Svecofennian, 1.86-1.65 Ga Trans-scandinavian Igneous Belt (TIB) and 1.66-0.93 Ga Sveconorwegian provinces. To the west these provinces are bordered by the 0.6-0.4 Ga Caledonides and in the southeast by Fanerozoic sediments.

2.1 Norrbotten province (2.8-1.87 Ga)

The northernmost part of Sweden includes Archean, Karelian and Svecofennian bedrock. The Archean bedrock is dominated by orthogneisses and highly metamorphosed supracrustal units while the Karelian units are dominated by rift-related greenstones. The Svecofennian units are represented by mafic to felsic volcanic rocks formed in shallow marine to terrestrial environment and with interbedded epiclastic sediments. Mafic intrusions are common and may have a layered character with ultramafic cumulates in the lower part. Ultramafic intrusions are rare and mostly small in size. Intrusions hosting Ni mineralization are mainly found in areas dominated by marine sedimentary rocks that often contain Fe-sulphides.

2.1 Västerbotten province (1.90-1.87 Ga)

Northern Västerbotten includes the Skellefte district with important Volcanogenic massive sulphide deposits hosted by submarine volcanic rocks. Those are overlaid and to the south bordered by submarine epiclastic sediments varying from graywacke to shale containing graphite and Fe-sulphides. Small ultramafic (peridotite) intrusions are common in eastern part of Västerbotten whereas mafic intrusions are mostly rare. Several intrusions of both mafic and ultramafic composition contain Ni-mineralization.

2.2 Bothnian Basin province (1.95-1.88 Ga)

The region between Skellefte district and Bergslagen is dominated by epiclastic rocks consisting mainly of graywacke and shale but with locally minor intercalation of volcanic rocks. Mafic intrusions occur locally and may have a layered character. A few of them has low grade Ni-mineralization.

2.3 Bergslagen province (1.90-1.88 Ga)

Bergslagen is the oldest mining district in Sweden with several different types of deposits. The region is dominated by felsic volcanic rocks with epiclastic sedimentary rocks mainly found at the base and the top. Carbonate rocks are common in the upper part of the volcanic sequence. Mafic intrusions occur in several places and have locally a layered character.

Intrusions of ultramafic composition are rare. Ni-mineralization has been discovered in several of the mafic intrusions with small scale mining in some of them.

2.4 TIB province (1.85-1.65 Ga)

TIB is an extensive north-south extending belt of mainly granitoids but locally containing also gabbroic rocks. In a few areas there are preserved associated volcanic rocks of low metamorphic grade and mainly felsic composition. Metasedimentary rocks are mostly rare and of epiclastic origin.

2.5 Sveconorwegian province (1.66-0.93 Ga)

The Sveconorwegian sub-province was formed during several tectonic events including subduction, rifting and collision and is divided in the Gothnian orogeny and the Grenvillian orogeny. Supracrustal rocks are variously metamorphosed and deformed and includes epiclastic sediment and mafic to felsic volcanic rocks. Plutonic rocks are mainly felsic in composition and mafic intrusions are rare.

2.6 Caledonian province (0.6-0.4 Ga)

The Caledonides are the product of a complete Wilson cycle and comprises tectonic units represented different evolutionary steps that are stacked in nappes of different metamorphic grade during the collisional stage. Mafic-ultramafic intrusions were formed mainly in the initial rifting stage and related to late back arc basins. Some of them have minor Ni-sulphide mineralization.

3 Ni-Cu sulphide deposits

Extensive exploration in mid-late 1900s resulted in the discovery of several Ni-Cu sulphide occurrences in northern Sweden and included deposits mainly related to ultramafic intrusions but in some cases also mafic intrusions. A distinctly different type was represented by serpentine altered dunites and peridotites in the Caledonides. Selected representative examples of these different types of Ni-deposits are described more in detail.

3.1 Kukasjärvi

The Kukasjärvi deposit was investigated by the Boliden company drilling in the late 1970s and early 1980s by 15 drill holes. It is hosted by a peridotite sill occurring in metasediments in southeastern Norrbotten. Ore minerals occur disseminated and are dominated by pyrrhotite with small amounts of pentlandite and chalcopyrite. The deposit is calculated to contain 2.6 Mt with 0.4% Ni and 0.4% Cu (Bergman & Kathol 2018).

3.2 Notträsk

Massive Ni-bearing pyrrhotite was first discovered in a road cut at Notträsk and later investigated by drilling. It occurs close to the margin of a 6x4 km large, and concentrically zoned funnel shaped 1.8 Ga intrusion in southern Norrbotten. Modal layering is steep at the margin but becomes gradually almost horizontal in the central part. It has a noritic marginal zone with xenoliths of graphitic metasediments followed by ferrogabbro, olivinegabbro, anorthosite, and troctolite towards the inner part (Arvanitidis 1982; Filén 2001). Massive pyrrhotite and disseminated sulphides comprising pyrrhotite and minor pentlandite and chalcopyrite are found in the marginal norite. Violarite, mackinawite, gersdorffite, cubanite, and cobaltite are rare constituents. The sulphur isotope composition of sulphides is on average 2.2‰ (Arvanitidis 2018).

3.3 Lainijaur

The Lainijaur deposit was discovered in 1940 and mined during 1941-1945 producing in total 0.1 Mt @ 2.2% Ni, 0.9% Cu, and 0.1% Co. It occurs in northern Västerbotten and is hosted by a differentiated intrusion varying in composition from olivine gabbro to granodiorite. The intrusion is hosted by metasediments and has the shape of a narrow laccolite with roots in a mafic dyke striking NE-SW. The ore varies from disseminated to massive consisting of pyrrhotite, chalcopyrite and pentlandite but include also minor vein style mineralization dominated by Ni-As sulphides. The massive ore occurs at the lower contact in close relation to the feeder dyke in the footwall. The disseminated ore occurs in the lower part of the gabbro and in the feeder dyke as sulphide droplets. Veins of nickeline, cobaltite, skutterudite, loellingite, rammelsbergite and asenopyrite occur in the massive ore and in the footwall metasediments (Grip 1961). The deposit is suggested to have an age of c. 1.87-1.89 Ga and to have formed from mantle-derived magmas produced during crustal extension (Martinsson 1996).

3.4 Älgliden

The Älgliden intrusion is a 3-km-long dike, up to 100 m wide in the central part. It strikes SW-NE parallel to steeply dipping extensional faults. It occurs in northern Västerbotten and has an age of 1.88 Ga. It consists mainly of olivine-rich norite with a fosterite content in olivine ranging from 72 to 76, and minor leucogabbro (Beijgarn et al. 2011; Cordier et al. 2019). The mineralization contains 0.2% Ni, 0.69% Cu, and 0.03% Co and consists of sulphide blebs, small stringers, and “net-textured” ore through the dike. The main sulphide minerals are pyrrhotite, pentlandite, and chalcopyrite with pyrrhotite partly replaced by pyrite within 10 m of the dike margins (Bejgarn et al. 2011). Sulphur isotope composition of sulphides have $\delta^{34}S$ values varying from 3.8 to 4.6 ‰ (Cordier et al. 2019).

3.5 Lappvattnet

The Lappvattnet deposit was discovered by drilling in 1973 and later investigated by trial mining. It is the first discovered occurrence related to small peritdotite bodies which intruded graphite bearing biotite gneiss in the Nickelbelt in eastern Västerbotten. Sulphide mineralization occurs in the ultramafic rocks but is most extensively developed in the gneiss occurring disseminated, as veinlets and breccia infill. The most high-grade ore occurs as sulphide rich mylonite and breccia forming lenses and tabular bodies with tectonic and sharp contacts to the gneiss. The mineralized interval is 1-10 m wide and continuous for 620 m and is estimated to contain 1 Mt @ 1.0% Ni and 0.2% Cu (Nilsson 1985). Hexagonal pyrrhotite and minor pentlandite occur disseminated in the peridotite and partly as rounded droplets. Massive and breccia ore is manly hosted by gneiss and consists of rather coarse-grained monoclinic pyrrhotite and minor pyrite, pentlandite, and chalcopyrite. Accessory minerals include mackinawite, sphalerite, gersdorffite, nickeline, and sperrylite (Nilsson 1985).

3.6 Rörmyrberget

Rörmyrberget is also part of the Nickelbelt. Disseminated Ni-mineralization consisting mainly of pyrrhotite and pentlandite is found in a 1700 m long and up to 320 m thick ultramafic intrusion. It comprises multiple sills with modal layering and is hosted by metasediments. Serpentine altered olivine cumulates are found in the lower part of the intrusions followed by peridotite and gabbro. The MgO content is up to 40 % in olivine cumulates and olivine has a forsterite content ranging from 82 to 91. Pentlandite is locally common and is in one orebody the dominating sulphide phase (Nilsson 1985). Later investigations have identified smaller high-grade ore lenses with a combined tonnage of 0.293 Mt @ 1.49% Cu, 0.14% Cu, and 8.54% S (Persson 1991).

3.7 Slättberg

Nickel was discovered in 1817 at Slättberg in northern Bergslagen and mining took place periodically between 1851 and 1943 with a total production of 20 000 tons of ore (Nilsson, 1985). Massive ore occurs in the central part of a 1600 m long and 3-6 m wide mafic dyke, but sulphides are also disseminated in the host rock. Pentlandite, millerite, and chalcopyrite occurs together with pyrrhotite and pyrite with massive ore surrounded by pyrite in a 1.2 to 2.7m wide zone. The pyrrhotite ore contained 1.2-2 % Ni and pyrite contained up to 0.5% Co (Lövstrand 1903).

3.8 Kuså

The Kuså deposit in Bergslagen is hosted by an intrusive complex ranging in composition from quartz monzodiorite through diorite–gabbro to pyroxenite and hornblendite with an age of 1.80 Ga (Ripa et al. 2017). Massive to disseminated ore occurs in a c. 10 m wide and moderately dipping zone having a tectonic lower contact. The ore contained 1.1 to 1.8 % Ni and Cu that was enriched towards the hanging wall (Löfstrand, 1903). Ore minerals are dominated by pyrrhotite, chalcopyrite and pentlandite with bravoite, cobaltite, linneaeite, and sperrylite as minor constituents (Ripa et al. 2017).

3.9 Kleva

Mining for Cu started in 1691 at Kleva but after discovery of high Ni grades in 1842 it was mined for Ni during 1845-1889, and for a few years during World War I. An estimated total production of 55000 tons of ore with 2-2.5% Ni and 0.5% Cu generated approximately 1000 tons of Ni. Sulphide mineralization is related to a 1.79 Ga mafic complex comprising gabbro, diorite, and minor norite and anorthosite within the TIB-province (Bjärnborg et al. 2015). Massive pyrrhotite-dominated mineralization occurs as irregular tabular and vein-shaped bodies in areas of disseminated mineralization. Pentlandite, chalcopyrite, pyrite, sphalerite, violarite, marcasite, mackinawite, magnetite, and ilmenite occur together with pyrrhotite. Chalcopyrite most commonly occurs in the outer parts of the lower grade mineralization, or as fracture fillings. Partly assimilated sedimentary rocks occur in mineralized areas within the gabbro (Grip 1961; Zakrzewski 1988).

3.10 Rönnbäcken

The Rönnbäcken deposit, located in the Caledonides, was discovered in the 1940s. Nickel sulfides occur in a serpentinized ultramafic intrusions originally consisting of olivine and pyroxene. Sulphides are very fine grained and include pentlandite, heazlewoodite and minor millerite and cobaltite. They occur disseminated and were formed during serpentinization by release of Ni from olivine. Metallurgical tests have generated concentrates with high Ni contents in the range of 26–36% Ni. Mineralization occurs in three separate ultramafic bodies and has a total tonnage of 600 Mt @ 0.10% Ni and 0.003% Co (indicated and inferred resource) (SRK Consulting 2022).

4 Discussion

Ni-Cu sulphide deposits occur in geological provinces of different ages in Sweden but most of them are of Paleoproterozoic age. Those related to mafic intrusions occur mainly in bedrock formed in arc settings, whereas those occurring in peridotite intrusions are more likely to have formed during events of extension. The genetic model for Ni-Cu sulphide deposits in general is well constrained and includes source of magma, metals, and sulphur, character of mineralization and ore forming processes (Barnes et al. 2016). The Ni-Cu sulphide

deposits in Sweden share most characteristics with typical magmatic Ni-Cu deposits worldwide, and the generally small size of the mafic hosted deposit is a characteristic feature of Ni-Cu sulphide deposits formed in arc environments.

The known deposits in Sweden could be divided into five different types based on character of host rock and origin of mineralization. Those are deposits related to peridotite sills, mafic dykes, mafic plutons, layered mafic intrusions and serpentinites. In general, the Ni/Cu ratio is related to magma composition with those related to peridotites having a Ni/Ni+Cu ratio less than 0.2, whereas those hosted by mafic rocks mostly vary from 0.3 to 0.5.

The first four types are generally located in areas including sulphide-bearing metasedimentary rocks suggesting external sulphur sources and silica contamination to be important to generate sulphur saturation. This is partly supported by sulphur isotope data and evidence of assimilated metasediments. However, only few of the deposits hosted by mafic intrusions are of typical marginal (or contact) type. Instead, massive and disseminated sulphides occur as irregular accumulations within the intrusions. Only the Lainijaur deposit which is related to a magmatic layered intrusion has massive ore accumulated at the lower contact and especially close to a feeder dyke containing disseminated sulphides. Deposits related to mafic dykes may be disseminated in character (Älgliden) or contain massive ore in the central part of the dyke (Slättberg). They are suggested to represent the roots of possible eroded marginal type deposit emplaced higher up in the crust.

Deposits related to peridotite sills are suggested to also be part of larger magmatic systems as the amount of Ni-Cu sulphide mineralization in these deposits is large in relation to the size of the intrusions. This is the case for most of the deposits occurring in the Nickel Belt in Västerbotten. These deposits are suggested to be related to larger magmatic systems where the main segregation of sulphides occurred deeper in the crust.

The Rönnbäcken deposit is different to traditional Ni-Cu sulphide deposits as it has a very low sulphide content and almost lacks pyrrhotite. During serpentinization low amounts of available sulphur occurring in accessory sulphides was combined with nickel released form olivine resulting in a low-grade dissemination of the Ni-rich sulphide heazlewoodite. Compared to traditional Ni-Cu sulphide deposits that are dominated by pyrrhotite and with pentlandite as main Ni-sulphide it is possible to generate a Ni-concentrate with much higher Ni-contents.

5 Conclusions

Several different types of Ni-Cu sulphide deposits have been discovered in Sweden during the last 150 years of exploration and several of them have also been mined in small scale. But the economic potential of the known Ni deposits is restricted as most deposits are small in size and/or low grade. However, as several of these deposits are suggested to be part of larger magmatic systems, further research and exploration could maybe result in more significant discoveries. The Nickelbelt in Västerbotten may be the most promising area but also mafic layered intrusions with more extensively developed contact-type mineralization could have potential. Deposits related to the serpentinization of peridotites/dunites have large tonnages but low grade. The low sulphide content makes these deposits interesting as tailings will cause less environmental problems and as they will generate Ni-concentrates with a very high Ni-content.

References

Arvanatides (1982) The geochemistry and petrogenesis of the Notträsk mafic intrusion, northern Sweden. PhD Thesis Stockholms Universitet Geological Institution.

Barnes SJ, Cruden AR, Arndt N, Saumur BM (2016) The mineral system approach applied to magmatic Ni-Cu-PGE sulphide deposits. Ore Gel Rev 76: 296–316. http://dx.doi.org/10.1016/j.oregeorev.2015.06.012

Bergman S, Kathol B (2018) Synthesis of the bedrock geology in southern Norrbotten County, northern Sweden. Swedish Geological Survey Rap Medd 144. ISSN 0349-2176 ISBN 978-91-7403-410-3.

Bejgarn T, Årebäck H, Weihed P, Nylander J (2011) Geology, petrology and alteration geochemistry of the Palaeoproterozoic intrusive hosted Älgträsk Au deposit, northern Sweden. Geol Soc Lond Spec Publ 350: 105–132.

Bjärnborg K, Schersten A, Söderlund U, Maier WD (2015) Geochronology and geochemical evidence for a magmatic arc setting for the Ni-Cu mineralized 1.79 Ga Kleva gabbro-diorite intrusive complex, southeast Sweden. GFF 137: 83–101. https://doi.org/10.1080/11035897.2015.1015265.

Cordier C, Coin K, Arndt NT, Cartigny P (2020) The Älgliden Ni-Cu deposit: magmatic sulfides in a subduction setting. Min Dep 55:1173–1196. https://doi.org/10.1007/s00126-019-00921-4

Filén B (2001) Swedish layered intrusions anomalous in PGE-Au. Swedish Geological Survey Res Papers C833 33-45.

Grip E (1961) Geology of the nickel deposit at Lainijaur in northern Sweden. Sveriges Geologiska Undersökning Ser C577.

Löfstrand G (1903) Slättberg och Kuså nickelgrufor. GFF 25:103–122 (in Swedish).

Martinsson E (1996) Geochemistry and petrogenesis of the Palaeoproterozoic nickel-copper bearing Lainijaur intrusion, northern Sweden. GFF 118:97–109. https://doi.org/10.1080/11035899609546234.

Nilsson G (1985) Nickel-copper deposits in Sweden. In: Papunen H, Gorbunov GI (eds) Nickel-copper deposits of the Baltic Shield and Scandinavian Caledonides. Geol Surv Finland Bull 333:313–362.

Persson G (1991) Rörmyrbergets nickelförekomst. Slutrapport etapp VIII. NSG unpublished report 91046 (in Swedish).

Ripa M, Kampmann TC, Hellström FA (2017) SIMS U-Pb zircon geochronology at the Kuså Ni-Cu deposit, sout-central Sweden. GFF 139: 233–240.. https://doi.org/10.1080/11035897.2017.1332096

SRK Consultying (2022) Preliminary economic assessment update for the Rönnbäcken nickel project, Sweden. Unpublished report SRK Consulting UK..

Zakrzewski MA (1988) Mineral parageneses of the sulfide ore-deposits of Bergslagen metallogenic province. 1. Ni-Cu of southern Sweden. Geol en Mijnbouw 67:357–362.

Post-volcanic modification of komatiite-associated nickel sulfide mineralization: A case study of the Cassini deposit, Yilgarn Craton

Helen B. McFarlane[1], Margaux Le Vaillant[1], Stephen J. Barnes[1], Si-Yu Hu[1]
[1]CSIRO Mineral Resources, Australia

Abstract. Representing the first study of the recent greenfields discovery, the Cassini nickel sulfide (NiS) deposit of the Archean Yilgarn Craton, this investigation used an innovative integration of geochemistry and structural geology to elucidate the post-volcanic modification of komatiite associated NiS mineralization. This approach commenced with a new lithological classification, derived from the company whole rock geochemical database, of the host komatiite sequences, basalt and alteration. This was coupled with structural logging to constrain the subsurface geometries of the primary magmatic features and to unravel subsequent overprinting regional Neoarchean deformation. Nickel tenor analysis revealed two possible magmatic flow channels. The earliest deformation generated overthrusts over the massive and net textured sulfides. Both the Cassini ore bodies and the basal contact were passively refolded during ENE-WSW deformation, with the best preservation of the classic mineralization profile associated with parasitic F_2 synclines on the western limb of the Widgiemooltha anticline. The F_2 axial trend is subparallel to the highest tenor channel, providing critical guidance for understanding modification of the primary channel morphology. Analysis revealed significant deformation but limited mechanical remobilization. Furthermore, the study has significant implications for improving prediction of magmatic NiS deposits in poly-deformed terranes.

1 Introduction

Komatiitic ultramafic lavas are a common feature of Archean greenstone belts around the world and are of notable economic significance due to their association with nickel sulfide (NiS) deposits (Lesher et al. 2002). They are characterized by magmas with MgO contents greater than 18 percent, and flow profiles defined by textural features including lower B-zone cumulates underlying spinifex textures of the A-zone and fine-grained flow tops (e.g., Barnes 2006). In an undeformed setting, these classic morphological features develop through the interaction of high flux, ultra-high temperature komatiitic magmas with sediment and hydrated seafloor basalt. Accumulation of a sulfide melt pool or channel at base of the lava tube is associated with the thermal erosion of the footwall basalt and the progressive development of characteristic open basal contacts and pinch out contacts (e.g., Staude et al. 2017).

To enhance exploration for these deposits, it is critical to understand the spatial distribution and morphology of volcanological features to delineate ore bodies within. Identification and prediction of these features is complicated by subsequent post-volcanic modification, however, may be achieved based on our proposed approach. Here we examine the structural history of the recently discovered, and thus far unstudied, Cassini NiS deposit (Mincor Resources) of the Yilgarn Craton in order to unravel the deformation overprint and better understand primary channel geometries and the distribution of economic NiS mineralization.

2 Geological Setting

The Cassini NiS deposit is located in the Kalgoorlie Terrane of the Eastern Goldfields Superterrane (EGST) of the Archean Yilgarn Craton, Western Australia (Cassidy et al. 2006).

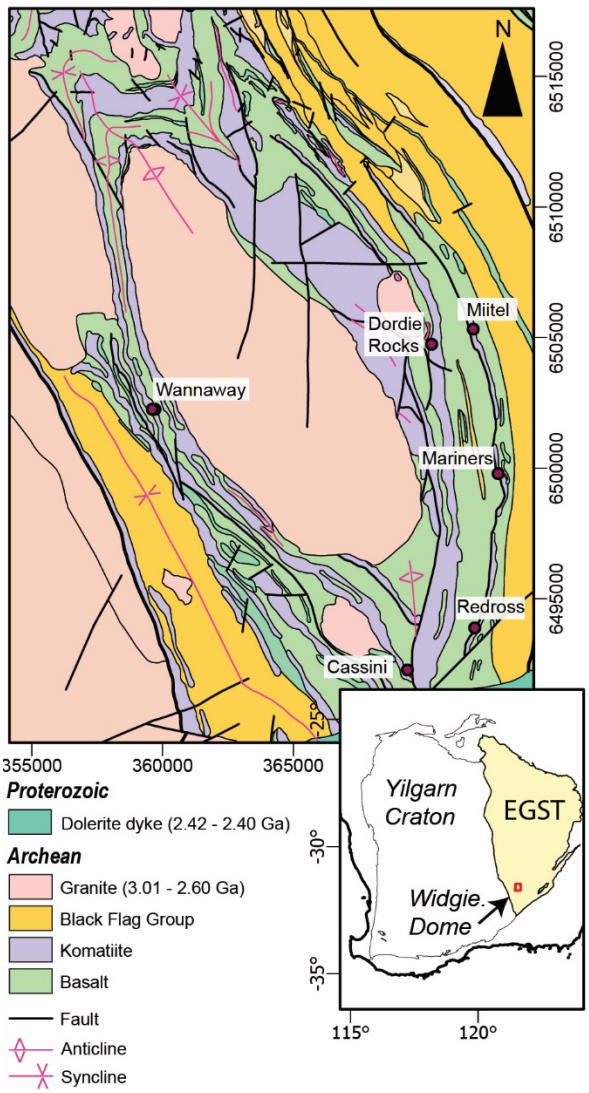

Figure 1. Simplified geological map of the Widgiemooltha Dome showing NiS deposits, including Cassini (modified from GSWA 2022). Inset shows Yilgarn Craton in Western Australia.

The craton comprises expansive granite-greenstone terranes with a dominant NNW-striking crustal architecture. Greenstone belts of the EGST comprise 2.72–2.69 Ga mafic-ultramafic igneous suites and overlying volcaniclastic and siliciclastic units of the Black Flag Group. Ultramafic units contain komatiite associated NiS deposits, including those within the archetypal Kambalda Dome (Barnes and Perring 2007). Approximately 45 km SSW of the Kambalda Dome, the Cassini deposit is located at the southern apex of the Widgiemooltha Dome and is hosted in the Mount Morgan Komatiite (Figure 1). Separated by the tholeiitic Mount Edwards Basalt, the overlying Widgiemooltha Komatiite is host to the Type-1 Wannaway, Mariners, Miitel and Redross deposits (McQueen 1981a; Lesher et al. 2002). Multiple phases of granitic plutonism accompanied polyphase deformation and metamorphism of the mafic-ultramafic rocks in both the Widgiemooltha and Kambalda domes (Witt et al. 2020; Seat et al. 2004; Stone et al. 2005). Peak metamorphic conditions for Widgiemooltha are estimated at ~600 ºC and 4 kbar (McQueen 1981b). Alteration at Cassini is dominated by talc-carbonate assemblages with relict serpentinization preserved in the southern areas. Metamorphic garnet is present in the footwall basalt in the core of the Widgiemooltha anticline.

3 Methodology

Whole rock geochemistry from the company assay database were reprocessed to determine rock types and zonation of the komatiitic flows. From this, a series of geochemical classification plots was generated using ioGas software. Volatile-free and sulfide-free normalisation of whole-rock analyses was performed for lithological classification and excludes rocks with >5% S (>approx. 15% sulfide), according to Barnes (2022). These were visualised in 3D to better constrain the geometries of the host komatiite prior to deformation.

Structural analysis included examination and measurement of magmatic and structural features preserved in oriented diamond drill core and evaluation of the current resource model. Structural investigation of host rock lithologies focussed on the intensity of metamorphism and deformation. Structural observations were integrated with new lithological classifications using the Leapfrog Geo software.

Mineralogical and microstructural analysis of key samples used both transmitted and reflected light microscopy and scanning electron microscope (SEM) analysis. Samples were scanned with an SEM equipped with TESCAN Integrated Mineral Analyser (TIMA) software to automatically generate mineralogy maps for each sample. The scanning electron beam current was approximately 8 nA and accelerating voltage was 25 KV with a dwell time of 125 ms yielding a resolution of 10–12 µm per pixel, with a working distance of 15.0 mm.

4 Geochemistry

Ultramafic rocks at the Cassini deposit are serpentinized, metamorphosed and variably talc-carbonate altered. As such, there is poor preservation of primary magmatic textures classically employed to determine the facies, zonation, and geometries of the primary komatiitic flows and the associated channel. Lithological classification and zonation within the komatiitic sequence (Figure 2) identified from geochemical data was based primarily on a combination of Mg# (molar MgO/(MgO+FeO)), Al_2O_3 and $Al2O_3/TiO_2$, with further information from other alteration-immobile element components including Cr, Zr, and Ti.

Two main komatiite categories were defined, based on MgO weight % (volatile-free), with a third lithology distinguished due to elevated Cr contents but lower MgO numbers than expected, which are interpreted as the result of alteration. Definitions include: komatiitic olivine cumulates (Kom cmlt) with MgO > 32.5%; komatiites flow margins and spinifex textured flows (Kom FT), comprising relatively olivine-poor components of komatiite flows, with

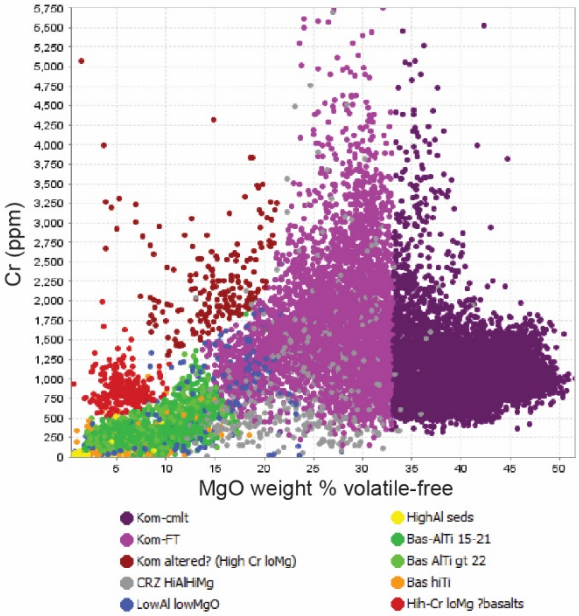

Figure 2. Lithological classification of company whole rock geochemical database showing lithology types grouped by MgO and (wt. %) and Cr concentrations (ppm).

MgO < 32.5%, but above ~ 15% MgO; and, altered komatiite (Kom alt) featuring high Cr but low MgO, likely due to MgO loss with alteration. Altered komatiite was frequently noted along structural trends. Various basalt lithologies were defined, which all have lower MgO contents than the komatiites (<15% MgO) and were divided in function of Al and Ti contents. Classification defined komatiitic basalt, high Al/Ti basalt and high Ti basalt. Nickel tenor (calculated composition in 100% sulfide) showed a wide range independent of the sulfide content in the rock, ranging from around 2.5%

to 20% in disseminated, matrix or net-textured and massive ores. The spatial disposition of these tenor variations in 3D space displayed two shoots with contrasting grade distribution.

5 Cassini mineralization

The current mineral resource of Cassini is 1.4 Mt at 4.0 % Ni for total Ni 58,200t (Mincor Resources 2022). Mineralization at Cassini is characterised as both Type-1, comprising massive sulfides resting on an open contact overlain by net texture and disseminated sulfides, and Type-5 (Lesher et al. 2002). Poor preservation of the classic mineralization profile is consistent with significant post-volcanic deformation. The deposit comprises numerous massive sulfide bodies at the contact between the Mount Morgan Komatiite and the footwall basalt, plunging moderately to the SE to SSE. The orebodies sit on the western limb pf the regional scale Widgiemooltha anticline. The ore assemblages predominantly comprise massive pyrrhotite (Po) and pentlandite (Pn). Few true pinch out structures related to thermal erosion by massive sulfides of the footwall basalt are noted. Localised mechanical remobilization is described below.

6 Structural framework

The structural framework revealed an early deformation event (D_1) associated with low angle shearing and the overthrusting of footwall basalt over disseminated, matrix or net-textured and massive sulfides along the basal contact of the Mount Morgan Komatiite. This creates features that mimic pinch outs. Both textural observations and analysis of new lithological classification from the geochemistry reveal localised overturning of portions of the komatiitic sequences. Evidence of larger scale thrusting and repletion of basalt units was inconclusive given the scale of the study and the available datasets. Massive nickel sulfide occurrences display strong deformation, and patchy development of a ductile Po-Pn S_1 foliation subparallel to magmatic contacts (Figure 3). The deformation event resulted in narrow high strain zones along lithological contacts, extensively overprinting primary textures and geometries, but limited evidence of remobilisation in the central ore zone.

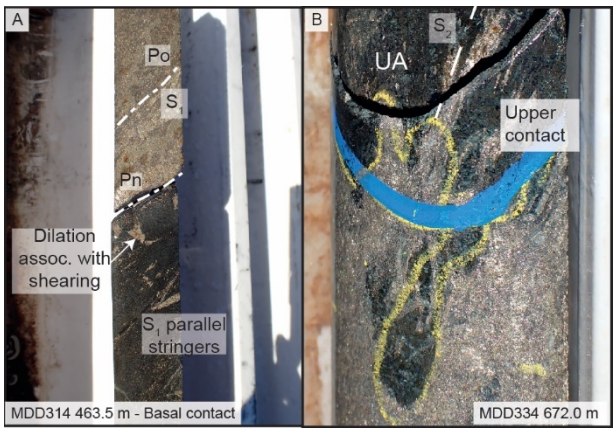

Figure 3. Representative ore textures from Cassini showing (a) Massive sulfides displaying foliation (S_1) parallel to the underlying weakly deformed basal contact containing minor stringer sulfides; and (b) localised mechanical remobilization of sulfides along the S_2 foliation plane, axial planar to the regional folding. UA = amphibole bearing metamorphosed ultramafic.

Rare F_1 folds plunge towards the ENE or SW, suggesting an approximate NNW-SSE shortening regime. The dominant architecture of the deposit is attributed to refolding of the ore body and D_1 low-angle structures by NNW-SSE trending, tight, F_2 folds, with a steeply ENE-dipping axial surface, associated with ENE-WSW D_2 shortening. The bulk of the massive sulfide ore as Cassini is seated in a parasitic F_2 synform on the western limb of the major anticlinal axial surface of the Widgiemooltha Dome. Both the Cassini ore bodies and F_2 folds are co-axial, plunging shallowly to moderately to the SSE, showing parallelism with the highest Ni tenors in the southern portion of the deposit. More intense deformation at Cassini North coincides with more intense deformation and mechanical remobilisation, reflected in associated with widespread Ni tenor distribution, extensive attenuation and dislocation of ore, analogous to the Wannaway N02 ore body (Seat et al., 2004).

These F_2 synforms represent the sites of the best preservation of massive sulfide ore. Mechanical sulfide remobilisation is noted along the S_2 plane (Figure 3b) but is spatially restricted to approximately 50cm above the contact or limited by overlying D_1 overthrusts. More extensive mechanical remobilization associated with shearing and attenuation along the fold limb is noted on the eastern limb of the anticline.

The eastern flank of the antiform is truncated by a high strain to mylonitic, steeply (> 70°) east dipping reverse fault that developed during ongoing E-W to ESE-WNW shortening, juxtaposing the host komatiites with highly altered, low MgO basalt, and altered B zone komatiitic rocks to the east. Both the antiform and reverse faults are gently refolded or displaced during the later minor deformation.

7 Conclusions

The results of this study highlight the control of post-volcanic, polyphase deformation on the subsurface

geometries of the Cassini orebody and the distribution of economic Ni mineralization, linked with the primary channel orientation, relative to the major structures. New geochemical classification of the volcanic facies of the host komatiitic sequence highlight lithological relationships and distribution following deformation. Furthermore, analysis of the distribution and disposition of Ni tenor reveals a high-grade channel in the south, a possible second low-grade channel. The most extensive deformation and sulfide remobilisation is documented in Cassini North. Coupled geochemical and structural analysis has the potential to address some of the significant challenges of defining the geometries of narrow, often geophysically blind, komatiite associated NiS deposits in poly-deformed terranes.

Acknowledgements

The project was co-funded by Mincor and the Australian Government Innovations Connections Program. Mincor Resources NL are thanked for their support, knowledge and enthusiasm during the course of this project.

References

Geological Survey of Western Australia (GSWA) (2022) 1:100 000 State interpreted bedrock geology of Western Australia, April 2022 update. Geological Survey of Western Australia, digital data layer, www.dmp.wa.gov.au/geoview.

Barnes SJ (2022) Lithogeochemistry in exploration for intrusion-hosted magmatic Ni-Cu-Co deposits. Geological Society of London. Collection. https://doi.org/10.6084/m9.figshare.c.6267664.v3

Barnes SJ (2006) Komatiites: Petrology, Volcanology, Metamorphism, and Geochemistry in Nickel Deposits of the Yilgarn Craton: Geology, Geochemistry, and Geophysics Applied to Exploration. Society of Economic Geologists Special Publication 13, pp. 13–49.

Barnes SJ (2006) Komatiite-hosted nickel sulfide deposits: Geology, geochemistry, and genesis. Society Of Economic Geologists, Special Publication 13, pp. 51-97.

Cassidy K, Champion D, Krapez B, Barley M, Brown S, Blewett R, Groenewald P, Tyler I (2006) A revised geological framework for the Yilgarn Craton, Western Australia. Geological Survey of Western Australia, Record 8:1-15.

Lesher C, Keays RR, Cabri L (2002) Komatiite-associated Ni-Cu-PGE deposits: Geology, mineralogy, geochemistry and genesis. Canadian Institute of Mining, Metallurgy and Petroleum 54:579-618.

McQueen K (1981a) Volcanic-associated nickel deposits from around the Widgiemooltha Dome, Western Australia. Economic Geology 76:1417-1443.

McQueen K (1981b) The nature and metamorphic history of the Wannaway nickel deposit, Western Australia. Economic Geology 76:1444-1468.

Mincor Resources NL (2022) Annual Shareholder Report 2022, ASX Announcement https://www.mincor.com.au/site/investor-centre/asx-announcements. Accessed 01 March 2023.

Seat Z, Stone W, Mapleson D, Daddow B (2004) Tenor variation within komatiite-associated nickel sulphide deposits: insights from the Wannaway Deposit, Widgiemooltha Dome, Western Australia. Mineralogy and Petrology 82:317-339.

Staude S, Barnes SJ, Le Vaillant M (2017) Thermomechanical erosion of ore-hosting embayments beneath komatiite lava channels: textural evidence from Kambalda, Western Australia. Ore Geology Reviews 90:446-464.

Stone WE, Beresford SW, Archibald NJ (2005) Structural setting and shape analysis of nickel sulfide shoots at the Kambalda dome, Western Australia: Implications for deformation and remobilization. Economic Geology 100:1441-1455.

Witt WK, Cassidy KF, Lu Y-J, Hagemann SG (2020) The tectonic setting and evolution of the 2.7 Ga Kalgoorlie–Kurnalpi Rift, a world-class Archean gold province. Mineralium Deposita 55:601-631.

Mineralogical study and structural controls of Co-Ni-Fe and Cu of F53 deposit in the Aït Ahmane area (Bou Azzer inlier, Anti-Atlas, Morocco).

Mohamed Ez-Zghoudy [1], Moha Ikenne [1], Mustapha Souhassou [2], Said Ilmen [3], Ilya R PROKOPYEV [4], Zaineb Hajjar [5], Mehdi Ousbih [1], Fatiha Askour [1], Lhou Maacha [6], Mohamed Zouhair [6]

1 LAGAG, Faculty of Sciences, Ibn Zohr University, BP. 8106, Cite Dakhla, Agadir, Morocco

2 EGERNE, Polydisciplinary Faculty of Taroudant, Ibn Zohr University, Agadir, Morocco

3 CAG2M, Polydisciplinary Faculty of Ouarzazate, Ibn Zohr University, BP. 638, 45000, Ouarzazate, Morocco

4 Sobolev Institute of Geology and Mineralogy, Siberian Branch of the Russian Academy of Sciences, 3 Academician Koptyug Ave, Novosibirsk 630090, Russia.

5 Laboratory of Geosciences, Water and Environment (L-G2E), Faculty of Sciences in Rabat, Mohammed V University in Rabat. 4 Avenue Ibn Battouta, B.P. 1014 RP, Rabat, Morocco.

6 MANAGEM Group, Twin Center, Casablanca, Morocco

Abstract. The Bou Azzer mining in the central part of the Anti-Atlas Belt in Morocco is one of the world's main producers of cobalt. The cobaltiferous mineralizations in Bou Azzer are spatially and genetically linked to serpentinized peridotites. Among these deposits is the F53 deposit in the Aït Ahmane area, which is located in the eastern part of the Bou Azzer inlier.

The F53 deposit shows two morphological types of mineralization. The EMPA analysis shows that massive contact mineralizations hosted in quartz-calcite lenses located in the N120° tectonic contact between serpentinized peridotites and quartz diorites is characterized by the presence of Ni and Co monoarsenides (nickeline, langisite, modderite), diarsenides of Co-Ni-Fe (safflorite, löllingite, and rammelsbergite), triarsenides of Co (skutterudite) and Co-Ni-Fe sulfoarsenides marked by a dominance of gersdorffite. The sulfides of Cu, Zn, and Pb are later than the Co-Ni-Fe arsenides.

The vein-type mineralizations hosted in quartz-carbonate veins oriented N00° to N40° intersect the quartz diorite. This mineralization is characterized by the absence of nickel minerals and the presence of Co-Fe diarsenides (safflorite and löllingite), Co triarsenides (skutterudite), and Co-Fe sulfoarsenides with the dominance of cobaltite. Late Cu, Pb, and Zn sulfides are less abundant in this case.

1 Introduction

The deposits of Bou Azzer are located in the Anti-Atlas about 90 km to the south-southeast of the Ouarzazate city in Morocco (Fig. 1A). The mineralization Co-Ni-As is spatially associated with extensive serpentinite bodies which resulted from the alteration of Neoproterozoic ophiolite sequences including peridotite protoliths (Leblanc, 1981). Many deposits and mineralized occurrences were identified along the axis of the inlier over a length of 45 km, from the Mechoui deposit at the western part to the Aït Ahmane eastward (Fig. 1B). These ore deposits are located on the edges or in the immediate vicinity of a wide band of serpentinized peridotites of Neo-proterozoic age.

The Aït Ahmane sector (Fig. 1B) is located, about 35 km from the Bou Azzer Mine, in the eastern part of the Bou Azzer inlier. This sector is characterized by an ophiolitic complex considered one of the oldest known worldwide. In the Aït Ahmane area, several Co–Ni-As-bearing veins are intimately related to the serpentinized peridotite massif (Fig. 1B). Among these mineralized veins, we identify the deposit of F53 which is located about 1.5 km in the south of Aït Ahmane village, and is located at the contact between the serpentinized peridotites massif and quartz diorites (Fig. 2).

The F53 deposit is well-known for its Co–Ni–As mineralizations that are identified in quartz-carbonate veins cutting the quartz diorite and serpentinites, and/or in the faulted contact between quartz diorite and serpentinites (Fig. 2).

Locally, the F53 deposit is formed by the following geological facies (Fig. 2):

- Serpentinized peridotites outcrop in the form of several N120° trending bands or lenses, (2 km wide and 8 km long) from Ightem to Ait Abdellah villages. They are easily recognizable in the field with their visible minerals composed of asbestos-chrysotile, ghosts of pyroxenes, crystals or stringers of magnetite, chromite (Admou et al., 2013).
- Ultramafic cumulates are characterized by a gray color and are essentially magnesian with very large crystals often well-preserved. These cumulates are more or less serpentinized. These are composed mainly of dunites, pyroxenites, wehrlites and sometimes gabbros.
- Isotropic gabbros and microgabbros are outcrop either as isolated intrusions or form the host of the vein complex. Sometimes, they gradually pass to microgabbros and diabases and are more abundant than sheeted gabbros (Admou et al., 2013).

- Quartz diorite: This plutonic intrusion is rich in quartz with a gray to gray-green tint with amphibole, biotite and plagioclase (Admou et al., 2013). This massif outcrops to the south of Aït Ahmane and cutted by dense swarm of quartz-carbonate veins and lenticular quartz veins, which are isolated or in bundles (Fig. 2). Its contact with the serpentinite massif is generally faulted and frequently interspersed with lenses of listvenites and/or quartz and calcite.

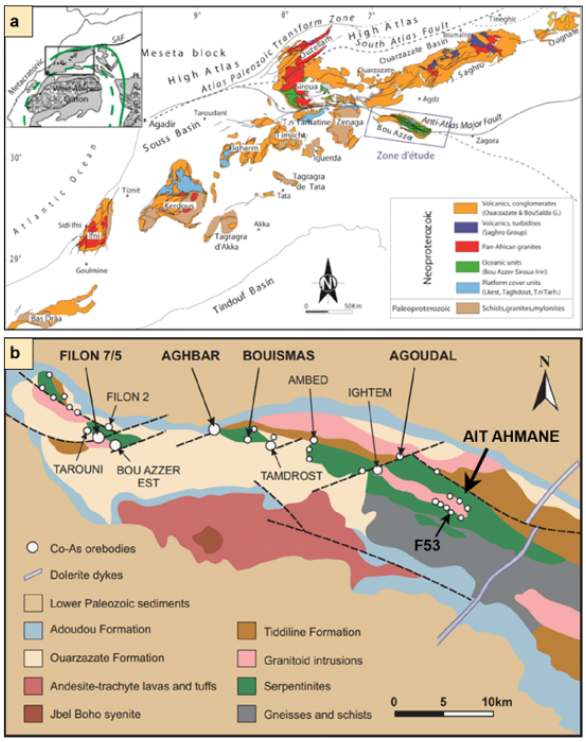

Fig. 1. A: Geological map of the Anti-Atlas mountain showing the position of the Bou Azzer inlier. B: Generalized geological map of the Bou Azzer inlier showing the distribution of the main cobalt-arsenide orebodies in relation to the serpentinized peridotites massifs; the size of the circles is roughly proportional to the size of the orebodies and showing the location of F53 deposit in Aït Ahmane area.

2 Methodology

Field work and sampling of the F53 deposit were undertaken in 2019 and these samples cover the whole mineralogical diversity of the veins. Selected samples were studied by optical microscopy in reflected and transmitted light using an Olympus BX60 polarizing microscope equipped with a Nikon digital camera DXM1200 system. The chemical composition of ore minerals was determined by EMPA using a JEOL JXA8200 electron microprobe equipped with five wavelength dispersive spectrometers (WDS) at the Eugen Stumpfl electron microprobe laboratory of the Siberian Branch of the Russian Academy of Sciences (Novosibirsk, Russia). The mapping and digital collection of geological data and structural measurements in the field was done mainly using the ArcPad 10.2 mobile application and the data processing was done by Win-Tensor software. We use the Win-Tensor software (5.9.2 version) for the structural analysis and paleo stress reconstruction.

3 Results

3. 1 Structural control of mineralization in the F53 deposit

Based on the study of Ez-zghoudy et al., 2023 in the F53 deposit of Aït Ahmane, the mineralization is controlled by two main types of faults. The first family of faults WNW-ESE which is represented by major overlapping faults generally oriented N110° to N120° (WNW-ESE) formed during the Pan-African compressive phase characterized by a maximum compressive stress σ1 horizontal oriented N30°to N40° (Fig. 2).

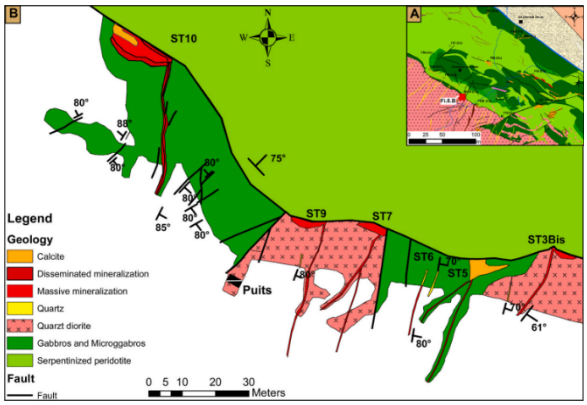

Fig. 2. Geological survey in the underground level − 280 showing the different mineralized veins of the F53 deposit of Aït Ahmane (Ez-Zghoudy et al., 2023).

This family of overlapping faults with a sinistral strike-slip oriented N110° to N120° generally controls the mineralized bodies (contact mineralization) rich in Co–Ni–Fe arsenides in the form of lenses located along the tectonic faults between serpentinized peridotites and quartz diorite or gabbros (Fig. 2). The second family of faults corresponds to tension gashes and normal fault oriented N00° to N40° previously formed and reactivated in sinistral reverse faults oriented N00° to N40° during the NW-SE Hercynian compressional phase (Fig. 2). These faults with quartz-carbonate fillings oriented N00° to N40° with an average dip of 75° to the east intersect the quartz diorite.

3. 2 Mineralogical study of Co-Ni-Fe arsenides and sulfoarsenide

The mineralogical studies of Co-Ni-Fe arsenides and sulfoarsenide by EPMA show that the mineralization of the F53 deposit is mainly composed by:

- Monorsenides: are represented by nickeline which is obviously identified in the contact type of ores as a dendrite in inclusions in the skutterudite, the second mineral is langisite observed in the contact type ore associated with rammelsbergite and gersdorffite. The last is modderite found in inclusions in safflorite.
- Diarsenides (Fig. 3) are composed of the safflorite observed only in the contact type of ore as isolated rosettes surrended by gersdorffite rims, the löllingite occurs in the contact type ore as zoned fibroradial clusters or associated to arsenopyrite grains, the rammelsbergite is observed only in the contact type ore, occurring as inclusions in gersdorffite or embedded in large skutterudite crystals.

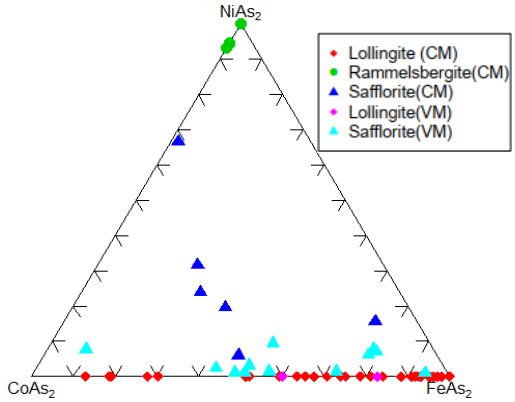

Fig. 3. $CoAs_2$-$FeAs_2$-$NiAs_2$ triangular plot (apfu) showing the variation of the chemical and mineralogical composition of diarsenides between the contact mineralization (CM) and vein mineralization (VM) of the F53 deposit.

- Triarsenides: EPMA analysis of triarsenides shows the presence of three skutterudite generation in F53 deposit from Aït Ahmane area. The first generation is the Ni-skutterudite (Skutterudite I) identified in the contact ore type; occurring as zoned crystals and in contact with gersdorffite. The second generation is Co-skutterudite (Skutterudite II), observed as a massive beach and more often as isolated cubic crystals in the quartz-carbonate gangue. The third generation is the relatively Fe-skutterudite (Skutterudite III) contains gold inclusions.
- Sulfoarsenide minerals (Fig. 4) are represented by gersdorffite identified only in the contact type ore. cobaltite is more abundant in the mineralized veins. the arsenopyrite occurs frequently at the edges of löllingite concretions and sometimes as prismatic crystals isolated in the gangue. the alloclasite was observed just in the contact mineralization adjacent to the edges of the nickeline and gersdorffite. the glaucodot isolated automorphic crystals in the quartz-carbonate gangue and westerveldite are observed as isolated automorphic crystals in the gangue and in association with skutterudite and sometimes as inclusions in cobaltite.

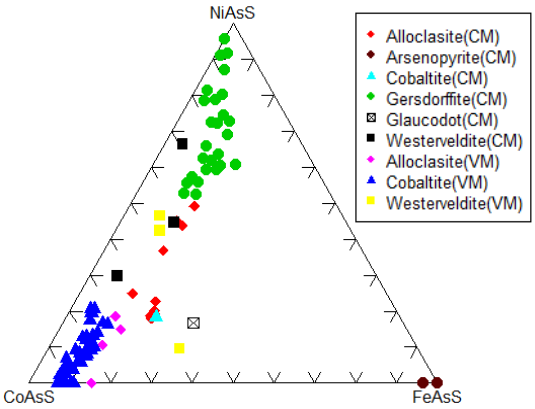

Fig. 4. CoAsS-FeAsS-NiAsS triangular plot (apfu) showing the variation of the chemical and mineralogical composition of sulfoarsenides between the contact mineralization (CM) and vein mineralization (VM) of the F53 deposit.

- Sulphides containing chalcopyrite fill the fractures in the arsenide ore and cavities in the quartz-carbonate gangue. Bornite was observed as filling of fractures through the arsenides. The covellite is included in chalcopyrite. Djurleite occurs as a microcrack filler in Co arsenide minerals. Roxbyite filling microcracks in Co arsenide minerals. Sphalerite constitutes the filling of the voids of the interstices and the microcracks in the skutterudite. Wurtzite occurs as a cavity and fissure filler in Co-Ni-Fe arsenide minerals. Molybdenite [MoS2], occurs in disseminated form in the gangue.
- Native bismuth [Bi] corresponds to the native element identified in the contact mineralization, it is observed either in inclusion in the löllingite or in association with nickeline, embedded in patches of the bornite.

4 Conclusion

The F53 deposit presents two morphological types of mineralization formed in different tectonic regimes and shows variable chemical and mineralogical compositions. The first is the

contact mineralization hosted in the N120° tectonic contact between the serpentinized peridotites and the quartz diorite. The analysis by EMPA show that this type is characterized by the presence of Ni-rich monoarsenide (Nickeline and langisite), diarsenides (Ni-safflorite, Co-löllingite, Fe-löllingite and rammelsbergite), the abundance of triarsenides rich in Ni, Co and Fe (Skutterudite I, skutterudite II and skutterudite III) and sulfoarsenide with Ni, Co and Fe (Gersdorffite, arsenopyrite, cobaltite, alloclasite, westerveldite and glaucodot), it is noted that cobaltite is very rare in this case, the presence of native elements (Bismuth) and sulfides of Cu, Zn, Pb and Mo filling voids and microcracks affecting Co-Ni-Fe arsenides and quartz-carbonate gangue. The second type is vein mineralization in the form of mineralized quartz-carbonate veins oriented N00° to N40° intersecting quartz diorite. The analysis by EMPA on the samples taken from the vein mineralization showed the absence of Ni-rich arsenides (Nickeline, langisite, rammelsbergite and gersdorffite) and also Fe sulfoarsenides (Arsenopyrite) and the presence of diarsenides poor in Ni and rich in Co and Fe (Co-safflorite, Fe-safflorite and Fe-löllingite), triarsenides low in Ni (Skutterudite II and Skutterudite III) and sulfoarsenides rich in Co and poor in Ni and Fe (Cobaltite, alloclasite, westerveldite) with the abundance of cobaltite, The sulfides of Cu, Zn, Pb are less abundant with the absence of molybdenite and native elements (Bismuth).

Acknowledgments

This study is part of Ph.D thesis of the first author (ME). Managem group is very thankful for their support and logistics during field work. The team of laboratory of the Siberian Branch of the Russian Academy of Sciences (Novosibirsk, Russia) for EMPA analysis.

References

Admou, H., Razin, P., Egal, E., Youbi, N., Soulaimani, A., Blein, O., Chèvremont, P., Gasquet, D., Barbanson, L., Bouabdelli, M., Anzar, C., 2013. Notice explicative de la Carte géologiques du Maroc (1/50 000), feuille Aït Ahmane. Notes Mém. Serv. Géol. Maroc.

Ez-Zghoudy, M., Ikenne, M., Souhassou, M., Alaeddine Belfoul, M., Gouiza, M., Ilmen, S., Ousbih, M., Karfal, A., Maacha, L., Zouhair, M., 2023. Structural controls on the Co and Ni-bearing arsenides from the Bou Azzer mine (Case of Aït Ahmane F53 vein deposit): Implications for mineral exploration. Journal of African Earth Sciences.

Leblanc, M., 1981. Ophiolites précambriennes et gîtes arséniés de cobalt (Bou Azzer, Maroc). Notes et mém. Serv. Géol. Maroc. 280, 311p. Leblanc, M., Billaud, P., 1982. Cobalt arsenide orebodies related to an upper Proterozoic ophiolite: Bou Azzer (Morocco). Econ. Geol. 77, 162–175. https://doi.org/10.2113/gsecongeo.77.1.162.

Maacha, L., 2013. Etudes Métallogéniques Et Géophysiques des Minéralisations Cobaltifères et Cuprifères de Bou-Azzer El Graara Anti-Atlas Maroc : Les Minéralisations de Cuivre de la Plateforme de Bleida. UNIVERSITE CADDI AYYAD FACULTE DES SCIENCES SEMLALIA- MARRAKECH, Maroc.

Mineralogical distribution of platinum-group elements (PGE) in the UG2 and Merensky Reefs at the Kalkfontein farm, Bushveld Igneous Complex

Anastasia M Nailana[1], Napoleon Q Hammond[1]
[1]University of Limpopo, Department of Geology and Mining, South Africa

Abstract. A study on the UG2 and Merensky Reefs at Kalkfontein farm located in the southern sector of the Eastern Limb of the Bushveld Igneous Complex, was undertaken to investigate the platinum-group elements (PGE) mineralogical characteristics, variation and distribution in these reefs. The distribution of the total platinum group minerals (PGM) in the UG2 show the following modal proportions, PGE sulphides (60%), PGE arsenides (13%), PGE alloys (10%), PGE sulphoarsenides (9%) and PGE bismuthotellurides (8%), while in the Merensky, PGE sulphides account for about 33% of the total PGM, PGE bismuthotellurides forms about 30%, PGE arsenides form 18%, PGE sulphoarsenides 10%, and PGE alloys, 6%. The PGM show close association with various mineral phases in both the UG2 and the Merensky. The base metal sulphides, which are dominated by pentlandite and chalcopyrite, show much closer association with the PGM in the UG2 than in the Merensky. The grain size of the PGM measured as equivalent circle diameter (ECD) vary from 0.73 to 32 µm and 0.87 µm to 27 µm in diameter in the UG2 and Merensky Reefs, respectively. Generally, more than 80% of the PGM are less than 10 µm in both the UG2 and Merensky.

1 Introduction

The platinum group minerals (PGM) are a diverse group of minerals that concentrate the platinum-group elements (PGE; Os, Ir, Ru, Rh, Pt, and Pd), and the mineralization is associated with mafic-ultramafic intrusions. The Bushveld Igneous Complex in South Africa hosts the world's largest resources of PGE. They are mostly mined from the Merensky Reef, UG2 Reef and Platreef ore deposits. They are situated in the complex's Rustenburg Layered Suite (RLS). The mineralogical and related metallurgical processing characteristics of Bushveld ores in the UG2 and Merensky Reefs has attracted many studies for some time now (e.g., Penberthy et al. 2000; Chetty et al. 2009) with an ultimate goal to provide vital information that can be used to improve the recovery of the PGE from the ore during beneficiation. This study investigated the PGE mineralogical variation and distribution in the Upper Group 2 (UG2) and the Merensky Reefs at the Kalkfontein farm, at the Two Rivers Platinum (TRP) Mine in the southern sector of Eastern Limb of the Bushveld Igneous Complex (Fig. 1), by determining the modal distribution of the PGM phases, their mineral association and their grain size distribution.

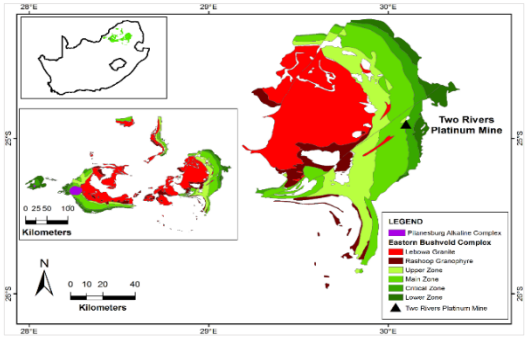

Figure 1. Simplified geological map of the Bushveld Igneous Complex with location of Two Rivers Platinum Mine indicated with a black triangle on the map.

1.2 Geology of the study area

Both the UG2 and Merensky Reefs are present in Kalkfontein farm. Three UG2 Reef facies are defined at the farm at the mine, namely, the UG2 Normal Reef, UG2 Split Reef and the UG2 Multiple Split Reef. The UG2 Normal Reef is approximately 1.5 m to 2 m thick and is characterized by a thick main chromitite layer (approximately 1.2 m thick). The UG2 Split Reef is approximately 2 m to 2.5 m thick, comprising of up to 2 m thick of main chromitite layer but separated into two by an internal pyroxenite/norite. The UG2 Multiple Split Reef is approximately 4.5 to 5 m thick and is characterized by main chromitite layer (2.5 m thick) and separated into three or more by internal pyroxenite/norite (McLaren and De Villiers 1982). In all the facies types, the main chromitite layers are underlain by pegmatoidal feldspathic pyroxenite and overlain by feldspathic pyroxenite.

2 Methodology

Six boreholes from in the Kalkfontein farm were logged and sampled for the study, samples were taken from two UG2 Normal Reef (BH 8206 and KFN 008), one UG2 Split Reef (KFN 014), one UG2 Multiple Split Reef (BH 8026) and two Merensky Reef (KFN 043 and BH 8026). Fifty-four polished blocks prepared from selected samples were analysed using A FEI600F field emission Mineral Liberation Analyser PGM characterization. Sixteen polished blocks selected from high PGE grade areas correlated with the assay data were analyzed for the PGM chemical composition using electron probe micro-analyses.

3 Results and discussion

3.1 Petrography and PGM characterization

Base metal sulphides (BMS) are uncommon in the UG2 samples, however when present, they occur as inclusions in silicates and chromite, or interstitial to the chromite grains and between chromite and silicates grain boundaries (Fig. 2a and b). In general, the BMS in the UG2 Reef are fine to medium grained with subhedral to anhedral morphology. The BMS in the UG2 and Merensky Reefs includes pentlandite, chalcopyrite, pyrrhotite, pyrite, millerite and galena. However, pentlandite and chalcopyrite are the most dominant in the UG2 Reef, while chalcopyrite, pentlandite and pyrrhotite dominate in the Merensky Reef. Cumulus chromite grains makes up about 60% of the total volume in the UG2 Reef, with silicates and BMS accounting for the balance. In the Merensky Reef, silicate minerals comprise 80% by volume with the remainder being BMS. Chromite grains occur in lesser extent in the reef and exhibit anhedral to subhedral morphology. The chromite grains are irregularly fractured with PGM filled within the fractures in some cases (Fig. 2a).

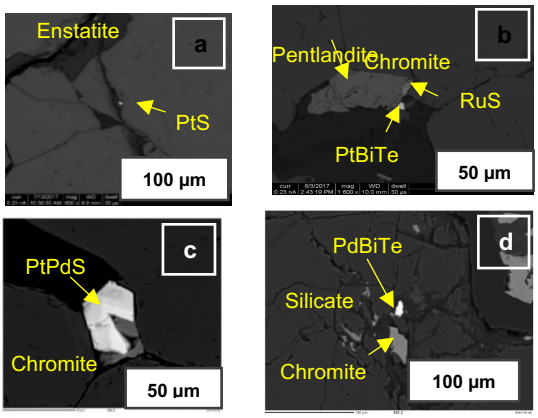

Figure 2. Backscattered electron images of PGM textural association in UG2 and Merensky Reefs. **a.** PtS within chromite fracture (from UG2 Reef). **b.** RuS_2 and PtBiTe associated with pentlandite (from UG2 Reef). **c.** Subhedral PtPdS interstitial to chromite (from the UG2 Reef). **d.** PdBiTe inclusion in silicate (from the Merensky Reef).

The PGM identified in the UG2 share grain boundaries with silicates, chromite and BMS (Fig. 2a, b and c) and in the Merensky PGM occur as silicates inclusions (Fig. 2d). The PGM occur in euhedral to anhedral shape and rounded to sub rounded shapes. Following Bachmann et al. (2018), the PGM in the UG2 and Merensky Reefs were grouped into PGE sulphides, PGE arsenides, PGE sulphoarsenides, PGE bismuthotellurides and PGE alloys. In the UG2, PGE sulphides accounted for nearly 60% of the total PGM grains (2480) counted, followed by PGE sulphoarsenides 13%, PGE alloys 10%, PGE arsenides 9%, and PGE bismuthotellurides 8% (Fig. 3a). In the Merensky Reef, PGE sulphides constitute about 34% of the total PGM grains (692) counted, followed by PGE bismuthotellurides at 31%, PGE arsenides 22%, PGE sulphoarsenides 7% and PGE alloys forming 6% (Fig. 3b). VIn the UG2, the PGE sulphides is dominated by cooperite (PtS, PtPdS), ranging from 50 to 75 % of the total PGE-sulphides, followed by laurite (RuS_2), forming about 16 to 40% of the total PGE sulphides. The PGE sulphoarsenides show a range between the hollingworthite (RhAsS)-irarsite (IrAsS)-platarite (PtAsS) solid-solutions, and sperrylite ($PtAs_2$), dominating the PGE arsenides. The PGE bismuthotellurides is dominated by michenerite (PdBiTe), ranging from 57 to 80% of the total grains followed by maslovite (PtBiTe). The PGE alloys is highly variable in composition. Like in the UG2, PGE sulphides in the Merensky Reef is dominated by cooperite (PtS) and braggite PtPdS), which together constitute between 71 to 80% of the total PGE sulphides. The PGE arsenide occur mostly as sperrylite, while the PGE sulphoarsenides form a PtAsS-PtRhAsS-PtPdAsS solid-solution series. The PGE bismuthotellurides occur as maslovite (PtBiTe) and michenerite (PdBiTe), and an intermediary PtPdBiTe, in almost equal proportions.

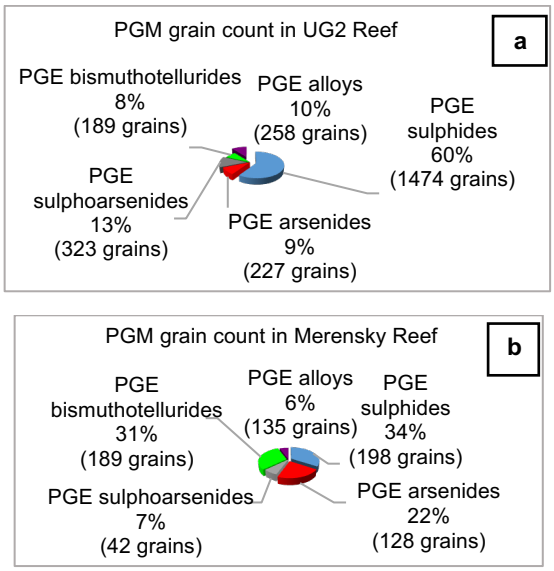

Figure 3. a. PGM grain count distribution in the UG2 Reef. **b.** PGM grain count distribution in the Merensky Reef.

3.2 PGM grain size distribution

The grain size of the PGM range from 0.73 to 32 µm and 0.87 µm to 27 µm in diameter in the UG2, Reef and Merensky Reef (equivalent circle diameter), respectively. The grain size distributions of the PGM in KFN 008 and KFN 014 are similar, where approximately, 97 wt. % of the grains passing through 19 µm, and approximately 70 wt. % passing 15 µm. Similarly, the cumulative grain size distribution in BH 8206 and BH 8026 also exhibit similar trend, with approximately 97 wt. % passing 19 µm, while approximately 50 wt. % 16 µm and 15 µm in BH 8206 and BH 8026, respectively (Fig. 4a). The cumulative grain size

distribution of the PGM in the Merensky Reef are slightly heterogeneous. Particularly, in the sieve size between 10 µm and 18 µm. The PGM in KFN 043 are much finner than the PGM in BH 8026. In KFN 043 the grain size of 30 wt. % passed 10 µm, while in BH 8026, less than 10 wt. % of PGM grain size passed 10 µm (Fig. 4b).

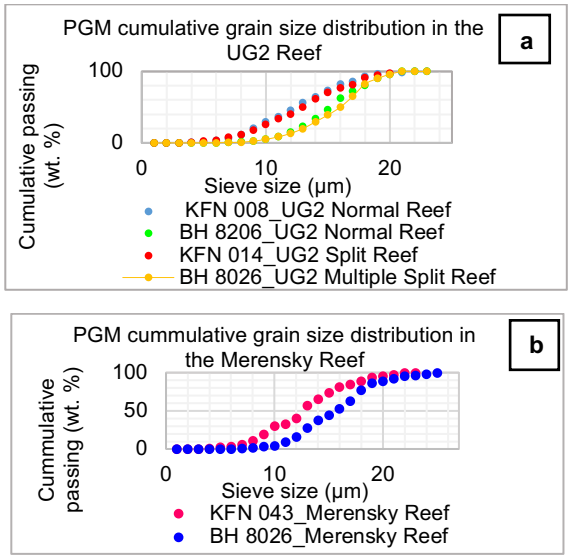

Figure 4. a. PGM cummulative grain size distribution in the UG2 Reef. **b.** PGM cumulative grain size distribution in the Merensky Reef.

3.3 PGM mineral association

The PGM mineral association is illustrated in Fig. 5 and shows mineral association with base metal sulphides, primary silicates, secondary silicates and oxides. Common minerals associated with the PGM in the UG2 are BMS, which are dominated by chalcopyrite, pentlandite and pyrrhotite, constitute a range between 35 to 65 area % of the total minerals associated with the PGM. However, chalcopyrite and pentlandite constitute over 80 area % of the base metal sulphides. Primary silicates indicate a range between 10 and 30 area % of the total mineral associated with the PGM, while secondary silicates constituting about 8 % of the total mineral association. In the Merensky Reef, primary silicates accounted for most of the minerals associated with the PGM. This is followed by base metal sulphides in a range from 20 to 32 area %, secondary silicates (14%) oxides (3%) which includes chromite.

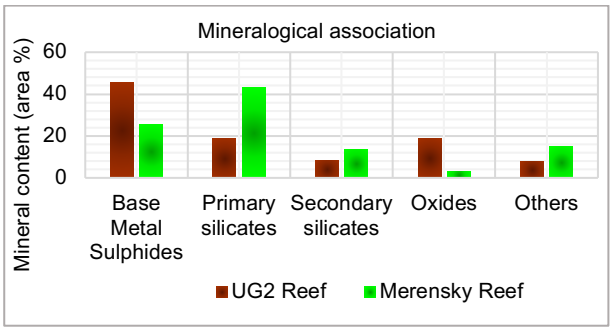

Figure 5. The minerals associated with the PGM in the UG2 Reef and in the Merensky Reef.

4 Conclusion

Magmatic Ni–Cu–PGE sulphide deposits form by segregation of immiscible droplets of dense sulphide melt from mafic to ultramafic magmas, where the PGE partition strongly into the sulphide melt S-saturation of the basaltic melts when emplaced in the crust, with the PGE having experimentally determined partition coefficients estimated between 1400–36000 (Barnes and Lightfoot 2005). Several theories have been proposed for the PGE mineralization in the UG2 and Merensky Reefs in the Bushveld Igneous Complex to explain their origin. For example, supersaturation of sulphides in the UG2 Reef may have been due to contamination or chromite precipitation (Naldrett and von Gruenewaldt 1989). Barnes and Maier (1999) proposed that the PGE supersaturation in the reef might have formed by sulphides solubility and ultimately sulphides immiscibility, which can be obtained by fractional crystallization of the magma as the temperature decreases, a reduction in the quantity of ferrous iron, or by mixing two compositionally distinct magmas. The Merensky Reef is thought to have formed from a magma pulse that contained entrained sulphides (Lee and Butcher 1990), hence the elevated sulphides content. Seabrooke et al. (2006) proposed that the Merensky Reef overall PGE concentration was the result of two independent mineralizing episodes, one linked to the creation of the chromitite layer and the other to sulphide mineralization. Other theories have documented that PGE enrichment is attributed to post-magmatic fluids (Ballhaus and Stumpfl 1986).

Although there are local variations in lithologies and mineralogy in the PGE-bearing reefs in the Bushveld Igneous Complex, the results from the study are consistent with general observation by several workers (e.g., Penberthy et al. 2000; Rose 2016) in the Eastern Bushveld Igneous Complex. The PGM show marked association with base metal sulfides (BMS). Approximately, 60% of the PGM in the UG2 Reef will be recovered considering that they occur as PGE sulphides, which have the fastest floating rates, while about 34% of the PGM will be recovered in the Merensky Reef under similar conditions. The PGM have significantly smaller average grain sizes of 7 and 10 µm for the UG2 and Merensky Reefs, respectively, and for optimum PGM recovery the ore needs to be milled to grain sizes of up to less than 3 µm. The PGM in UG2 Reef are mostly associated with base metal sulphides, and about 46% of PGM in the UG2 Reef are most likely to be recovered due to their association with the BMS which are naturally floatable. The secondary silicates minerals are more abundant in the Merensky Reef, and this may lead to poor recoveries. Therefore, longer flotation times would be required to increase

the flotation effectiveness. The marked association of PGE tellurides, arsenides and PGE alloys and secondary silicates, is consistent with the remobilisation and recrystallisation of some of the PGM during hydrothermal alteration subsequent to their initial primary crystallization.

Acknowledgements

National Research Foundation are thanked for funding the project from 2021 to 2022.

References

Bachmann K, Osbahr I, Tolosana-Delgado R, Chetty D, Gutzmer J (2018) Variation in platinum group mineral and base metal sulfide assemblages in the Lower Group chromitites of the western Bushveld Complex, South Africa. The Canadian Mineralogist 56(5):723-743

Ballhaus CG, Stumpfl EF (1986) Sulfide and platinum mineralization in the Merensky Reef: evidence from hydrous silicates and fluid inclusions. Contributions to Mineralogy and Petrology 94(2):193-204

Barnes SJ, Maier WD (1999) The fractionation of Ni, Cu and the noble metals in silicate and sulphide liquids. Short Course Notes-Geological Association of Canada 13:69-106

Barnes SJ, Lightfoot PC (2005) Formation of magmatic nickel sulfide deposits and processes affecting their copper and platinum group element contents. Int J Miner Process Int J Miner Process 93:246–255

Chetty D, Gryffenberg L, Lekgetho TB, Molebale IJ (2009) Automated SEM study of PGM distribution across a UG2 flotation concentrate bank: implications for understanding PGM floatability. J S Afr I Min Metall 109:587–593

Lee CA, Butcher AR (1990) Cyclicity in the Sr isotope stratigraphy through the Merensky and Bastard Reef units, Atok section, eastern Bushveld Complex. Economic Geology 85(4):877-883

Maier WD (2005) Platinum-group element (PGE) deposits and occurrences: Mineralization styles, genetic concepts, and exploration criteria. Journal of African Earth Sciences 41(3):165-191

McLaren CH, De Villiers JPR (1982) The platinum-group chemistry and mineralogy of the UG-2 chromitite layer of the Bushveld complex. Economic Geology 77(6):1348-1366

Penberthy CJ, Oosthuyzen EJ, Merkle RKW (2000) The recovery of platinum-group elements from the UG-2 chromitite, Bushveld Complex – a mineralogical perspective. Miner Petrol 68:213-222

Rose DH (2016) A process mineralogical investigation of the Merensky Reef and UG-2 at the Two Rivers Platinum mine with emphasis on ore characterization. University of Johannesburg (South Africa)

Seabrook CL, Cawthorn RG, Kruger FJ (2006) The Merensky Reef, Bushveld Complex: Mixing of Minerals Not Mixing of Magma. Economic Geology 100:1191-1206

Mineralogical constraints and evidence for crustal interaction in the Ni-rich systems of the Curaçá Valley mineral district, Bahia, Brazil.

Tercio Nunes[1], Gema Olivo[1], John Thompson[2], Filipe Porto[2]; Anderson Lima[2]; Pablo Graia[2] *[1]Department of Geological Science and Geological Engineering, Queen's University, Kingston, ON, Canada[2]Ero Copper corp., Vancouver, BC, Canada*

Abstract. The Curaçá Valley district is well-known for Cu sulfide mineralization in Proterozoic mafic-ultramafic intrusions with unusually high Cu:Ni ratios. Despite the overall predominance of chalcopyrite-bornite-rich mineralization in mafic-ultramafic intrusions, Ni-rich mineralized zones have been identified within the Vermelhos and Umburana sulfide systems. The Vermelhos system is associated to chalcopyrite-pyrrhotite-pentlandite mineralization predominantly hosted in orthopyroxenite, norite and gabbro-norite, with abundant phlogopite-spinel (+/- apatite-monazite and tellurides). The Umburana system is characterized by pyrrhotite- pentlandite-pyrite mainly hosted in hornblende-websteriteunits, which are overlain by orthopyroxenite with low-grademineralization. Both systems exhibit evidence of complex interactions with wall-rocks, including abundant country- rock xenoliths surrounded by reaction margins (e.g., phlogopite-rich rims). "Pegmatoidal" bodies are common at the contacts between the mafic-ultramafic intrusions and gneisses, and are interpreted as partial melts of country rocks during intrusion emplacement. The interaction of the mafic-ultramafic magmas with country rocks, including S-bearing gneisses, could have played an important role in forming the Ni-Cu sulfide mineralization associated with phlogopite-spinel-telluride-apatite-monazite. The mineralization in the Umburana system may represent crystallization from monosulfide solid solution (MSS), whereas Vermelhos was dominated by fractionated intermediate solid solution (ISS), overprinted by hydrothermal alteration.

1 Introduction

The mafic-ultramafic intrusions in the Curaçá Valley mineral district were emplaced in the highly metamorphosed terrains of the Paleoproterozoic Itabuna-Salvador-Curaçá belt, within the northern part of the São Francisco craton, Brazil (Oliveira et al 2004). These mafic-ultramafic intrusions host abundant Cu-mineralization (Figure 1), making the district the second largest Cu-producer in Brazil (Ero-Copper 2022a).

The mineralized zones are mainly characterized by chalcopyrite-bornite rich breccias hosted in orthopyroxenite and norite, containing abundant phlogopite-spinel, with local apatite-monazite and zircon (Maier and Barnes 1999; Teixeira et al. 2010). Within the Curaçá Valley's deposits, the Vermelhos and Umburana's systems host the highest Ni contents but display different Cu:Ni ratios and distinct host rock characteristics (Ero-Copper 2019, 2022b). The processes by which these systems were formed are still controversial, and little is known about the relationship between the Cu-rich and Ni-rich mineralization.

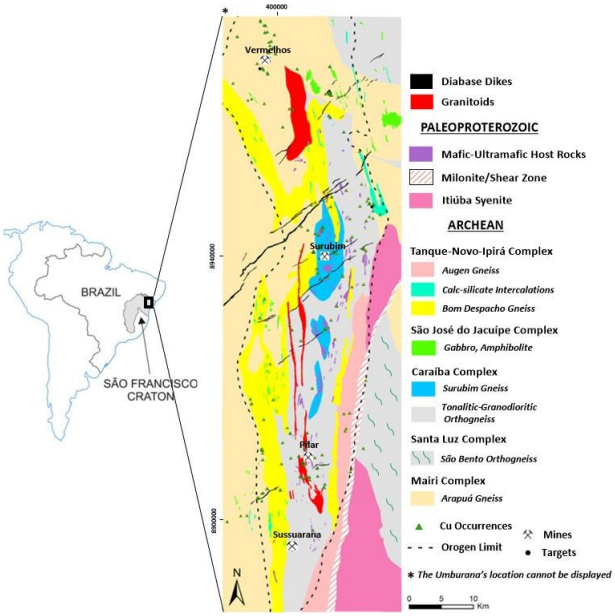

Figure 1. Geological map of the Curaçá Valley district, exhibiting the main Cu mines, occurrences, and mafic-ultramafic hosting intrusions.

2 Ni-rich mineralized systems

2.1 The Vermelhos system

Vermelhos has Cu:Ni values ranging from 6 to 40 in mineralized mafic-ultramafic rocks (Ero-Copper 2019). The Ni-rich zones are characterized by chalcopyrite(+/-bornite)-pyrrhotite-pentlandite in breccias with high content of phlogopite, various spinels and minor apatite (+/-monazite). PGE- bearing tellurides and electrum occur locally in the mineralized zones. The host rocks includeorthopyroxenite, norite, gabbro-norite with minor clinopyroxenite and websterite units.

The magmatic phases associated to the host rocks include (in different proportions) orthopyroxene, clinopyroxene, plagioclase, phlogopite, apatite, monazite and various types of spinels (some enriched in Al and Zn; Nunes et al. 2022). The earlymagmatic sulfides include pyrrhotite, pentlandite and minor Ni-tellurides. Chalcopyrite, several precious metals tellurides (including PGMs) and electrum, mostly occur filling corroded zones and fractures in the magmatic silicates, some Cr-spinels and pyrrhotite-pentlandite (Figure 2). Chalcopyrite is rarely seen in sharp contact with pyrrhotite- pentlandite. Chlorite, K-mica, epidote, carbonate,

serpentine, talc, and violarite replaced the early phases, which were also cut by late magnetite veins. Age-dating based on microprobe data (Suzuki and Adachi 1994) of monazite in the Ni-rich zones, confirmed late-overprinting of the mineralized system.

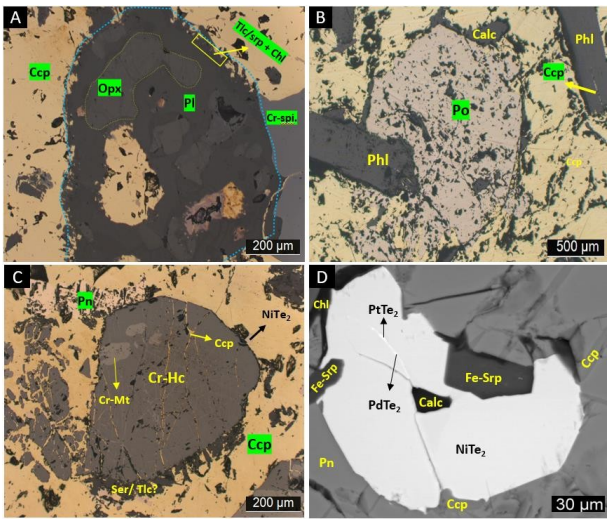

Figure 2. Optical (A-C) and backscattered-electron (BSE) images (D): **A)** Chalcopyrite (Ccp) filling corroded zones in orthopyroxene (Opx) and plagioclase (Pl), which are replaced by talc(Tlc)/serpentine (Srp) + chlorite (Chl) in the contact margins; **B)** Pyrrhotite (Po) and phlogopite (Phl) inclusions in Ccp, which fills cleavage plans in Phl and partially corroded zones in Po; **C)** Ccp filling fractures in the Cr-rich hercynite (Cr-Hc) which exhibit exsolutions of Cr-rich magnetite (Cr-Mt); **D)** Pd-Pt tellurides and Ccp filling fractures in Ni-telluride and spatially related to pentlandite (Pn), Fe-serpentine (Fe-Srp) and chlorite (Chl).

2.2 The Umburana system

Umburana contains mineralization with the lowest Cu:Ni ratios discovered to date hosted within mafic-ultramafic rocks in the district, ranging from 0.1 to 8 (Ero-Copper 2022b). The mineralization is composed of pyrrhotite-pentlandite-pyrite occurring as disseminated/blebs, net-textured, veins and massive/breccia, with only minor chalcopyrite, phlogopite and apatite (+/-monazite). The intrusion consists of an upper orthopyroxenite with minor mineralization overlying a hornblende-websterite with significant mineralization (Figure 3).

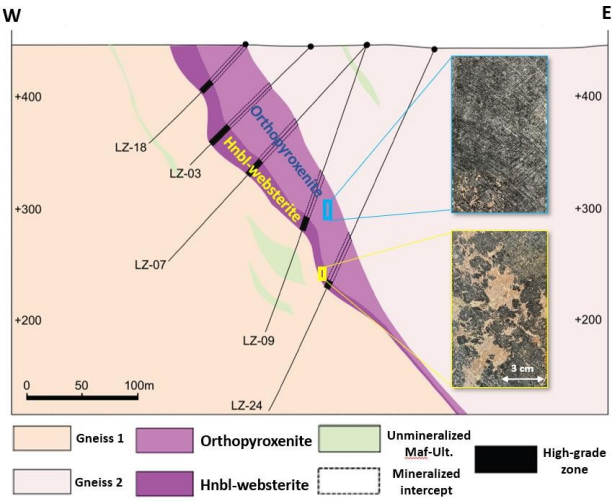

Figure 3. Geological section of the Umburana's LZ target, exhibiting the two main host rocks.

The orthopyroxenite unit (11-17.3% Mg; 0.09-0.16% Cr) contains orthopyroxene and minor clinopyroxene as cumulate phases with intercumulus plagioclase, hornblende and minor phlogopite (+/- apatite-monazite). Pyrrhotite and pentlandite occur as interstitial among the silicates (Figure 4).

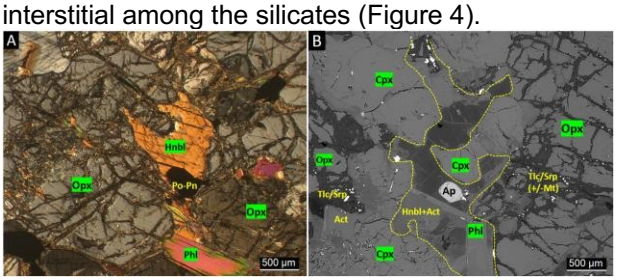

Figure 4. Optical (A) and BSE (B) images: **A)** Orthopyroxene (Opx) cumulates, and hornblende (Hnbl) and phlogopite (Phl) as intercumulus phases with interstitial pyrrhotite (Po) and pentlandite (Pn); **B)** Opx and clinopyroxene (Cpx) cumulates with Hnbl-plagioclase(Pl)-apatite(Ap)-Phl as intercumulus phases. Talc(Tlc)/serpentinte(Srp)-magnetite(Mt) occur filling corroded zones mostly in Opx, and actinolite (Act) in Hnbl and Cpx.

The hornblende-websterite (8.5-11% Mg; ~0.08% Cr) is the main mineralized unit, sitting stratigraphically below the orthopyroxenite. In this unit the orthopyroxene is highly altered by talc/serpentine and minor calcite, with remnants of intercumulus clinopyroxene, hornblende, plagioclase and minor apatite (+/- monazite). Pentlandite occurs in rims around pyrrhotite (forming loop textures in the high-grade zones) and both occur in sharp contact with chalcopyrite. Pyrite is mainly found as large inclusions in the pyrrhotite- pentlandite rich zones, with the latter two filling in corroded and fractured zones in the former (Figure 5).

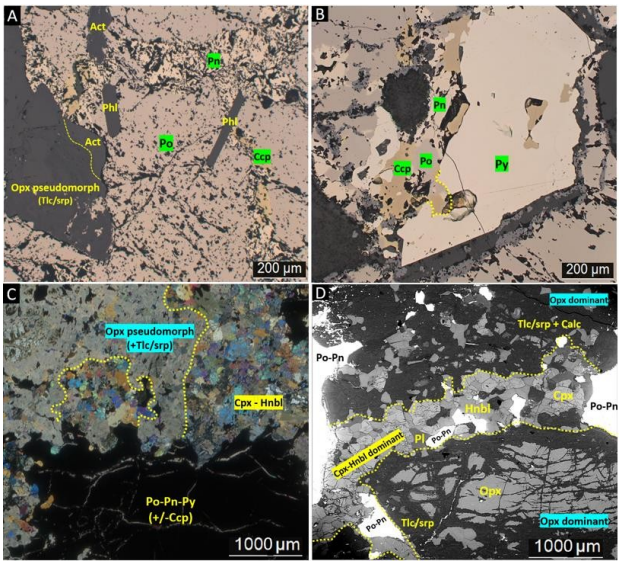

Figure 5. Optical (A-C) and BSE (D) images: **A)** Po with Pn rims and in sharp contact with Phl and Act inclusions; **B)** Po-Pn-Ccp and Tlc/Srp-Mt filling corroded zones in Py; **C)** Po-Pn-pyrite (Py) in contact with Cpx-Hnbl and highly altered Opx; **D)** Po-Pn as droplets/blebs in Cpx-Hnbl and filling corroded zones in altered Opx.

3 Evidence of crustal interaction

Complex interactions with wall-rocks are observed within the mineralized zones in the Umburana and Vermelhos systems. Wall-rock xenoliths have marginal reaction zones enriched in phlogopite and garnet. “Pegmatoidal” bodies are commonly presentin the contact zones of the mafic-ultramafic intrusions with the country rocks and surrounding some xenoliths in the mineralized zones. Some of the intercumulus phases of the Umburana host rocks exhibit similar mineralogy as the xenoliths, including plagioclase and apatite (+/- monazite; Figure 6). S-bearing paragneisses occur near the mineralized intrusions of both systems and might have introduced some S to the mafic-ultramafic magmas.

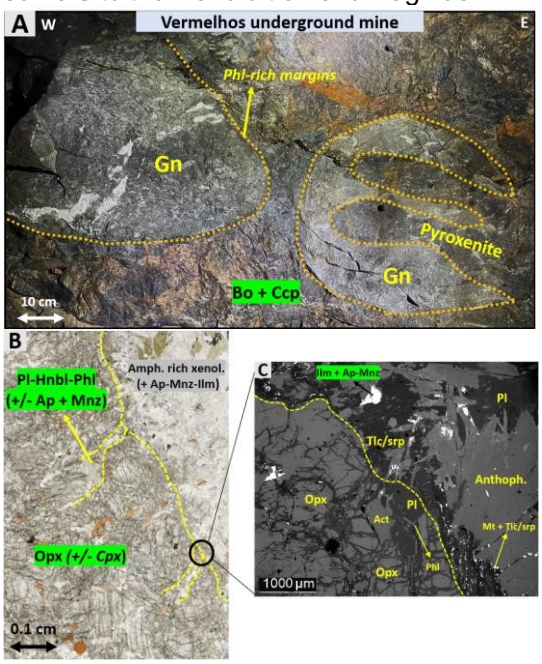

Figure 6. A) Country rock gneiss (Gn) xenoliths in highly mineralized zones of the Vermelhos underground mine; **B)**Pl-Hnbl-Phl-Ap-monazite (Mnz) as intercumulus phases inthe orthopyroxenite unit of Umburana, in contact withamphibole rich xenolith containing Ap-Mnz-ilmenite(Ilm); **C)** BSE image showing in detail the contact of the xenolith with cumulate Opx and intercumulus Pl-Act-Phl.

4 Preliminary interpretations

4.1 Parageneses

Based on the mineralogical and textural associations of this work, we propose the following paragenetic sequences (Figure 7) for the Umburana and Vermelhos systems:

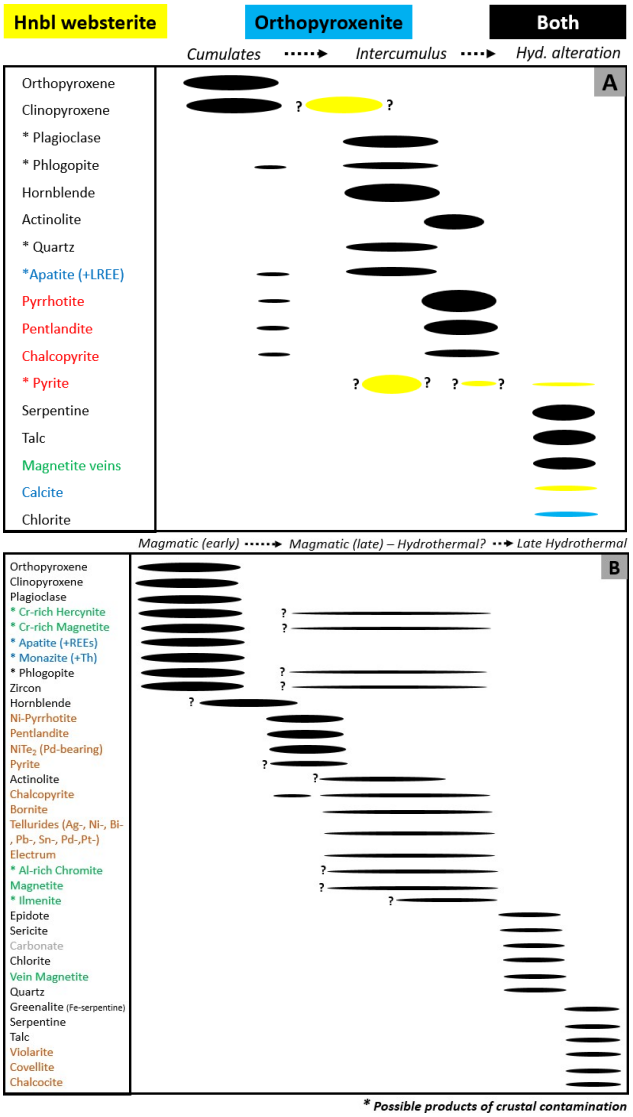

Figure 7. Paragenetic sequences of **A.** Umburana and **B.** Vermelhos.

4.2 Metallogenic model

Field and textural evidence suggest extensive interaction between wall-rocks and mafic-ultramafic magmas at the time of emplacement and crystallization. It is likely that contamination with crustal rocks influenced the igneous mineral assemblage with crystallization of orthopyroxene,

clinopyroxene, hornblende, phlogopite, various spinels (Al-Zn rich), apatite (+/- monazite) and sulfides.

The Umburana system is related to magmas that crystallized cumulus orthopyroxene, clinopyroxene +/- phlogopite) and intercumulus clinopyroxene-hornblende (+/- plagioclase-phlogopite-apatite-monazite). Based on the textural association seen in the hornblende-websterite unit where remnant clinopyroxene-hornblende-pyrrhotite-pentlandite occur between highly altered cumulus orthopyroxene, we interpret that the magma that formed the hornblende-websterite was emplacedinto the orthopyroxenite, and is the main host of thesulfide mineralization (Figure 8). The sulfide assemblage including pyrrhotite-pentlandite (+/- chalcopyrite) probably represents crystallizationfrom mono-sulfide solid solution (MSS).

The Vermelhos' host rocks were derived from mafic-ultramafic magmas that crystallized orthopyroxene, clinopyroxene and a greater amount of spinel (up to 50%), phlogopite (up to 60%) and plagioclase (up to 20%) in comparison to Umburana. Given the higher abundance of chalcopyrite and thus lower Cu:Ni values, mineralization may have crystallized largely from intermediate solid solution (ISS) to form chalcopyrite (+/- bornite) after early MSS (pyrrhotite-pentlandite).

Late hydrothermal alteration including chlorite, K-mica, epidote, carbonate, serpentine, talc, violarite and magnetite veins overprinted the system and locally remobilized the sulfides.

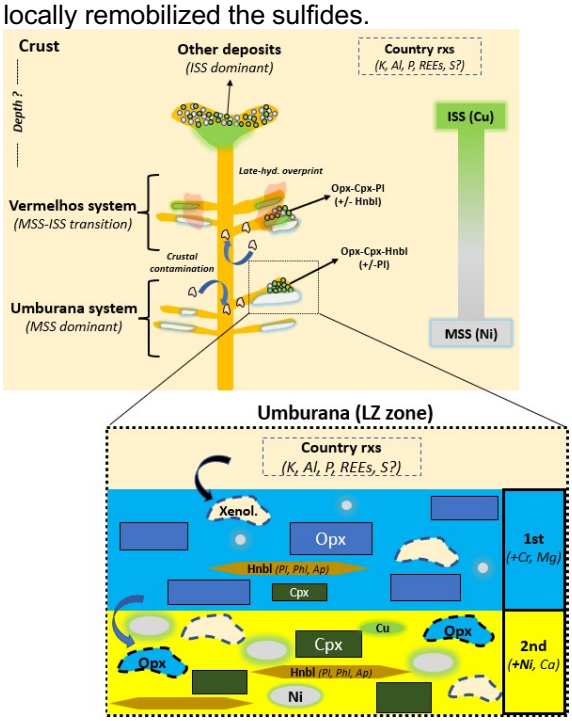

Figure 8. Metallogenic model of the Umburana and Vermelhos systems in the Curaçá Valley district.

5 Final remarks

- The host rocks in the Ni-rich Umburana and Vermelhos systems are pyroxene dominant, with the major differences related to the higher amount of clinopyroxene-hornblende in the highly mineralized zones of Umburana and more cumulate plagioclase and phlogopite-spinels- tellurides in Vermelhos.
- Chalcopyrite occurs as a minor phase and is coeval with pyrrhotite-pentlandite in the Umburana system, whereas in Vermelhos it is abundant and most of it postdates thosesulfides.
- Complex wall-rock interaction with mafic-ultramafic magmas likely led to crustal contamination within the mineralized zones of both systems, with possible addition of sulphur. This might explain the abundance of phlogopite, spinels (+Al-Zn) and minor apatite (+/-monazite), especially seen in Vermelhos. However, the exact timing and extent of the country rocks assimilation remains to be quantified.
- The different Cu:Ni ratios observed in both systems could be explained by extreme sulfide fractionation processes, in which Umburana would represent crystallization from MSS and Vermelhos predominantly ISS.

Acknowledgements

We thank Ero Copper Corp. for sponsoring this research, as well as Queen's University, Brian Joy and Agatha Dobosz for the analytical support.

References

Ero-Copper (2019): Ero-Copper news release, December 3, 2019. https://erocopper.com/news/ero-copper-intersects-51.8-meters-grading-3.49-copper-including-33.4-meters-grading-4.96-copper-in-pilar-mine-deepening/

Ero-Copper (2022a): Ero-Copper news release, January 6, 2022. https://erocopper.com/news/ero-copper-announces-updated-mineral-reserves-and-resources-for-the-mcsa-mining-complex-and-the-nx-gold-mine/

Ero-Copper (2022b): Ero-Copper news release, September 29, 2022. https://erocopper.com/news/ero-copper-announces-discovery-of-nickel-sulphide-system-in-the-curaca-valley-intercepts-16.5-meters-grading-1.22-nickel/

Maier W.D., and Barnes S.J. (1999): The origin of Cu sulfide deposits in the Curaca Valley, Bahia, Brazil; evidence fromCu, Ni, Se, and platinum-group element concentrations.Economic Geology, 94(2), 165-183.

Nunes, T. A. (2022). PDAC 2022 poster: "The Ni-PGE rich zones of the Vermelhos Cu-Deposits, Curaçá Valley District, Brazil: Constrains on the Spinel Composition".

Oliveira E.P. et al (2004): Contrasting copper and chromium metallogenic evolution of terranes in the Palaeoproterozoic Itabuna–Salvador–Curaçá orogen, São Francisco craton,Brazil: new zircon (SHRIMP) and Sm–Nd (model) ages and their significance for orogen-parallel escape tectonics.Precambrian Research, 128(1-2), 143-165.

Suzuki K., and Adachi M. (1994). Middle Precambrian detrital monazite and zircon from the Hida gneiss on Oki-Dogo Island, Japan: their origin and implications for the correlation of basement gneiss of Southwest Japan and Korea. Tectonophysics, 235(3), 277-292.

Teixeira J. B. G., et al. (2010): IV-Depósitos de Cobre do Valedo Rio Curaçá, Bahia. Modelos de Depósitos de Cobre do Brasil e sua Resposta do Intemperismo, 73-95.

Chemistry of major sulfides from Ni-Cu (PGE) mineralization at the Ransko ore district (Bohemian Massif): A result from LA-ICPMS study

Jan Pašava[1], Irina Andronikova[1], Vojtěch Wertich[1,2], Lukáš Ackerman[3], Petr Rambousek[1], Ondřej Pour[1], Karel Malý[4]
[1]Czech Geological Survey, Prague, Czech Republic
[2]Masaryk University, Brno, Czech Republic
[3]Institute of Geology, Czech Academy of Sciences, Prague, Czech Republic
[4]Aurum Discovery Ltd., Kells, Republic of Ireland

Abstract. The concentrations of platinum-group (PGE) and chalcophile elements in base metal sulfides (BMS) represented by pyrrhotite (Po), pentlandite (Pn), chalcopyrite (Cp) and cubanite (Cub) from the Ransko Ni-Cu (Co-PGE) deposit (Bohemian Massif) were determined by laser ablation-inductively coupled plasma-mass spectrometry (LA-ICPMS). In high-grade ore, the pyrrhotite shows a strong enrichment in Ag, Ir and Rh whereas the pentlandite is enriched in Cu, Pd and Ir. Cubanite is compared to chalcopyrite significantly enriched in Ag, Sb, Re, Os and Au whereas chalcopyrite shows slightly higher median Pd and Cd values. Rhenium, Os, Ir, Ru, and Rh occur mostly in solid solution in pyrrhotite and pentlandite from high-grade ore, which has been interpreted to represent monosulfide solid solution (mss) cumulates. The distribution of TABS (Te + As + Bi + Sb + Sn) in BMS indicates crustal contamination.

1 Geology and Mineralization

The Ransko massif is the ultra(mafic) body located in a transition zone between the Moldanubian, the Kutná Hora crystalline unit and the Hlinsko Zone in the Bohemian Massif, Czech Republic (Figure 1).

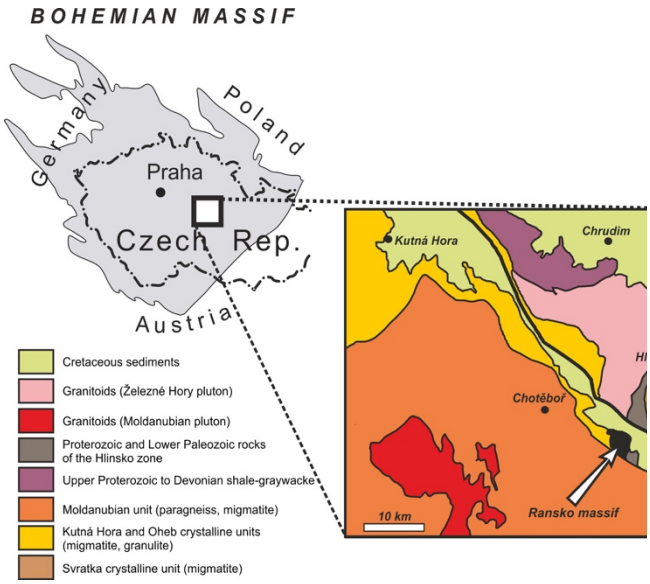

Figure 1. Geoloical position of the Ransko gabbro-peridotite massif (from Mísař 1974 modified by Ackerman et al. 2013).

It represents a strongly differentiated intrusive complex formed by peridotites and gabbroic rocks (gabbro, troctolite) with a magmatic segregation of low-grade Ni–Cu ores, a unique ore type in the Bohemian Massif. The exact geotectonic position of the Ransko massif and its relationship to adjacent units has been subject to several discussions (e.g. Synek and Oliveriová 1993, Štědrá and Nahodilová 2009, Pertoldová et al. 2010). While the Moldanubian and Kutná Hora units experienced polyphase Variscan high-grade metamorphism (~340 Ma), the adjacent part of the Hlinsko Zone was suggested to be Upper Proterozoic (Pitra and Guiraud 1994).

The Ransko massif has been subject of mining activity for a long time. For example, iron mining (oxidized, Fe-enriched caps) and smelting has been documented from the 14th until the end of the 19th century. Exploration for Ni-Cu-Co ores started in 1950s and resulted in finding of nine smaller ore bodies (e.g., Jezírka). Low grade Ni–Cu magmatic mineralization in troctolites is confined to a 3 km long and 1 km wide ore zone cutting the massif in a NE-SW direction (Mísař 1974). The ore zone is characterized by strong serpentinization and uralitization of the host rocks. Individual ore bodies are developed close to the contact of olivine-rich rocks (peridotite, troctolite) with gabbro, and particularly in the zones exhibiting varied alternation of troctolites with (olivine)gabbro. The Ni–Cu sulfide mineralization is not bound to a particular rock type but occur in various rock types as irregular lenses and horizons in a relatively strongly mineralized zone containing pyrrhotite and pyrite. Isolated and irregular occurrences of disseminated Cu-Ni ores were also discovered in troctolites and plagioclase-bearing peridotites. Within the Ni–Cu ores, Pašava et al. (2003) detected anomalous PGE concentrations with Pt+Pd contents up to ~0.7 ppm and revealed the presence of platinum-group minerals (PGM).

Based on paleomagnetic data, the Ransko massif was firstly assumed to be of Lower Cambrian age (Marek 1970). However, Re–Os data of barren and mineralized rocks from the Jezírka Ni–Cu body yield a regression of 341.5 ± 7.9 Ma assuming its Variscan age (Ackerman et al. 2013). This is exactly the same age of the mafic stock hosting Ni-Cu (PGE) mineralization at Aguablanca (Spain) (Romeo et al. 2006). Strongly mineralized Ransko peridotite with mantle like $^{187}Os/^{188}Os$ values suggest that PGE are predominantly of mantle origin. On the other hand, radiogenic $^{187}Os/^{188}Os$ values detected in barren and low mineralized samples indicate crustal

contamination of parental magmas during their emplacement.

2 Results and Discussion

2.1 Samples and Methods

The polished sections of low (RAN7- olivine gabbro with 0.11 wt% Cu and 0.09 wt% Ni and RAN17- troctolite with 0.46 wt.% Ni and 0.19 wt.% Cu) and high Cu-Ni (R1- troctolite with 2.3 wt% Cu and 1.6 wt% Ni) mineralization from the Jezírka deposit from Ransko were first studied using a reflected light microscopy and afterwards by a FE–SEM scanning microscopy using Tescan Mira3 GMU housed at the Czech Geological Survey (CGS).

Trace elements in sulfides were analyzed at the LA-ICPMS laboratory at the CGS using Agilent 7900 ICP-MS coupled with an Analyte Excite Excimer 193 nm LA system equipped with a two-volume HelEx ablation cell. Up to 30 isotopes were detected depending on the mineral (^{49}Ti, ^{51}V, ^{53}Cr, ^{55}Mn, ^{57}Fe, ^{59}Co, ^{60}Ni, ^{65}Cu, ^{66}Zn, ^{71}Ga, ^{74}Ge, ^{75}As, ^{77}Se, ^{101}Ru, ^{103}Rh, ^{107}Ag, ^{108}Pd, ^{111}Cd, ^{115}In, ^{118}Sn, ^{121}Sb, ^{125}Te, ^{185}Re, ^{188}Os, ^{193}Ir, ^{195}Pt, ^{197}Au, ^{201}Hg, ^{205}Tl, ^{208}Pb, and ^{209}Bi). We do not report Ru data for Pn and Rh data for Cp and Cub because of polyatomic interferences (Trubač et al. 2018).The laser was fired with spot size of 35-40 µm and fluence of 3.9-4.7 J/cm^2 with a laser pulse rate of 10 Hz. The GLITTER 3.0 software was used as a data reduction program. Internal standardization was based on Fe concentration determined by the SEM analysis and/or on the stoichiometric Fe values. Two reference materials were used for external calibration: the USGS MASS-1 (Wilson et al., 2002) and UQAC-FeS-1 (Savard et al. 2018, Duran et al. 2019) sulfide pellets. The UQAC-FeS-5 (Savard et al. 2018) and GSE-2g, a syntetic basalt material supplied by USGS (Mayers et al. 1976) were used for quality control.

2.2 Mineralogy

The ore minerals includes pyrrhotite, pentlandite, chalcopyrite and cubanite with minor pyrite, (Cr)magnetite, picotite, mackinawite, valleriite, ilmenite, galena, sphalerite, cobaltite–gersdorffite, native bismuth, gold, PGM represented by michenerite, froodite and sperrylite and tellurides represented by tsumoite, hessite and unnamed Bi-Ni telluride (Vavřín and Frýda 1998, Pašava et al. 2003 and references therein).

In this study, we newly identified an unnamed Pd-Bi-Sb phase in close association with michenerite and froodite, melonite (NiTe) in form of inclusions in pyrrhotite, and clausthalite (PbSe). Our high-grade ore sample (R1) is mainly composed of pyrrhotite, pentlandite and cubanite (Figure 2A) whereas low-grade ore (samples RAN-07 and RAN-17) is characterized by dominating pyrrhotite, pentlandite and chalcopyrite (Figure 2B).

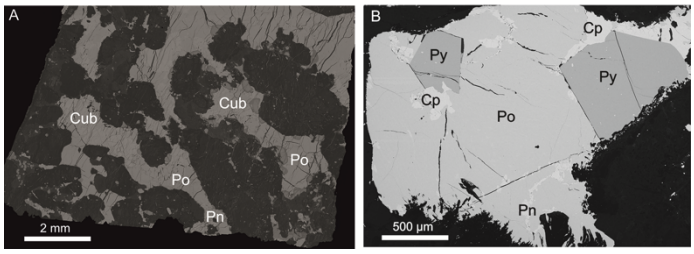

Figure 2. Photomicrographs of typical ore from Ransko. **A** – high-grade ore with pyrrhotite (Po), pentlandite (Pn) and cubanite (Cub). **B** – low-grade ore with pyrrhotite, pentlandite and chalcopyrite. Abbreviations: Cub – cubanite, Cp – chalcopyrite, Pn – pentlandite, Po – pyrrhotite and Py – pyrite.

2.3 Trace element concentrations in Base Metal Sulfides (BMS)

The ranges of concentrations of PGE in major base metal sulfides are shown on Figure 3.

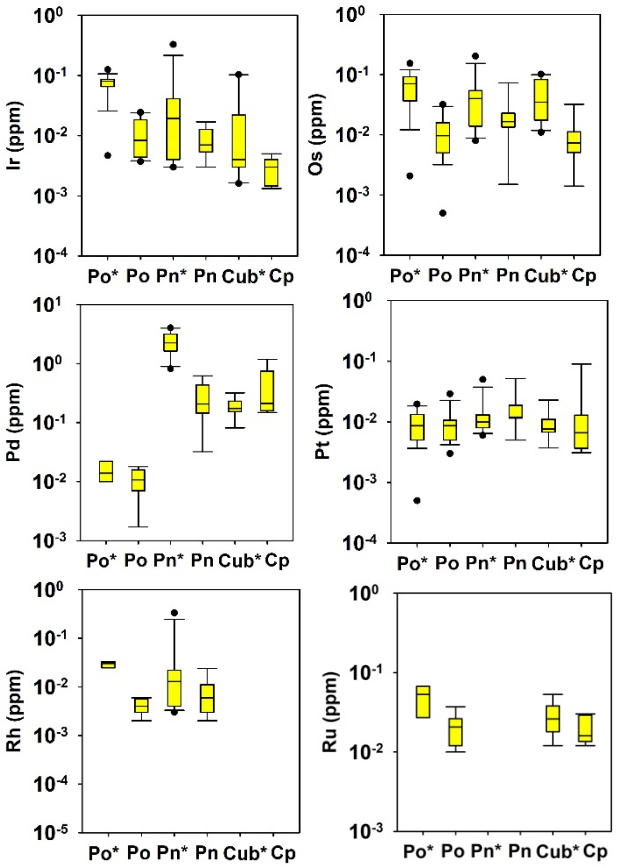

Figure 3. Box and whiskers plots for PGE in sulfides from Ransko. Po – pyrrhotite, Pn – pentlandite, Cub – cubanite, Cp – chalcopyrite, * sulfide from high-grade ore. The boxes are framed by 25th and 75th percentile, line within the box indicates median value. Whiskers displays 10th and 90th percentile and outliers are shown as one symbol representing 5th and 95th percentile.

The median concentrations of other selected trace elements (including TABS) in major BMS are shown in Table 1.

Iridium and Rh show the highest median values in Po from high-grade ore while Pt and Pd are dominating in high-grade ore Pn. Both the sulfides

have the highest median Os values. Such distribution reflects very likely concentration of these metals in monosulfide solid solution similarly as reported from other Ni-Cu deposits (e.g. Aguablanca, NW Spain - Piña et al. 2012). Chalcopyrite is characteristic of the highest median values of Te, Cd, In and Zn while Cub bear peak median values of Ag, Re, Bi and Sb.

To investigate the role of crustal assimilation on the metal contents, we used As and Sb concentrations (Samalens et al. 2017; Mansur et al. 2021) in Pn (Figure 4). Both elements are incompatible with MSS and ISS and therefore, their concentrations in the sulfide liquid tend to increase with progressive fractionation.

Table 1. The median concentrations of selected trace elements in major BMS from Ransko (values in ppm).

	Po	Pn	Cub	Po	Pn	Cp
	high-grade ore			*low-grade ore*		
Co	13	1588 3	0.28	62.1 1	3354 3	0.34
Cu	0.84	482. 2	2357 70	1.02 5	28.9 2	3299 96
Zn	0.55	1.01	205.7	0.58	1.03	474.3 1
As	0.43	0.89	0.39	0.40	0.89	0.30
Se	84	72.4	73.9	55.9	62.0	47.5
Ag	1.2	6.2	14.6	0.13	2.5	1.32
Cd	0.08	0.18	11.0	0.05	0.18	19.30
In	0.00 3	0.00 6	0.10	0.00 5	0.00 4	0.15
Sn	0.14	0.15	0.19	0.15	0.17	0.12
Sb	0.19	0.15	12.87	0.17	0.21	0.16
Re	0.05 6	0.08 6	0.161	0.08 5	0.02 1	0.003
Au	0.00 5	0.01 6	0.017	0.00 5	0.02 2	0.005
Tl	0.01	0.05		0.00 3	0.03	
Pb	1.23	2.58	5.62	0.87	4.73	4.16
Bi	0.75	0.51	0.90	0.28	0.89	0.45
Te	0.22	0.28	2.22	0.52	0.6	2.54

The values of Sb/Se and As/Se ratios in Pn from both types of ore at Ransko are well comparable with other magmatic Ni-Cu deposits which show external input of As and Sb in the sulfide liquid through crustal assimilation (see Mansur et al. 2021). High Sb values and a negative correlation between Sb/Se and As/Se in low grade ore likely reflect different crustal sources (lithologies).

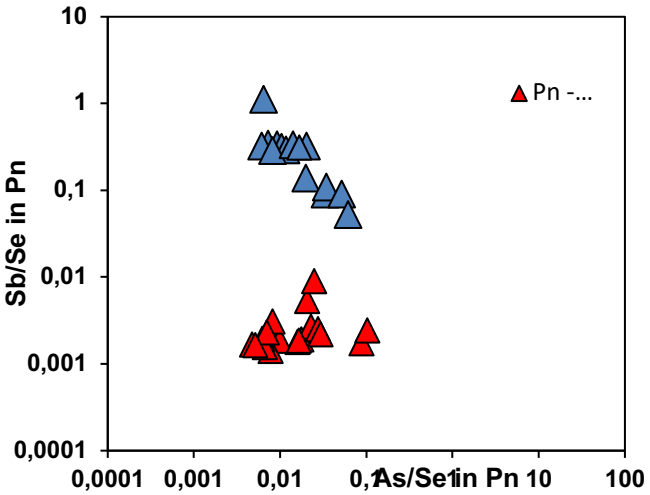

Figure 4. Binary plot of Sb/Se and As/Se in pentlandite (Pn) from the Staré Ransko Ni-Cu deposit.

In magmatic sulfide deposits, a fraction of the PGE is hosted by BMS, whereas the remaining PGE with TABS form PGM (e.g., Junge et al. 2015). Within Ni-Cu deposits, the effect of fractional crystallization on the composition of BMS is dominantly relative to the effect of PGM exsolution. Mansur et al. (2021) concluded that although there is no clear negative correlation between PGE and TABS concentrations in Pn, there is an increase in concentrations of both PGE and TABS from Cu-poor to Cu-rich ores (e.g., Pn from Noril'sk-Talnakh) which is consistent with the situation at Ransko (Figure 5).

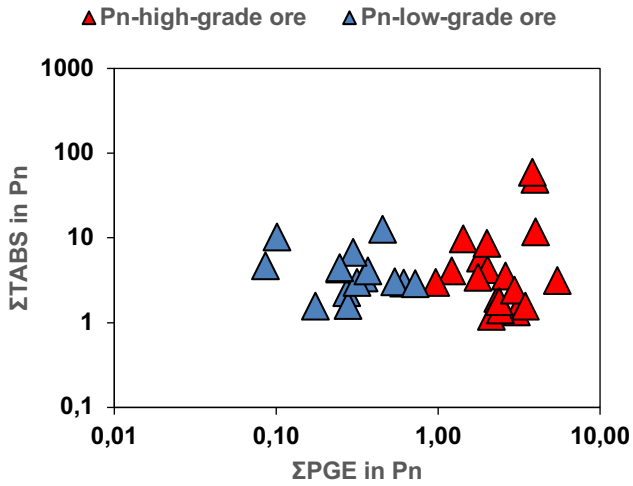

Figure 5. Binary plot of ΣTABS versus ΣPGE in Pn from Ransko Ni-Cu deposit. ΣTABS: Te + As + Bi + Sb + Sn. ΣPGE: Pt + Pd + Rh + Ir + Os.

To evaluate the influence of the R-factor on the BMS composition we used mantle normalized plots for strongly to highly (Figure 6 a,b), and slightly to moderately chalcophile elements (Figure 7 a,b). The elements are disposed from left to right in order of increasing partition coefficient into a sulfide liquid relative to silicate liquid ($D^{sulf/sil}$). The Po and Pn show similar shapes (Figure 6 a,b) suggesting similar R-factors during their formation.

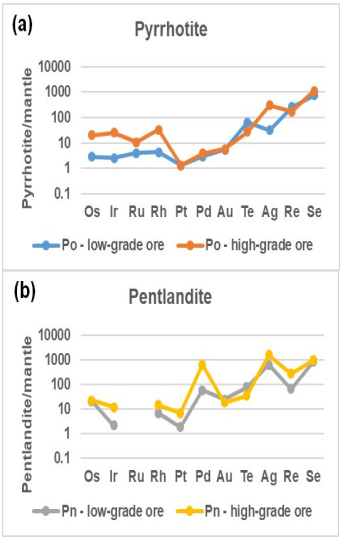

Figure 6. Strongly and highly chalcophile element primitive mantle normalized diagrams for median compositions of **(a)** Po and **(b)** Pn from Ransko. Primitive mantle values from Lyubetskaya and Korenaga (2007).

The median values of IPGE (Ir, Os, Ru) are higher in Po from high-grade ore in relation to Po from low-grade ore. The Pn from high-grade ore is typical of a strongly positive Pd and Ag anomalies while the Pn from low-grade ore shows more negative Ir, Pt and Re anomalies.

The mantle-normalized patterns for median Po composition are relatively flat and have slightly negative Cd, Co and In anomallies, a strong negative Zn anomaly and a strong positive Sb anomaly (Figure 7a). The patterns for median Pn compositions are similar to those for Po, but in contrast, Pn shows strongly positive Co anomaly not observed in Po patterns (Figure 7b).

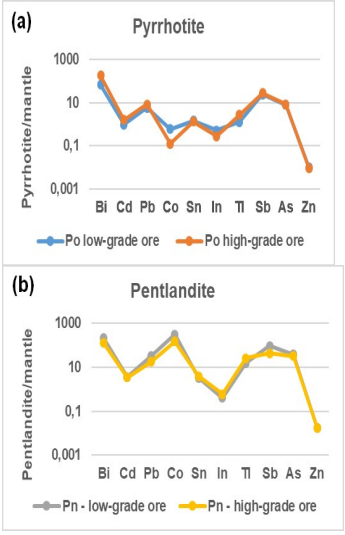

Figure 7. Slightly and moderately chalcophile element primitive mantle normalized TABS diagrams for median compositions of **(a)** Po and **(b)** Pn from Ransko.

Conclusions

The results of LA-ICPMS study of BMS at Ransko can be summarized as follows:

(1) In high-grade ore, the pyrrhotite shows a strong enrichment in Ag, Ir and Rh whereas the pentlandite is enriched in Cu, Pd and Ir. Cubanite is highly enriched in Ag, Sb, Re, Os and Au whereas chalcopyrite shows slightly higher median Pd and Cd values.

(2) Rhenium, Os, Ir, Ru, and Rh occur mostly in solid solution in pyrrhotite and pentlandite from high-grade ore representing monosulfide solid solution cumulates.

(3) The values of Sb/Se and As/Se ratios in pentlandite from both types of ore at Ransko most likely reflect external input of As and Sb in the sulfide liquid by crustal assimilation. This is also supported by the distribution of slightly to moderately chalcophile elements.

(4) There is an increase in concentrations of both PGE and TABS from Cu-poor to Cu-rich ores.

Acknowledgements

This study has been co-funded by the European Union (SEMACRET, Grant Agreement no. 101057741) and UKRI. It is also a contribution to the Strategic Research Plan of the Czech Geological Survey (DKRVO 2023-2027). We thank an anonymous reviewer for useful comments.

References

Ackerman L, Pašava J, Erban V (2013) Re–Os geochemistry and geochronology of the Ransko gabbro–peridotite massif, Bohemian Massif. Mineral Deposita 48:799-804

Duran CJ, Dube-Loubert H, Page P, Barnes SJ, Roy M, Savard D, Cave BJ, Arguin JP, Mansur ET (2019) Applications of trace element chemistry of pyrite and chalcopyrite in glacial sediments to mineral exploration targeting: Example from the Churchill Province, northern Quebec, Canada. J Geochem Explor 196:105-130

Faryad SW (2009) The Kutná Hora Complex (Moldanubian zone, Bohemian Massif): A composite of crustal and mantle rocks subducted to HP/UHP conditions. Lithos 109:193-208

Holub M, Jelínek E, Komínek E, Pluskal jr. O (1992) Genetic model of sulfide mineralization of the Ransko gabbro peridotite massif (Bohemia, Czechoslovakia). Sborník geologických věd, ložisková geologie, 30:7-42

Junge M, Wirth R, Oberthür T, Melcher F, Schreiber A (2015) Mineralogical siting of platinum-group elements in pentlandite from the Bushveld Complex, South Africa. Mineral Deposita 50:41–54

Lyubetskaya T, Korenaga J (2007) Chemical composition of earth's primitive mantle and its variance: 1. method and results. J Geophys Res 112:B03211

Mansur ET, Barnes SJ, Duran CJ (2021) An overview of chalcophile element contents of pyrrhotite, pentlandite, chalcopyrite, and pyrite from magmatic Ni-Cu-PGE sulfide deposits Mineral Deposita 56:179-204

Marek F (1970) Odhad stáří ranského bazického masívu podle paleomagnetických dat. Bulletin of the Czech Geological Survey 45:99-102 (in Czech with English abstract)

Mísař Z (1974) The Ransko gabbro - peridotite massif and its mineralization (Czechoslovakia). Prague, Charles University, 215 p.

Mísař Z (1979) Sulfide mineralization in the Ransko gabbro-peridotite massif, Czechoslovakia. Can Mineral 17:299-307

Myers AN, Havens RG, Connor JJ, Conklin NM, Rose HJ JR (1976) Glass Reference Standards for the Trace-Element Analysis of Geological Materials-Compilation of Interlaboratory Data. Geological Survey Professional Paper 1013 UNITED STATES Government printing Office, Washington

Pašava J, Vavřín I, Frýda J, Janoušek V, Jelínek E (2003) Geochemistry and mineralogy of Platinum-group elements in the Ransko gabbro-peridotite massif, Bohemian Massif, Czech Republic. Mineral Deposita 38:298-311

Pertoldová J, Verner K, Vrána S, Buriánek D, Štědrá V, Vondrovic L (2010) Comparison of lithology and tectonometamorphic evolutionof units at the northern margin of the Moldanubian Zone: implications for geodynamic evolution in the northeastern part of the Bohemian Massif. J Geosci 55:299-319

Piña R, Gervilla F, Barnes SJ, Ortega L, Lunar R (2012) Distribution of platinum-group and chalcophile elements in the Aguablanca Ni-Cu sulfide deposit (SW Spain): evidence from a LA-ICP-MS study. Chem Geol 302:61-75

Pitra P, Guiraud M (1996) Probable anticlockwise P-T evolution in extending crust: Hlinsko region, Bohemian Massif. J Metamorph Geol 14:49-60

Romeo I, Lunar R, Capote R, Quesada C, Dunning GR, Piña R, Ortega L (2006) U/Pb age constraints on Variscan Magmatism and Ni–Cu–PGE metallogeny in the Ossa-Morena zone (SW Iberia). J. Geol. Soc. London 163:837-846

Samalens N, Barnes SJ, Sawyer EW (2017) The role of black shales as a source of sulfur and semimetals in magmatic nickel-copper deposits: example from the Partridge River Intrusion, Duluth Complex, Minnesota, USA. Ore Geol Rev 81:173-187

Savard D, Bouchard-Boivin B, Barnes SJ, Garbe-Schönberg D (2018) UQAC-FeS: A new series of base metal sulfide quality control reference material for LA-ICP-MS analysis. In Proceedings of the 10th International Conference on the Analysis of Geological and Environmental Materials, Sydney, Australia, 8-13 July 2018

Synek J, Oliverová D (1993) Terrane character of the north-eastmargin of the Moldanubian Zone: the Kutná Hora Crystalline Complex, Bohemian Massif. Geol Rund 82:566-582

Štědrá V, Nahodilová R (2009) High-pressure metabasic rocks from the Kutna Hora Complex: geological position and petrology of exotic lithologies along the segmented Moldanubian margin, Bohemian Massif. J Geosci 54:135-157

Vavřín I, Frýda J (1998) Michenerite PdBiTe and froodite $PdBi_2$ from the Cu-Ni mineralization in the Ransko Massif, Czech Republic. Mineral. Petrol. 63:141-146

Wilson SA, Koenig AE, Ridley WI (2002) Development of sulfide calibration standards for the laser ablation inductively-coupled plasma mass spectrometry: J. Anal. At. Spectrom. 17: 406-409

Trubač J, Ackerman L, Gauert Ch, Ďurišová J, Hrstka T (2018) Platinum-Group Elements and Gold in Base Metal Sulfides, Platinum-Group Minerals, and Re-Os Isotope Compositions of the Uitkomst Complex, South Africa. *Econ Geol* 113: 439–461

Ilmenite-hosted fluid inclusions: Snapshot of magmatic fluid chemistry in mafic rocks

Anthony Pochon[1, 2], Daniel J. Kontak[3], Eric Gloaguen[1, 2], Johann Tuduri[1, 2], Giada Iacono-Marziano[1], Héctor R. Campos Rodríguez[1], Val Mollé[1], Tom Chatelin[1],
[1]ISTO, UMR 7327, Université d'Orléans, CNRS, BRGM, Orléans, France
[2]BRGM, Orléans, France
[3]Harquail School of Earth Sciences, Sudbury, Canada

Abstract. As volatiles play a major role in the igneous ore systems, this study aims to characterize the magmatic fluid chemistry of two early Carboniferous mafic magmatic systems related to Variscan Sb deposits, the Saint-Jean-du-Doigt intrusion in the French Armorican Massif and the San Antonio sill swarm in the Central Iberian zone. As unusual proxy, magmatic ilmenite from these two settings hosting abundant primary fluid inclusions were fully characterized texturally and chemically in order to assess their origin and determine their compositions. Results show that similar ilmenite textures and nature of fluid inclusions characterize the two mafic bodies. Qualitative studies, using SEM-EDS and LA-ICP-MS analyses of evaporate mound and LA-ICP-MS analyses of fluid inclusion rich areas, reveal the trapped fluids are multi-component and are dominated by Na-Ca-S-Sr in Saint-Jean-du-Doigt and San Antonio areas, but in different proportions. In addition, variable amounts of Sb, As, Zn, Mo, W, Pb, Cu, Zr and Hf are present. The data clearly demonstrate that mafic magmatic fluids may contain a non-negligible content of metals and metalloids. Although incomplete, the results reveal that magmatic fluids from the early Carboniferous mafic magmatism contain Sb and thus might constitute a source of Sb in the Variscan belt.

1 Introduction

Volatiles play a major role in the evolution of magmas from their generation in the mantle to eruption at the surface. In particular, water exerts a key control for ore forming processes (e.g., Hedenquist and Lowenstern 1994) and can be used as a vector for metals. Indeed, the abundance of H_2O leads to specific late-magmatic mineral assemblages and strongly controls replacement processes (Putnis and Austrheim 2010). The role and the importance of magmatic aqueous fluids in ore-forming processes is well established in classical felsic systems (e.g. porphyry deposits), but is markedly less constrained in upper crustal mafic magmas. Consequently, the magmatic-hydrothermal transition is not commonly investigated in mafic rocks.

Nevertheless, in the past few years the role of volatiles in mafic igneous ore systems has been revaluated, as well evidenced for conventional magmatic Ni-Cu sulfide deposits (Iacono-Marziano et al. 2022). In the European Variscan belt, spatial links have been demonstrated between mafic intrusions and "*unconventional*" Sb deposits (Pochon et al. 2016, 2018). Indeed, early Carboniferous mafic magmatism is spatially related with some Sb deposits in the external unthickened domains of the belt, *i.e.* the Central Iberian-Armorican zone (Figure 1, Pochon et al. 2016). Here the Sb is not directly associated with dolerite dikes and sills at surface, but instead with mafic bodies present at depth. This raises the question of whether magmatic fluids may supply Sb and related metal and metalloids to the hydrothermal system. In one of these early Carboniferous mafic intrusions ilmenite has been shown to be an excellent proxy of the magmatic-hydrothermal transition, as it has been shown to host fluid inclusions (FIs) enriched in metals and metalloids (Pochon et al. 2023).

In order to assess the role of mafic magmatic fluid as a metal carrier and potential source, we focussed on two mafic magmatic systems, the Saint-Jean-du-Doigt (SJDD) intrusion in the French Armorican Massif (Pochon et al. 2023) and the San Antonio sill swarm (SA) in the Central Iberian zone (Extremadura, Spain). These two intrusive complexes: (i) have similar emplacement ages (i.e. 347 ± 4 Ma for SJDD, Barboni et al. 2013 and 354 ± 5.4 Ma for SA, Campos et al. 2022); (ii) are located in the same geodynamical domain (Figure 1); and (iii) are likely to be the counterpart of early Carboniferous mafic bodies located below the Sb occurrences at depth.

To address the above, we have texturally and chemically characterized ilmenite-hosted FIs from the mafic rocks of these two magmatic systems. These data, when combined with detailed information about alteration history of the rocks, allow the tracking of the magmatic-hydrothermal transition of the intrusions and the composition of the fluids produced by magma degassing.

2 Methodology

Reflected light microscopy and SEM were used to characterize textures of ilmenites and their areas hosting FIs in samples from the SJDD gabbro (Armorican Massif) and the SA gabbroic sills (Central Iberian zone). As ilmenite absorbs infrared light, micro-thermometric studies could not be performed. However, as the ilmenites contain high abundances of FIs, qualitative information about their chemistry was obtained by comparing trace element compositions of FI-free and FI-bearing ilmenites obtained via LA ICP-MS.

In addition, qualitative measurements of key elements and complexing agents present in the trapped fluid were obtained in SJDD ilmenite with a procedure modified after Kontak (2004). Samples were rapidly heated around 500-600°C to induce FI decrepitation and subsequently quenched by

immediately switching off the heating source. The resulting evaporate mounds that formed on the sample surfaces were characterized for their major and trace element composition using a SEM-EDS technique, EPMA maps and LA ICP-MS traverses.

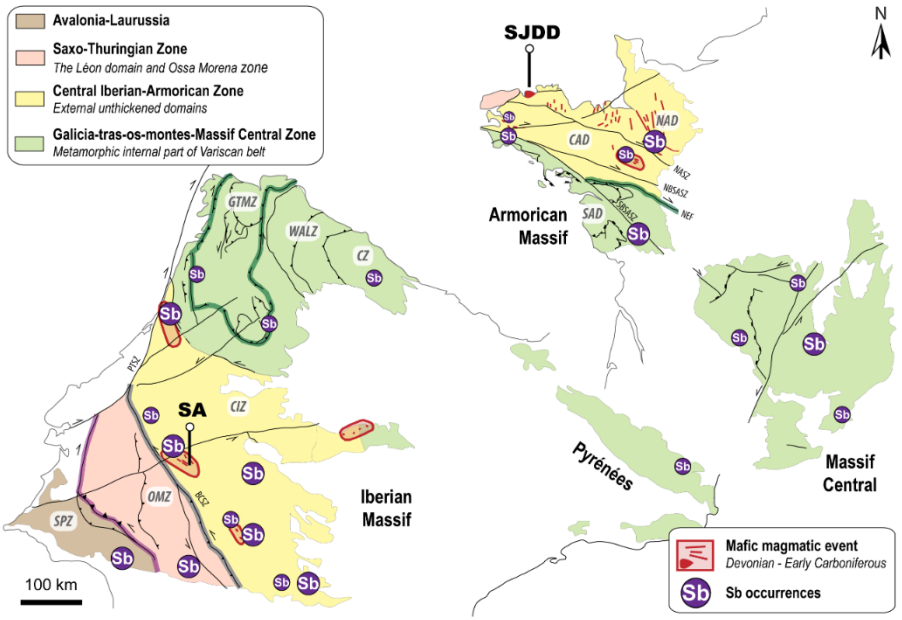

Figure 7. Schematic representation of the west European Variscan belt representing the main terranes and showing the relationship between early Carboniferous mafic magmatism and hydrothermal Sb deposits (modified from Ballouard et al. 2018). NAD: North Armorican domain, CAD: Central Armorican domain, SAD: South Armorican domain, GTMZ: Galicia-Trás-os-Montes zone, WALZ: West Asturian-Leonese zone, CZ: Cantrabrian zone, CIZ: Central Iberian zone, OMZ: Ossa Morena zone, SPZ: South Portuguese zone, NASZ: north Armorican shear zone, NBSASZ: northern branch of the south Armorican shear zone, SBSASZ: southern branch of the south Armorican shear zone, NEF: Nort-sur-Erdre fault.

3 Results

3.1 Textural relation and ilmenite composition

Both the SJDD gabbro and the SA dolerite host similar textured ilmenite with high abundances of FIs equally distributed in the host phase (Figure 2a).

Ilmenite crystals are subhedral to anhedral and occur in direct contact with almost all major minerals, i.e. along grain boundaries between plagioclase, clinopyroxene and amphibole. Ilmenite hosts a high density of crystal defects, which consist of vacancy aggregates, i.e. voids that likely formed during crystal growth and consist of trapped FIs (Pochon et al. 2023).

Most ilmenite crystals show both FI-free and FI-bearing areas, with FI-rich zones in the core areas (up to 15 % of the total crystal surface), whereas FI-free zones typically mantle the latter and also occur more rarely within the crystal (Figure 2a, b). Ilmenite is often rimmed by titanite (i.e. ~10 µm-thick zone around ilmenite) with the contact between the two phases being irregular (i.e. corroded), and some blocky rutile crystals are sometimes present in the rims. The FIs show either negative crystal or irregular shapes with sizes ranging between 0.5 and 5 µm and are either organized in sub-parallel trails, which occur parallel to the elongation (i.e. the c-axis) of the ilmenite, or are randomly distributed.

The contents of two relevant trace elements (Ni and Sb) in ilmenite are plotted in a univariate boxplot (Figure 2c) which distinguishes between FI-free and FI-rich zones. The Sb content shows a net enrichment from FI-free to FI-rich areas. For SJDD, FI-free ilmenite has a mean Sb value of 0.51 ppm, whereas FI-rich ilmenite has mean Sb value of 3.02 ppm. A similar enrichment is observed for SA where FI-free ilmenite has a mean Sb value of 3.22 ppm, whereas FI-rich ilmenite has a mean Sb value of 16.32 ppm. As Sb is strongly incompatible in ilmenite (Klemme et al. 2006), the Sb enrichment in the ilmenite clearly suggests it is carried by FIs. In contrast, Ni, a compatible element in ilmenite (Shepherd et al. 2022), does not seem to be affected by the presence of FIs with similar mean values for FI-free and FI-rich areas (Figure 2c).

Other trace elements (not shown) that are clearly enriched in FI-rich areas of SJDD ilmenite are Sr (FI-free: 0.17 ppm, FI-rich: 0.56 ppm), Mo (FI-free: 1.13 ppm, FI-rich: 11.1 ppm), Pb (FI-free: 0.14 ppm, FI-rich: 1.44 ppm), and W (FI-free: 0.32 ppm, FI-rich: 4.97 ppm).

3.2 Compositions of evaporate mounds

After heating, the presence of evaporate mounds is easily observed, using reflected light, at the ilmenite surface in the form of circular mounds that are commonly surrounded by an aureole of smaller debris. However, mounds with irregular or linear shape are also observed.

Chemically, the evaporate mounds are invariably multi-component and dominated by Na-Ca (∑ ≈ 70 wt. %) in variable proportions and by S (≈ 30 wt. %). These three elements are present in all mounds, whereas K, Ba and Cl are much less present (i.e. only to 36%, 6%, and 6% of analysed mounds, respectively). The K/Ca and K/Na ratios are relatively low, with a mean value of 0.06 and 0.03, respectively. An EPMA map of an evaporate mound is displayed in Figure 3 to illustrate its typical circular texture and the major element distribution.

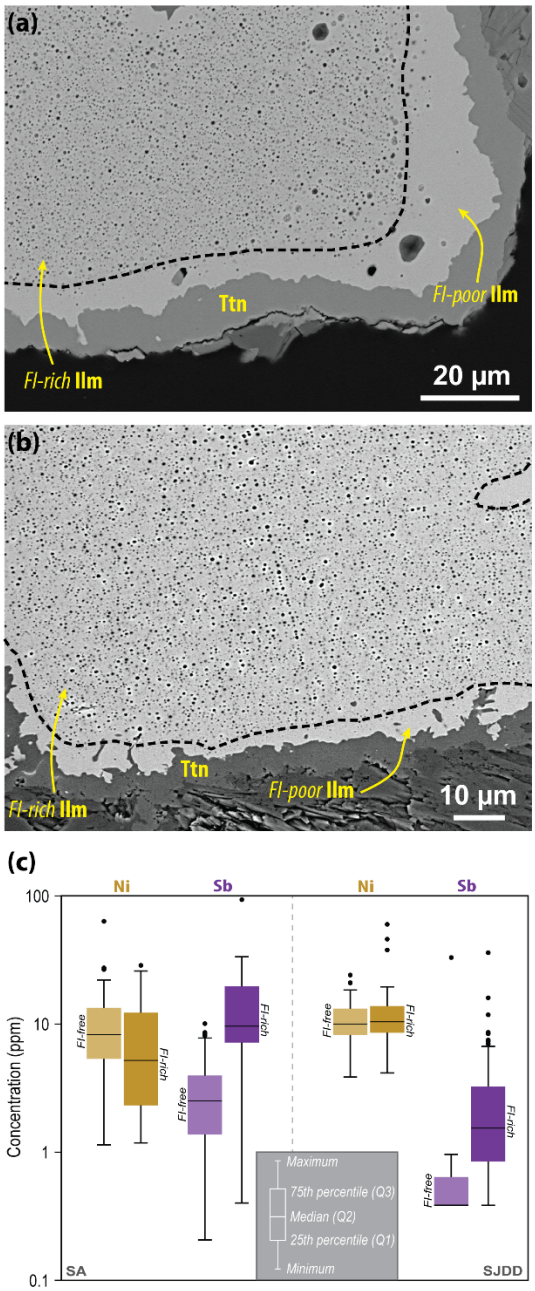

Figure 8. Selected BSE images illustrating the typical texture of ilmenite-hosted FIs from (a) SJDD and (b) SA mafic bodies. (c) Boxplot of the Ni and Sb contents obtained by LA ICP-MS for FI-rich and FI-poor ilmenites from the two study areas.

The LA ICP-MS traverses on the evaporate mounds give interesting information about the metal composition of the fluids. These traverses confirm that all the mounds are invariably dominated by Na-Ca-S, and always accompanied by Sr (Figure 4). In addition, variable amounts of Sb, As, Zn, Mo, Pb, and Cu, and more rarely Zr and Hf, are observed. Additionally, in the same ilmenite grain evaporate mounds may have different composition, that is either Na- or Ca-dominant, but the ∑(Na+Ca)/Ca (in wt. %) remains similar at 2-3:1.

The LA ICP-MS analyses indicate that As and Sb contents increase by 600-650% (i.e. a factor of 7-7.5, respectively) from ilmenite to the evaporate mound, whereas the Cu content increases by 300%. In contrast, the V and Ni contents are not affected by the presence of the mound.

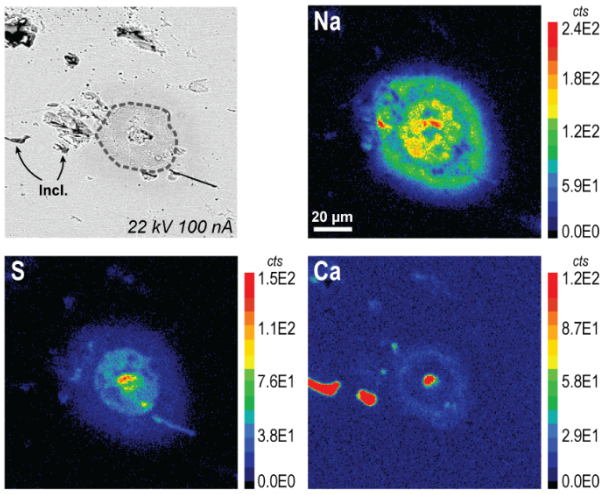

Figure 9. Selected BSE image of decrepitate mound on ilmenite, highlighted by dashed grey line, with X-ray elemental maps of Na, S, and Ca. Incl. = mineral inclusions.

4 Discussion and conclusions

Similar unusual textures suggesting FIs in magmatic ilmenite are observed in the SJDD gabbro (France) and the SA gabbroic sills (Spain), two mafic bodies belonging to the early Carboniferous mafic magmatic event in the Variscan belt. This raises the question of whether this type of texture is restricted to this particular magmatism or can be found in other mafic rocks. The peculiarity of SJDD and SA magmatic rocks is that they seem to crystallize from magmas with reduced redox conditions, as suggested by the occurrence of ilmenite in the absence of titano-magnetite. In the case of SJDD, a detailed study of mineral alteration suggests autometasomatism of the pluton via orthomagmatic fluids which induced plagioclase saussuritization, amphibole crystallization and clinopyroxene replacement, and ilmenite transformation into titanite and rutile (Pochon et al. 2023). This indicates a relatively high volatile content for the mafic magma and accounts for the occurrence of a fluid phase during the late magmatic and the high-temperature hydrothermal stages.

The presence of evaporate mounds clearly confirms that the voids decorating ilmenite surfaces represent evacuated FIs. The composition of the latter fluid is invariably dominated by Na-Ca-S; these

three elements are symptomatic of the presence of FIs (Kontak et al. 2004). In addition, it is important to note that: (i) whenever present, the K content is low; and (ii) Cl is rarely present, meaning S is the major solute anion in exsolved fluids.

Although they are both qualitative methods, “indirect” analyses (i.e. comparison of LA ICP-MS analyses of FI-free and FI-rich area) and the “direct” analysis (i.e. LA ICP-MS traverses) show similar information, namely a non-negligible content of metals and metalloids that are incompatible with ilmenite, firstly Sb, Mo and Pb.

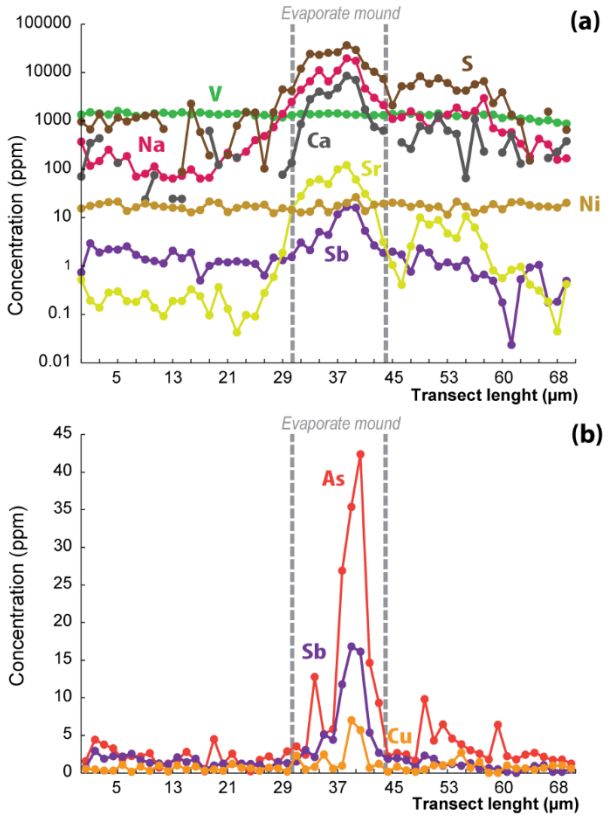

Figure 10. LA-ICP-MS traverse of decrepitate mound on ilmenite. All elements are in ppm except S, which is in count per second (CPS).

An additional important point to mention is the incompleteness of the information derived from the analyses of evaporate mounds. Indeed, the evaporate mounds only represent the tip of the iceberg, as an unknown amount of the decrepitated FI component is vaporized during it decrepitation. Thus, it is likely that some of the volatile component may have escaped, hence only a partial amount of the original metal budget was trapped in the newly crystallized evaporate mounds. Therefore, the next step should be the quantitative analyses of the trapped fluids and their metal and metalloid content, in order to estimate a possible contribution of magmatic fluids from the early Carboniferous mafic magmatism to Sb mineralization in the Variscan belt.

Acknowledgements

This work was achieved in the framework of the ERA-MIN2 Aureole project funded by the ANR (grant ANR-19-MIN2-0002) for the French partners. We also acknowledge the LabEx VOLTAIRE (ANR-10-LABX-100-01) and EquipEx PLANEX (ANR-11-EQPX-0036) for providing support to the EPMA and LA-ICP-MS laboratories.

References

Ballouard C, Poujol M, Mercadier J, Deloule E, Boulvais P, Baele JM, Cuney M, Cathelineau M (2018) Uranium metallogenesis of the peraluminous leucogranite from the Pontivy-Rostrenen magmatic complex (French Armorican Variscan belt): the result of long-term oxidized hydrothermal alteration during strike-slip deformation. Miner Deposita 53:601–628.

Barboni M, Schoene B, Ovtcharova M, Bussy F, Schaltegger U, Gerdes A (2013) Timing of incremental pluton construction and magmatic activity in a back-arc setting revealed by ID-TIMS U/Pb and Hf isotopes on complex zircon grains. Chem Geol 342:76–93.

Campos HR, Gloaguen E, Pochon A, Iacono-Marziano G, Mollé V, Higueras P, Lorenzo S, Maria Esbri J (2022) Mafic magmatism and Sb mineralization: geochemical insights from the Central Iberian Zone, Spain, SGA2022: 16th Biennial meeting, pp. 22.

Hedenquist JW, Lowenstern JB (1994) The role of magmas in the formation of hydrothermal ore deposits. Nature 370(6490):519–527.

Iacono-Marziano G, Le Vaillant M, Godel BM, Barnes SJ, Arbaret L (2022) The critical role of magma degassing in sulphide melt mobility and metal enrichment. Nat Commun 13:2359.

Klemme S, Günther D, Hametner K, Prowatke S, Zack T (2006) The partitioning of trace elements between ilmenite, ulvospinel, armalcolite and silicate melts with implications for the early differentiation of the moon. Chem Geol 234:251–263.

Kontak DJ (2004) Analysis of evaporate mounds as a complement to fluid-inclusion thermometric data: case studies from granitic environments in Nova Scotia and Peru. Canad Mineral 42:1315–1329.

Pochon A, Gapais D, Gloaguen E, Gumiaux C, Branquet Y, Cagnard F, Martelet G (2016a) Antimony deposits in the Variscan Armorican belt, a link with mafic intrusives? Terra Nova 28:138–145.

Pochon A, Gloaguen E, Branquet Y, Poujol M, Ruffet G, Boiron MC, Boulvais P, Gumiaux C, Cagnard F, Gouazou F, Gapais D (2018) Variscan Sb-Au mineralization in Central Brittany (France): A new metallogenic model derived from the Le Semnon district. Ore Geol Rev 97:109–142.

Pochon A, Iacono-Marziano G, Gloaguen E, Tuduri J, Erdmann S (2023) High-temperature alteration during cooling of mafic intrusions: Insights from the Saint-Jean-du-Doigt intrusive complex (Armorican Massif, France). Lithos 436–437:106977.

Putnis A, Austrheim H (2010) Fluid-induced processes: Metasomatism and metamorphism. Geofluids 10:254–269.

Shepherd K, Namur O, Toplis MJ, Devidal JL, Charlier B (2022) Trace element partitioning between clinopyroxene, magnetite, ilmenite and ferrobasaltic to dacitic magmas: an experimental study on the role of oxygen fugacity and melt composition. Contrib Mineral Petrol 177:90.

Magnetite composition as petrogenetic and fertility indicator for Fe-Ti-V-(P) mineralization in Archean mafic-ultramafic intrusions within the Superior Province, Canada

Anne-Aurélie Sappin[1], Michel G. Houlé[1]
[1] Geological Survey of Canada, Lands and Mineral Sector, Natural Resources Canada, Québec City

Abstract. Magnetite composition from several Archean mafic to ultramafic intrusions within the Superior Province was characterized to be used as petrogenetic and fertility indicator for Fe-Ti-V-(P) mineralization. The composition of magnetite could be partially influenced by a number of factors, including the presence of exsolutions and inclusions and the element partitioning with co-crystallized minerals. Nevertheless, the global composition of magnetite in compatible (e.g., Mg, V, Cr) and incompatible (e.g., Al, Mn, Ti) elements provides helpful information regarding the degree of differentiation of each host intrusion but also among themselves. In magnetite discrimination diagrams (e.g., Ca+Al+Mn versus Ti+V, Ni+Cr versus Ti+V), magnetite from these Archean intrusions is characterized by lower Ti+V values than expected, with magnetite composition mostly plotting within fields for hydrothermal deposits rather than within fields for Fe-Ti-V-(P) deposits. Considering that the Fe-Ti-V-(P) deposit fields in these diagrams were mainly defined based on Fe-oxides hosted within Proterozoic and Phanerozoic Fe-Ti deposits, the preliminary results suggest that magnetite from Archean Fe-Ti deposits has lower Ti and/or V contents than magnetite from younger deposits.

1 Introduction

It is now well established that magnetite is a useful petrogenetic tracer and suitable indicator mineral for mineral exploration (e.g., Dare et al. 2012, 2014; Duran et al. 2020 and references therein). However, despite the numerous studies published in recent years, only a few of them focussed on magnetite associated with Fe-Ti-V-(P) deposits hosted by Archean mafic and ultramafic intrusions (e.g., Polivchuk 2017; Arguin et al. 2018; Mathieu 2019). The Superior Province with its numerous prospective units for this type of mineralization appears as an ideal area to study the compositional variations of magnetite in Archean mafic-ultramafic intrusions hosting Fe-Ti-V-(P) mineralization. As part of this study, eight Meso- to Neoarchean mafic and ultramafic intrusions distributed throughout the province were selected to characterize their magnetite composition (Fig. 1). These intrusions include the Croal Lake (i.e., Kasabonika), Big Mac, and Butler (East and West) intrusions from the Ring of Fire intrusive suite and the Highbank-Fishtrap intrusive complex within the Oxford-Stull domain, the Oxtoby Lake and Wabassi Main intrusions within the Uchi domain, the Baie Chapus Pyroxenite within the La Grande Rivière domain, and the Rivière Bell and Lac Doré complexes within the Abitibi greenstone belt in the Wawa-Abitibi terrane. The determination of the chemical composition of their magnetite will help to understand which factors influence their composition, how magnetite can be used as petrogenetic and fertility indicator for Fe-Ti-V-(P) mineralization in Archean mafic to ultramafic intrusions, and the efficiency of discrimination diagrams to determine the mineral deposit setting in which magnetite formed.

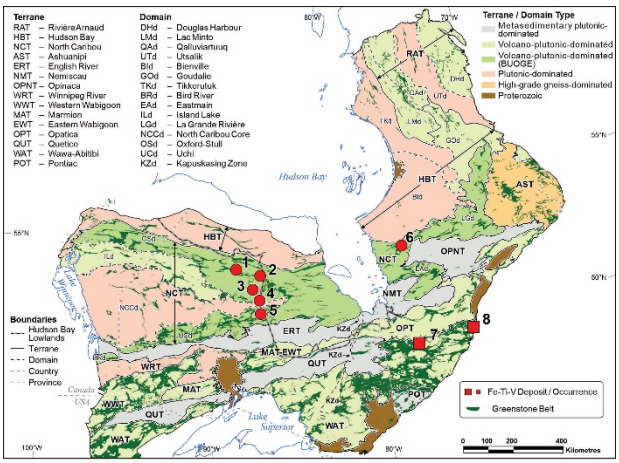

Figure 1. Geological map showing the location of the studied mafic to ultramafic intrusions across the Superior Province (after Houlé et al. 2020). Terrane and domain boundaries are modified from Stott et al. (2010), Percival et al. (2012), and SIGÉOM (2020). Intrusion names: 1 – Croal Lake; 2 – Big Mac; 3 – Butler West and East; 4 – Highbank-Fishtrap; 5 – Oxtoby Lake and Wabassi Main; 6 – Baie Chapus Pyroxenite; 7 – Rivière Bell; 8 – Lac Doré.

2 Sampling and methodology

Magnetite of the studied intrusions is hosted by either oxide-bearing mafic to ultramafic rocks (<40% Fe-Ti oxides) or by semi-massive to massive Fe-Ti oxides (40–80% and >80% Fe-Ti oxides, respectively). The oxide-bearing samples are from the mafic-dominated Croal Lake, Big Mac, Butler, Highbank-Fishtrap, Oxtoby Lake, Wabassi Main, and Lac Doré intrusions and the ultramafic-dominated Baie Chapus Pyroxenite. The semi-massive and massive Fe-Ti oxide samples are from the Croal Lake, Big Mac, Highbank-Fishtrap, and Baie Chapus intrusions and the mafic-dominated Rivière Bell intrusion.

Magnetite grains were analyzed by EPMA at the Université Laval (Québec, Canada) and by LA-ICP-MS at the Geological Survey of Canada (Ottawa, Canada) to determine their trace element contents.

The spot analyses by EPMA mostly exclude the ilmenite exsolutions/inclusions, whereas those by LA-ICP-MS include the ilmenite exsolutions formed during subsolidus exsolution-oxidation processes.

3 Magnetite composition from mafic to ultramafic intrusion

In the oxide-bearing mafic and ultramafic rocks, magnetite composition in compatible elements (e.g., Mg, V, Ni, and Cr) and incompatible elements (e.g., Al, Mn, and Ti) during fractionation processes varies from intrusion to intrusion (Figs. 2A, 2B). Magnetite from the Croal Lake, Big Mac, Butler, and Highbank-Fishtrap intrusions has high Cr and locally V contents. Magnetite from the Oxtoby Lake intrusion has low Mg contents, relatively low Cr, Al, and Mn contents, and the lowest Ti contents. Magnetite from the Wabassi Main intrusion has the highest Mg and Co contents and high V, Ni, Cr, Al, Mn, and Ti contents. Magnetite from the Lac Doré complex has low V contents, relatively low Mg and Cr contents, and the lowest Ni contents, but high Mn, Ti, and Zn contents. In addition, magnetite from the Baie Chapus Pyroxenite has the highest Ni contents, relatively high Mg contents, and low V, Cr, and Al contents.

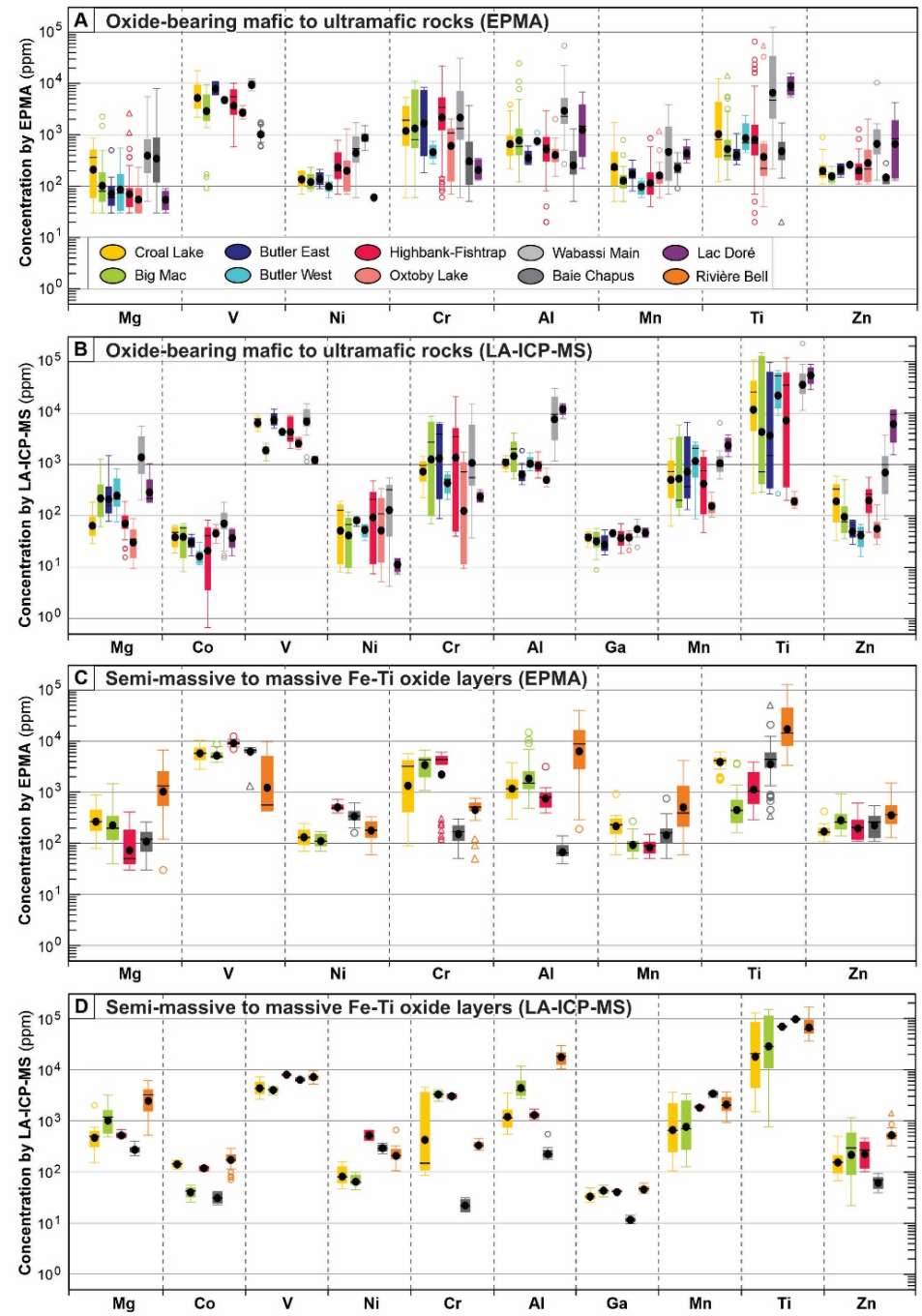

Figure 2. Box and whisker plots of selected trace elements in magnetite analyzed by (A) EPMA and (B) LA-ICP-MS in the oxide-bearing samples and (C) EPMA and (D) LA-ICP-MS in the semi-massive to massive Fe-Ti oxide layers. The upper and lower margins of the box represent the upper 75% and lower 25% of the data. The whiskers represent the upper and lower threshold values (95% of the data). Median values are shown as solid black lines and mean values as solid black circles. Outliers are shown as open circles and far outlier as open triangles along the whisker.

Similarly, the chemical signature of the magnetite from the semi-massive and massive Fe-Ti oxides differs from one intrusion to another (Figs. 2C, 2D). Magnetite from the Croal Lake and Big Mac intrusions has relatively high Mg and Cr contents. In contrast, magnetite from the Highbank-Fishtrap complex has relatively low Mg contents but high Cr contents. In the Rivière Bell complex, the Fe-oxides have been affected by regional/local metamorphism and most of their primary composition, except for V and Cr, has been modified (Polivchuk 2017); these Fe-oxides show relatively low V and Cr contents. Finally, magnetite from the Baie Chapus Pyroxenite has intermediate Ni contents, relatively high Mn contents, locally low Mg and Zn contents, and the lowest Co, Cr, Al, and Ga contents.

4 Discrimination diagram

In all the discrimination diagrams used to distinguish magnetite from hydrothermal or Fe-Ti-V-(P) deposits and defined based on Fe-oxide compositions determined by EPMA (e.g., Dupuis and Beaudoin 2011; Méric 2011; Fig. 3), magnetite from the studied Archean intrusions shows significantly lower Ti+V contents than expected and plots predominantly within the field for hydrothermal deposits rather than within the field for Fe-Ti-V-(P) deposits for our EPMA results. An exception is the Rivière Bell magnetite, which plots predominantly within the Fe-Ti-V deposit field. In contrast, the LA-ICP-MS data for the magnetite grains generally plot within the Fe-Ti-V-(P) deposit fields in these discrimination diagrams.

5 Discussion and conclusions

Trace element contents of magnetite obtained by EPMA are generally in good agreement with those obtained by LA-ICP-MS (Fig. 2). However, some of these data show small discrepancies, like for Al, Mn, Ti, and Zn (Fig. 2). These differences are related to the presence of exsolutions, in particular ilmenite exsolutions that are incorporated during the LA-ICP-MS analyses and not in the EPMA analyses and commonly explain the variations in Al, Mn, and Ti. But some of these variations (e.g., for Si, Ca, and Zn) are better explained by the presence of mineral inclusions (e.g., silicates, sulfides). The composition of magnetite is also influenced by the co-crystallizing minerals. In the Baie Chapus Pyroxenite, for example, magnetite grains in the pyroxenite have a relatively primitive composition with high Mg and Ni contents and low Al contents (Figs. 2A, 2B). However, they show lower Cr and V contents than expected (Figs. 2A, 2B). These low Cr contents could result from the fractional crystallization of chromite at depth, whereas the depletion in V of magnetite from the pyroxenite could be explained by the high proportion of clinopyroxene in this rock type, in which V also partitions ($D_V^{Cpx/Basaltic\ melt}$ = 3.1: Hart and Dunn 1993).

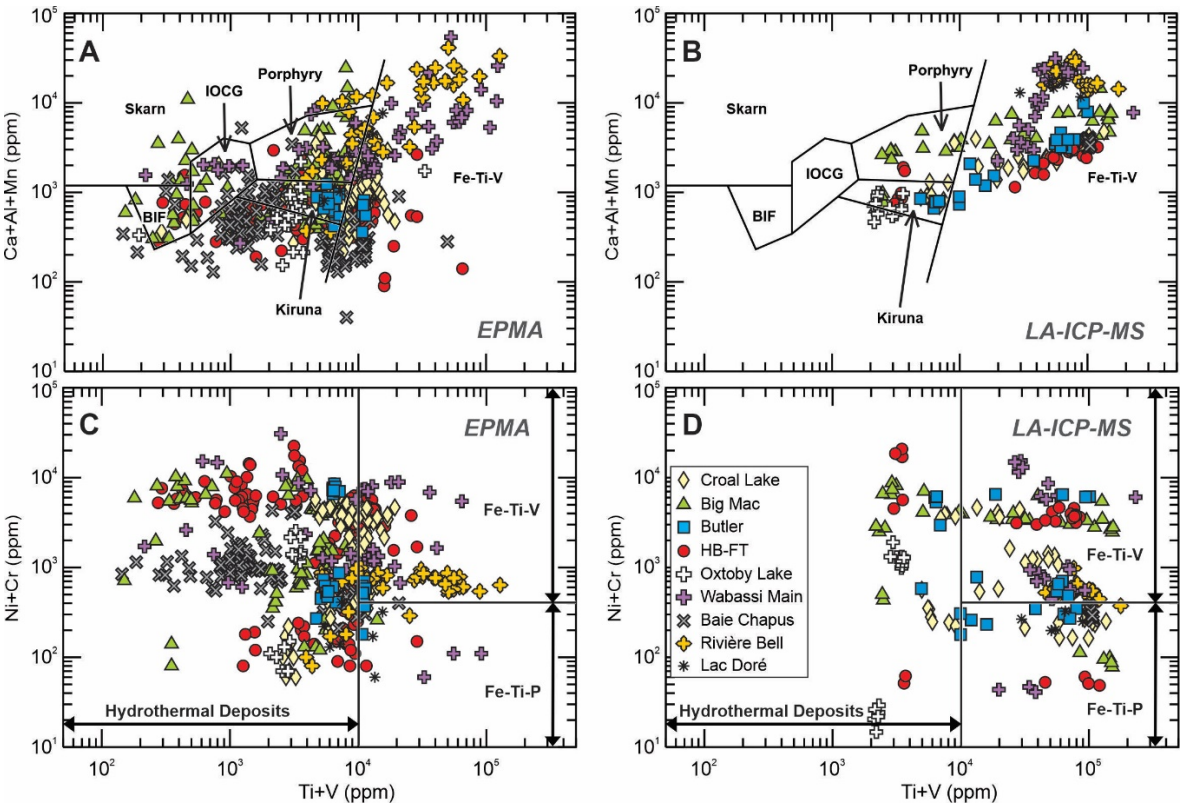

Figure 3. Discrimination diagrams of magnetite composition from hydrothermal and Fe-Ti-V-(P) deposits. Ca+Al+Mn versus Ti+V diagram for results determined by (A) EPMA and (B) LA-ICP-MS. Ni+Cr versus Ti+V diagram for results determined by (C) EPMA and (D) LA-ICP-MS. Each data point represents an individual magnetite grain. Abbreviations: BIF = banded iron formation, IOCG = iron oxide copper-gold. The fields in discrimination diagrams (A) and (B) are from Dupuis and Beaudoin (2011), and those in (C) and (D) are from Méric (2011).

The overall composition of magnetite, however, appears to be mainly independent of the host-rock type and gives us clues regarding the degree of fractionation of the host intrusion. Based on the chemical signature of magnetite from the studied mafic-dominated intrusions (Fig. 2), it appears that the Rivière Bell and Lac Doré complexes have the most evolved composition, whereas the Croal Lake, Big Mac, Butler, Highbank-Fishtrap and Wabassi Main intrusions are the most primitive. Identifying the most primitive and evolved intrusions will help detecting which intrusions in the Superior are most likely to host Fe-Ti-V-P mineralization.

In the discrimination diagrams, it appears that for results determined by EPMA (Figs. 3A, 3C), magnetite from the studied Archean intrusions has lower Ti+V contents than magnetite from the Proterozoic and Phanerozoic Fe-Ti deposits used to construct the diagrams. The distinct chemical signature of the Rivière Bell magnetite (higher Ti+V contents; Figs. 3A, 3C) could be due to omnipresent fine ilmenite exsolutions in the Fe-oxide grains and/or late Ti remobilization during metamorphism (Polivchuk 2017). Preliminary results suggest that the contradiction between the Archean and Proterozoic/Phanerozoic magnetite composition could be explained by lower Ti and/or V contents in magnetite from Archean Fe-Ti deposits than from younger deposits. Further investigations are necessary to explain this difference but factors such as the change in the fugacity of oxygen or a variation in the quantity of ilmenite exsolutions can be considered. Interestingly, the LA-ICP-MS data appear better at correctly predicting the deposit type in these diagrams (Figs. 3B, 3D) as the Ti contents determined by LA-ICP-MS are often higher than those determined by EPMA. However, a fair amount of the LA-ICP-MS data points still fall into other hydrothermal deposit types (Figs. 3B, 3D).

Acknowledgements

Support for this study was provided through the Ni-Cr-PGE Systems Project's "Activity NC-2.2: Ni-Cr metallotect: Synthesis, updates, and revised models for the Superior Province" of the NRCan's Targeted Geoscience Initiative Program. We thank Northern Shield Resources Inc. (C. Vaillancourt, I. Bliss, R.-L. Simard, and G. Budulan) and R. Metsaranta from the Ontario Geological Survey for supplying representative samples; M. Choquette (Université Laval) for its technical support during EPMA analysis; and Z. Yang, D. Petts, and S.E. Jackson (Geological Survey of Canada) for their assistance with LA-ICP-MS analyses.

References

Arguin J-P, Page P, Barnes S-J, Girard R, Duran C (2018) An integrated model for ilmenite, Al-spinel, and corundum exsolutions in titanomagnetite from oxide-rich layers of the Lac Dore Complex (Quebec, Canada). Minerals 8: 1-39.

Dare SAS, Barnes S-J, Beaudoin G (2012) Variation in trace element content of magnetite crystallized from a fractionating sulphide liquid, Sudbury, Canada: implications for provenance discrimination. Geochimica et Cosmochimica Acta 88: 27-50.

Dare SAS, Barnes S-J, Beaudoin G, Meric J, Boutroy E, Potvin-Doucet C (2014) Trace elements in magnetite as petrogenetic indicators. Mineralium Deposita 49: 785-796.

Dupuis C, Beaudoin G (2011) Discriminant diagrams for iron oxide trace element fingerprinting of mineral deposit types. Mineralium Deposita 46: 319-335.

Duran CJ, Barnes S-J, Mansur ET, Dare SAS, Bedard LP, Sluzhenikin SF (2020) Magnetite chemistry by laser ablation-inductively coupled plasma-mass spectrometry records sulphide fractional crystallization in massive nickel-copper-platinum group element ores from the Norilsk-Talnakh mining district (Siberia, Russia): implications for trace element partitioning into magnetite. Economic Geology 115: 1245-1266.

Hart SR, Dunn T (1993) Experimental cpx/melt partitioning of 24 trace elements. Contributions to Mineralogy and Petrology 113: 1-8.

Houlé MG, Lesher CM, Sappin A-A, Bédard M-P, Goutier J, Yang XM (2020) Overview of Ni-Cu-(PGE), Cr-(PGE), and Fe-Ti-V magmatic mineralization in the Superior Province: Insights on metallotects and metal endowment. In: Bleeker W, Houlé MG (eds) Targeted Geoscience Initiative 5: Advances in the understanding of Canadian Ni-Cu-PGE and Cr ore systems – Examples from the Midcontinent Rift, the Circum-Superior Belt, the Archean Superior Province, and Cordilleran Alaskan-type intrusions. Geological Survey of Canada, Open File 8722, pp. 117-139.

Mathieu L (2019) Origin of the vanadiferous serpentine–magnetite rocks of the Mt. Sorcerer area, Lac Doré layered intrusion, Chibougamau, Québec. Geosciences 9: 110.

Méric J (2011) Caractérisation géochimique des magnétites de la zone critique de l'intrusion magmatique de Sept-Îles (Québec, Canada) et intégration à une base de données utilisant la signature géochimique des oxydes de fer comme outil d'exploration. Internship report, Université du Québec à Chicoutimi.

Percival JA, Skulski T, Sanborn-Barrie M, Stott GM, Leclair AD, Corkery MT, Boily M (2012) Geology and tectonic evolution of the Superior Province, Canada. In: Percival JA, Cook FA, Clowes RM (eds) Tectonic Styles in Canada: The LITHOPROBE Perspective. Geological Association of Canada, Special Paper 49, pp. 321-378.

Polivchuk M (2017) The formation of vanadium deposits in the Archean Riviere Bell Complex, Quebec: insights from Fe-Ti oxide chemistry. MSc thesis, University of Ottawa.

SIGEOM (2020) Système d'information geominière du Québec. Ministère de l'Énergie et des Ressources naturelles du Québec. http://sigeom.mines.gouv.qc.ca. Accessed 9 February 2020.

Stott GM, Corkery MT, Percival JA, Simard M, Goutier J (2010) A revised terrane subdivision of the Superior Province. In: Summary of Field Work and Other Activities 2010. Ontario Geological Survey, Open File Report 6260, pp. 20-1–20-10.

Crustal S sources for komatiite hosted Ni deposits and implications for sulfide transport and deposition

Anne Brandt Virnes[1], Marco L. Fiorentini[1], Stefano Caruso[1,2], Kim Baublys[3], Quentin Masurel[1], Nicolas Thebaud[1]
[1]Centre for Exploration Targeting, School of Earth Sciences, The University of Western Australia, Perth, WA
[2]Commonwealth Scientific and Industrial Research Organization, Mineral Resources, Kensington, WA
[3]School of Earth and Environmental Sciences, The University of Queensland, Brisbane, Qld

Abstract. Previous S isotope works suggested that the Mount Keith and Cliffs komatiite hosted Ni deposits in the Yilgarn Craton of Western Australia formed in different volcanic environments. The Mount Keith deposit was interpreted to have formed near the komatiite vent and a VMS style S source in the felsic volcanic substrate, whereas the Cliffs deposit formed at a distal position on a basaltic substrate. It was inferred that the felsic stratigraphic substrate at Mount Keith was more prospective than the mafic substrate at Cliffs. However, recent modelling of metal upgrading during transport of assimilated crustal sulfides in komatiites indicates a positive relationship between the travel distance and the resulting metal tenors of the deposited sulfides. This relationship has not been observed between the Mount Keith and Cliffs deposits. New S isotope data from the Cliffs Ni deposit confirm the presence of a VMS style source in the immediate footwall to the deposit. We suggest that the Cliffs Ni deposit also formed in a rift environment, proximal to its crustal S source. This implies that rift environments where bimodal magmatism occurs, mafic-hosted systems may be as prospective as felsic-hosted ones, significantly increasing the search space for high-tenor mineralisation associated with komatiites.

1 Introduction

Komatiites require assimilation of crustal sulfur to form Ni deposits (e.g., Lesher and Burnham 2001; Ripley and Li 2013; Barnes et al. 2016). Sulfur isotopes applied to the Type I Cliffs and Type II Mount Keith komatiite hosted Ni deposits, Agnew-Wiluna Greenstone Belt (AWB), Western Australia, showed that both deposits likely assimilated Archaean seawater derived, volcanogenic massive sulfides (VMS; Bekker et al. 2009). Our previous work confirmed a VMS style sulfide source for the Mount Keith Ni deposit and showed that komatiite hosted Ni sulfides largely preserve their crustal mass-independent S isotopic signatures (MIF-S, denoted $\Delta^{33}S$; Virnes et al., 2023).

VMS style sulfides in the AWB were mainly identified in felsic volcanic rocks underlying the Mount Keith Ultramafic Unit (MKU), whereas basalt underlying the Cliffs Ultramafic Unit (CLU) was thought to only contain sedimentary sulfides (Bekker et al. 2009; Fiorentini et al. 2012; Perring 2015). The felsic volcanic rocks were interpreted to mark the central part of a palaeo-rift, with the basalt dominating in rift-distal environments (Fiorentini et al. 2012). As the Cliffs and Mount Keith Ni deposits both sourced VMS style sulfides, it was inferred that the deposits formed proximal and distal to the palaeo-rift and the VMS style S source, respectively. Most komatiite hosted Ni deposits in the AWB are associated with felsic volcanic substrates, with few exceptions such as Cliffs. Felsic hosted komatiites were thus deemed more prospective for Ni deposits than mafic hosted bodies in bimodal systems (Fiorentini et al. 2012).

Recent work by Yao and Mungall (2021) showed that metal tenors of magmatic sulfides are positively correlated with distance from their crustal S source. However, the metal tenors of the Cliffs Ni deposit are not markedly higher than those from the Mount Keith Ni deposit (Perring 2015). This questions whether Cliffs really formed distal to the rift axis and from its crustal S source as previously proposed. Perring (2015) reported potential VMS style sulfides from the basal footwall to CLU, which until now had not been analysed for S isotopes. Their presence, however, suggests that the Cliffs Ni deposit, and basaltic hosted komatiite ores in general, may also have formed close to the rift and crustal S source.

To test this hypothesis, we characterised the S isotopic composition of sedimentary and VMS style sulfide horizons in the predominantly basaltic footwall to the CLU and compared them to that of the magmatic sulfides from the Cliffs Ni deposit. This dataset is used to evaluate if even basaltic hosted systems in the AWB formed proximal to a rift environment and thus can be considered as prospective for Ni mineralisation. These results are also used to discuss the transport and depositional mechanisms for komatiite hosted ore systems.

2 Regional geology

The AWB is located in the central northern part of the Archaean Yilgarn Craton, Western Australia (Fig. 1; Cassidy et al. 2006) and consists of a ca. 2825-2655 Ma greenstone succession comprising basalt, komatiite, felsic volcanic and volcaniclastic rocks, conglomerate and minor shale and chert (Hayman et al. 2015; Gole et al. 2019; Masurel et al. 2022). The greenstone succession has been divided into 5 cycles comprising 1) early mafic-ultramafic volcanism related to crustal thinning of proto-Yilgarn; 2) craton-wide felsic and mafic volcanism likely related to uplift from plume impingement; 3) early rift related bimodal volcanism followed by a main ultramafic-mafic plume related LIP event, which formed the CLU; 4) felsic volcanism and granitic doming during late stage plume event; 5) basin inversion and formation of molasse style conglomerates (Masurel et al. 2022).

The Cliffs Ni deposit in located in the Mount Keith region in the northern part of the AWB (Fig. 1). The stratigraphic substate to the CLU hosting the Cliffs Ni deposit consists mainly of the massive to pillowed Never Can Tell Basalt (NCBT; Hayman et al. 2015), and minor Mount Keith Dacite (MKD; Rosengren et al. 2008), which are both part of the cycle 3 incipient rift related bimodal volcanism (Masurel et al. 2022).

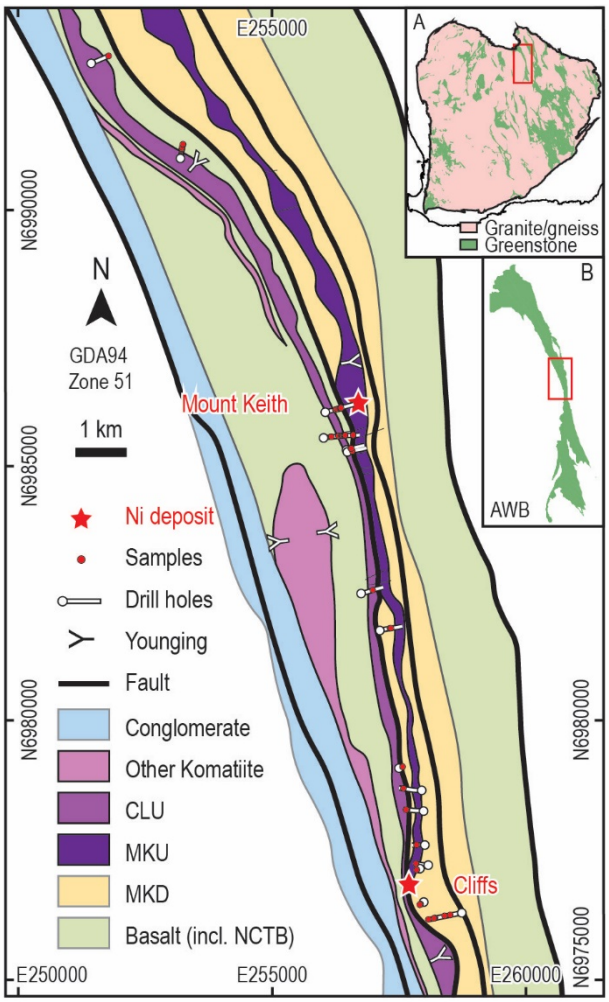

Figure 11. Geology of the Mount Keith region, Agnew-Wiluna Greenstone Belt (AWB; inset B), Yilgarn Craton (inset A), with drill hole traces and sample locations. CLU: Cliffs Ultramafic Unit, MKU: Mount Keith ultramafic Unit, MKD; Mount Keith Dacite, NCTB: Never Can Tell Basalt. Modified from Perring (2015).

3 Materials and methods

Fifty-one samples were collected from 18 drill cores from the Mount Keith region (Fig. 1). All samples were classified based on their sulfide parageneses, which was corroborated via petrographic analysis using optical microscopy. Eleven samples were magmatic Ni sulfides from the CLU at the Cliffs Ni deposit, 25 and 3 samples were of VMS style sulfides from NCTB and MKD, respectively, and 12 samples were interflow sediments from NCTB. All samples were analysed for multiple S isotopes by EA-IRMS at the Stable Isotope Geochemistry Laboratory, University of Queensland, following a modified procedure described in Baublys et al. (2004). Historical S isotope data from the CLU (Bekker et al. 2009) are presented with the results.

4 Results

Magmatic Ni sulfides from the CLU consist mainly of pyrrhotite, pentlandite and minor chalcopyrite. They vary from disseminated blebby and cloudy droplets in serpentinised olivine cumulate (Fig. 2A) to massive sulfide lenses at the base of the CLU unit (Fig 2B). Values of $\delta^{34}S$ range from ca. -5.8‰ to -0.3‰ with a median of ca. -3.1‰ (Fig. 3A). The $\Delta^{33}S$ values range from and ca. -1.3‰ to +0.1‰ with a median of ca. -0.51‰ (Fig. 3A).

Sedimentary sulfides occur as nodules or finely disseminated to bedding-parallel stringers in shales and mudstones (Fig 2C). Sulfide phases are mostly pyrrhotite and lesser chalcopyrite, partially replaced by metamorphic pyrite. Values of $\delta^{34}S$ range from ca. -5.7‰ to +4.8‰ with a median of ca. +2.0‰. The $\Delta^{33}S$ values range from ca. -0.3‰ to +3.9‰ with a median of ca. +1.2‰ (Fig. 3A). Sedimentary sulfides were observed in the central and northern part of the region, with the most positive $\Delta^{33}S$ values found mainly in the Mount Keith mine area (Fig. 3B).

The VMS style sulfides are pyrrhotite and lesser chalcopyrite, often replaced by metamorphic pyrite. Sulfides occur as disseminations, amygdule fillings, interpillow- and fragment vein fill (Fig. 2D and E) and semi-massive lenses in their host rocks. Values of $\delta^{34}S$ range from ca. -6.4‰ to +10.9‰ with a median of ca. +2.3‰. The $\Delta^{33}S$ values range from ca. -1.5‰ to +3.6‰ with a median of ca. -0.3‰ (Fig. 3A). The most negative $\Delta^{33}S$ values occur in the north and south of the region, while the least negative values coincide with the presence of sedimentary sulfides in the central part of the region (Fig. 3B).

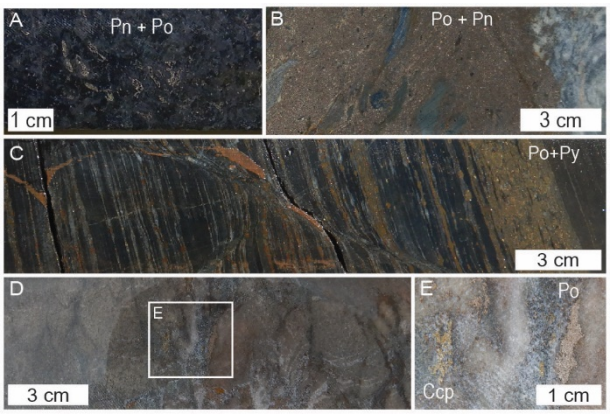

Figure 12. Examples of sulfide styles. A) Cloudy disseminations in CLU. B) Massive sulfide in CLU. C) Nodular and bedding-parallel stringer sulfides in shale. D) Vein sulfides in hydrothermally altered, bleached fragmental basalt. E) Close up on vein sulfides in D.

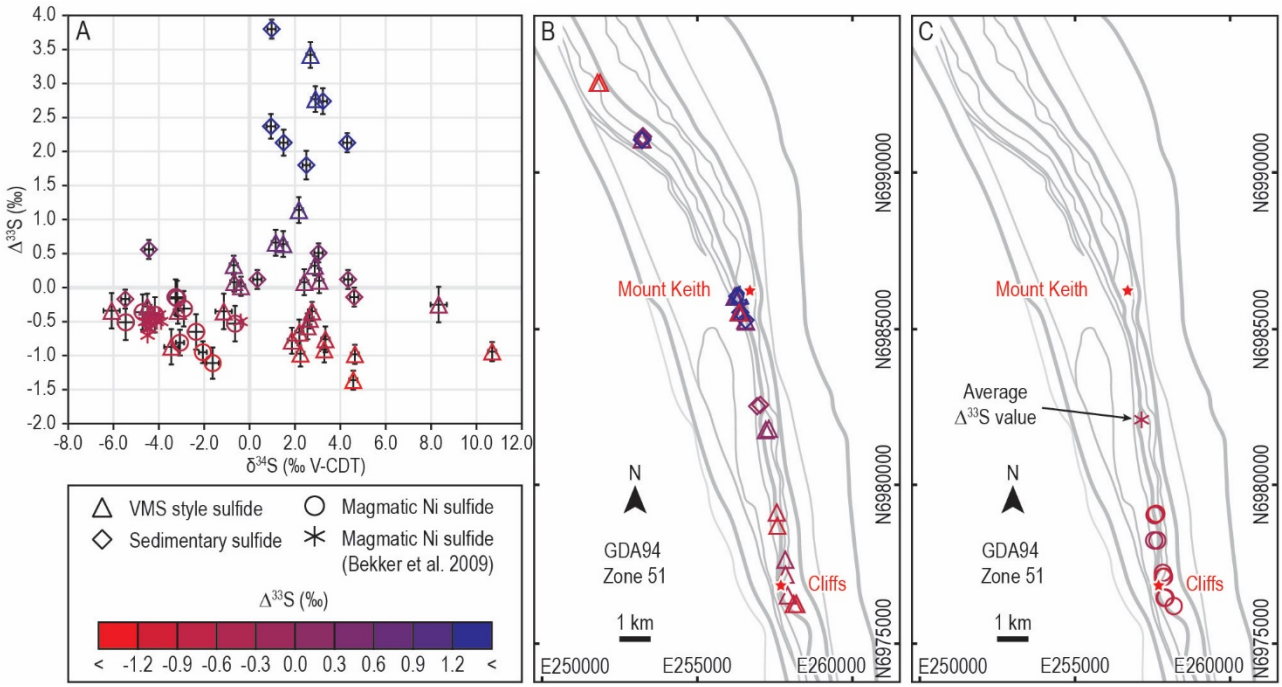

Figure 13. A) Plot of $\delta^{34}S$-$\Delta^{33}S$ coloured by $\Delta^{33}S$ variation. Error bars are 2σ absolute uncertainties. B) Spatial distribution and $\Delta^{33}S$ variability of sulfides in the stratigraphic footwall to the CLU. C) Spatial distribution and $\Delta^{33}S$ variability of magmatic Ni sulfides from the CLU.

5 Discussion

5.1 Sulfur source reservoirs in the Mount Keith region

The sedimentary sulfides in the Mount Keith region generally have positive $\delta^{34}S$ and $\Delta^{33}S$ values (Fig. 3A), consistent with a MIF-S reduced species transformed into sulfide without significant mass-dependent fractionation (Johnston 2011). The hydrothermal sulfides show a wider range in $\delta^{34}S$ values and are generally $\Delta^{33}S$ negative or plot around ~0‰ (Fig. 3A), indicative of being derived from both seawater and magmatic reservoirs (Johnston 2011). The wide range of $\delta^{34}S$ values suggests a predominantly closed system with respect to the sea water sulfate reservoir during the time of sulfide precipitation (Seal 2006), consistent with the AWB forming as a failed continental rift closed off from the wider ocean (Masurel et al. 2022). A minor set of hydrothermal sulfides have positive $\Delta^{33}S$ values (Fig. 3A) and coincide spatially with $\Delta^{33}S$ positive sedimentary sulfides (Fig. 3B), suggesting that the former may have reworked pre-existing sedimentary sulfides.

5.2 Mafic-hosted komatiite systems may form proximal to their crustal S source

Based on the dataset of by Bekker et al. (2009) the mafic hosted CLU and related Ni mineralisation was proposed to have formed at a distal position to the rift axis and its crustal S source (Fiorentini et al. 2012). Our new dataset has identified sulfides related to VMS style hydrothermal alteration in the NCTB immediately beneath the CLU-NCTB contact. The S-isotopic signatures of these hydrothermal sulfides (Fig. 3B) are similar to those in the overlying Cliffs Ni deposit (Fig. 3C), and generally provide a better fit compared to the other occurrences in the region. The correlation between the magmatic and hydrothermal $\Delta^{33}S$ values highlights the increased possibility that the Cliffs Ni deposit formed proximal to its S source. The Cliffs Ni deposit thus need not be a distal version of the komatiite system that formed the Mount Keith Ni deposit. This is consistent with the lack of significantly different metal tenors between the two deposits (Perring 2015) as otherwise predicted by the models of Yao and Mungall (2021).

5.3 Implications for the dynamics of sulfide metal enrichment during transport

Yao and Mungall (2021) showed that significant lateral travel distance of assimilated crustal sulfide droplets was needed for them to equilibrate with enough silicate melt to concentrate economic levels of metals. However, the fact that Cliffs Ni deposit formed proximal to its crustal S source precludes extensive lateral movement of the sulfide liquid. Consequently, this indicates that pre-enrichment of metals in the sulfide liquid must happen close to the S source, prior to deposition as a typical Type I basal massive sulfide mineralisation.

A possible mechanism for such proximal metal enrichment involves the komatiite lava flowing over topographical steps (such as faults) in the substrate (Yao and Mungall 2022). Complex flow patterns, vortices and eddies are created in the wake of these steps, significantly increasing the potential for entrapment and re-entrainment of transported sulfide droplets. This effectively increases the amount of silicate melt that the sulfide can interact

with during very limited lateral transport (Yao and Mungall 2022). The multitude of faults, high topographical variation, and increased likelihood of VMS style sulfide occurrences make proximal parts of rift settings ideal locations for the enhancement of this process (e.g., Corti et al. 2018). The magmatic $\Delta^{33}S$ signatures and the proximity to the potential crustal VMS style S source indicates that, similar to the Mount Keith deposit, the Cliffs Ni deposit also formed in such a rift proximal environment. This supports that mafic parts of bimodally hosted komatiite systems should be considered as prospective as the felsic counterparts.

6 Conclusions

Contrary to previous models, the mafic hosted Cliffs Komatiite Ni deposit likely formed proximal to a palaeo-rift axis and a VMS style crustal S source, suggesting that mafic hosted komatiite ore systems are equally prospective as felsic hosted systems in bimodal volcanic regions.

The proximity of the Ni deposit to its crustal S source emphasises the importance of complex flow dynamics and multistage entrapment and re-entrainment of assimilated and transported sulfide droplets rather than extensive lateral flow and distal deposition of sulfide mineralisation.

Acknowledgements

ABV is supported by the UWA Postgraduate Award for International Students and the UWA International Fee Scholarship. This project was funded by the Minerals Research Institute of Western Australia (MRIWA) M530 Yilgarn 2020 collaborative research project. BHP NickelWest is thanked for facilitating fieldwork, access to drill cores, sampling, and technical support.

References

Barnes SJ, Cruden AR, Arndt N, Saumur BM (2016) The mineral system approach applied to magmatic Ni–Cu–PGE sulphide deposits. Ore Geology Reviews 76:296-316. doi: https://doi.org/10.1016/j.oregeorev.2015.06.012.

Baublys KA, Golding SD, Young E, Kamber BS (2004) Simultaneous determination of δ33SV-CDT and δ34SV-CDT using masses 48, 49 and 50 on a continuous flow isotope ratio mass spectrometer. Rapid Communications in Mass Spectrometry 18:2765-2769. doi: https://doi.org/10.1002/rcm.1681.

Bekker A, Barley ME, Fiorentini ML, Rouxel OJ, Rumble D, Beresford SW (2009) Atmospheric Sulfur in Archean Komatiite-Hosted Nickel Deposits. Science 326:1086-1089. doi: https://doi.org/10.1126/science.1177742.

Cassidy KF, Champion DC, Krapez B, Barley ME, Brown SJA, Blewett RS, Groenewald P, Tyler IM (2006) A revised geological framework for the Yilgarn Craton, Western Australia. Geological Survey of Western Australia, Record 2006/8.

Corti G, Molin P, Sembroni A, Bastow ID, Keir D (2018) Control of Pre-rift Lithospheric Structure on the Architecture and Evolution of Continental Rifts: Insights From the Main Ethiopian Rift, East Africa. Tectonics 37:477-496. doi: https://doi.org/10.1002/2017TC004799.

Fiorentini ML, Beresford SW, Barley ME, Duuring P, Bekker A, Rosengren N, Cas R, Hronsky J (2012) District to Camp Controls on the Genesis of Komatiite-Hosted Nickel Sulfide Deposits, Agnew-Wiluna Greenstone Belt, Western Australia: Insights from the Multiple Sulfur Isotopes. Economic Geology 107:781-796. doi: https://doi.org/10.2113/econgeo.107.5.781.

Gole MJ, Western E, Diragitch A (2019) A revised stratigraphic model for the 2.7 Ga Agnew-Wiluna greenstone belt, Yilgarn Craton, Western Australia. Ore and Energy Resource Geology 1:100001. doi: https://doi.org/10.1016/j.oreoa.2019.100001.

Hayman PC, Thébaud N, Pawley MJ, Barnes SJ, Cas RAF, Amelin Y, Sapkota J, Squire RJ, Campbell IH, Pegg I (2015) Evolution of a ~2.7Ga large igneous province: A volcanological, geochemical and geochronological study of the Agnew Greenstone Belt, and new regional correlations for the Kalgoorlie Terrane (Yilgarn Craton, Western Australia). Precambrian Research 270:334-368. doi: https://doi.org/10.1016/j.precamres.2015.09.016.

Johnston DT (2011) Multiple sulfur isotopes and the evolution of Earth's surface sulfur cycle. Earth-Science Reviews 106:161-183. doi: https://doi.org/10.1016/j.earscirev.2011.02.003.

Lesher CM, Burnham OM (2001) Multicomponent elemental and isotopic mixing in Ni-Cu-(PGE) ores at Kambalda, Western Australia. The Canadian Mineralogist 39:421-446. doi: https://doi.org/10.2113/gscanmin.39.2.421.

Masurel Q, Thébaud N, Sapkota J, De Paoli MC, Drummond M, Smithies RH (2022) Stratigraphy of the Agnew-Wiluna Greenstone Belt: review, synopsis and implications for the late Mesoarchean to Neoarchean geological evolution of the Yilgarn Craton. Australian Journal of Earth Sciences 69:1149-1176. doi: https://doi.org/10.1080/08120099.2022.2102076.

Perring CS (2015) Volcanological and Structural Controls on Mineralization at the Mount Keith and Cliffs Komatiite-Associated Nickel Sulfide Deposits, Agnew-Wiluna Belt, Western Australia—Implications for Ore Genesis and Targeting. Economic Geology 110:1669-1695. doi: https://doi.org/10.2113/econgeo.110.7.1669.

Ripley EM, Li C (2013) Sulfide Saturation in Mafic Magmas: Is External Sulfur Required for Magmatic Ni-Cu-(PGE) Ore Genesis? Economic Geology 108:45-58. doi: https://doi.org/10.2113/econgeo.108.1.45.

Rosengren NM, Cas RAF, Beresford SW, Palich BM (2008) Reconstruction of an extensive Archaean dacitic submarine volcanic complex associated with the komatiite-hosted Mt Keith nickel deposit, Agnew-Wiluna Greenstone Belt, Yilgarn Craton, Western Australia. Precambrian Research 161:34-52. doi: https://doi.org/10.1016/j.precamres.2007.06.012.

Seal RR, II (2006) Sulfur Isotope Geochemistry of Sulfide Minerals. Reviews in Mineralogy and Geochemistry 61:633-677. doi: https://doi.org/10.2138/rmg.2006.61.12.

Virnes AB, Fiorentini ML, Barnes SJ, Caruso S, Martin LAJ, Aleshin ME, Schoneveld LE, Roberts MP, Masurel Q, Thebaud, N (2023) Decoupling of sulfur isotope signatures from platinum group elements in komatiite-hosted ore systems: evidence from the Mount Keith MKD5 Ni Deposit, Western Australia. Manuscript submitted for publication.

Yao Z-s, Mungall JE (2021) Kinetic controls on the sulfide mineralization of komatiite-associated Ni-Cu-(PGE) deposits. Geochimica et Cosmochimica Acta 305:185-211. doi: https://doi.org/10.1016/j.gca.2021.05.009.

Yao Z-s, Mungall JE (2022) Transport and deposition of immiscible sulfide liquid during lateral magma flow. Earth-Science Reviews 227:103964. doi: https://doi.org/10.1016/j.earscirev.2022.103964.

Magmatic Black Shale Assimilation and the Formation of Sulphide Deposits – Perspectives from Experiments and Thermodynamic Simulations

Ville J. Virtanen[1]
[1]*Institute des Sciences de la Terre d'Orléans (ISTO), CNRS-Université d'Orléans-BRGM, France*

Abstract. Magmatic assimilation of sulphur (S)-bearing black shales can lead to the formation of economically significant Cu-Ni(-PGE) sulphide deposits. Liberation of S from black shales as well as the chemical interaction between the black shale and magma are complex non-linear processes that are intricately linked to the deposition of sulphide, yet these remain poorly understood. Experimental work and computational thermodynamic simulations can shed light on the details of these processes and help in identifying key parameters for exploration purposes. Here, I review recent experiments and thermodynamic simulations of magmatic black shale assimilation related to the mineralized intrusions of the Duluth Complex. The experiments show what reactions contribute to progressive S liberation during black shale devolatilization and partial melting. The thermodynamic simulations demonstrate the effects of black shale assimilation on magmatic sulphide precipitation. Collectively, the results provide new details to many of the processes suggested previously on the basis of field observations and geochemical data, the two main pillars of any experimental or computational work.

1 Introduction

Assimilation of sedimentary sulphur (S) by high-temperature komatiitic and basaltic magmas greatly improves the probability for the formation of economically important Cu-Ni(-PGE) sulphide deposits (e.g., Ripley and Li 2013; Barnes et al. 2016). However, it has been established that a close spatial association between S-rich sedimentary rocks and magmas with high assimilation potential is not an unambiguous indicator for sulphide deposits (Barnes et al. 2016). Clearly, all S-rich sedimentary rocks are not equally suitable sources for S and our understanding of the processes controlling S liberation during assimilation is still inadequate to explain the reasons why.

The predominant mode of S assimilation depends on the type of sedimentary rock and can vary as a function of temperature. Magmatic assimilation of oxidized S from anhydrite evaporites is driven by dissolution and limited by sulphate-saturation of the magma (e.g., Iacono-Marziano et al. 2017). In the case of sulphide-bearing black shales, S can be mobilized by devolatilization fluids (e.g., Ripley 1981; Thériault and Barnes 1998; Virtanen et al. 2021) or it can be transported to the magma in the form of sulphide xenocrysts or xenomelts when the host silicate material melts (e.g., Thériault and Barnes 1998; Queffurus and Barnes 2014; Samalens et al. 2017; Virtanen et al. 2021). The S liberating processes in the black shales are controlled by the main silicate and sulphide phases as well as the carbonaceous materials. Characterizing the S liberating reactions from the natural rocks can be difficult as the reaction products may be overprinted upon cooling or alteration. Laboratory experiments enable constraining the up-temperature reactions in strictly controlled conditions and without the effects of overprinting processes.

For sulphide deposits to form by assimilation, the magma must react with the S-bearing material liberated from the host sedimentary rock, which changes the magma chemistry. Again, constraining the important chemical changes affecting the sulphide saturation based on the natural rock record can be difficult due to several possible overprinting processes during cooling, magmatic recharge, or alteration. Thermodynamic simulations have shown that addition of siliciclastic sedimentary material tends to lower the sulphur content at sulphide saturation (SCSS) of magmas, hence enhancing sulphide precipitation (e.g., Ripley and Li 2013). However, the most important assimilation-induced chemical factors that control sulphide precipitation remain elusive. Modern thermodynamic modelling software, such as the Magma Chamber Simulator, enable simulating phase equilibria in continuously assimilating magmas with strict constraints on mass and heat balance (Bohrson et al. 2014). These computational simulations can help us to characterize how assimilation changes the chemical composition and phase equilibrium in the magma and contribute to sulphide precipitation.

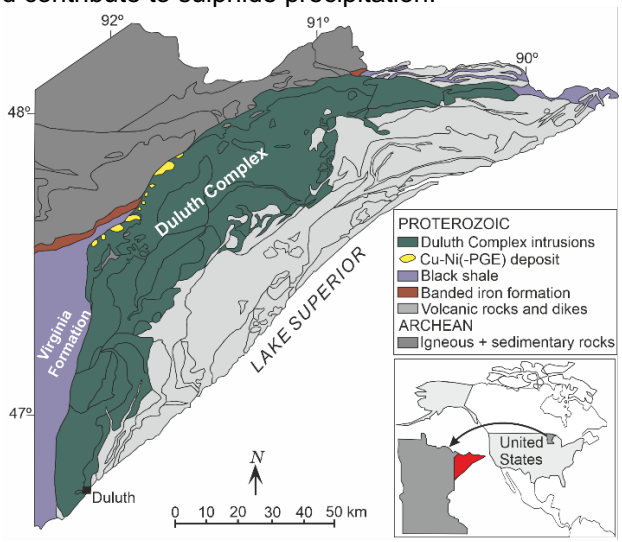

Figure 1. Geological map showing the locations of the Duluth Complex and the Virginia Formation.

The purpose of this abstract is to review the experimental work and thermodynamic simulations conducted by the author to study how black shale assimilation caused the formation of the Cu-Ni(-PGE) sulphide deposits (currently subeconomic) of the Duluth Complex, Minnesota (Fig. 1). The experiments highlight how S can be liberated from black shales, while the thermodynamic simulations focus on the sulphide precipitation in continuously assimilating magmas. A more comprehensive synthesis of the methodology and results is presented in Virtanen (2022).

2 Sulphur assimilation and magmatic sulphide saturation

2.1 Black shale devolatilization and partial melting

Virtanen et al. (2021) conducted heating experiments using a natural black shale from the Virginia Formation (Fig. 1) as the starting material. Several authors have proposed these black shales as the source of S in the Duluth Complex deposits (e.g., Ripley 1981; Thériault and Barnes 1998; Queffurus and Barnes 2014; Samalens et al. 2017). The experiments were done with externally heated pressure vessels at 200 MPa and the temperature range was 700–1000 °C. The experiments were rapidly quenched and the solid run products characterized using scanning electron microscopy. Speciation of the non-quenchable fluid phase was estimated based on mass balance calculations and thermodynamic simulations of the COHS (carbon, oxygen, hydrogen, sulphur) system.

The run products of the 700 °C experiment contain remnants of metastable muscovite and chlorite indicating incomplete devolatilization. The devolatilization fluid, however, is in equilibrium with homogeneous Cu-bearing pyrrhotite, which completely replaces the original sedimentary pyrite and chalcopyrite (Fig. 2a-b). This implies a faster equilibration rate for the sulfide-fluid system compared to that of the silicate devolatilization reactions. Mass balance calculation shows that 45 wt.% of the total S (as H_2S) and 60 wt.% of the total Cu are hosted in the fluid phase. Extrapolating these results to the devolatilized volume of the Virginia Formation, shows that the amount of liberated S is large enough to supply all of the inferred sedimentary S (ca. 75 wt.%; Ripley 1981) in the Cu-Ni(-PGE) deposits of the Duluth Complex. The same amount of fluid contains 4 Mt of Cu, which corresponds to the equivalent of roughly 15 wt.% of Cu in the Duluth Complex deposits (Listerud and Meineke 1977).

Progressing partial melting of the black shale is observed in the experiments conducted at 800–900 °C. The continuous silicate melt network hinders pervasive fluid percolation, as observed by isolated fluid bubbles and variable Cu contents in pyrrhotite. Compared to the experiment at 700 °C, pyrrhotite at 800–900 °C accommodates higher concentration of Cu at constant S/metal, which in a closed experimental system means that Cu and S partition back to the pyrrhotite from the fluid at increasing temperature. These observations imply impeded S and Cu liberation at low degrees of black shale partial melting.

At 1000 °C, silicate melt is the volumetrically dominant phase. Rounded Cu-(Ni-)bearing pyrrhotite is accompanied with Cu-rich sulphide melt and both are generally attached to fluid bubbles (Fig. 2c). The net density of the sulphide-fluid composite droplets is considerably lower than that of pure sulphide, which promotes sulphide transport between the extensively molten black shale and magma. Furthermore, if the magma is, or becomes, fluid-saturated, the sulphide-fluid pairing can aid transport of the suspended sulphides from the feeder system to the emplacement level.

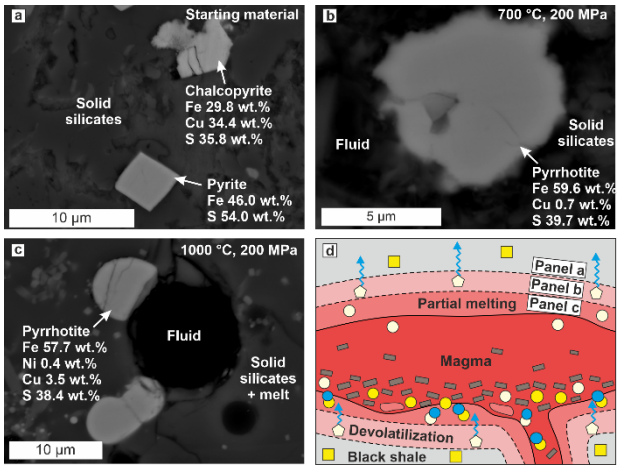

Figure 2. Back-scattered electron images of sulphides and associated phases in **a** the natural black shale starting material and the quenched experiment run product at **b** 700 °C, 200 MPa and **c** 1000 °C, 200 MPa. **d** a schematic assimilation model based on the experiment results. Yellow squares represent pyrite and chalcopyrite in the black shale host rock. White pentagons represent pyrrhotite and blue arrows fluid in devolatilization zone. White, yellow, and blue circles represent pyrrhotite and Cu-rich sulphide melt, and fluid bubbles, respectively, in partial melting zone. Silicate crystallization in the magma is indicated with brown rectangles.

Collectively, the experimental results support a view of two main stages for selective S liberation from black shales. First, devolatilization fluids can mobilize significant amounts of S and Cu, which can potentially be transported to the magma or become concentrated to suitable domains in the host rock (Fig. 2d). It should be noted that the formation of this S-bearing fluid requires the presence of pyrite and carbonaceous material in the sedimentary rock. In regionally metamorphosed black shales, pyrite may already be replaced by pyrrhotite, which is thermodynamically stable with the devolatilization fluid and hence S liberation is not expected. Subsequently, as the black shale becomes extensively partially molten, sulphide-fluid composite droplets tend to form (Fig. 2c-d). The composite droplets suspended in the partial melt are

more likely to be transported to the magma from the footwall and feeder conduit walls compared to denser unattached sulphides (Fig. 2d). This process requires extensive partial melting and is most likely to occur in xenoliths or in settings where heating is enhanced by flowing magma.

2.2 Magmatic black shale assimilation and sulphide saturation

Using the Magma Chamber Simulator, Virtanen et al. (2022) conducted thermodynamic simulations to study how black shale assimilation affects the SCSS in magma. For the simulations, we selected a basaltic parental magma composition relevant to the mineralized Duluth Complex intrusions and a black shale composition identical to the one used in the abovementioned experiments. The effects of selective assimilation of black shale partial melt and bulk assimilation on the SCSS were compared with closed-system fractional crystallization of the same magma. Mass balance of S in the magma was calculated by treating S as a trace element, because thermodynamic simulation of sulphide phase equilibrium is not currently possible with the Magma Chamber Simulator. As shown in the experiments, up-temperature S mobilization in a black shale is a complex non-linear process and cannot be precisely modelled with a constant partition coefficient. For that reason, three different coefficients were tested for S partitioning between the black shale residual and partial melt in the selective assimilation simulations: 1) completely compatible (Kd = 100), 2) equally compatible (Kd = 1), and 3) completely incompatible (Kd = 0.001). The simulation results were compared to the natural sulphide deposits to determine how effective S liberation from the black shale is required, which in turn was tentatively related to the S liberation processes identified in the experiments.

The simulations showed that the basaltic parental melt had thermodynamic potential to assimilate at least 40 wt.% of pre-heated black shale relative to the original mass of the magma regardless of the mode of assimilation (selective or bulk). Assimilation of >20 wt.% is required to replace the olivine-plagioclase dominant cumulates with orthopyroxene-plagioclase assemblages as observed in some of the natural Duluth Complex intrusions. All of the major element oxide contents, including H_2O, in the magma respond to the assimilation in such way that the SCSS diminishes. The change in magma chemistry is not only a result of the chemically mixed black shale material but is further enhanced by the changes in crystallizing phase assemblage. The formation of orthopyroxene-plagioclase cumulates as well as the first-order chemical changes affecting the SCSS are more pronounced with selective assimilation of partial melt than bulk assimilation.

One important observation is that although assimilation of S-poor black shale partial melt lowers the SCSS in the magma, the early sulphide precipitation is only slightly enhanced compared to closed-system fractional crystallization due to the diluting effect of the assimilated melt. In fact, this scenario leads to an overall sulphide grade of 0.3 wt.%, which is lower than 0.4 wt.% produced by fractional crystallization alone (Fig. 3). It is hence considered unlikely that assimilation of crustal rocks that are S-poor relative to the magma, could lead to formation of high-grade sulphide deposits.

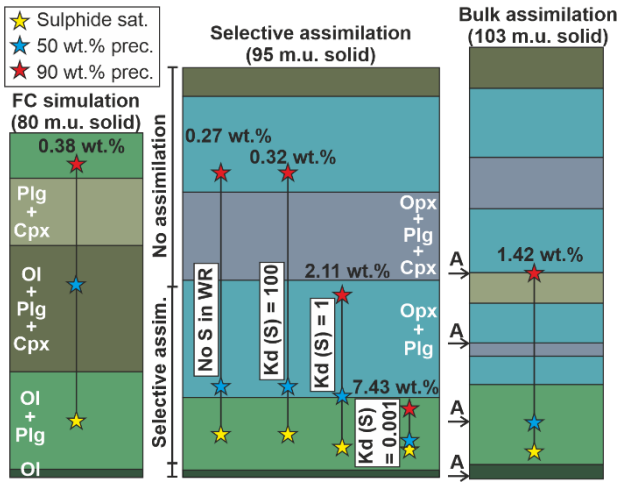

Figure 3. Thermodynamic simulation results showing cumulate stratigraphies with fractional crystallization (FC), FC + selective assimilation, and FC + bulk assimilation. Main minerals for each colour are indicated within the first two columns (Ol = olivine, Plg = plagioclase, Cpx = clinopyroxene, Opx + orthopyroxene). The column heights are scaled to the cumulates masses (mass units = m.u.). The stages of continuous selective assimilation and 10 wt.% bulk assimilation steps (A) are indicated left side of the relevant columns. The stars indicate the timing of sulphide saturation (yellow) as well as 50 (blue) and 90 wt.% (red) sulphides precipitated. The wt.% numbers indicate the average sulphide grade between the yellow and red stars without dynamic accumulation. The Kd values indicate bulk partition coefficients for sulphur (S) in the selectively assimilated black shale. See text for details about the simulations.

Based on the simulations, both selective and bulk assimilation can supply the magma with ca. 75 wt.% black shale-derived S as previously suggested for the Duluth Complex deposits (Ripley 1981). With bulk assimilation, this limit is reached when the amount of assimilated black shale is 40 wt.% relative to the original mass of the magma. Without dynamic accumulation, most of the sulphides will be scattered within the early olivine-plagioclase and the subsequent orthopyroxene-plagioclase cumulates with an average sulphide abundance of ca. 1.4 wt.% (Fig. 3). In the case of selective assimilation, S must be at least equally concentrated between the assimilated partial melt and residue (i.e., Kd ≤ 1) to fulfill the imposed natural constraint for the S mass balance. When S is equally compatible to the black shale residual and assimilated partial melt, the magmatic sulphides are distributed between the early olivine-plagioclase and orthopyroxene-plagioclase cumulates with an average grade of 2.1

wt.% (Fig. 3). Comparable S fluxes could arguably be generated either by S liberation via fluids or by sulphide transport via black shale partial melt. In the simulation where S is considered highly incompatible to the black shale residual (Kd = 0.001), the sulphides mostly reside within the olivine-plagioclase cumulates with an average grade of 7.4 wt.% (Fig. 3). It is clear that only fluid-mediated S assimilation could lead to comparably effective extraction of S from the residual black shale.

Roughly 70% of the Duluth Complex deposits are hosted in olivine-plagioclase cumulates, whereas the rest are within the orthopyroxene-plagioclase cumulates. Based on the data provided by Listerud and Meineke (1977), the average sulphide grade was tentatively estimated to be 7.3 wt.%. Comparing these natural data with the simulations, it seems that the olivine-plagioclase hosted sulphide deposits can readily form without significant dynamic accumulation if S extraction from the black shale is highly selective. With less effective S extraction from the black shale, more silicate melt is assimilated and the sulphides occur increasingly within the orthopyroxene-plagioclase cumulates. The grade of the simulated deposits is, however, low compared to the natural deposits, which means that subsequent dynamic sulphide accumulation is necessary.

3 Concluding remarks

The results from the experiments and thermodynamic simulations increase our understanding of the complexity behind the magmatic assimilation of S from black shales. As a black shale is heated by magma, it is first subjected to devolatilization and subsequently partial melting, which can both contribute to selective S and metal liberation from the solid residue. These processes are controlled by the mineralogy and carbonaceous materials in the black shale as well as by the heat flow from the magma, hence their relative importance has to be evaluated case specifically. The assimilated black shale material changes the chemistry and consequently phase equilibrium in the magma. These assimilation-induced changes tend to enhance sulphide precipitation from the magma but assimilation of external S seems to be required for economically important deposits to form.

Acknowledgements

Jussi S. Heinonen, Ferenc Molnár, Max Schmidt, Felix Marxer, Nicholas Barber, Nico Kueter, and Fabio Cafagna are thanked for their contributions to the conduction and interpretation of the experiments and numerical simulations.

References

Barnes SJ, Cruden AR, Arndt N, Saumur BM (2016) The mineral system approach applied to magmatic Ni-Cu-PGE sulphide deposits. Ore Geol. Rev. 76: 296–316. http://dx.doi.org/10.1016/j.oregeorev.2015.06.012

Bohrson WA, Spera FJ, Ghiorso MS, Brown GA, Creamer JB, Mayfield A (2014) Thermodynamic model for energy-constrained open-system evolution of crustal magma bodies undergoing simultaneous recharge, assimilation and crystallization: the Magma Chamber Simulator. J. Petrol. 55:1685–1717. https://doi.org/10.1093/petrology/egu036

Iacono-Marziano G. Ferrana C, Gaillard F, Di Carlo I, Arndt NT (2017) Assimilation of sulfate and carbonaceous rocks: Experimental study, thermodynamic modeling and application to the Noril'sk-Talnakh region (Russia). Ore Geol. Rev. 90:399–413. http://dx.doi.org/10.1016/j.oregeorev.2017.04.027

Listerud WH, Meineke DG (1977) Mineral resources of a portion of the Duluth Complex and adjacent rocks in St. Louis and Lake Counties, Northeastern Minnesota. Minnesota Department of Natural Resources Division of Minerals 93:1–84.

Queffurus M, Barnes S-J (2014) Selenium and sulphur concentrations in country rocks from the Duluth Complex, Minnesota, USA: Implications for formation of the Cu-Ni-PGE sulphides. Econ. Geol. 109:785–794. https://doi.org/10.2113/econgeo.109.3.785

Ripley EM (1981) Sulphur Isotopic Studies of the Dunka Road Cu-Ni Deposit, Duluth Complex, Minnesota. Econ. Geol. 76:610–620. https://doi.org/10.2113/gsecongeo.76.3.610

Ripley EM, Li C (2013) Sulfide saturation in mafic magmas: Is external sulfur required for magmatic Ni-Cu(-PGE) ore genesis? Econ. Geol. 108: 45–58. https://doi.org/10.2113/econgeo.108.1.45

Samalens N, Barnes S-J, Sawyer EW (2017) The role of black shales as a source of sulphur and semimetals in magmatic nickel-copper deposits: Example from the Partridge River Intrusion, Duluth Complex, Minnesota, USA. Ore Geol. Rev. 81:173–187. https://doi.org/10.1016/j.oregeorev.2016.09.030

Thériault RD, Barnes S-J (1998) Compositional variations in Cu-Ni-PGE sulphides of the Dunka Road Deposit, Duluth Complex, Minnesota; the importance of combined assimilation and magmatic processes. Canad. Mineral. 36:869–886.

Virtanen VJ (2022) Thermally induced processes in black shales and the formation of Cu-Ni(-PGE) deposits in and around mafic intrusions – an example from the Duluth Complex, Minnesota, United States. Dissertation, University of Helsinki.

Virtanen VJ, Heinonen JS, Barber ND, Molnar F (2022) Complex Effects of Assimilation on Sulfide Saturation Revealed by Modeling with the Magma Chamber Simulator: A Case Study on the Duluth Complex, Minnesota, USA. Econ. Geol. https://doi.org/10.5382/econgeo.4917

Virtanen VJ, Heinonen JS, Molnar F, Schmidt MW, Marxer F, Skyttä P, Kueter N, Moslova K (2021) Fluids as primary carriers of sulphur and copper in magmatic assimilation. Nat. Commun. 12:1–12. https://doi.org/10.1038/s41467-021-26969-3

Solubility of selected elements in the synthetic analogue of kotulskite (PdTe)

Anna Vymazalová[1], František Laufek[1], Marek Tuhý[1,2], Jan Kamenský[1,2],
[1]Czech Geological Survey, Prague, Czech Republic
[2]Institute of Geochemistry, Mineralogy and Mineral Resources, Faculty of Science, Charles University, Prague, Czech Republic

Abstract. The solubility of selected elements in the synthetic analogue of palladium telluride kotulskite (PdTe) was studied experimentally at 400 °C. We have investigated the solubility of ternary elements in kotulskite in the range 0 to 30 at. %, on the tie-line Pd-Te-X, with Pd = 50 at.%, with X = Ag, As, Bi, Cu, Sb, Sn, Se. For the purpose of this study silica-glass tube method was used, the experimental products were evaluated by means of X-ray powder-diffraction analysis, reflected light and electron microscopy. Assessed solid solution series and stable associations should be sought in assemblages with other PGM and known Pd tellurides, likely in magmatic Cu-Ni-PGE mineral deposits, associated with mafic and ultramafic igneous rocks.

1 Introduction

There are four known minerals among palladium tellurides: kotulskite (PdTe), merenskyite ($PdTe_2$), telluropalladinite (Pd_9Te_4), keithconnite ($Pd_{3-x}Te$). Further, there are known occurrences at natural conditions of phases $Pd_{13}Te_3$ and Pd_3Te_2 (e.g. Arnason et al., 1997). However, these occurrences have not yet been described as minerals. Among palladium tellurides, kotulskite (Genkin et al. 1963) and merenskyite (Kingston 1966) belong to the most abundant minerals, commonly found together among other platinum-group minerals and Cu-Ni-Fe sulphides. Palladium tellurides are generally found in Cu-Ni-PGE mineral deposits, associated with mafic and ultramafic igneous rocks. They also occur in other types of deposits, enriched in PGE, like porphyry copper/gold systems, sedimentary-hosted massive sulphides or metalliferous black shales.

We have experimentally investigated the solubility of selected elements (Ag, As, Bi, Cu, Sb, Sn, Se and Pb) in the synthetic analogue of kotulskite at 400 °C. Furthermore, we have studied the ternary Pd-X-tellurides in order to asses stable assemblages in the corresponding ternary systems. The evacuated silica tube method was applied for the purpose of this study. The experimental products were examined primarily with X-ray powder diffraction, and in polished sections by means of reflected light and electron microscopy.

2 Techniques and methods

2.1 Experimental

Experiments were performed in evacuated and sealed silica glass tubes in horizontal tube furnaces. Charges of about 300 mg were carefully weighed out from the native elements (palladium powder, 99.95% purity; tellurium ingot, 99.999% purity; and selected elements Ag, As, Bi, Cu, Sb, Sb, Se, Pb of 99.999% purity). The starting mixtures were first melted at 1000 °C for several hours. Then, the run products were ground in an agate mortar under acetone and reheated to 400 °C (for 3 to 4 months). After heating, quenching occurred by dropping the capsules in cold water. Phases in the run products were characterized by X-ray powder diffraction and, in polished sections examined under reflected light and with electron-microprobe techniques (EPMA).

2.2 Electron probe microanalyses

The EPMA analyses were performed with a JEOL JXA 8230 electron probe microanalyser in a wavelength-dispersion mode using an electron beam focussed to 1-2 μm. Pure elements were used as standards. Concentrations were quantified on the L_α lines for Pd, Te, As, Sb, Sn, Se, Pb; the L_β for Ag; the K_α for Cu and M_α for Bi; with an accelerating voltage of 15 keV, and a beam current of 10 nA. In a sample, compositional data were collected from several grains within a polished section.

2.3 X-ray diffraction analyses

The X-ray diffraction patterns (XRD) were collected in Bragg-Brentano geometry on Bruker D8 Advance diffractometer equipped with the Lynx Eye XE detector and Cu*K*α radiation source. The data were collected in the angular range from 10 to 140° 2Θ°.

3 Results and Discussion

We performed the experimental runs in a series Pd – X–Te, with X = Ag, As, Bi, Cu, Sb, Sn, Se and Pb, with compositional step from 5 to 10 at.%. In detail, the following experimental runs were studied Pd50(Te50-X) with X = 0.5, 10, 20, 30, some additional runs were also performed within Pd50-XTe50, with X= 10,20. Kotulskite dissolves up to 1 at.% Cu. Our investigations in the Pd-Sb-Te system, in the range up to $Pd_{50}(Te_{20}Sb_{30})$, confirmed the continuous solid solution (ss) between sudburyite and kotulskite (Figs 1-3). This is in agreement with the study of El-Boragy and Schubert (1971) at 400 °C, and also at 600 °C by Kim and Chao (1991). Furthermore, natural occurrences forming the

kotulskite – sudburyite (ss-PdTe – ss-PdSb) series are well established from various Cu-Ni-PGE deposits.

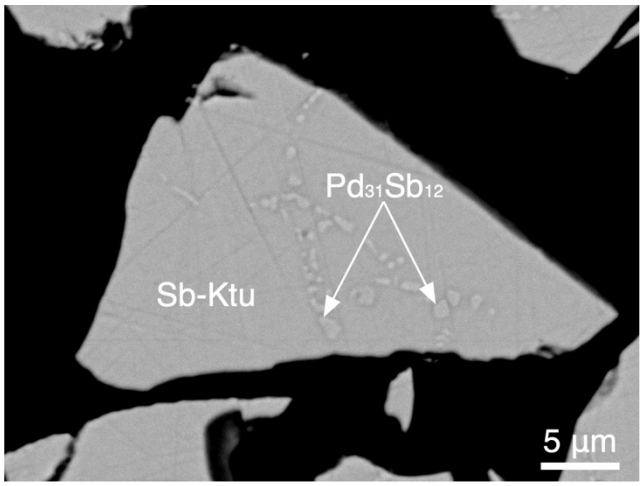

Figure 1. BSE image of kotulskite (dissolving 4.5 at. % Sb) forming a stable association with phase $Pd_{31}Sb_{12}$ (light). Run No KtSb 0.5, heated four months, T = 400 °C.

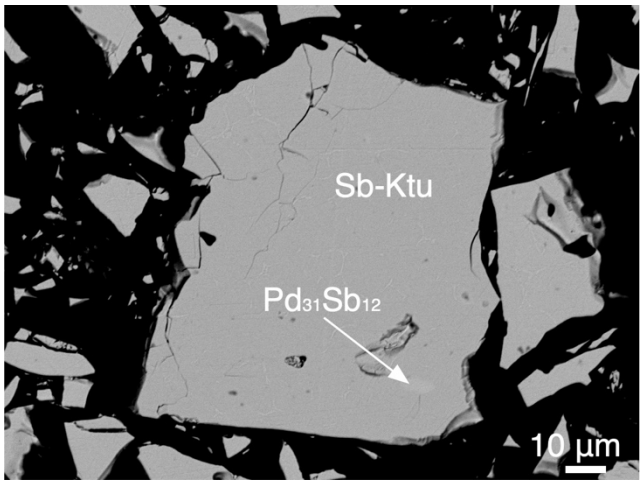

Figure 2. BSE image of kotulskite (dissolving 20 at. % Sb) Run No KtSb 20, heated four months, T = 400 °C.

Our experimental study has shown the maximum solubility of As in kotulskite up to 4 at.%. Kotulskite ss forms a stable association with palladoasrsenide and phase $PdAs_2$ at 400 °C(Fig.4). Kotulskite dissolves up to 19 at.% Sn as suggested by Vymazalová and Drábek (2010) and up to 10 at. % Se (Vymazalová et al. 2019).

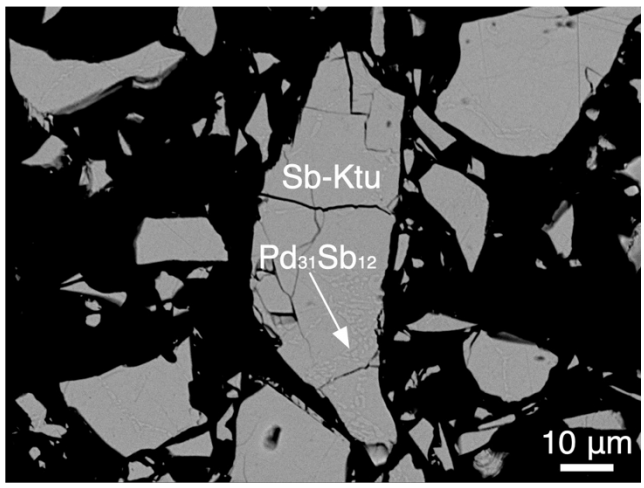

Figure 3. BSE image of kotulskite (dissolving 30 at. % Sb) in association with phase $Pd_{31}Sb_{12}$ (light inclusions). Run No KtSb 30, heated four months, T = 400 °C.

Kotulskite forms an extensive solid solution with Pb, dissolving up 30 at.% Pb (Vymazalová and Drábek 2011). It dissolves up to 10 at. % Se (Vymazalová et al. 2019). Kotulskite does not dissolve Ag at 400 °C which is in agreement with the experimental study of the system at 350 and 450 °C (Vymazalová et al. 2015). The system Pd-Bi-Te has been preliminarily experimentally studied by Evstigneeva et al. (2019) in the temperature range 350-550 °C. They detected the ss-PdTe – ss-PdBi association. The kotulskite – sobolevskite series were widely reported from a number of Cu-Ni-PGE mineral deposits associated with mafic and ultramafic igneous rocks (e.g. Evstigneeva et al. 1975, Sluzhenikin 2011, Cook et al. 2002, Barkov et al. 2002, among others).

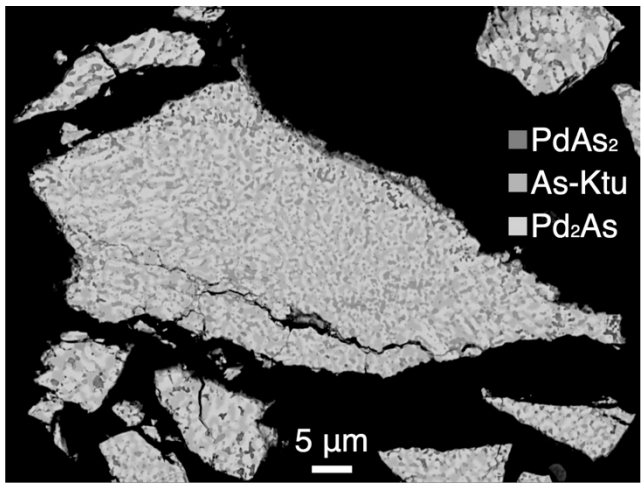

Figure 4. BSE image of stable association of kotulskite (dissolving 3 at. % As) in association with $PdAs_2$ and palladoarsenide Pd_2As. Run No KtAs30, heated four months, T = 400 °C.

The unit-cell parameters of selected kotulskite solid solutions are summarized in Table 1. Fig. 5 shows the evolution of unit-cell volume. The incorporation of Bi into the kotulskite structure results in a significant increase of the unit-cell

volume. Contrary to that, incorporation of Sb leads to a decrease up to 0.39 apfu of Sb, followed by a slight increase of the unit-cell volume. Minute incorporation of As (up to 0.05 apfu) results in a decrease of the unit-cell volume.

Table 1. The unit-cell parameters of selected kotulskite solid solutions

	Unit cell			Apfu 2		
	c (Å)	*c*(Å)	*V*(Å^3)	Te	X	Pd
PdTe	4.1523	5.6719	84.694	1	0	1
KtBi05	4.1602	5.669	84.971	0.87	0.13	0.99
KtBi10	4.1676	5.6676	85.252	0.80	0.20	0.99
KtBi20	4.1839	5.6744	86.024	0.60	0.40	1.00
KtBi30	4.1952	5.6824	86.609	0.40	0.60	1.01
KtSb05	4.1405	5.6544	83.951	0.93	0.09	0.98
KtSb10	4.1336	5.643	83.505	0.84	0.19	0.97
KtSb20	4.1098	5.6139	82.117	0.63	0.39	0.98
KtSb30	4.121	5.6252	82.735	0.39	0.61	1.00
KtAs05	4.1215	5.6474	83.082	1.01	0.03	0.96
KtAs10	4.1147	5.643	82.743	1.00	0.05	0.95

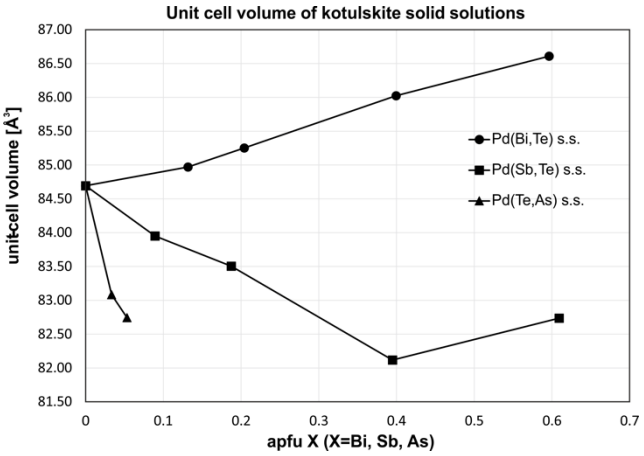

Fig. 5 The changes of unit-cell volume in kotulskite involving Bi, Sb and As.

3 Conclusions

We have proved a range of solid solutions in the systems Pd-X-Te, with X = Ag, As, Bi, Cu, Sb, Sn, Se and Pb at 400 ºC. We have assessed the maximum solubility of selected elements in kotulskite. In some cases, the solid solution series are misinterpreted as potential new minerals occurring in nature. We have further proved the stable association of kotulskite ss with palladoasrsenide and phase $PdAs_2$.The solid solution series established, and stable associations proved, can be found in Cu-Ni-PGE mineral deposits associated with mafic and ultramafic igneous rocks.

Acknowledgements

Financial support through the Project No 22-26485S from the Grant Agency of the Czech Republic (GACR) is gratefully acknowledged.

References

Arnason JG, Bird DK, Bernstein S, Kelemen PB (1997) Gold and platinum-group element mineralization in the Kruuse Fjord gabbro complex, east Greenland. Econ Geol 92: 490-501.

Barkov AY, Laflamme JHG, Cabri LJ, Martin RF (2002) Platinum-group minerals from the Wellgreen Ni-Cu-PGE deposit, Yukon, Canada. Can Min 40: 651-669.

Cook NJ, Ciobanu CL, Merkle RKW, Bernhardt H-J (2002) Sobolevskite, taimyrite, and Pt_2CuFe (tulameenite?) in complex massive talnakhite ore, Talnakh Orefield, Russia. Can Min 40: 329-340.

El-Boragy M, Schunert K (1971) Uber einige Varianten der NiAs-Familie in Mischungen des Palladiums mit B-Elementen. Z. Metallkunde 62: 314-323.

Evstigneeva PV, Nickolsky MS, Geringer NV, Vymazalová A, Nekrasov AN, Chareev DA (2019) Pt- and Pd-bismuthotellurides: phase relations in the Pt-Bi-Te and Pd-Bi-Te systems. Proceedings of the 15th Biennial SGA Meeting, 27-30 August 2019, Glasgow, UK.

Evstigneeva TL, Kovalenker VA (1975) Sobolevskite, a new bismuthide of palladium, and the nomenclature of minerals of the system PdBi-PdTe-PdSb. Int Geol Rev 18:856-866.

Genkin AD, Zhuravlev NN, Smirnova EM (1963) Moncheite and kotulskite - new minerals - and the composition of michenerite. Zapiski Vsesoyuznogo Mineralogicheskogo Obshchestva 92: 33-50.

Kim W-S, Chao GY (1991) Phase relations in the system Pd-Sb-Te. Can Min 29: 401-409.

Kingston GA (1966) The occurrence of platinoid bismuthotellurides in the Merensky Reef at Rustenburg platinum mine in the western Bushveld. Min Mag 35: 815-835.

Sluzhenikin SF (2011) Platinum-copper-nickel and platinum ores of Noril'sk region and their ore mineralization. Rus J Gen Chem 81: 1288–1301.

Vymazalová A, Chareev DA, Kristavchuk A, Laufek F Drábek M (2014) The system Ag-Pd-Se: Phase relations involving minerals and potential new minerals. Can Min 52: 77-89.

Vymazalová A, Drábek M (2010) The system Pd-Sn-Te at 400°C and mineralogical implications. II. The ternary phases. Canadian Mineralogist 48: 1051-1058.

Vymazalová A, Drábek M (2011) The Pd–Pb–Te system: phase relations involving pašavaite and potencial minerals. Can Min 49: 1679-1686.

Vymazalová A, Laufek F, Kristavchuk AV, Chareev DA, Drábek M (2015) The system Ag-Pd-Te: phase relations and mineral assemblages. Min Mag 79: 1813-1832.

Vymazalová A, Tuhý M, Laufek F (2019) Palladium and platinum seleno-tellurides and their associations. Proceedings of the 15th Biennial SGA Meeting, 27-30 August 2019, Glasgow, UK.

